

# Multi-Objective Optimization of Vertical Axis Wind Turbine Pitch Control

Optimal dynamic individual blade pitch control strategies to maximize power efficiency and minimize normal load and torque fluctuations

Saskia van Nieuwstadt



# Multi-Objective Optimization of Vertical Axis Wind Turbine Pitch Control

Optimal dynamic individual blade pitch control strategies  
to maximize power efficiency and minimize normal load  
and torque fluctuations

Thesis report

by

Saskia van Nieuwstadt

to obtain the degree of Master of Science  
in Sustainable Energy Technology  
at Delft University of Technology  
to be defended publicly on 15 July 2025

*Thesis committee:*

Chair: Prof.dr. D.A. (Dominic) von Terzi  
Supervisors: Dr. W. (Wei) Yu  
Adhyanth Giri Ajay  
External examiner: Dr. R.P. (Richard) Dwight  
Place: Faculty of Aerospace Engineering, Delft  
Project Duration: November, 2024 - July, 2025  
Student number: 5915368

An electronic version of this thesis is available at <http://repository.tudelft.nl/>.

Wind Energy Group, Faculty of Aerospace Engineering · Delft University of Technology  
Faculty of Electrical Engineering, Mathematics, and Computer Science · Delft University of Technology



Copyright © Saskia van Nieuwstadt, 2025  
All rights reserved.

# Abstract

Wind energy is central to many international climate goals which promote the transition to carbon-free energy sources. Most commercial wind turbines at present are horizontal axis wind turbines (HAWTs). However, vertical axis wind turbines (VAWTs) can fill two gaps in wind energy: offshore floating wind energy and urban wind energy, in part due to their insensitivity to the incoming wind direction, low center of gravity, high power density, and low noise production. Historically, VAWTs have suffered from fatigue issues, low power efficiency, and difficulty in self-starting. Active variable blade pitch control can address these issues. It can be used to maximize the power efficiency, minimize blade load fluctuations to alleviate fatigue, and minimize torque fluctuations. Numerous studies on VAWT blade pitching have been done in the past, both numerical and experimental, and both with fixed and variable blade pitch. Numerical studies use models with varying accuracy. If pitch optimization is conducted, the most common objective is maximizing the power coefficient,  $C_p$ . However, blade pitch control can also be used to improve the loading characteristics on a VAWT.

In this study, individual active variable blade pitch control optimization is performed with multiple objectives, recognizing that there are multiple uses of pitch control for VAWTs. The goal of this study is to develop an optimal pitch function(s) that maximizes  $C_p$  and minimizes the fluctuations in rotor normal force and torque. The pitch angle is implemented as a third-order sinusoidal function. This is a numerical study, which uses the two-dimensional actuator cylinder (2D AC) model. The unified non-dominated sorting genetic algorithm III (U-NSGA-III) is used to perform pitch function optimization. The multiple objectives are 1) maximize  $C_p$ , 2) minimize rotor normal load fluctuations, and 3) minimize rotor torque fluctuations. The objectives are built up in successive optimization cases resulting in three optimization problems, a single-, two-, and three-objective optimization problem, respectively. Solutions are found which achieve all three objectives at the same time. Adding the second and third objectives changes the optimal solutions, and the multiple objectives are important to consider because only maximizing  $C_p$  leads to an increase in unfavorable normal load and torque fluctuations.

When only maximizing  $C_p$  is considered, the power coefficient can be increased by 17.3% over the base case (with zero pitch). The power coefficient can be increased by 10.3% over the base case without increasing the normal load fluctuations or the torque fluctuations. The normal load fluctuations can be reduced by 22.1% compared to the base case while maintaining the power coefficient and torque fluctuations. The torque fluctuations can be reduced by 13.9% compared to the base case while maintaining the power coefficient and normal load fluctuations. The optimal pitch functions which maximize  $C_p$  and/or minimize the torque fluctuations require high variations in the pitch angle throughout the rotor revolution. Meanwhile, optimal pitch functions which minimize the normal load fluctuations require fewer oscillations (they resemble more first-order sinusoids). For the majority, the optimal pitch functions pitch the blade outward in the upwind half and inward in the downwind half of the revolution, though adjusting the pitch angle around the transitions between the upwind and downwind halves can increase the power coefficient. Optimal pitch functions which minimize the normal load fluctuations reduce the angle of attack and loads throughout most of the revolution and shift the loading on the rotor toward the downwind half as compared to the upwind half. Minimizing the torque fluctuations requires pitch functions with relatively large amplitudes. The pitch functions spread out the blade loading and power generation across the revolution by reducing the loads and power generation in the middle of the upwind and downwind regions and increasing them around the transitions between the upwind and downwind regions. In some cases, the optimal pitch functions are transferable to other operating conditions and turbine designs. They can lead to an increase in  $C_p$  for a certain range of tip speed ratios, however, the optimal pitch functions depend on the tip speed ratio. The optimal pitch functions and their effectiveness are similar when the turbine has three compared to two blades. Implementing an optimal pitch function found in this study can increase the power output of VAWTs while not compromising their structural integrity and/or alleviate fatiguing load fluctuations while maintaining the power output. Optimal blade pitching can lead to a significant improvement in the operating performance of VAWTs.

# Acknowledgments

I would like to thank my supervisor Wei Yu and daily supervisor Adhyanth Giri Ajay for their guidance throughout this thesis project. Thank you for engaging in weekly meetings, answering my questions, giving me feedback, and always replying quickly to emails and messages. Thank you for shaping the scope of this project with me and making it possible. Thank you, Wei, for your counsel on optimization, wind turbine aerodynamics, and state-of-the-art practices for HAWTs. Thank you, Adhyanth, for sharing your knowledge on VAWT aerodynamics and modeling. I would also like to thank Wim Bierbooms, the profile coordinator for wind energy in the Sustainable Energy Technology program, for helping me with the organizational steps of this thesis. I would like to thank David Bensason for answering my questions about VAWT loading in Adhyanth's absence, and Kevin Moore for providing airfoil polar data. Thank you also to everyone in the wind energy group at TU Delft.

I would like to thank my family and friends who supported me throughout my studies and who have always believed in me; especially my sister, for our weekly calls. I would like to thank my extended family here in the Netherlands with whom I have been able to spend more time with during my studies. I would also like to thank my friends back home who wrote letters or came to visit. Thank you also to my classmates, band mates, and teammates.

*Saskia van Nieuwstadt  
July, 2025  
Delft, the Netherlands*

# Contents

<b>List of Figures</b>	<b>ix</b>
<b>List of Tables</b>	<b>xiv</b>
<b>1 Introduction</b>	<b>1</b>
<b>I Literature Review</b>	<b>4</b>
<b>2 The Role of Vertical Axis Wind Turbines in Sustainable Energy Systems</b>	<b>5</b>
2.1 The Need for Wind Energy . . . . .	5
2.2 VAWT History . . . . .	6
2.3 The Advantages of VAWTs . . . . .	7
2.4 VAWT Disadvantages . . . . .	9
2.5 Pitch Control as a Solution . . . . .	9
<b>3 Vertical Axis Wind Turbine Modeling and Pitch Control</b>	<b>10</b>
3.1 Turbine Coordinate System . . . . .	10
3.2 VAWT Aerodynamics . . . . .	12
3.3 VAWT Numerical Models . . . . .	16
3.4 2D Actuator Cylinder Model Derivation . . . . .	18
3.5 Review of VAWT Pitch Control in Literature . . . . .	21
<b>4 Multi-Objective Optimization</b>	<b>37</b>
4.1 Classical Multi-Objective Optimization Methods . . . . .	37
4.2 Genetic Algorithms . . . . .	37
4.3 U-NSGA-III . . . . .	39
4.4 Post-Optimization Analysis . . . . .	41
<b>II Methodology</b>	<b>44</b>
<b>5 VAWT Model Implementation</b>	<b>45</b>
5.1 2D Actuator Cylinder Model Implementation . . . . .	45
5.2 Reference Turbine . . . . .	49
<b>6 Multi-Objective Optimization Implementation</b>	<b>53</b>
6.1 Functional Form of the Pitch Angle . . . . .	53
6.2 Optimization Problem Definition . . . . .	56
6.3 Optimization Algorithm and Parameters . . . . .	58
6.4 Optimization Problem Execution and Analysis . . . . .	62
<b>III Results</b>	<b>63</b>
<b>7 2D Actuator Cylinder Model Validation</b>	<b>64</b>
7.1 Model Sensitivity . . . . .	64
7.2 Model Verification and Validation . . . . .	68
<b>8 Optimal Pitch Results</b>	<b>75</b>
8.1 Base Case . . . . .	75
8.2 Single Objective: Maximize $C_p$ . . . . .	75
8.3 Two Objectives: Maximize $C_p$ and Minimize $\sigma(Q_n)$ . . . . .	78
8.4 Three Objectives: Maximize $C_p$ , Minimize $\sigma(Q_n)$ , and Minimize $\sigma(Q_t)$ . . . . .	85

---

8.5	Comparison Across Optimization Cases . . . . .	93
8.6	Physical Implications of the Pitching Motion . . . . .	98
8.7	Pitch Optimization Key Conclusions . . . . .	98
<b>9</b>	<b>Optimal Pitch Under Different Operating Condition and Turbine Design</b>	<b>100</b>
9.1	Different Operating Condition: Tip Speed Ratio . . . . .	100
9.2	Different Turbine Design: Number of Blades . . . . .	103
<b>IV</b>	<b>Conclusion</b>	<b>106</b>
<b>10</b>	<b>Conclusion</b>	<b>107</b>
<b>11</b>	<b>Recommendations</b>	<b>110</b>
	<b>References</b>	<b>116</b>
<b>A</b>	<b>Non-dominated Sorting Genetic Algorithm II</b>	<b>117</b>
<b>B</b>	<b>Additional 2D AC Model Validation</b>	<b>119</b>

# Nomenclature

## List of Abbreviations

(U)RANS	(Unsteady) Reynolds-Averaged Navier-Stokes
1D	One-Dimensional
2D	Two-Dimensional
3D	Three-Dimensional
AC	Actuator Cylinder
BEM	Blade Element Model
CFD	Computational Fluid Dynamics
CO <sub>2</sub>	Carbon dioxide
DMST	Double Multiple Streamtube Model
EU	European Union
HAWT	Horizontal Axis Wind Turbine
IEA	International Energy Agency
MOOP	Multiple-Objective Optimization Problem
MST	Multiple Streamtube Model
NACA	National Advisory Committee for Aeronautics
NO <sub>x</sub>	Nitrogen oxides
NSGA-II	Non-dominated Sorting Genetic Algorithm II
NSGA-III	Non-dominated Sorting Genetic Algorithm III
PIV	Particle Image Velocimetry
PM	Polynomial Mutation
PV	Photovoltaic
rpm	Revolutions per minute
Sandia, SNL	Sandia National Laboratories
SBX	Simulated Binary Crossover
SO <sub>2</sub>	Sulfur dioxide

U-NSGA-III Unified Non-dominated Sorting Genetic Algorithm III

VAWT Vertical Axis Wind Turbine

## List of Symbols

$\alpha$	Angle of attack
$\alpha_g$	Geometric angle of attack
$\alpha_{eff}$	Effective angle of attack
$\alpha_{ss}$	Static stall angle
$\Delta\theta$	Azimuthal range of AC section
$\epsilon_m$	Constrained value on objective function $m$ in the $\epsilon$ -constraint method
$\eta_c$	Crossover distribution index
$\eta_m$	Mutation distribution index
$\lambda$	Tip speed ratio
$\mathbf{x}_i$	Individual/solution $i$ , a vector of decision variables
$\Omega$	Rotational speed
$\phi_i$	Phase shift of the $i$ th harmonic of the pitch function
$\pi(\mathbf{x})$	Reference point closest to $\mathbf{x}$
$\rho$	Air density
$\sigma$	Rotor solidity
$\theta$	Azimuth angle
$\theta_i, \theta_j$	AC control point azimuth position at index $i, j$
$\theta_p$	Pitch angle
$\varphi$	Inflow angle
$a$	Induction factor
$A_0$	Intercept/offset of the pitch angle
$A_i$	Amplitude of the $i$ th harmonic of the pitch function
$B$	Number of blades

$c$	Blade chord length	$n_i, n_j$	Domination count of solution $i, j$
$C_d$	Drag coefficient	$N_s$	Number of AC sub-sections/sub-elements
$C_l$	Lift coefficient	$N_{el}$	Number of AC sections/elements
$C_n$	Normal force coefficient	$N_{pop}$	Population size
$C_p$	Power coefficient	$n_{var}$	Number of decision variables
$C_T$	Thrust coefficient	$O_t$	Offspring population (at generation $t$ )
$C_t$	Tangential force coefficient	$P$	Power
$D$	Rotor diameter	$p$	Pressure
$d(\mathbf{x})$	Perpendicular distance between $\mathbf{x}$ and $\pi(\mathbf{x})$	$p_c$	Crossover probability
$d_i$	Crowding distance of solution $i$	$p_m$	Mutation probability
$f$	Control point scaling factor	$P_t$	Parent population (at generation $t$ )
$F_D$	Drag force	$P'_t$	Mating parent population (at generation $t$ )
$f_e$	Excitation frequency	$P_H$	Number of partitions
$F_L$	Lift force	$Q_n$	(Nondimensional time-averaged) blade distributed body normal force
$F_l$	Last non-fully accommodated front	$Q_t$	(Nondimensional time-averaged) blade distributed body tangential force
$f_m$	Objective function $m$	$R$	Rotor radius
$F_n$	Normal blade force	$R_t$	Combined parent and offspring population (at generation $t$ )
$F_t$	Tangential blade force	$Re$	Reynolds number
$F_x$	x blade force	$S_i$	Set of solutions dominated by solution $i$
$f_x$	Volume force x component	$St$	Strouhal number
$f_y$	Volume force y component	$V_\infty$	Incoming/freestream wind speed
$g_x$	Second order (induced) volume force x component	$V_n$	Normal velocity
$g_y$	Second order (induced) volume force y component	$V_t$	Tangential velocity
$H$	Number of reference points/directions	$V_x$	x velocity
$I_{wi}$	Influence coefficient for direction $i$	$v_x$	Nondimensional x velocity
$K$	Number of accommodated solutions in $F_l$	$V_y$	y velocity
$k_0, k_1, k_2, k_3$	Induction factor polynomial coefficients	$v_y$	Nondimensional y velocity
$k_a$	Modified linear solution correction factor	$V_{ind,i}$	Induced velocity component in direction $i$
$l$	Rotor height/blade length	$V_{ind}$	Induced velocity
$M$	Number of objectives	$V_{rel}$	Relative velocity
$M_Z$	Blade pitching moment	$V_{rot}$	Rotational velocity
		$w$	Frequency multiplier of the pitch function

---

$w_x$	Nondimensional induced x velocity	$y$	Crosswind/lateral direction
$w_y$	Nondimensional induced y velocity	$y_j$	Evaluation control point y-coordinate
$x$	Streamwise direction	$z$	Vertical direction
$x_j$	Evaluation control point x-coordinate		

# List of Figures

2.1	Two types of wind turbines, (a) a horizontal axis wind turbine (HAWT) and (b) a vertical axis wind turbine (VAWT), specifically an H-rotor. Images from [34] and [35]. . . . .	5
3.1	The VAWT coordinate system. . . . .	10
3.2	A VAWT divided into two halves: upwind and downwind. . . . .	11
3.3	Dimensions of a VAWT: the rotor radius $R$ , blade length $l$ , and chord length $c$ . The VAWT has three blades ( $B = 3$ ). Figure modified from [4]. . . . .	11
3.4	The blade pitch angle sign convention. A positive pitch angle corresponds to rotating the leading edge inward. . . . .	12
3.5	Velocity components experienced by a VAWT blade: freestream wind velocity $V_\infty$ , rotational velocity $V_{rot}$ , and induced velocity $V_{ind}$ . Their vector sum is the relative velocity $V_{rel}$ . Figure based on [28]. . . . .	13
3.6	Decomposition of the VAWT blade forces and angles. Figure based on [28]. . . . .	14
3.7	Typical power curve of a wind turbine, including the full load and partial load regions, as well as important wind speed demarcations. . . . .	15
3.8	The actuator cylinder model coordinate system, showing the sign convention of the nondimensional, time-averaged blade forces. Figure based on [39]. . . . .	19
3.9	Regions of the AC: I in front of the cylinder, II inside the cylinder, and III in the wake of the cylinder. The region an evaluation point is in determines which * and ** terms are added in the induced velocity. Figure based on [39]. . . . .	20
3.10	VAWT pitch control can be broken down into several categories. . . . .	22
3.11	Variable pitch laws developed by Lazauskas [16] for three different blade pitch systems. The tip speed ratio is 3 (the author also analyzes tip speed ratios of 2 and 4). Pinson is the sinusoidal system. Note that Gamma is the pitch angle ( $=\theta_p$ ). Note that Lazauskas [16] uses the opposite pitch sign convention as used in this study. Figure from [16]. . . . .	24
3.12	Example of a collective pitch control mechanism with secondary links connected to an eccentric rotation point. Figure modified from [11]. . . . .	25
3.13	(a) Collective variable pitch law developed by Jain and Abhishek [26] for several pitch amplitudes. Note that Jain and Abhishek [26] use the opposite pitch sign convention as used in this study. (b) The relationship between $C_p$ and tip speed ratio for different pitch amplitudes, leading to the pitch strategy that maximizes power output over a range of tip speed ratios (bold line). Figure modified from [26]. . . . .	26
3.14	Three variable pitch laws developed by Staelens <i>et al.</i> [18], with increasing smoothness. (a) The effective angle of attack, and (b) the pitch angle. Figure modified from [18]. . . . .	27
3.15	Optimal variable pitch law developed by Paraschivoiu <i>et al.</i> [9]. Note that $\tau$ is the pitch angle ( $=\theta_p$ ). Note that Paraschivoiu <i>et al.</i> [9] use the opposite pitch sign convention as used in this study. Figure from [9]. . . . .	28
3.16	Variable pitch law developed by Hwang <i>et al.</i> [20]. Note that the opposite pitch sign convention is used. Figure modified from [20]. . . . .	28
3.17	Variable pitch control law developed by Zhang <i>et al.</i> [21] (a) for maximum power output, and (b) optimum. Figure modified from [21]. . . . .	29
3.18	Variable pitch control law developed by Guo <i>et al.</i> [19]. $\theta_p = 1^\circ$ upwind and $\theta_p = -2^\circ$ downwind. Figure modified from [19]. . . . .	30
3.19	Variable pitch control law developed by Abbaszadeh <i>et al.</i> [22], created by optimizing the angle of attack spline $\alpha$ compared to the original geometric angle of attack $\alpha_g$ . Figure modified from [22]. . . . .	31
3.20	(a) Variable pitch law developed by Rainone <i>et al.</i> [23]. (b) Blade orientations during the revolution. Figure modified from [23]. . . . .	31

3.21	Example variable pitch curves developed by Houf [24] for the objective of (a) maximizing power or (b) minimizing power. Results are shown for a tip speed ratio of 4 and various solidities. Houf [24] also optimizes at other tip speed ratios, which yields different shapes of the pitch curve. Note that the opposite pitch sign convention is used. Figure from [24]. . . . .	32
3.22	(a) The relationship between $C_p$ and reduction in torque ripple. (b) Three examples of sinusoidal pitch laws developed by Erfort <i>et al.</i> [13], for different combinations of $C_p$ and torque ripple reduction. Figure modified from [13]. . . . .	33
3.23	(a) Solutions to the two-objective optimization problem in Le Fouest and Mulleners [5] shown in the objective space, for the on-design condition ( $\lambda = 3.2$ ). Axes are normalized by the zero-pitch values. The Pareto-optimal front is shown in color. (b) The variable pitch curves. They are third-order sinusoids. (c) The angle of attack. The black curve is the angle of attack for the zero-pitch case. Figure modified from [5]. . . . .	34
4.1	Flowchart of the non-dominated sorting algorithm. . . . .	39
4.2	Flowchart of the U-NSGA-III algorithm. . . . .	42
4.3	Graphical depiction of the hypervolume for two dimensions. . . . .	43
5.1	Control point indices in the AC model when (a) $j \leq N_{el}/2$ and (b) $j > N_{el}/2$ . Control points $j$ and $N_{el} + 1 - j$ are directly across from each other on the cylinder (one upwind, one downwind) and have the same y-value. . . . .	47
5.2	The SNL 0018/50 airfoil shape compared to the NACA 0018 airfoil. Figure from [49]. . . . .	50
5.3	The airfoil polars of the SNL 0018/50 airfoil from QBlade [31] for $Re = 1 \times 10^6$ . (a) The lift coefficient and (b) the drag coefficient. . . . .	51
5.4	(a) Combinations of tip speed ratio and freestream wind speed which meet the $Re = 1 \times 10^6$ operating condition. (b) Power coefficient of the turbine at those tip speed ratios, calculated using the 2D AC model. . . . .	51
6.1	Normal load curve of the Sandia 34-m turbine for $0^\circ$ pitch generated by the AC model, with a Fourier function fit with increasing number of harmonics: (a) second-order, (b) third-order, and (c) fourth-order. . . . .	54
6.2	Normal load curve of the Sandia 34-m turbine for $0^\circ$ pitch generated by the AC model, with a polynomial function fit: (a) seventh-order and (b) ninth-order. . . . .	55
6.3	Parameter study to determine the number of partitions, $P_H$ , and therefore the number of reference directions, $H$ . The two-objective optimization case was run with $H = 10, 20, 30, 40, 50, 60, 70, 80, 90$ , and $100$ . . . . .	61
7.1	Azimuthal resolution sensitivity study conducted for the AC model considering eight different discretization levels. (a) Power coefficient $C_p$ and (b) thrust coefficient $C_T$ . The right y-axis shows the percent error with respect to $\Delta\theta = 0.5^\circ$ ( $N_{el} = 720$ ). . . . .	65
7.2	Azimuthal resolution sensitivity study conducted for the AC model considering eight different discretization levels. (a) Angle of attack, (b) normal force, and (c) tangential force. A limited number of $\Delta\theta$ are shown for clarity of the figure. . . . .	65
7.3	Computation time of the AC model depending on the azimuthal resolution. . . . .	66
7.4	Effect of including the tangential load terms and/or new modified linear correction $k_a$ from Cheng <i>et al.</i> [8] in the AC model. (a) Angle of attack, (b) normal force, and (c) tangential force. . . . .	66
7.5	Sensitivity of the AC model to the scaling factor $f$ used to shift the control points slightly inside ( $f = 0.999$ ) or outside ( $f = 1.001$ ) the cylinder. (a) Angle of attack and (b) normal and tangential forces. The model was run with $N_{el} = 36$ . . . . .	68
7.6	AC model compared to AC model results in De Tavernier [4]. (a) Angle of attack and (b) normal and tangential forces for $0^\circ$ constant pitch. $B = 2$ , $R = 1$ m, $c = 0.1$ m, $\lambda = 3$ , and $V_\infty = 1$ m/s. The airfoil polars are $C_l = 2\pi \sin \alpha$ and $C_d = 0$ . . . . .	69
7.7	AC model compared to AC model results in De Tavernier and Ferreira [30]. (a) Angle of attack and (b) normal and tangential forces for $0^\circ$ constant pitch. $B = 3$ , $R = 1$ m, $c = 0.0667$ m, $\lambda = 3$ , and $V_\infty = 1$ m/s. The airfoil polars are $C_l = 1.1 \cdot 2\pi \alpha$ and $C_d = 0$ . . . . .	70
7.8	AC model compared to results for the Sandia 34-m turbine generated in QBlade (free wake vortex model) [31]. (a) Angle of attack and (b) normal and tangential forces for $0^\circ$ constant pitch. $B = 2$ , $R = 16.774$ m, $c = 0.91$ m, $\lambda = 4$ , and $V_\infty = 4.0659$ m/s. The Reynolds number is $1 \times 10^6$ and the corresponding SNL 0018/50 airfoil polars are from QBlade [31]. . . . .	70

7.9	AC model compared to PIV experimental results in LeBlanc and Ferreira [14]. Normal and tangential force coefficients for $0^\circ$ constant pitch. $B = 2$ , $D = 1.48$ m, $c = 0.075$ m, $\lambda = 4$ , and $V_\infty = 4$ m/s. The Reynolds number is 80,000 and the airfoil is NACA 0021. . . . .	71
7.10	AC model compared to CFD results in Rezaeiha <i>et al.</i> [6]. (a) Angle of attack and (b) normal force coefficient for $0^\circ$ , $2^\circ$ , and $-2^\circ$ fixed pitch. $B = 3$ , $D = 1$ m, $c = 0.0575$ m, $\lambda = 4$ , and $V_\infty = 7$ m/s. The Reynolds number is 115,000 and the airfoil is NACA 0015; the corresponding airfoil polars are from [6]. . . . .	72
7.11	The varying pitch angle used in De Tavernier [4]. . . . .	73
7.12	AC model compared to AC model results in De Tavernier [4]. (a) Angle of attack and (b) normal force for dynamic pitch. $B = 2$ , $R = 1$ m, $c = 0.1$ m, $\lambda = 4$ , and $V_\infty = 1$ m/s. The airfoil polars are $C_l = 2\pi\alpha$ and $C_d = 0$ . . . . .	74
8.1	Evolution of the maximum power coefficient across generations. The simulation is ended after 89 generations when the convergence criterion is met. The dotted line shows when no feasible solution was yet found. . . . .	76
8.2	Optimal solution which maximizes $C_p$ . (a) The optimal pitch function, (b) angle of attack, (c) blade normal force coefficient, (d) blade tangential force coefficient, (e) power coefficient, and (f) thrust coefficient as a function of azimuthal angle. The forces are normalized by $\frac{1}{2}\rho(2R)V_\infty^2$ . Values are compared to the base case with zero pitch (dashed gray line). . . . .	77
8.3	(a) Evolution of the Pareto front across generations in the two-objective case, along with the initial population; with (b) zoomed in on the region of interest. . . . .	79
8.4	(a) The hypervolume across generations and (b) the change in hypervolume between two successive generations. The simulation is ended after 200 generations when the convergence criterion is met. The dashed red line shows the threshold used for the termination criterion. The dashed vertical line shows when a feasible solution is first found. . . . .	79
8.5	The generational distance (a) between two successive generations and (b) with respect to the 200th generation. The dashed vertical line shows when a feasible solution is first found. . . . .	80
8.6	The Pareto-optimal front for the two-objective optimization case: maximize $C_p$ and minimize $\sigma(Q_n)$ . Solution A increases $C_p$ the most, while maintaining normal load fluctuations. Solution C decreases normal load fluctuations the most, while maintaining power efficiency. Solution B is a compromise, which achieves some improvement in both objectives at the same time. The color of the solutions is sorted from high $C_p$ (dark purple) to low $C_p$ (blue). The axes are normalized with respect to the base case and the dashed lines show unity. . . . .	80
8.7	The optimal pitch functions for the two-objective optimization case. Solution A increases $C_p$ the most, while maintaining normal load fluctuations. Solution C decreases normal load fluctuations the most, while maintaining power efficiency. Solution B is a compromise, which achieves some improvement in both objectives at the same time. . . . .	81
8.8	The trend in the optimal values of the decision variables with the objective functions. (a) Amplitude of the first harmonic ( $A_1$ ), (b) amplitude of the second harmonic ( $A_2$ ), and (c) amplitude of the third harmonic ( $A_3$ ). (d) The trend in the maximum angle of attack with the objective functions. . . . .	82
8.9	Example solutions to the two-objective optimization problem. Solution A increases $C_p$ the most, while maintaining normal load fluctuations. Solution C decreases normal load fluctuations the most, while maintaining power efficiency. Solution B is a compromise, which achieves some improvement in both objectives at the same time. (a) The optimal pitch function, (b) angle of attack, (c) blade normal force coefficient, (d) blade tangential force coefficient, (e) power coefficient, and (f) thrust coefficient as a function of azimuthal angle. The forces are normalized by $\frac{1}{2}\rho(2R)V_\infty^2$ . Values are compared to the base case with zero pitch (dashed gray line). . . . .	84
8.10	(a) The hypervolume across generations and (b) the change in hypervolume between two successive generations. The simulation is ended after 396 generations when the convergence criterion is met. The dashed red line shows the threshold used for the termination criterion. The dashed vertical line shows when a feasible solution is first found. . . . .	85
8.11	The generational distance (a) between two successive generations and (b) with respect to the 396th generation. The dashed vertical line shows when a feasible solution is first found. . . . .	86

- 8.12 The Pareto-optimal front for the three-objective optimization case: maximize  $C_p$ , minimize  $\sigma(Q_n)$ , and minimize  $\sigma(Q_t)$ . Solution A increases  $C_p$  the most, while maintaining normal load and torque fluctuations. Solution C decreases normal load fluctuations the most, while maintaining power efficiency and torque fluctuations. Solution D decreases torque fluctuations the most, while maintaining power efficiency and with a slight reduction in normal load fluctuations. Solution B is a compromise, which achieves some improvement in all objectives at the same time. The color of the solutions is sorted from high  $C_p$  (dark purple) to low  $C_p$  (blue). The axes are normalized with respect to the base case. . . . . 87
- 8.13 The Pareto-optimal front for the three-objective optimization case: maximize  $C_p$ , minimize  $\sigma(Q_n)$ , and minimize  $\sigma(Q_t)$ . (a) The Pareto front in the  $C_p$ - $\sigma(Q_n)$  plane, (b) in the  $C_p$ - $\sigma(Q_t)$  plane, and (c) in the  $\sigma(Q_n)$ - $\sigma(Q_t)$  plane. Solution A increases  $C_p$  the most, while maintaining normal load and torque fluctuations. Solution C decreases normal load fluctuations the most, while maintaining power efficiency and torque fluctuations. Solution D decreases torque fluctuations the most, while maintaining power efficiency and with a slight reduction in normal load fluctuations. Solution B is a compromise, which achieves some improvement in all objectives at the same time. The color of the solutions is sorted from high  $C_p$  (dark purple) to low  $C_p$  (blue). The axes are normalized with respect to the base case and the dashed lines show unity. . . . . 87
- 8.14 The Pareto-optimal front in the  $C_p$ - $\sigma(Q_n)$  plane for the three-objective optimization case vs. the two-objective optimization case (gray points). The three-objective case does not achieve as high  $C_p$  or as low normal load fluctuations as the two-objective case. The axes are normalized with respect to the base case and the dashed lines show unity. . . . . 88
- 8.15 The optimal pitch functions for the three-objective optimization case. Solution A increases  $C_p$  the most, while maintaining normal load and torque fluctuations. Solution C decreases normal load fluctuations the most, while maintaining power efficiency and torque fluctuations. Solution D decreases torque fluctuations the most, while maintaining power efficiency and with a slight reduction in normal load fluctuations. Solution B is a compromise, which achieves some improvement in all objectives at the same time. . . . . 88
- 8.16 Example solutions to the three-objective optimization problem. Solution A increases  $C_p$  the most, while maintaining normal load and torque fluctuations. Solution C decreases normal load fluctuations the most, while maintaining power efficiency and torque fluctuations. Solution D decreases torque fluctuations the most, while maintaining power efficiency and with a slight reduction in normal load fluctuations. Solution B is a compromise, which achieves some improvement in all objectives at the same time. (a) The optimal pitch function, (b) angle of attack, (c) blade normal force coefficient, (d) blade tangential force coefficient, (e) power coefficient, and (f) thrust coefficient as a function of azimuthal angle. The forces are normalized by  $\frac{1}{2}\rho(2R)V_\infty^2$ . Values are compared to the base case with zero pitch (dashed gray line). . . . . 91
- 8.17 Case 1 optimal solution and Case 2 solution A, which achieve the maximum  $C_p$ . The Case 1 optimal solution increases the normal load fluctuations compared to the base case while Case 2 solution A does not. (a) The optimal pitch function, (b) angle of attack, (c) blade normal force coefficient, (d) blade tangential force coefficient, (e) power coefficient, and (f) thrust coefficient as a function of azimuthal angle. The forces are normalized by  $\frac{1}{2}\rho(2R)V_\infty^2$ . Values are also compared to the base case with zero pitch (dashed gray line). . . . . 94
- 8.18 Case 1 optimal solution and Case 3 solution A, which achieve the maximum  $C_p$ . The Case 1 optimal solution increases the normal load and torque fluctuations compared to the base case while Case 3 solution A does not. (a) The optimal pitch function, (b) angle of attack, (c) blade normal force coefficient, (d) blade tangential force coefficient, (e) power coefficient, and (f) thrust coefficient as a function of azimuthal angle. The forces are normalized by  $\frac{1}{2}\rho(2R)V_\infty^2$ . Values are also compared to the base case with zero pitch (dashed gray line). . . . . 95
- 8.19 Case 2 solution C and Case 3 solution C, which achieve the minimum normal load fluctuations. Case 2 solution C increases the torque fluctuations compared to the base case while Case 3 solution C does not. (a) The optimal pitch function, (b) angle of attack, (c) blade normal force coefficient, (d) blade tangential force coefficient, (e) power coefficient, and (f) thrust coefficient as a function of azimuthal angle. The forces are normalized by  $\frac{1}{2}\rho(2R)V_\infty^2$ . Values are also compared to the base case with zero pitch (dashed gray line). . . . . 97

9.1	(a) Power coefficient and (b) thrust coefficient across tip speed ratios when the Case 3 solution A pitch function is applied, compared to the case with zero pitch. The pitch function maximized $C_p$ without increasing normal load or torque fluctuations when $\lambda = 4$ . The marker indicates the optimization condition. . . . .	100
9.2	The optimal pitch functions for two different tip speed ratios: 4 and 5.5. The solutions are the three-objective optimization case solution A, which increases $C_p$ the most, while maintaining normal load and torque fluctuations. . . . .	101
9.3	(a) Power coefficient and (b) thrust coefficient across tip speed ratios when the Case 3 solution A pitch function is applied, compared to the case with zero pitch. The pitch function maximized $C_p$ without increasing normal load or torque fluctuations when $\lambda = 5.5$ . The marker indicates the optimization condition. . . . .	102
9.4	Solutions to the three-objective optimization problem with 2 vs. 3 blades. Solution A (left column) increases $C_p$ the most, while maintaining normal load and torque fluctuations. Solution C (middle column) decreases normal load fluctuations the most, while maintaining power efficiency and torque fluctuations. Solution D (right column) decreases torque fluctuations the most, while maintaining power efficiency and with some reduction in normal load fluctuations. The optimal pitch function (top row), the blade normal force coefficient (middle row), and the blade tangential force coefficient (bottom row) as a function of azimuthal angle. The forces are normalized by $\frac{1}{2}\rho(2R)V_\infty^2$ . Values are also compared to the two- and three-bladed base cases with zero pitch (dashed lines). . . . .	104
A.1	NSGA-II procedure. The next generation $P_{t+1}$ is created from the parent population $P_t$ and offspring population $O_t$ via non-dominated sorting and crowding distance sorting. Figure modified from Deb [42]. . . . .	118
B.1	AC model compared to experimental results using strain gages in LeBlanc and Ferreira [15]. Normal force coefficient for different fixed pitch offset: $0^\circ$ , $5^\circ$ , and $-5^\circ$ . $B = 2$ , $D = 1.48$ m, $c = 0.075$ m, $\lambda = 4$ , and $V_\infty = 4$ m/s. The Reynolds number is 80,000 and the airfoil is NACA 0021. . . . .	119
B.2	Experimental normal force coefficient for different fixed pitch offset, showing the mean and standard deviation. $\beta$ is the pitch angle. Figure from LeBlanc and Ferreira [15]. . . . .	120

# List of Tables

2.1	Summary of the advantages and disadvantage of vertical axis wind turbines (compared to horizontal axis wind turbines) [3]–[11], [13], [37]. . . . .	8
5.1	Specifications of the Sandia 34-meter reference turbine and the modifications made for this study [32].	52
6.1	Upper and lower bounds on the decision variables. . . . .	56
6.2	Optimization cases. . . . .	57
6.3	Parameters used in the genetic algorithm for all optimization cases. . . . .	60
6.4	Number of generations and function evaluations for each optimization case. . . . .	61
8.1	Power and thrust coefficients in the single-objective optimization case. . . . .	76
8.2	Power and thrust coefficients in the two-objective optimization case. . . . .	83
8.3	The trends in the optimal values of the decision variables with the objective functions for the three-objective optimization case. . . . .	89
8.4	Power and thrust coefficients in the three-objective optimization case. . . . .	90
9.1	Objective function values of the base case (zero pitch) with three blades. . . . .	103
9.2	Optimal objective function values for two vs. three blades. Values are shown as a percent difference with respect to the respective (three-bladed or two-bladed) base case. . . . .	104

# Introduction

Wind energy is essential in sustainable energy systems. It is a renewable and carbon-free energy source. Wind energy is expected to continue growing drastically in the coming years [1], [2]. Most commercial wind turbines at present are horizontal axis wind turbines (HAWTs). Vertical axis wind turbines (VAWTs) are an alternative to HAWTs. In a VAWT, the axis of rotation of the blades is vertical with respect to the ground. Modern VAWTs have been in development since the 1920s, with the invention of the lift-based Darrieus turbine [3]. There have been two main periods of VAWT development:  $\Phi$ -rotors in the 1980s in the United States and Canada, and predominantly H-rotors since the 2010s in Europe [3]. The present study is in the context of this renewed interest in VAWTs.

VAWTs have several advantages over HAWTs, leading to two promising applications in future wind energy: multi-megawatt floating offshore turbines and small-scale urban turbines [4]–[11]. The advantages of VAWTs include an insensitivity to the incoming wind direction, a low center of gravity, easier installation and maintenance (and thus lower associated costs), low land use relative to power generation, lower rotational speed which produces less noise and causes fewer bird collisions, and scalability [4]–[7], [11]. At the same time, VAWTs have complex aerodynamics which have hindered their development [4]. These complex aerodynamics include a 3D, unsteady, complicated flow field; dynamic stall; blade-vortex interactions; and incoming flow to the blades which constantly varies throughout the turbine revolution [4]–[6]. The blades experience unsteady loading, which leads to vibrations and fatigue [4], [5], [9], [12], [13]. Historically, VAWTs have suffered from fatigue issues, as well as low power efficiency and difficulty in self-starting [3], [5], [8]–[11], [13]. Introducing pitch control in VAWTs can address some of these challenges.

Numerous studies on VAWT blade pitching have been done in the past, both numerical and experimental, and both with fixed and variable blade pitch [5], [6], [9]–[26]. Blade pitch control can increase the power efficiency in the partial load region, alleviate structural loads and fatiguing load fluctuations on the blades, reduce torque fluctuations, improve the turbine's self-starting ability, and contribute to wake control [5], [9], [11]–[14], [16], [18]–[20], [23], [24], [27], [28]. The most common aim in VAWT pitch studies thus far is maximizing the power coefficient,  $C_p$  (e.g. [9], [16], [18]–[22], [25]). This study focuses on the application of pitch control to minimize normal load fluctuations and torque fluctuations, in addition to increasing power efficiency.

The objective of this study is to develop an optimal pitch control strategy for VAWTs that maximizes  $C_p$ , minimizes rotor normal load fluctuations, and minimizes rotor torque fluctuations. Individual active variable blade pitch control optimization is performed considering these multiple objectives, which are built up in successive optimization cases. With further development, including the implementation of variable pitch control, there is an opportunity for VAWTs to fill critical gaps in wind energy.

## 1.1. Research Questions

The research question is: What is the optimal active blade pitch control strategy for a vertical axis wind turbine to fulfill the simultaneous objectives of maximizing the power generation and minimizing detrimental fluctuations in rotor normal load and torque?

- *What research related to optimal VAWT blade pitching has been done in the literature?*
  - *Is the method numerical or experimental? What types of numerical modeling techniques are used?*
  - *What type of blade pitch is used (fixed or variable, passive or active, collective or individual)?*
  - *What is the optimal blade pitch kinematics? How is it derived?*

- *What are the improvements in power ( $C_p$ ) and/or loading?*
- *What are the trends between blade pitch angle and loading?*
- *What is a suitable numerical method to model vertical axis wind turbines?*
- *What methods are used to model vertical axis wind turbines?*
- *What is the two-dimensional (2D) actuator cylinder (AC) model? What is its physical basis?*
  - *What is the mathematical derivation of the 2D AC model? What are the inputs and outputs?*
  - *How accurate is the 2D AC model?*
  - *What are the assumptions and limitations of the 2D AC model?*
- *What functional form should be used to represent the pitch angle? What are the parameters to be optimized?*
- *What multi-objective optimization method is suitable?*
- *What is the optimal pitch function to maximize the power coefficient?*
- *What is the optimal pitch function(s) to maximize the power coefficient and minimize the rotor normal load fluctuations?*
- *What is the optimal pitch function(s) to maximize the power coefficient, minimize the rotor normal load fluctuations, and minimize the rotor torque fluctuations?*
- *How general are the optimal pitch functions? Are they applicable to different turbine designs and operating conditions? How do the optimal pitch functions change when the turbine design or operating condition changes?*

## 1.2. Methodology

A vertical axis wind turbine with varying pitch is modeled using the 2D actuator cylinder (AC) model [29]. We use the modified linear solution of the AC model, and perform sensitivity analyses on the model, including to the number of elements used in the discretization of the cylinder. The model implementation is verified against 2D AC codes from the literature [4], [30] and validated against other numerical models and experiments [6], [14], [31] for zero pitch, fixed non-zero pitch, and variable pitch cases. The actuator cylinder and optimization code are implemented in Python.

This study optimizes a pitch function in the form of a third-order sinusoid:  $\theta_p = A_0 + A_1 \sin(\theta w + \phi_1) + A_2 \sin(2\theta w + \phi_2) + A_3 \sin(3\theta w + \phi_3)$ , where  $\theta_p$  is the pitch angle. The optimization problem thus has eight decision variables:  $A_0, A_1, A_2, A_3$  (the amplitudes),  $\phi_1, \phi_2, \phi_3$  (the phase shifts), and  $w$  (the frequency) of the harmonics. The functional form of the pitch angle is chosen considering the literature and also considering the second objective of minimizing the normal load fluctuations, prompting a function to be fit to the normal load curve. The pitch function is smooth and continuous, which makes it practically feasible to implement.

The pitch optimization is performed considering a single turbine design at a single operating condition. The reference turbine is based on the Sandia National Laboratories (SNL/Sandia) 34-meter turbine [32]. It is a large, real-life turbine with performance and load data available. The turbine used in this study is a 2-bladed H-rotor with a diameter of 33.548 m and chord length of 0.91 m. The SNL 0018/50 airfoil comprises the blades. It is operated at the conditions of 4.0659 m/s incoming wind speed and tip speed ratio of 4, resulting in a Reynolds number of  $1 \times 10^6$ .

This study focuses on three objectives: maximizing the power coefficient, minimizing the normal load fluctuations, and minimizing the torque fluctuations. The objectives are built up sequentially, meaning that a single-objective, two-objective, and three-objective optimization problem are solved in turn. The optimization algorithm used for all the optimization cases is the unified non-dominated sorting genetic algorithm III (U-NSGA-III) [33]. The algorithm is terminated based on convergence in the objective space. This results in 8,900, 20,000, and 39,600 total function evaluations for the single-, two-, and three-objective optimization cases, respectively.

## 1.3. Report Outline

CHAPTER 2 elaborates on the motivation for this research. It justifies why wind energy is important and provides background on VAWTs. The advantages of VAWTs are discussed, leading to two important applications of VAWTs. Disadvantages are also discussed, and how pitch control can address them.

CHAPTER 3 explains the aerodynamic theory behind VAWTs, the numerical methods used to model VAWTs, and the existing literature on VAWT pitch control. The theoretical background of VAWT aerodynamics is expounded,

including a brief discussion on unsteady aerodynamic effects which play an important role in VAWT aerodynamics. Four categories of VAWT numerical models are explained, then the physical and mathematical derivation of the 2D AC model is presented. Finally, the summary of existing literature on VAWT blade pitch control includes different approaches to pitching the blades, including fixed vs. variable pitch. It describes how different active variable pitch laws were derived.

CHAPTER 4 discusses multi-objective optimization methods, with a focus on genetic algorithms. It outlines the steps in the U-NSGA-III algorithm and describes methods to analyze the performance of the algorithm after optimization has been executed.

CHAPTER 5 details the implementation of the 2D AC model in a computer code. The reference turbine which is used in this study is also described, including the justification for the selection of the reference turbine, its geometrical properties, and its operating condition.

CHAPTER 6 details the multi-objective optimization problems in this study and their implementation in a computer code, including the problem definition (decision variables, objective functions, and constraints). It explains how the functional form of the pitch angle was determined. The chapter describes the parameters used in the U-NSGA-III algorithm and the termination criterion of the optimization algorithm.

CHAPTER 7 covers the 2D AC model sensitivity study and validation.

CHAPTER 8 analyzes the results of this study in terms of the optimal pitch functions. Several case studies are analyzed. It highlights the important conclusions from each of the optimization cases.

CHAPTER 9 studies the effect of pitch control with different operating conditions and turbine design. It investigates the applicability of the optimal pitch functions to different tip speed ratios and number of blades, and how the optimal pitch functions change with different inputs.

# Part I

## Literature Review

# The Role of Vertical Axis Wind Turbines in Sustainable Energy Systems

Wind energy is essential in sustainable energy systems. The reliance on wind energy is clearly laid out in several international climate goals [1], [2]. Section 2.1 explains why the use of wind energy will increase. Vertical axis wind turbines are a type of wind turbine which can contribute to this harnessing of wind energy. In a vertical axis wind turbine (VAWT), the rotor's axis of rotation is vertical with respect to the ground. This is in contrast to the currently more popular horizontal axis wind turbine (HAWT) in which the axis of rotation is horizontal. Figure 2.1 shows a VAWT compared to a HAWT. There are several different rotor designs for VAWTs, including the  $\Phi$ -rotor, H-rotor, V-rotor, X-rotor, and helical shapes [4]. VAWTs have been under development for several decades, however, they have not reached technical maturity nor taken off commercially the same way HAWTs have. Section 2.2 briefly outlines this history. Yet, VAWTs have some promising use cases, particularly in multi-megawatt floating offshore projects and in small-scale turbulent urban settings. Section 2.3 describes the advantages of VAWTs in more detail. Section 2.4 follows on with explaining some of the disadvantages of VAWTs. However, many of these disadvantages can be addressed with pitch control, as explained in Section 2.5.



**Figure 2.1:** Two types of wind turbines, (a) a horizontal axis wind turbine (HAWT) and (b) a vertical axis wind turbine (VAWT), specifically an H-rotor. Images from [34] and [35].

## 2.1. The Need for Wind Energy

Wind energy is a renewable, carbon-free source of energy. The anthropogenic emissions of carbon dioxide ( $\text{CO}_2$ ) in the energy sector are contributing to global temperature rise [1]. The energy sector includes electricity, transportation,

and industry. Currently, most of this energy production globally still comes from fossil fuels, which emit CO<sub>2</sub>. These fossil fuels should be replaced by wind energy and other sources of sustainable energy in order to mitigate the effects of climate change.

Many governments world-wide have recognized the need to transition our energy supply to carbon-free sources of energy. There is an international climate goal to keep the global average temperature below 2° Celsius above preindustrial levels [1]. Central to this goal is using more renewable energy free of CO<sub>2</sub> emissions, particularly wind and solar photovoltaic (PV) energy. Furthermore, the European Union (EU) has the goal to be carbon neutral by 2050 [2]. Wind energy plays an essential role in these climate targets. Wind energy, behind solar PV energy, is expected to be the main source of generating electricity in the 2050 Scenario. By 2030, the target for wind energy is 2,891 GW of total installed capacity (onshore and offshore), which will generate approximately 7,400 TWh of electricity in 2030. For reference, the total installed capacity of wind energy in 2023 was 1,021 GW [36]. Thus, in order to reach the international climate goals, wind energy needs to continue to grow drastically in the coming years. Fortunately, wind energy has enormous potential, and tapping into that potential will fulfill wind energy's important role in carbon-free energy systems [1], [2], [36].

Wind energy is projected to play a large role not only in electricity generation, but also in the electrification of the transportation, industry, and building sectors. Currently, carbon-emitting fossil fuels are used in the energy sector for transportation (i.e. cars, trucks, ships, airplanes), industrial processes (such as making steel and concrete), and heating buildings [1]. These activities need to be electrified in order to meet the 2050 net zero carbon goal [36]. This electrification will engender a 50-100% increase in the demand for renewable energy capacity, including wind energy. Wind energy can help achieve the decarbonization of the transportation, industry, and building sectors, which will avoid significant amounts of CO<sub>2</sub> emissions.

Beyond the compelling need for wind energy as a way of reducing energy-related CO<sub>2</sub> emissions, there are other reasons to use more wind energy. According to Letcher [1], the cost of generating electricity from wind onshore and offshore has approximately halved in the last ten years. Wind energy is now cost-competitive with the conventional means of generating electricity from fossil fuels. Furthermore, the International Energy Agency (IEA) still expects the cost of wind energy to reduce even more, particularly for floating offshore wind [36]. Wind energy also creates jobs, which can strengthen the economy [1]. In 2023, approximately 1.4 million people worldwide worked in the wind energy industry [36]. With the ongoing growth of wind energy, that figure will also rise.

Furthermore, burning fossil fuels not only emits the greenhouse gas CO<sub>2</sub>, but also other pollutants such as sulfur dioxide (SO<sub>2</sub>), nitrogen oxides (NO<sub>x</sub>), and particulates. In contrast, wind energy is pollution-free [1]. The manufacturing and transportation of wind turbines do produce some greenhouse gas emissions, but the amount is relatively small. In sum, a 1 MW wind turbine offsets approximately 2,360 metric tonnes of CO<sub>2</sub>. According to the IEA, in 2023, wind energy helped avoid 202,145 metric tonnes of CO<sub>2</sub> emissions in the EU [36]. Wind turbines also do not emit any SO<sub>2</sub>, NO<sub>x</sub>, or particulates [1]. According to the IEA, in 2023, wind energy also helped avoid 3.8 metric tonnes of SO<sub>2</sub> emissions and 654 metric tonnes of NO<sub>x</sub> emissions in the EU [36]. Other ways in which wind energy has less impact on the environment than electricity from fossil fuels is that wind farms use virtually no water and fuel does not have to be mined from the ground [1].

Increasing the share of wind energy in the energy mix also supports energy independence and energy security [1], [36]. A country would not have to rely on the import of foreign fossil fuels, which is not a secure source of energy. Rather, tapping into their domestic wind resource increases a country's energy independence. Diversifying the power supply to include many different sources of energy reduces a country's reliance on any one source of energy and secures its energy system in case one source fails to deliver.

Evidently, there is great impetus to intensely increase the installed capacity of wind energy in the coming years. Almost all of the wind turbines installed today are horizontal axis wind turbines, and many large wind farms using HAWTs are still planned. Yet, as the use cases of wind turbines increases for the aforementioned reasons, there is an opportunity for vertical axis wind turbines to fill critical gaps in wind energy.

## 2.2. VAWT History

The predecessor of modern-day vertical axis wind turbines was invented in the 1920s by the French engineer Georges Darrieus [3]. Darrieus' turbine concept was lift-based, in contrast to the prior drag-based VAWTs dating back to 9th-century Persia and before. Many research groups at universities and companies have pursued the VAWT concept since.

The oil crisis in the 1970s led governments to investigate alternative sources of energy, including wind energy [3], [4]. The period of development of VAWTs in the 1980s is typified by  $\Phi$ -rotors designed and built in the United States and Canada [3]. Organizations including the National Research Council of Canada, Sandia National Laboratories (US), FloWind (US), and DAF Indal (Canada) made  $\Phi$ -rotors with various designs (size, material, drivetrain, support structure, etc.) and rated power in the 100-500 kW range. The largest of these turbines was ÉOLE, built in 1987—at 110-m total height, 64-m diameter, and 3.8 MW rated power. The 34-m-diameter turbine built by Sandia achieved what is most likely the highest power coefficient measured for a VAWT: 0.43. Each of the turbines built in this period failed for different specific reasons, but Möllerström *et al.* [3] note some potential reasons why VAWTs failed to succeed commercially compared to HAWTs in this period: because of issues of fatigue and durability and turbines failing not-long into their operation, and because HAWTs were introduced to the market which proved to be more reliable and economical than VAWTs. De Tavernier [4] adds that the challenge of understanding the complex aerodynamics of VAWTs makes them difficult to design and has hindered their development.

More recently, research and development into VAWTs has revived in Europe. Beginning in the 2010s, universities and companies have committed effort to developing H-rotors in particular, including Vertical Wind AB (Sweden), NENUPHAR (France), and ANew Institute (Poland) [3]. There are many different VAWT designs currently being researched. The present study is in the context of this renewed interest in VAWTs.

### 2.3. The Advantages of VAWTs

VAWTs have several key advantages over HAWTs which could make them better candidates for future wind energy applications. Firstly, VAWTs are insensitive to the incoming wind direction [4], [5]. This means that the wind can come in from any azimuthal direction and the VAWT actuation surface (which is a three-dimensional (3D) cylinder) will always be perpendicular to the wind direction. Therefore, the turbine's aerodynamic performance is independent of the wind direction [7]. This is beneficial in urban environments where the wind constantly changes direction [10]. The turbine's omni-directionality also means that a yaw system is not needed because VAWTs do not encounter the issue of yaw misalignment, unlike HAWTs [4], [6], [10], [37].

Secondly, VAWTs rotate at slower speeds than HAWTs [4]–[6]. This produces less noise. Noise is a major factor that needs to be considered in wind turbine/farm design. Especially in urban settings, it is beneficial for a wind turbine to create less noise. The slower turbine rotation also makes collisions with birds less likely [5].

Thirdly, VAWTs have a much lower center of gravity compared to HAWTs [4], [5], [7]. The low center of gravity is due to the generator and other heavy electrical and mechanical drivetrain components being at the base of the turbine [4]–[6]. The mechanical and electrical parts being close to the ground also lessens the structural loads on the tower and eases installation and maintenance, thereby also reducing these costs. A VAWT's low center of gravity is beneficial to floating offshore uses [5], [37].

Fourthly, VAWTs can be placed closer together than HAWTs [4], [11]. This means that wind farms consisting of VAWTs can have a higher power density (extracted power per unit ground area [11]) and smaller footprint than wind farms consisting of HAWTs like we see today [4]. HAWTs require far separation in both the streamwise and crosswind directions, yielding a low power density of 2-3 W/m<sup>2</sup> and large wind farms [11]. Not only can VAWTs be placed closer together because they have a faster recovery of wind speed in the wake, but their wake can also be controlled [4]. VAWTs can be arranged in a wind farm such that there is constructive interference among the turbines and the wakes, thereby increasing the total power yield of the farm [11]. According to Benedict *et al.* [11], VAWT wind farms can achieve a power density around 30 W/m<sup>2</sup> in this way. The higher power density of VAWT wind farms means that offshore wind farms can be smaller in size, easing installation and maintenance, which lowers costs, and reducing the impact on marine life and shipping routes. VAWTs can also be added to existing HAWT wind farms to increase the power output (up to an order of magnitude according to Le Fouest and Mulleners [5]). Furthermore, the power density of a single VAWT is much higher than that of a single HAWT. The high power density of a turbine is beneficial in urban areas where space is a constraint [11].

In addition, VAWTs can have lower manufacturing costs because the blades can be simpler than those of HAWTs [6]. For example, straight-bladed H-rotors do not require any twist, change in airfoil, or narrowing along the blade. However, this is not the case for  $\Phi$ -rotors and some other more unique VAWT designs. Finally, VAWTs are easy to scale [4], [6]. This decreases turbine design costs and is especially useful when scaling the turbine up to >20 MW [4].

#### VAWT Applications

These characteristics lead to two main promising applications of VAWTs: multi-megawatt offshore turbines floating in deep water where the wind resource is strong, and small-scale turbines in urban settings where the wind is highly

turbulent [4]–[6].

The first main application area is deep offshore floating wind turbines [4]–[8]. In some areas, there is limited space for wind turbines onshore, so placing them offshore is appealing. The wind resource is also better offshore than it is onshore [4]. Farther offshore, the wind resource is even better. These areas tend to have deep water, which necessitates floating wind turbines. While floating offshore wind turbines are presently in an early stage of development, there are challenges for making floating HAWTs. HAWTs are top-heavy since the rotor and drive train are situated at the top of the tower, and the tower is a long lever arm between where the wind force is applied on the rotor and the foundation, creating a moment that has to be counteracted. Thus, floating HAWTs require a heavy and costly floating foundation [4]. VAWTs, on the other hand, could be a more economical solution for multi-megawatt floating offshore turbines [4], [8]. VAWTs have a low center of gravity, which can make the floating structure less expensive. The low center of gravity also facilitates maintenance, which is more difficult offshore than it is onshore. Another factor that aids maintenance and installation is that VAWTs can be placed closer together, so the overall footprint of an offshore wind farm can be smaller.

The second main application area is wind turbines in turbulent urban environments [4]–[6], [9]–[11]. Harnessing wind energy in urban areas is appealing so that electricity generation is at the site of electricity consumption, thereby minimizing the losses and costs associated with transmitting electricity and reducing the required capacity of the electricity grid [10], [11]. VAWTs are more suitable for urban environments than HAWTs because they are insensitive to the wind direction and can immediately react to changes in wind velocity. Due to the many obstacles in cities, the wind constantly changes direction and magnitude. VAWTs, for example small-scale rooftop turbines, can still extract energy from this highly turbulent flow. VAWTs also produce less noise than HAWTs, which is advantageous in urban settings because people live nearby. Furthermore, space is a constraint in urban areas and VAWTs have a much higher power density than HAWTs [11]. As an additional note, the wind is also turbulent in the mountains, which could be another application of VAWTs [9].

**Table 2.1:** Summary of the advantages and disadvantage of vertical axis wind turbines (compared to horizontal axis wind turbines) [3]–[11], [13], [37].

<b>Two Main Applications:</b>	
<ul style="list-style-type: none"> <li>• Multi-MW deep-water floating offshore</li> <li>• Small-scale turbulent urban</li> </ul>	
<b>Advantages</b>	<b>Disadvantages</b>
Insensitive to wind direction <ul style="list-style-type: none"> <li>• Yaw system not needed</li> <li>• Suitable in turbulent wind</li> </ul> Slower rotational speed <ul style="list-style-type: none"> <li>• Less noise</li> <li>• Bird collisions less likely</li> </ul> Low center of gravity <ul style="list-style-type: none"> <li>• Lighter/cheaper floating foundation</li> </ul> Easier maintenance <ul style="list-style-type: none"> <li>• Less maintenance cost</li> </ul> Can be placed close together <ul style="list-style-type: none"> <li>• Power dense wind farm</li> <li>• Smaller wind farm footprint</li> </ul> Better wake recovery and control <ul style="list-style-type: none"> <li>• Higher wind farm efficiency</li> </ul> High power density Easily scalable	Complex aerodynamics <ul style="list-style-type: none"> <li>• Unsteady loads</li> <li>• Dynamic stall</li> <li>• Vibrations</li> </ul> Fatigue issues Lower single-turbine efficiency Difficult self-starting

## 2.4. VAWT Disadvantages

The main disadvantages of VAWTs revolve around their complex aerodynamics, which are not yet fully understood [4]–[6]. The flow field around a VAWT is complicated, three-dimensional, and unsteady. The incoming flow to a blade (both magnitude and direction) varies throughout the turbine rotation. Therefore, the blades experience unsteady loading which is difficult to predict. For example, the torque is inconsistent throughout a rotation, which in turn causes vibrations [9]. Additionally, VAWT blades are prone to dynamic stall, which decreases efficiency and induces dynamic loads which compromise structural integrity. Moreover, when a blade passes through the downwind half, it is in the wake of the upwind half, so blade-wake interactions occur, which may cause fluctuations in loading [4]. There is also a variation in loading that occurs at the frequency of one turbine revolution causing fluctuating blade loads and therefore fatigue [7].

Historically, VAWTs have suffered from fatigue issues [3], [5], [8] and have been less efficient than HAWTs [5], [8]–[10]. Benedict *et al.* [11] point out that fixed-pitched VAWTs have a very low efficiency. VAWTs also tend to be close to the ground, where the wind speed is not as high as it is at the higher altitude of HAWT rotors; therefore VAWTs can have a lower power output [9]. Lastly, VAWTs suffer from self-starting issues. It is difficult for a VAWT to self-start depending on the wind condition [9], [11]. Starting from zero, the VAWT needs to ramp up to its design tip speed ratio. The problem is that at low tip speed ratios, the power coefficient is negative, and this needs to be overcome before the VAWT can operate at its design tip speed ratio [13].

## 2.5. Pitch Control as a Solution

Introducing pitch control in VAWTs can address some of the previously-mentioned challenges of low efficiency, fatigue issues, and difficulty in self-starting. Blade pitch control has long been used in HAWTs to control the power generation in the full load region. The role of blade pitching in that case is to reduce the rotor thrust to limit the power generation to the rated power. Blade pitch control in VAWTs can be used to serve the same purpose—to reduce the rotor thrust to limit the power in the full load region [24], [27]. However, blade pitching in VAWTs has wider applicability and can be used to serve fundamentally different purposes.

Most prominently, variable pitch control can be used to maximize the power generation (and aerodynamic efficiency) in the partial load region [5], [11]–[14], [18]–[20], [23], [24], [27]. Because the relative velocity of the wind with respect to the blade constantly changes throughout the turbine revolution, optimal blade pitching can maximize the energy extraction of the blade. The pitch angle can be changed dynamically in order to achieve the optimal angle of attack at each azimuthal position, which will maximize the power efficiency ( $C_p$ ) of the VAWT [5], [16], [18]. Changing the angle of attack also avoids or reduces dynamic stall, which increases the turbine's power output [5], [9], [16], [22], [23]. Blade pitching can also achieve increased power output while not increasing the thrust force (loading on the blades) [24].

Variable blade pitch control can also be used to reduce the rotor thrust force (while maintaining power) in order to decrease the loading on the blades and increase their (fatigue) life [14], [24], [27]. Blade pitching can also minimize load fluctuations, such as by smoothing the torque ripple or minimizing vibrations caused by dynamic stall [9], [12], [13]. Thus, pitch control can alleviate fatigue issues, which was an issue for many of the early VAWTs as discussed in Section 2.2. Improving the turbine's loading characteristics is beneficial for the turbine from a structural and lifetime point of view.

Variable pitch can also improve a VAWT's self-starting ability [9], [12], [13], [16], [19], [26]. Lastly, pitch control can be used to control the wake of a VAWT [14], [24], [28], which can create more favorable wind conditions for a downstream turbine.

## Vertical Axis Wind Turbine Modeling and Pitch Control

Now that the importance of vertical axis wind turbines in sustainable energy systems has been established, and in particular the usefulness of pitch-controlled VAWTs, we now expound the aerodynamic theory and modeling of VAWTs. First, Section 3.1 briefly defines the coordinate system with respect to a VAWT which will be used throughout this study. Then, Section 3.2 explains the aerodynamic theory behind VAWTs. Next, Section 3.3 outlines the numerical methods for modeling VAWTs. The model which is used in this study—the 2D Actuator Cylinder model—is described in detail in Section 3.4. Lastly, Section 3.5 summarizes the VAWT pitch control strategies in the literature.

### 3.1. Turbine Coordinate System

The coordinate system used to define a VAWT is shown in Figure 3.1. We look at the turbine from the top and cut a two-dimensional (2D) cross-section view with the x-axis pointing to the right, the y-axis  $90^\circ$  from it following the right-hand-rule, and the origin at the center of the rotor. The x-direction is also called the streamwise direction and the y-direction is called the crosswind (or crossflow) direction.  $\theta$  is the azimuth angle of the blade. It is defined to be positive in the counter-clockwise direction and  $\theta = 0^\circ$  is aligned with the positive y-axis. The freestream wind,  $V_\infty$ , comes in from the left, at an azimuth angle of  $\theta = 90^\circ$ . It travels in the positive x-direction. The rotor rotates in the counter-clockwise direction at rotational speed  $\Omega$ . The normal direction refers to the direction perpendicular to the direction of rotation and the tangential direction is parallel to, or along, the direction of rotation.

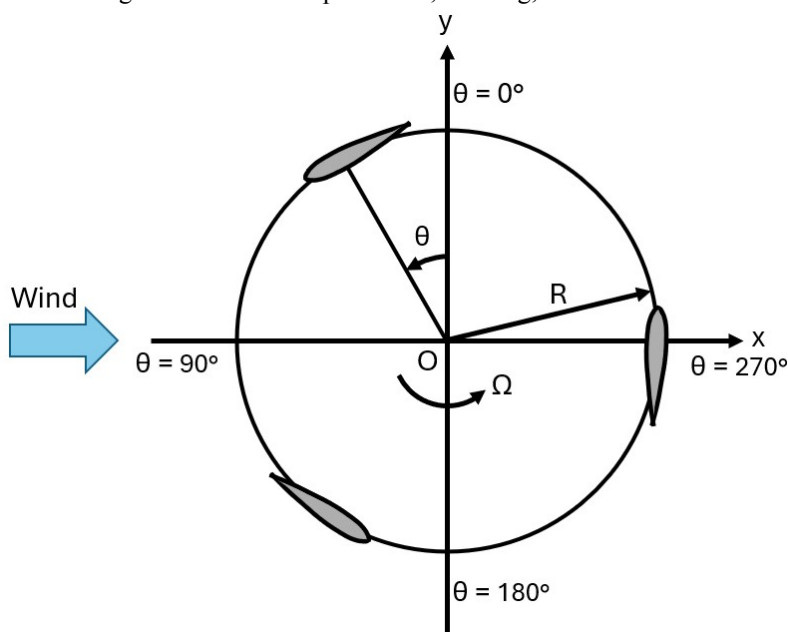


**Figure 3.1:** The VAWT coordinate system.

We divide the rotor in half: we will refer to the upwind half and downwind half throughout the rest of this study. The halves are shown in Figure 3.2. The upwind half is in the front side of the rotor, on the side of the incoming wind ( $0^\circ < \theta < 180^\circ$ ), and the downwind half is in the back side of the rotor ( $180^\circ < \theta < 360^\circ$ ), after the wind has already passed through the upwind half.

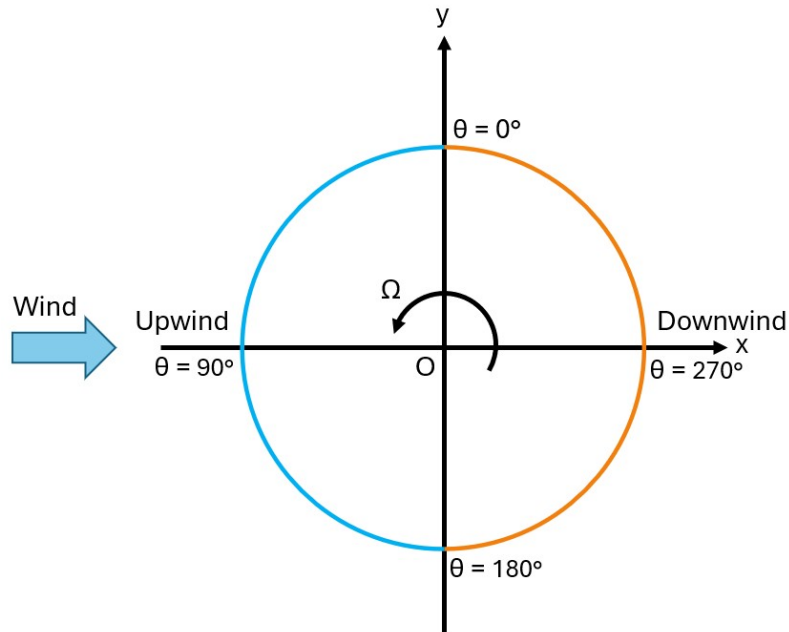


**Figure 3.2:** A VAWT divided into two halves: upwind and downwind.

The turbine rotor is defined by a radius  $R$ , or diameter  $D = 2R$ . It has a certain height  $l$ , which is also the length of the blades, considering a straight-bladed H-rotor. The blades stretch in the vertical direction, or  $z$ -direction. The number of blades is given by  $B$  and each blade is an airfoil with chord length  $c$ . The blades are evenly spaced around the rotor and the airfoils are identical. Figure 3.3 shows these dimensions of a VAWT.

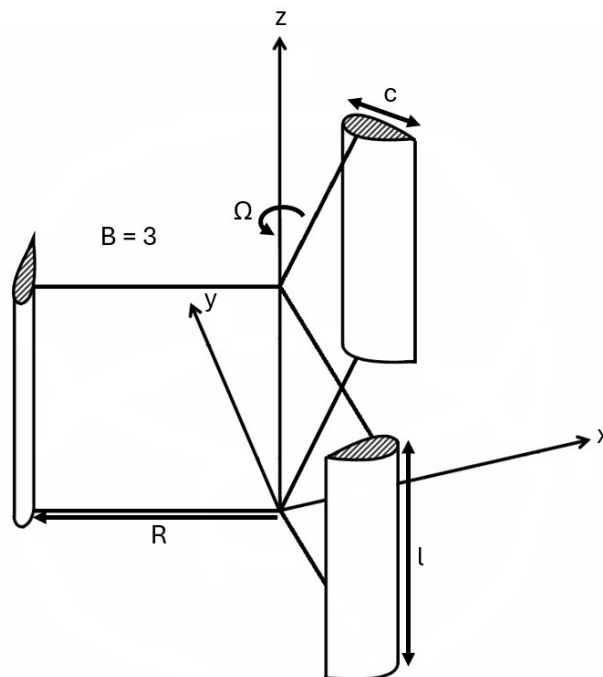


**Figure 3.3:** Dimensions of a VAWT: the rotor radius  $R$ , blade length  $l$ , and chord length  $c$ . The VAWT has three blades ( $B = 3$ ). Figure modified from [4].

There are a couple of important dimensionless parameters for wind turbines. These are the tip speed ratio  $\lambda$ , and rotor solidity  $\sigma$ . The tip speed ratio is the ratio between the rotational speed of the blade and the freestream wind speed (Equation 3.1) [28]. The solidity is the ratio of the area of the blades to the projected area of the rotor (Equation 3.2) [28].

$$\lambda = \frac{\Omega R}{V_\infty} \quad (3.1)$$

$$\sigma = \frac{Bc}{2R} \quad (3.2)$$

### 3.1.1. Pitch Angle Sign Convention

In the literature, different conventions are used for the sign of the blade pitch angle,  $\theta_p$ . In this study, we use the sign convention that blade pitch is positive when the leading edge rotates inward, towards the turbine rotation axis. Therefore, when the pitch angle is positive, the angle of attack increases for each azimuthal position, and when the pitch angle is negative, the angle of attack decreases [14]. Figure 3.4 shows the pitch sign convention on a VAWT airfoil.

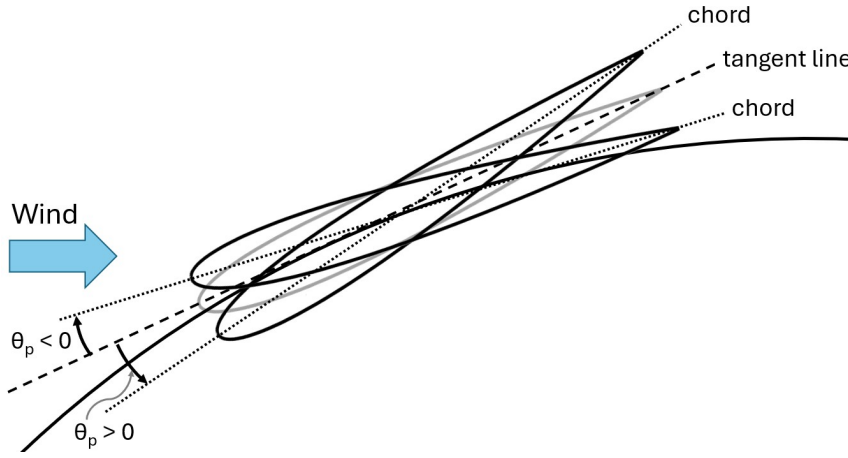


**Figure 3.4:** The blade pitch angle sign convention. A positive pitch angle corresponds to rotating the leading edge inward.

## 3.2. VAWT Aerodynamics

A vertical axis wind turbine standing in the flow of air extracts energy from that air via its blades. Here, we explain how the motion of air around a blade leads to aerodynamic forces. A 2D blade element experiences some velocity of incoming flow. This velocity comprises of three components: one due to the surrounding freestream wind velocity ( $\vec{V}_\infty$ ), one due to the blade's rotation about the turbine's vertical axis ( $\vec{V}_{rot}$ ), and the last is an induced velocity which is caused by the presence of the wind turbine in the flow ( $\vec{V}_{ind}$ ) (Figure 3.5) [28]. The rotational velocity is  $\vec{V}_{rot} = \Omega R$ .

The total relative velocity,  $\vec{V}_{rel}$ , of the flow with respect to the blade is a vector sum of these components [28]:

$$\vec{V}_{rel} = \vec{V}_\infty + \vec{V}_{rot} + \vec{V}_{ind} \quad (3.3)$$

Considering the turbine coordinate system defined in Section 3.1, we can decompose  $\vec{V}_{rel}$  into x- and y- components and into normal and tangential components [28]:

$$V_x = V_\infty + \Omega R \cos \theta + V_{ind,x} \quad (3.4)$$

$$V_y = \Omega R \sin \theta + V_{ind,y} \quad (3.5)$$

$$V_n = V_x \sin \theta - V_y \cos \theta \quad (3.6)$$

$$V_t = V_x \cos \theta + V_y \sin \theta \quad (3.7)$$

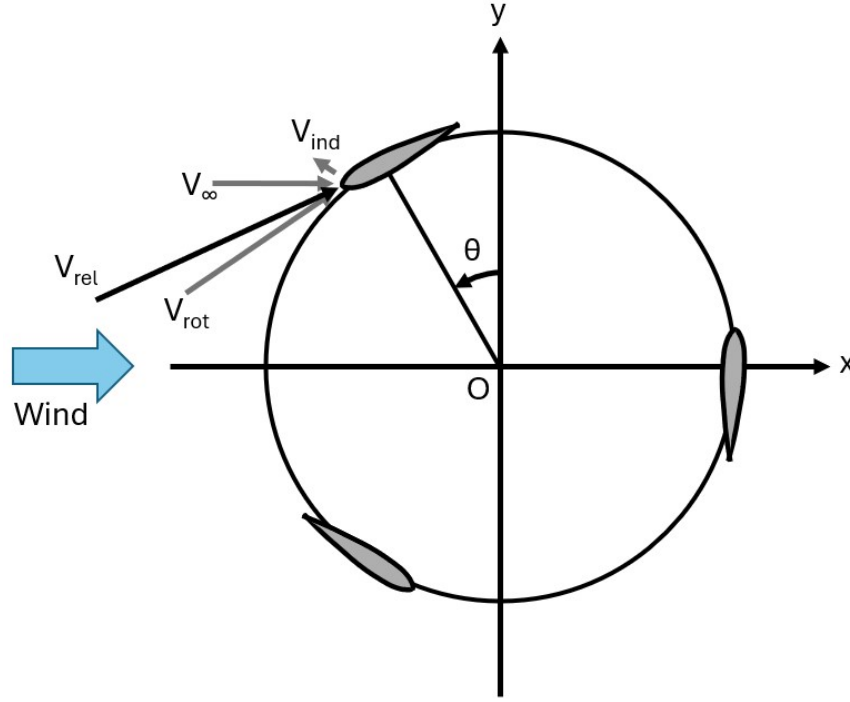


**Figure 3.5:** Velocity components experienced by a VAWT blade: freestream wind velocity  $V_\infty$ , rotational velocity  $V_{rot}$ , and induced velocity  $V_{ind}$ . Their vector sum is the relative velocity  $V_{rel}$ . Figure based on [28].

The induced velocities are often expressed as nondimensional local velocity perturbation components,  $w_x$  and  $w_y$ , in the x- and y-directions, respectively. This is relevant in the 2D AC model formulation described in Section 3.4. So then we can write:

$$V_{ind,x} = V_\infty w_x \quad (3.8)$$

$$V_{ind,y} = V_\infty w_y \quad (3.9)$$

The magnitude of the relative velocity can be expressed as:

$$V_{rel} = \sqrt{V_x^2 + V_y^2} = \sqrt{V_n^2 + V_t^2} \quad (3.10)$$

Now considering the angle of the flow with respect to the 2D blade element (see Figure 3.6), the angle between the relative velocity and the airfoil chord line is known as the angle of attack,  $\alpha$  [28]. The angle between the relative velocity and the tangent to the blade rotational path is known as the inflow angle,  $\varphi$ . The difference between these two angles is due to the fact that the blade can be pitched. The pitch angle,  $\theta_p$ , is the angle between the airfoil chord line and the tangent to the blade rotational path. These angles are related according to the equation below:

$$\alpha = \varphi + \theta_p \quad (3.11)$$

The inflow angle can be directly computed from the flow velocity components:

$$\varphi = \tan^{-1}\left(\frac{V_n}{V_t}\right) \quad (3.12)$$

The motion of the flow around the airfoil creates aerodynamic lift and drag forces. For each airfoil and operating Reynolds number, there are lift and drag coefficients,  $C_l$  and  $C_d$ , which depend on  $\alpha$  (these coefficients are called the airfoil polars). The lift force,  $F_L$ , is perpendicular to the flow direction (relative velocity), and the drag force,  $F_D$ , is parallel to the flow direction (see Figure 3.6). They are calculated as [28]:

$$F_L(\theta) = \frac{1}{2} \rho V_{rel}^2(\theta) c C_l(\alpha) \quad (3.13)$$

$$F_D(\theta) = \frac{1}{2} \rho V_{rel}^2(\theta) c C_d(\alpha) \quad (3.14)$$

where  $\rho$  is the air density.

Next, we can perform a coordinate transformation to get the normal ( $F_n$ ) and tangential ( $F_t$ ) forces [28]:

$$F_n(\theta) = F_L(\theta) \cos \varphi + F_D(\theta) \sin \varphi \quad (3.15)$$

$$F_t(\theta) = F_L(\theta) \sin \varphi - F_D(\theta) \cos \varphi \quad (3.16)$$

These forces are also shown in Figure 3.6. The normal force is positive pointing inward. The tangential force is positive in the direction of rotation (counter-clockwise). All the aforementioned forces (lift, drag, normal, tangential) are per unit span.

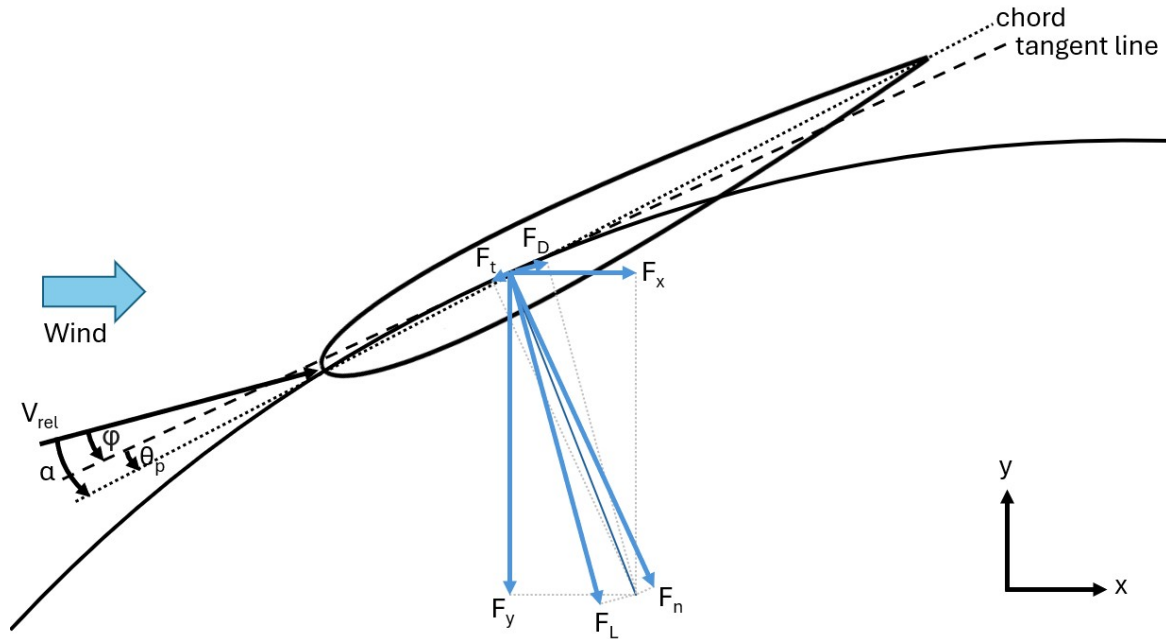


**Figure 3.6:** Decomposition of the VAWT blade forces and angles. Figure based on [28].

The force can also be decomposed into x- and y-components, as shown in Figure 3.6. The x-component, which is in the streamwise direction, is important because it is related to the rotor thrust. It is calculated for a single blade as:

$$F_x = F_n(\theta) \sin \theta - F_t(\theta) \cos \theta \quad (3.17)$$

And the average rotor thrust over one revolution considering all the blades is given by the thrust coefficient [28]:

$$C_T = \frac{1}{0.5\rho(2R)V_\infty^2} \frac{B}{2\pi} \int_0^{2\pi} (-F_n(\theta) \sin \theta + F_t(\theta) \cos \theta) d\theta \quad (3.18)$$

Lastly, given the blade forces, we can calculate the average power of the rotor over one rotation. The tangential force is the force component that contributes to torque, and thus power generation. Power is calculated as the torque multiplied by the rotational speed, integrated and averaged over the rotation [28]:

$$P = \frac{B}{2\pi} \int_0^{2\pi} F_t(\theta) \Omega R d\theta \quad (3.19)$$

And the power coefficient is [29]:

$$\begin{aligned} C_p &= \frac{P}{0.5\rho(2R)V_\infty^3} \\ &= \frac{1}{0.5\rho(2R)V_\infty^3} \frac{B}{2\pi} \int_0^{2\pi} F_t(\theta) \Omega R d\theta \end{aligned} \quad (3.20)$$

The power coefficient represents how much power the turbine extracts from the available power in the wind [28].

The performance of a wind turbine is characterized by its power curve. Figure 3.7 shows a typical such power curve, where the turbine's power is plotted against the wind speed. The curve is separated into different regions. In the full load region, the turbine outputs its maximum power, which is called the rated power. In this region, the goal is to keep the power output constant, which involves limiting the energy which the turbine extracts from the wind, so that the turbine's rated power is not exceeded. The full load region starts at the rated wind speed, which is when the turbine first achieves its rated power. Below the rated wind speed is the partial load region. In this region, the goal is to extract the maximum power from the wind possible. The power output increases with the wind speed and the relationship is cubic. The partial load region starts at the cut-in wind speed, which is when the turbine is turned on and starts producing power. When the wind speed is below the cut-in wind speed, the turbine is idling or standing still. There is also an upper wind speed limit, called the cut-out wind speed, at which the turbine is turned off and stops producing power. Above the cut-out wind speed, the turbine is again idling or standing still. In this study, we focus on the partial load region where the goal is to maximize the power output.

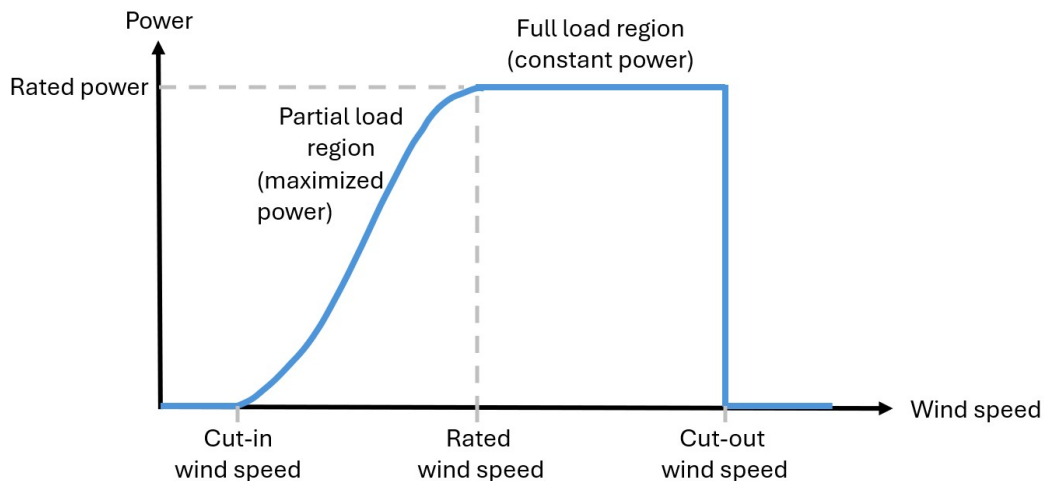


**Figure 3.7:** Typical power curve of a wind turbine, including the full load and partial load regions, as well as important wind speed demarcations.

### 3.2.1. Unsteady VAWT Aerodynamics

There are several unsteady aerodynamic phenomena which are important to consider for VAWTs because the incoming flow to a blade continuously varies throughout its revolution. Here, we briefly discuss dynamic stall, flow curvature, dynamic inflow, and blade-vortex interaction.

Dynamic stall can occur when there are fast, large changes in the angle of attack of an airfoil. The changing angle of attack leads to an unsteady flow field around the airfoil [23]. For a VAWT, the angle of attack constantly changes and can exceed the static stall angle because the blade rotates around a vertical axis—and adding blade pitch also changes the inflow experienced by the blade. The relative velocity of the wind varies and so does the inflow angle [4]. So, the angle of attack varies, and therefore the pressure distribution on the blade varies, ultimately leading to dynamic blade loads [4].

A dynamic motion can suddenly change the angle of attack and initiate dynamic stall. A leading edge vortex forms on the airfoil's suction surface, grows, and convects down the airfoil [4], [23]. When the vortex spans the whole airfoil, the lift force is very large, even though the angle of attack is beyond the static stall angle. When the vortex passes the trailing edge of the airfoil, the flow fully separates from the airfoil. There is sudden stall and a sharp drop off in the lift force and a huge increase in the drag force. For a VAWT, this means a large decrease in the power generation when dynamic stall occurs.

Flow curvature refers to the perceived curvilinear inflow by the blade. Because of the vertical orientation of the rotation axis of a VAWT, as the blades rotate around the axis, the inflow appears curved with respect to the blade instead of rectilinear [11], [37]. Therefore, the angle of attack varies at different points along the blade chord. Flow curvature has greater consequences for turbines with higher chord-to-radius ratios. The effect of flow curvature can be compensated for by either 1) adding an equivalent angle of attack, or 2) adding camber to the airfoil (which also introduces an additional incidence angle) and considering the virtual airfoil in rectilinear flow [4]. The experience

of flow curvature is analogous to an extra angle of attack, or a positive blade pitch angle offset. The lift force is increased, which makes the normal force more positive (less negative in the downwind half) [26]. The tangential force increases in the upwind half, but it is negative in the downwind half. Ultimately, the power extraction increases in the upwind half but power loss increases in the downwind half.

Dynamic inflow is the phenomenon where the change in induction lags behind a change in loading on the rotor. The loading on a VAWT constantly changes, but in response, the induced velocity changes gradually; it does not change instantaneously when the loading changes [4].

Finally, for VAWTs, blade-vortex interaction occurs. When a blade in a VAWT passes through the upwind half of the revolution, it sheds vortices. Because the axis of rotation is vertical, a blade in the downwind half of the revolution is in the wake generated in the upwind half [4]. Though not the main velocity component, the induced velocity of a blade passing through the downwind half undergoes large variations due to the unsteady flow [4]. This in turn can cause fluctuations in the blade angle of attack and loads.

### 3.3. VAWT Numerical Models

The aerodynamics of a VAWT can be represented by a numerical model. There are four broad categories of VAWT models: streamtube models, the actuator cylinder (AC) model, vortex models, and computational fluid dynamics (CFD) models. The models involve different levels of complexity, accuracy, and computational requirement [7], [8], [28], [37], [38].

#### 3.3.1. Streamtube Models

The streamtube models are based on one-dimensional (1D) momentum theory, just like the actuator disk model for HAWTs [28]. The rotor is replaced with an infinitely-thin actuator disk(s) which exerts a force on the flow. The conservation of momentum dictates that this force is equal to the change in streamwise momentum flow in front of versus behind the disk [8]. The momentum model calculates the induced velocity, which is assumed to be constant across the disk [28]. The model is solved iteratively with the Blade Element Model (BEM), which calculates the blade forces.

There are several ways to represent a VAWT rotor in the streamtube models. The simplest is a single streamtube. This is a very simplified model where the VAWT rotor is replaced by a single equivalent actuator disk, which is located at the rotor's center [28]. Therefore, only one induction value is calculated and assumed to apply to the whole rotor.

However, the loading in the upwind half and downwind half of a VAWT are very different. In the double streamtube model, there is one actuator disk for the upwind half and one actuator disk for the downwind half [28]. The downwind disk is in the wake of the upwind disk and it is assumed that the wake is fully developed by the time it reaches the downwind disk [28]. The outlet flow velocity of the upwind disk is assumed to be the inlet flow velocity of the downwind disk. However, the effect of the downwind disk on the upwind disk is neglected. Two different induction values are calculated, one for the upwind half and one for the downwind half. However, the induction value is the same in the crosswind direction.

In the multiple streamtube (MST) model, the crosswind direction is divided into several independent streamtubes [28]. Each streamtube has one equivalent actuator disk aligned with the center of the rotor which represents a section of the rotor. Thus, there are different induction values in the crosswind direction, but the same induction value for the upwind and downwind halves. It is assumed that the loads in one streamtube do not affect the other streamtubes, so the induction in the crosswind direction is not considered [8], [28]. Ferreira *et al.* [38] found that the MST model is not accurate.

Finally, the double multiple streamtube (DMST) model represents a VAWT rotor with multiple actuator disks in the crosswind direction in addition to separate upwind and downwind actuator disks [28]. Therefore, a different induction value is calculated for each crosswind section and upwind/downwind half. Again, the streamtubes in the crosswind direction are independent, meaning they do not influence each other.

The DMST model has been commonly used to model VAWTs in the past [7], [8], for example, [9], [13], [16], [18], [21], [26] used DMST in their studies of pitch optimization. The DMST model is computationally inexpensive which is why it has been used often [7]. However, the streamtube models are not a very realistic representation of VAWTs. They are 1D, so the crosswind induction is ignored. This is not accurate considering the rotation of the blades around a vertical axis so that they move in both the streamwise and crosswind directions. Furthermore, dividing the rotor

into actuator disks does not capture the curved actuation surface [7]. The streamtube models also do not consider unsteady aerodynamics such as dynamic stall, flow curvature, and dynamic inflow; but, external dedicated models can be added to the streamtube models to simulate these effects [4], [9], [16], [26]. Streamtube expansion can also be added [16]. Several authors have found that the DMST model is less accurate than the AC model and vortex models [8], [37], [38]. Cheng *et al.* [8] found that the DMST is less accurate at predicting the aerodynamic power and loads than the AC model. Ferreira *et al.* [38] compared several VAWT models, including the MST and DMST, and concluded that the streamtube models are inaccurate due to their assumptions and should not be used unless some corrections are added. Thus, while the DMST model is computationally efficient, we do not use it in this study because it has proved to be inaccurate.

### 3.3.2. The Actuator Cylinder Model

In the actuator cylinder (AC) model, a VAWT is represented by a 2D or 3D actuator cylinder instead of an actuator disk. This better represents the actuation surface of a (straight-bladed) VAWT. The details of the model are further explained in Section 3.4. Essentially, the actuator cylinder exerts the distributed reaction of the blade forces on the flow [28]. The governing equations are the Euler equations and continuity equation, which are used to calculate the induced velocity from the forces [28], [29]. The induced velocity in both the streamwise and crosswind directions is calculated. The AC model is also solved iteratively with BEM. Often, only the linear solution is solved, with a correction factor to account for the nonlinear part of the solution, in what is called the *Modified Linear* solution [28]. In this study, we use the 2D AC model.

A 3D VAWT rotor can be represented either by a series of 2D actuator cylinders, or by the 3D actuator cylinder model [28]. In the former, numerous independent 2D AC sections are stacked vertically. The ACs are not considered to interact in the vertical direction, and tip effects can be added [8], [28]. In the latter, the 3D momentum and continuity equations can be used to derive the 3D AC equations [28].

According to De Tavernier *et al.* [28], the AC model is more accurate than the streamtube models. The AC considers some physical phenomena which are neglected in the streamtube models. The AC includes the effect of one element or streamtube on the others. This includes the effect of the downwind elements on the upwind elements. Cheng *et al.* [8] also found that their AC model implementation is accurate compared to other numerical models as well as experimental data. Madsen *et al.* [7] validated that the AC modified linear solution is highly accurate in that it matches the result of the full AC model well. In their comparison of VAWT models, Ferreira *et al.* [38] found good agreement between the AC model and several vortex models. The authors did however note some differences between the models due to the time-averaged nature of the AC model. Another simplification in the AC model that affects its accuracy is that it does not resolve discrete vortices in the wake, unlike vortex models and CFD [37]. This includes the vortices in the downwind half, which were created in the upwind half, and interact with the blades as they pass through the downwind half, so this could lead to inaccuracies in the blade loads and induced velocity calculated by the AC in the downwind half. Additionally, unsteady effects such as dynamic stall, flow curvature, and dynamic inflow are not implicitly modeled in the AC, but can be incorporated with additional models to make the VAWT model more accurate [4], [8], [37].

The modified linear solution of the AC model has a very low computational requirement [7], [8]. It is much more computationally efficient and faster in particular compared to vortex models and CFD models [37]. The low computational requirement of the AC model is important considering the optimization performed in this study. The optimization routine requires repeated evaluations of the VAWT model, so it is critical that the model can be executed in a short amount of time. This is even more important considering we have multiple optimization cases with an increasing number of objectives, which require an increasing number of function evaluations to converge to the optimal solutions. Therefore, considering the accuracy and computational efficiency of the AC model [7], [8], [28], [37], it is selected as the method to model VAWTs in the present study.

### 3.3.3. Vortex Models

There are many different models that belong to the category of vortex models. They are based on Helmholtz's vortex theorem and Kelvin's circulation theorem [4]. The VAWT is modeled by a vortex system consisting of a bound vortex along each blade, two trailing vortices at the blade tips, and wake vortices which are shed at each time step by the blade when the bound vortex changes [4]. The vorticity field is used to calculate the induced velocity. Each vortex segment has a strength which determines the induced velocity via the Biot-Savart law. Each blade can be represented by a lifting line or lifting surface (also called panel method) to calculate the blade loads, from which the strength (circulation) of the bound vortex can be calculated [4]. The wake is represented by a series of vortices. The

velocity in the wake is calculated in space and time, and either the free-wake or fixed-wake method can be used [4]. Many vortex models implicitly model dynamic stall, flow curvature, dynamic inflow, and blade-vortex interaction. The models can be 2D or 3D. They are solved in time and the solution is unsteady, but they are too computationally intensive for the purposes of this study.

### 3.3.4. Computational Fluid Dynamics Models

Computational fluid dynamics (CFD) models also encompass a broad range of implementations. They use the Navier-Stokes equations to compute the induced velocity [4]. The Navier-Stokes equations are an expression of the momentum and continuity equations. In CFD models, they are solved numerically, not analytically. CFD inherently models dynamic stall, flow curvature, dynamic inflow, and blade-vortex interaction [4]. Turbulence can be modeled in several different ways. CFD models can be 2D or 3D. CFD models are more accurate than other VAWT models, but they are computationally intensive [4]. The computing requirement is much too high for use in this study.

## 3.4. 2D Actuator Cylinder Model Derivation

The 2D actuator cylinder model was originally developed by Madsen [29]. It extends the concept of the actuator disk which is used to model HAWTs. Whereas the swept area of a HAWT is a disk, the swept area of a VAWT is a cylinder. Therefore, in the AC model, a VAWT is represented with a cylindrical actuation surface and a distributed force is applied to it. The force that is applied on the flow by the VAWT is the reaction of the blade forces (the fluid applies a force on the blades, and in turn the blades apply a reaction force on the fluid), which in the AC model is applied in a distributed, or averaged, way across the actuator cylinder [4]. This volume force acting on the cylindrical actuation surface creates a pressure jump across the surface [29]. Given the force field as input, the output of the AC is the flow velocity. The model is solved iteratively with the Blade Element Model (BEM): BEM uses the flow velocity field output from the AC model to determine the force field (blade loads), and the AC model uses the force field output from BEM to determine the flow velocity field [4], [29].

The governing equations of the AC model are the 2D, steady, incompressible Euler equations and the continuity equation [4], [29]. The AC is a quasi-steady model [8] and yields a solution that is steady in time. The flow is assumed to be inviscid and incompressible (meaning the density  $\rho$  is constant) [4], [29]. The actuator cylinder is assumed to stretch infinitely in the  $z$ -direction, thereby the flow is two dimensional.

The blade forces are expressed in nondimensional, time-averaged terms.  $F_n(\theta)$  is the normal blade force component and  $F_t(\theta)$  is the tangential blade force component. Both are expressed per unit length (span). The forces are multiplied by  $B/2\pi R$  which represents time-averaging in one revolution [4]. Then they are divided by  $\rho V_\infty^2$  for non-dimensionalizing. This yields the nondimensional, time-averaged blade load components  $Q_n(\theta)$  and  $Q_t(\theta)$  in Equation 3.21 [4].  $Q_n(\theta)$  and  $Q_t(\theta)$  are obtained by solving the BEM. The sign convention is shown in Figure 3.8:  $Q_n$  is positive pointing outward, and  $Q_t$  is positive in the counter-clockwise direction (in the direction of the rotor rotation).

$$Q_n(\theta) = \frac{BF_n(\theta)}{2\pi R\rho V_\infty^2} \quad (3.21)$$

$$Q_t(\theta) = -\frac{BF_t(\theta)}{2\pi R\rho V_\infty^2}$$

In the original formulation developed by Madsen [29], only the blade normal force was included in the calculation of the induced velocities. Cheng *et al.* [8] included both the normal and tangential blade forces when calculating the induced velocities, which is the formulation used here. Note, however, that Cheng *et al.* [8] found that including the tangential blade forces has a very small effect on the aerodynamic loads.

The nondimensional velocity components  $v_x$  and  $v_y$  are:

$$v_x = 1 + w_x \quad (3.22)$$

$$v_y = w_y \quad (3.23)$$

where  $w_x$  and  $w_y$  are velocity perturbations which represent the induced velocity. They are the changes in local wind speed that occur because the VAWT is standing in the flow [8], [37].

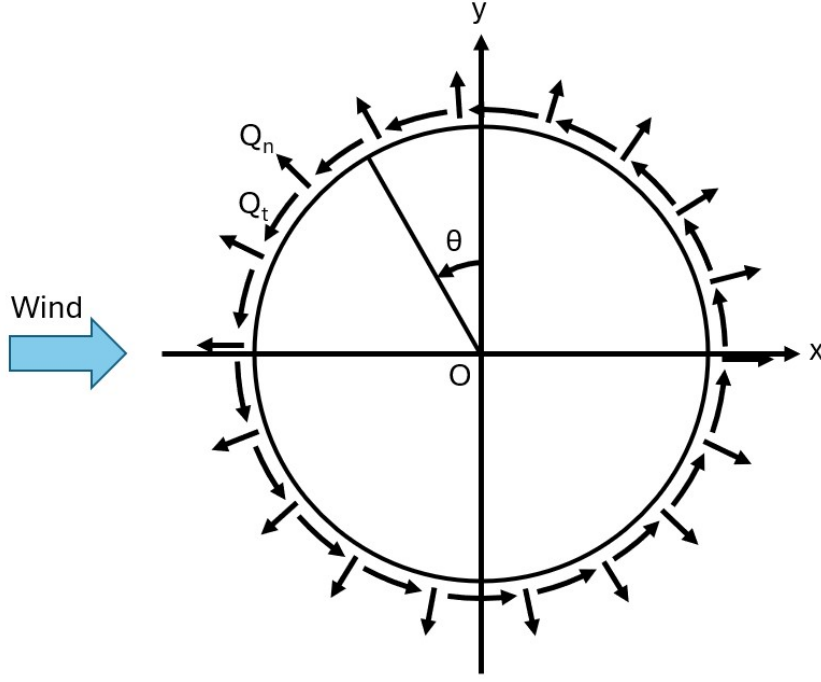


**Figure 3.8:** The actuator cylinder model coordinate system, showing the sign convention of the nondimensional, time-averaged blade forces. Figure based on [39].

Plugging these velocity components into the (nondimensionalized) Euler and continuity equations yields Equation 3.24 and 3.25 [29].

$$\frac{\partial w_x}{\partial x} + w_x \frac{\partial w_x}{\partial x} + w_y \frac{\partial w_x}{\partial y} = -\frac{\partial p}{\partial x} + f_x \quad (3.24)$$

$$\frac{\partial w_y}{\partial x} + w_x \frac{\partial w_y}{\partial x} + w_y \frac{\partial w_y}{\partial y} = -\frac{\partial p}{\partial y} + f_y$$

$$\frac{\partial w_x}{\partial x} + \frac{\partial w_y}{\partial y} = 0 \quad (3.25)$$

where  $f_x$  and  $f_y$  are volume force components and  $p$  is the pressure. Madsen [29] writes Equation 3.24 in terms of a linear volume force,  $f$ , and an induced or second order volume force,  $g$ :

$$\frac{\partial w_x}{\partial x} = -\frac{\partial p}{\partial x} + f_x + g_x \quad (3.26)$$

$$\frac{\partial w_y}{\partial x} = -\frac{\partial p}{\partial y} + f_y + g_y$$

where

$$g_x = -(w_x \frac{\partial w_x}{\partial x} + w_y \frac{\partial w_x}{\partial y}) \quad (3.27)$$

$$g_y = -(w_x \frac{\partial w_y}{\partial x} + w_y \frac{\partial w_y}{\partial y}) \quad (3.28)$$

This distinction is important when solving the AC model because often only the linear solution corresponding to  $f$  is used. The nonlinear solution corresponding to  $g$  is computationally expensive to solve, and is therefore rarely solved [4], [8]. Equations 3.26 and 3.25 can be solved for the pressure field  $p(f)$  and the induced velocity components  $w_x$  and  $w_y$ , the details of which are in Madsen [29]. The final solution is a sum of a linear part (which is a function of  $f$ ) and a nonlinear part (which is a function of  $g$ ) [7]. The linear solution to the AC is given by Equation 3.29 [4]. Note that the  $g_x$  and  $g_y$  terms are ignored.

$$\begin{aligned}
w_x(x, y) = & -\frac{1}{2\pi} \int_0^{2\pi} Q_n(\theta) \frac{-(x + \sin \theta) \sin \theta + (y - \cos \theta) \cos \theta}{(x + \sin \theta)^2 + (y - \cos \theta)^2} d\theta \\
& -\frac{1}{2\pi} \int_0^{2\pi} Q_t(\theta) \frac{-(x + \sin \theta) \cos \theta - (y - \cos \theta) \sin \theta}{(x + \sin \theta)^2 + (y - \cos \theta)^2} d\theta \\
& - Q_n(\cos^{-1}(y))^* - Q_t(\cos^{-1}(y)) \frac{y}{\sqrt{1-y^2}}^* \\
& + Q_n(-\cos^{-1}(y))^{**} - Q_t(-\cos^{-1}(y)) \frac{y}{\sqrt{1-y^2}}^{**} \\
w_y(x, y) = & -\frac{1}{2\pi} \int_0^{2\pi} Q_n(\theta) \frac{-(x + \sin \theta) \cos \theta - (y - \cos \theta) \sin \theta}{(x + \sin \theta)^2 + (y - \cos \theta)^2} d\theta \\
& + \frac{1}{2\pi} \int_0^{2\pi} Q_t(\theta) \frac{-(x + \sin \theta) \sin \theta + (y - \cos \theta) \cos \theta}{(x + \sin \theta)^2 + (y - \cos \theta)^2} d\theta
\end{aligned} \tag{3.29}$$

Equation 3.29 can be evaluated at any coordinate point  $(x, y)$ , which is normalized by the rotor radius  $R$ , giving the induced velocity at any point in the flow field. When the evaluation point is inside the cylinder, then the \* terms are included (see Figure 3.9). When the evaluation point is in the wake, behind the cylinder, then both the \* and \*\* terms are included. This is so the induced x-velocity is continuous across the cylinder surface [29]. Intuitively, this can be thought of a pressure drop each time the cylinder actuation surface is crossed which affects the flow field. Note that the AC model yields the induced velocity, so the freestream velocity and rotational velocity need to be added in order to get the total relative velocity,  $\vec{V}_{rel}$ .

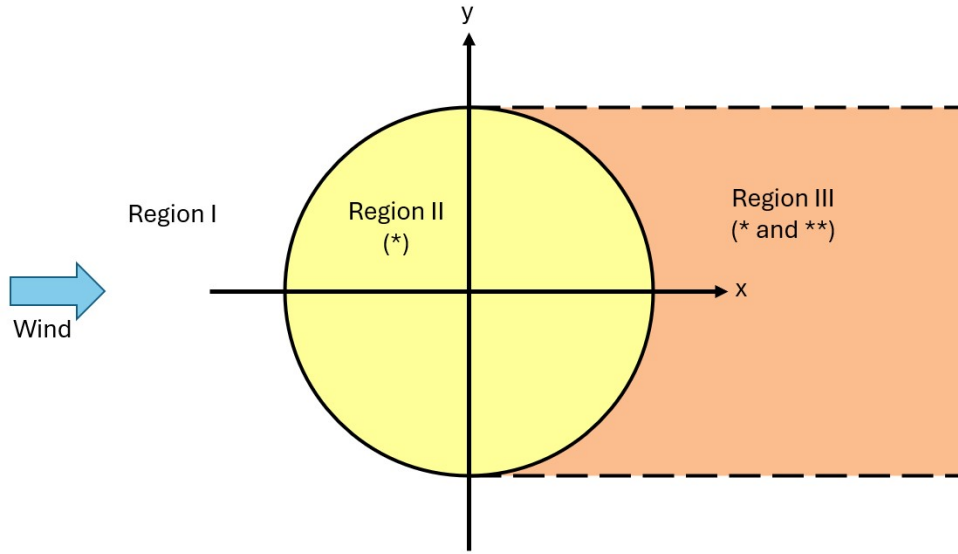


**Figure 3.9:** Regions of the AC: I in front of the cylinder, II inside the cylinder, and III in the wake of the cylinder. The region an evaluation point is in determines which \* and \*\* terms are added in the induced velocity. Figure based on [39].

The nonlinear solution is solved through iteration using a partly analytical/numerical method [29]. It requires discretizing the spatial domain around and including the actuator cylinder and using interpolation. Various numerical and analytical integration and differentiation techniques are used. The nonlinear solution is not included in this study, again, due to computational complexity. A correction factor is, however, incorporated to account for the nonlinear solution.

### 3.4.1. Modified Linear Solution

Madsen *et al.* [7] developed the so-called *Modified Linear* model of the AC in order to model the induction part within an aeroelastic model. Therefore, the modified linear model has to have a low computational requirement yet

still be accurate. The basic idea is to multiply the linear solution by a correction factor,  $k_a$ , which makes up for the fact that the nonlinear part was excluded [4].

When comparing the linear model to the full AC model, Madsen *et al.* [7] noticed a few discrepancies. Firstly, the power and thrust coefficients,  $C_p$  and  $C_T$ , line up until the tip speed ratio is about 2.5 (at which point  $C_p \approx 0.5$  and  $C_T \approx 0.65$ ). At higher tip speed ratios, the linear model overestimates  $C_p$  and  $C_T$ . Secondly, for the most part, the linear model overestimates the normal and tangential blade forces (when  $\lambda = 4$ ). Larsen and Madsen [37] note that the deviations are more pronounced on the downwind half of the rotor. Thirdly, the differences between the two models in the calculated velocity magnitude and direction of the flow field become greater as the tip speed ratio increases. However, it is observed that the linear solution has generally the same shape as the full solution with respect to loading (normal and tangential) and flow velocity (magnitude and direction), so multiplying the linear solution by some factor could lead to a solution more in line with the full solution.

In order to derive the correction factor, the linear 2D actuator disk model is used, solved via a similar method to the 2D AC model. For uniform loading on a VAWT, the relation 3.30 between the thrust coefficient and induction factor results [7], [37].

$$C_T = 4a_{linear} \quad (3.30)$$

However, from BEM theory for HAWTs, there is the relation in Equation 3.31 [7], [37].

$$C_T = 4a - 4a^2 = 4a(1 - a) \quad (3.31)$$

In order to achieve the same induction factor in the linear solution of the actuator disk as results from BEM, we need to multiply  $a_{linear}$  with the correction factor:  $k_a = \frac{1}{1-a}$  [7]. The induction factor  $a$  used in this expression is based on the average thrust coefficient of the full rotor using the actuator disk model [4], [7]. In practice,  $a$  is calculated using the polynomial relationship between  $C_T$  and  $a$  in Equation 3.32, which is used in the BEM theory applied to HAWTs [37].

$$a = k_3 C_T^3 + k_2 C_T^2 + k_1 C_T + k_0 \quad (3.32)$$

where

$$\begin{aligned} k_3 &= 0.0892074 \\ k_2 &= 0.0544955 \\ k_1 &= 0.251163 \\ k_0 &= -0.0017077 \end{aligned}$$

Madsen *et al.* [7] find that the modified linear solution is accurate (compared to the full AC solution), even when the loading is high. It also has a very low computational requirement. Madsen *et al.* [7] only use the normal force when calculating the induced velocities.

Cheng *et al.* [8] found that the  $k_a = \frac{1}{1-a}$  correction factor derived by Madsen *et al.* [7] still deviates from the full AC solution for some operating conditions. In particular, at high tip speed ratios, Madsen *et al.* [7]'s modified linear solution underestimates the power coefficient. Therefore, Cheng *et al.* [8] propose a change to the  $k_a$  factor for large induction factor,  $a$ , which corresponds to cases when the tip speed ratio is high. The new modified linear solution is in Equation 3.33 [8].

$$k_a = \begin{cases} \frac{1}{1-a} & a \leq 0.15 \\ \frac{1}{1-a} (0.65 + 0.35e^{-4.5(a-0.15)}) & a > 0.15 \end{cases} \quad (3.33)$$

The coefficients in Equation 3.33 were empirically determined [8]. We multiply the linear solution,  $w_x$  and  $w_y$ , by  $k_a$  to obtain the so-called *Modified Linear* solution. Cheng *et al.* [8] compared the new modified linear solution with experimental data and found that it predicts the power very well.

### 3.5. Review of VAWT Pitch Control in Literature

Previous researchers have recognized the importance of blade pitching to improve the performance of VAWTs and have consequently invented different pitch strategies. The baseline case is zero pitch, in which the pitch angle of all

the blades is fixed to a constant  $0^\circ$  throughout the rotation of the turbine. Some researchers have analyzed the effect of different non-zero fixed pitch offsets. Others have turned to variable, or dynamic, blade pitching. In variable pitching, the pitch angle of the blades varies throughout the turbine revolution, which can be done in a passive or active manner. Some researchers achieve active pitch collectively through a linkage mechanism, while others implement individual blade pitching. Figure 3.10 shows a flowchart of these different categories of pitch strategy. In this section, we summarize the various VAWT pitch strategies in the literature, addressing each of the categories in turn.

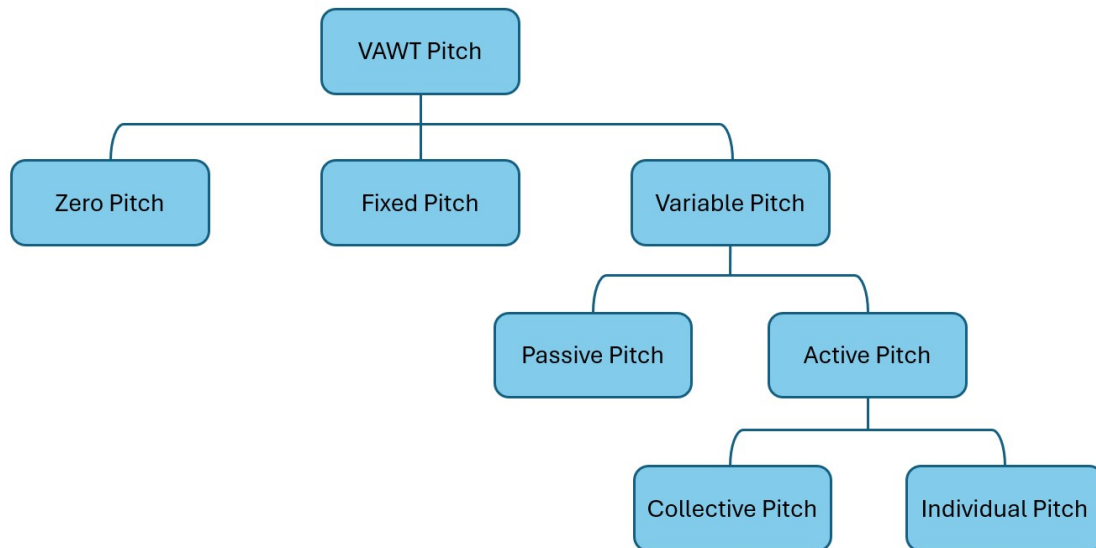


**Figure 3.10:** VAWT pitch control can be broken down into several categories.

### 3.5.1. Fixed Pitch

When the blade pitch is fixed, a single value of pitch offset is held constant throughout the turbine rotation. We distinguish this case from zero fixed pitch because here we consider a non-zero fixed pitch offset. While a fixed pitch strategy is not optimal, it has been shown that a small negative pitch offset can improve the turbine's performance compared to zero pitch [6], [19]. Fixed blade pitch is also simple and cheap to implement in a turbine [6], so an improvement in power can be achieved for relatively little effort. Furthermore, analyzing the effect of different fixed pitch offsets at different azimuthal positions can elucidate an optimal variable pitch strategy. The studies summarized in this section analyze the effect of constant blade pitch offsets on the VAWT loading in addition to the power coefficient.

Rezaeiha *et al.* [6] studied the effects of fixed pitch angles using CFD. They use pitch angles from  $-7^\circ$  to  $3^\circ$  at increments of  $1^\circ$  ( $\theta_p = -7^\circ, -6^\circ, -5^\circ, -4^\circ, -3^\circ, -2^\circ, -1^\circ, 0^\circ, 1^\circ, 2^\circ, \text{ and } 3^\circ$ ). The authors use a low solidity turbine ( $\sigma = 0.172$ ) to minimize the blade-wake interactions and a moderate tip speed ratio ( $\lambda = 4$ ) to avoid dynamic stall. They implemented a 2D unsteady Reynolds-averaged Navier-Stokes (URANS) CFD model. The authors analyze the effect of fixed pitch angle on both the instantaneous and averaged loading. They found that a fixed pitch angle causes a shift in the instantaneous moment and x-force coefficients between the upwind and downwind halves of the rotor. Additionally, there is a shift in the instantaneous y-force coefficient between the top and bottom halves, but there is no shift in the instantaneous normal force coefficient. According to the authors, analyzing the instantaneous (per azimuth) loading and aerodynamics for the different fixed pitch angles can be used to determine an optimal dynamic pitch strategy to improve the power performance of the turbine even more than the optimal fixed pitch angle. For example, a positive pitch angle increases the instantaneous moment coefficient from  $\theta = 25^\circ$ - $90^\circ$ , while a negative pitch angle improves the moment coefficient from  $\theta = 0^\circ$ - $25^\circ$  and  $\theta = 90^\circ$ - $360^\circ$ . Of the negative pitch angles, a small  $\theta_p = -2^\circ$  is optimal during  $\theta = 90^\circ$ - $160^\circ$ , while a large  $\theta_p = -6^\circ$  is optimal during  $\theta = 160^\circ$ - $360^\circ$ . However, a more negative pitch angle of  $\theta_p = -7^\circ$  reduces the moment coefficient because the angle of attack is higher so there is more flow separation. When  $\theta_p = 3^\circ$ , stall is evident in both the instantaneous and averaged loading from  $\theta = 90^\circ$ - $160^\circ$  (upwind). There is a large reduction in  $C_p$ . Therefore, the pitch angle should not be greater than  $3^\circ$  in order to avoid stall upwind. Additionally, for  $\theta_p = 2^\circ$  and  $-7^\circ$ , the angle of attack exceeds the static stall angle, from  $\theta = 70^\circ$ - $135^\circ$  (upwind) for  $\theta_p = 2^\circ$  and from  $\theta = 260^\circ$ - $290^\circ$  (downwind) for  $\theta_p = -7^\circ$ , but there is no stall. This is because during the upstroke of a dynamic airfoil, the boundary layer has a higher resistance to flow separation, and stall is

therefore delayed. The authors also found that the dynamic airfoil polars are different than the static ones. They have hysteresis, and also depend on the fixed pitch angle. Considering averaged loading, represented by the power and thrust coefficients,  $C_p$  and  $C_T$ , the authors found that the optimal pitch angle is  $\theta_p = -2^\circ$  (for their turbine geometry and operating conditions). This results in a 6.6% increase in  $C_p$  and 2% increase in  $C_T$  compared to zero pitch.

LeBlanc and Ferreira [14] conducted a series of experiments with a two-bladed, 1.5-m-diameter H-rotor at fixed pitch angles of  $0^\circ$ ,  $5^\circ$ , and  $-5^\circ$ . They used particle image velocimetry (PIV) to measure the flow velocity field around the rotor. Later, they calculated the blade aerodynamic loads (normal and tangential forces) from the velocity field and its derivatives using a method by Noca [40]. Measurements were taken at six azimuthal positions, three upwind and three downwind:  $\theta \approx 60^\circ$ ,  $90^\circ$ ,  $120^\circ$ ,  $240^\circ$ ,  $270^\circ$ , and  $300^\circ$ . Measurements were taken at the blade mid-span so as to minimize 3D (tip) effects. Some main observations from LeBlanc and Ferreira [14] include that the positive pitch angle shifts the load from the downwind half to the upwind half, while the negative pitch angle shifts the load from the upwind half to the downwind half. For example, for  $\theta_p = -5^\circ$ , the angle of attack, forces, and energy extraction upwind are lower than the  $\theta_p = 0^\circ$  case, while they increase in the downwind half compared to the  $\theta_p = 0^\circ$  case (except the loading is impacted by stall). At  $5^\circ$  pitch angle, complete dynamic stall occurs at  $\theta = 120^\circ$ . This causes the normal force to drop substantially and the tangential force to become negative. The stall at  $\theta = 120^\circ$  makes the velocity, and loading, higher directly downwind at  $\theta = 240^\circ$ . At  $-5^\circ$  pitch angle, the flow remains attached throughout the upwind half, but there is deep stall downwind from  $\theta = 240^\circ$  to  $300^\circ$ . The authors reason that this is because the loading in the upwind half is lower, so the velocity in the downwind half is greater, which increases the angle of attack and leads to stall. The stall in the downwind region causes the normal load magnitude to decrease (when it is expected to increase compared to  $0^\circ$  pitch) and tangential load to be negative. In fact, the stall when  $\theta_p = -5^\circ$  causes the overall rotor thrust to be lower than the  $\theta_p = 0^\circ$  case. In the zero-pitch case, there is no deep stall. In summary, both positive and negative pitch angles can lead to dynamic stall, in the upwind and downwind halves, respectively. Therefore, both positive and negative limits should be placed on the blade pitch angle to avoid dynamic stall. A negative pitch angle appears more favorable upwind and a positive pitch angle more favorable downwind.

LeBlanc and Ferreira [15] performed further experiments on the same turbine, but this time using strain gages mounted to one of the struts to determine the blade normal force. Tangential loading was not included because it is hard to measure and assumed to have a small effect. The experiments were conducted at several fixed pitch angles:  $\theta_p = -5^\circ$ ,  $-3^\circ$ ,  $-2^\circ$ ,  $0^\circ$ ,  $2^\circ$ ,  $3^\circ$ , and  $5^\circ$ . The authors show that the azimuthal pattern of normal load changes when the blade pitch offset changes. A positive pitch angle shifts the normal loading earlier in the rotation. There are also signs of stall because after the peak load in the upwind region, the load drops off more rapidly with more positive pitch angle because the angle of attack is higher (partial stall also occurs at  $\theta_p = 0^\circ$ ). In contrast, a negative pitch angle shifts the normal loading later in the rotation. The magnitude of the peak load increases, up until  $\theta_p = -3^\circ$ . Stall in the upwind half is delayed because the angle of attack is lower. When the pitch angle is too negative ( $\theta_p = -5^\circ$ ), the normal loading in the downwind half is low, likely due to stall. The experiments were conducted at a low Reynolds number ( $8.1 \times 10^4$ ) but the authors predict that the relative changes in loading caused by different fixed pitch angles will apply across Reynolds numbers.

Guo *et al.* [19] used pitch angle control to try to improve the efficiency ( $C_p$ ) of VAWTs. First, the authors find a fixed pitch angle that can improve  $C_p$ . They study a range of fixed pitch angles using a numerical CFD simulation. They use a 2D, incompressible, URANS model. The fixed pitch angles span from  $-5^\circ$  to  $4^\circ$  at increments of  $1^\circ$  ( $\theta_p = -5^\circ$ ,  $-4^\circ$ ,  $-3^\circ$ ,  $-2^\circ$ ,  $-1^\circ$ ,  $0^\circ$ ,  $1^\circ$ ,  $2^\circ$ ,  $3^\circ$ , and  $4^\circ$ ). The authors analyze the instantaneous moment coefficient, x-force coefficient, and y-force coefficient. The moment coefficient is maximum upwind when  $\theta_p = 3^\circ$ , and downwind when  $\theta_p = -4^\circ$ . Upwind, if the pitch angle is greater than  $\theta_p = 3^\circ$ , stall occurs and there is a decrease in torque. The x-force coefficient (thrust) is maximum in the upwind region when  $\theta_p = 4^\circ$  and in the downwind region when  $\theta_p = -5^\circ$ . When the pitch angle is  $4^\circ$ , there is stall at the end of the upwind half. The authors found that the optimal fixed pitch angle is  $\theta_p = -1^\circ$ . This is when the maximum power coefficient  $C_p$  occurs, and it is 4.5% greater than when the pitch angle is zero. In fact,  $C_p$  is smaller than the zero-pitch case for all pitch angles other than  $\theta_p = -1^\circ$  and  $-2^\circ$ . We conclude that a fixed pitch angle impacts the turbine power coefficient and loading in different azimuth regions. In particular,  $\theta_p = -1^\circ$  is optimal and positive pitch is favorable upwind and negative pitch is favorable downwind. Later, the authors design a variable pitch law, as described in Section 3.5.2.

### 3.5.2. Variable Pitch

A fixed pitch strategy is still limited to low efficiencies [11]. Therefore, to increase a VAWT's power output, variable, or dynamic, pitch can be used. In variable pitching, the pitch angle of each blade changes throughout a revolution, depending on its azimuthal position. Variable blade pitching can be achieved in multiple ways: passive pitch, collective active pitch, and individual active pitch.

### Passive Variable Pitch

One way to dynamically pitch the blades is through passive pitch. In passive pitch, the blades are not being moved to a specific pitch angle based on some predefined law of pitch angle versus azimuthal angle [16]. Instead, they are free to pitch in reaction to the inertial and aerodynamic forces they experience, which reduces the angle of attack of the blades and therefore reduces the likelihood of stall [11], [16]. According to Benedict *et al.* [11], passive pitch systems result in very low efficiencies.

Lazauskas [16] explored variable pitch angles to address the issue of VAWT self-starting but also found that variable pitch can avoid stall and improve the power coefficient. Note that the author uses the opposite convention of pitch as is used in this study: positive pitch refers to the leading edge pointing outward. The author investigates three pitch control systems: a sinusoidal forced pitch system and two types of self-acting stabilized pitch controls—mass-stabilized and what the author calls “aero-pitch”. A self-acting stabilized pitch system allows the blades to pitch in reaction to the aerodynamic forces they experience, rather than forcing a prescribed pitch pattern on the blades. Thus, it is a passive variable pitch system. Each pitch control system is optimized, using the DMST model with flow curvature effects, streamtube expansion, and modified Boeing-Vertol dynamic stall. The sinusoidal forced pitch system is described further in the following section. The two self-acting stabilized pitch control systems are optimized while placing a maximum allowable amplitude on the pitch angle, in both the inward and outward directions. The optimal pitch kinematics depend on the tip speed ratio. Figure 3.11 shows the optimal pitch kinematics for a tip speed ratio of three. The optimized self-acting stabilized pitch systems achieve a higher  $C_p$  and lower self-starting wind speed than the fixed pitch and sinusoidal pitch systems. The author concludes that self-acting stabilized pitch control systems are hard to optimize due to parameter sensitivity, solution instability, and difficulty in defining an objective function. They suggest to optimize torque and power coefficients integrated over a finite number of tip speed ratios instead.

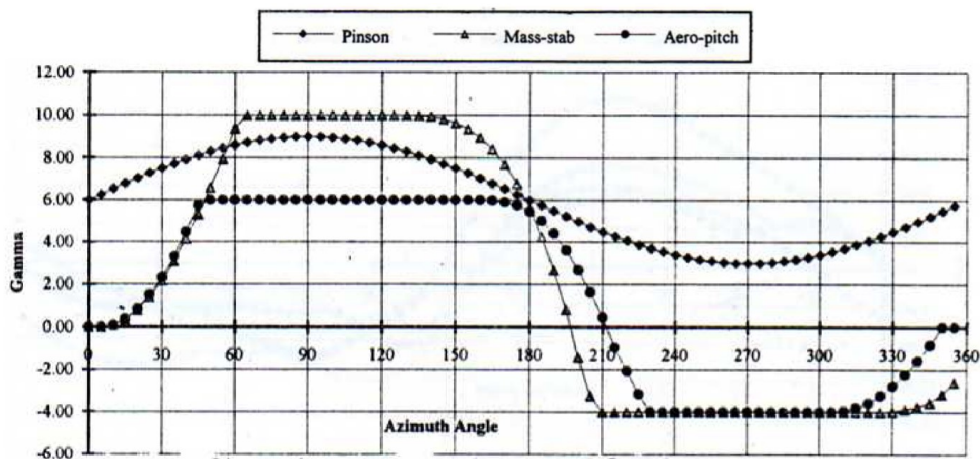


**Figure 3.11:** Variable pitch laws developed by Lazauskas [16] for three different blade pitch systems. The tip speed ratio is 3 (the author also analyzes tip speed ratios of 2 and 4). Pinson is the sinusoidal system. Note that Gamma is the pitch angle ( $=\theta_p$ ). Note that Lazauskas [16] uses the opposite pitch sign convention as used in this study. Figure from [16].

### Active Variable Pitch

In contrast to passive variable pitch, active variable pitch forces the blades to pitch according to a predetermined pitch law. The pitch angle of a blade is usually scheduled with azimuthal angle. Staelens *et al.* [18] and Erfort *et al.* [13] note that scheduling the blade’s pitch angle according to the azimuthal position means that the pitch strategy depends on the wind direction. On the other hand, VAWTs have the advantageous feature of being insensitive to the incoming wind direction. However, by using a wind vane on top of the turbine to measure the wind direction, the pitch law can be adjusted accordingly so that the VAWT is still insensitive to the incoming wind direction [13], [26]. An active variable pitch law can be realized in two ways: a collective mechanism which pitches all the blades simultaneously, or the individual pitch of each blade with separate actuators [12].

#### Collective Pitch

Several researchers have fabricated VAWTs whose blades can pitch dynamically via a type of four-bar linkage mechanism. Following Liang *et al.* [12], we refer to this type of pitch control as collective pitch. An example is

shown in Figure 3.12. In essence, each blade is attached to the center of the rotor by a main link, usually at the blade 1/4-chord [23]. A secondary link attaches the trailing side of the blade to an eccentric rotational point [17], [23]. The eccentric point is offset from the center of the rotor by some distance which represents the third link. The blade is the fourth link. The turbine rotates around the center of the rotor, and the secondary rotation of the eccentric point can be executed by a central actuator [22]. In this way, all the blades pitch together, or collectively. A collective pitch system can improve the  $C_p$ , but for most azimuthal positions, the blade angle is not optimum [23]. Additionally, according to Abbaszadeh *et al.* [22], the linkage mechanism requires a lot of maintenance and can fail easily.

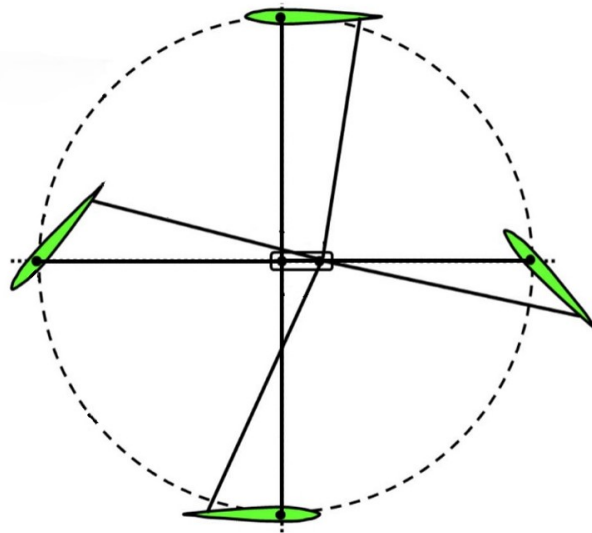


**Figure 3.12:** Example of a collective pitch control mechanism with secondary links connected to an eccentric rotation point. Figure modified from [11].

Benedict *et al.* [11] studied variable pitch using a collective four-bar linkage pitch mechanism because it is a simple mechanism for realizing variable pitch and is practically implementable. They developed a 2D, compressible RANS CFD model and conducted wind tunnel experiments to validate their model against. The authors vary the maximum amplitude of the pitch angle between  $\pm 20^\circ$ ,  $\pm 25^\circ$ ,  $\pm 30^\circ$ , and  $\pm 35^\circ$ . The maximum/minimum pitch amplitudes occur around  $\theta = 90^\circ$  and  $270^\circ$ . The pitch profile is symmetric between the upwind and downwind halves, with the blade pitching outward in the upwind half and inward in the downwind half. The authors found that the pitch amplitude has a strong effect on the turbine efficiency, with the highest  $C_p$  occurring for a pitch amplitude of  $\pm 20^\circ$  to  $\pm 25^\circ$ . When the pitch amplitude is too high ( $\pm 35^\circ$ ) the  $C_p$  becomes significantly lower likely due to stall. The authors also found that lower pitch amplitudes are more favorable for higher tip speed ratios. They also compared a turbine with collective variable pitch ( $\pm 20^\circ$  pitch amplitude) to one with fixed pitch. The fixed-pitch turbine pitched the blades  $20^\circ$  outward throughout the whole revolution. The variable-pitch turbine has a much higher  $C_p$  across tip speed ratios than the fixed-pitch turbine. The fixed-pitch turbine has a very low efficiency because in the downwind region, the blade is pitched in the incorrect direction. Therefore, the angle of attack is large, giving rise to flow separation and stall, which even affects the flow field upwind so the power extraction in the upwind half is also lower than with variable pitch. Lastly, the authors found that the flow physics are fundamentally the same across Reynolds numbers. The  $C_p$  is slightly higher in the upwind half with increasing Reynolds number but the  $C_p$  downwind is similar across Reynolds number. Therefore, their experimental-scale study at low Reynolds number is scalable to real-world turbines with high Reynolds number.

Hwang *et al.* [20] created an experimental water turbine with cycloidal pitch variation, which is implemented with a linkage mechanism. In the linkage mechanism, the maximum pitch angle amplitude and pitch phase angle can be defined, which determine the resulting pitch kinematics. The authors found the optimal turbine geometric characteristics, operating conditions, and cycloidal pitch law via CFD with the aim of maximizing the efficiency ( $C_p$ ) of the turbine. They found that the optimal cycloidal pitch variation has a maximum blade pitch amplitude of  $9^\circ$  and pitch phase angle of  $5^\circ$ . This pitch law leads to a 70% increase in  $C_p$  compared to the zero-pitch case. The authors also conclude that the pitch angle variation is related to the tip speed ratio: when the tip speed ratio increases, the maximum pitch amplitude should decrease and the pitch phase angle should increase. The authors

subsequently implemented individual variable pitch control (see the following section on *Individual Pitch*), which achieves a higher  $C_p$  than the collective pitch control.

Jain and Abhishek [26] performed a numerical study of a VAWT with a collective pitch mechanism. The blades are pitched using a four-bar linkage mechanism, in which the length of the eccentric link can be changed, so that the amplitude of the pitch angle can be varied. The resulting pitch curve is nearly sinusoidal, and is shown in Figure 3.13a for several pitch amplitudes. Note that the authors use the opposite convention for the sign of the pitch angle as we use in this study. The authors use the DMST model, and add unsteady aerodynamic and flow curvature effects, which the authors show are critical for improving the accuracy of the model. In the study, the non-dimensional parameters solidity and tip speed ratio are important parameters for characterizing VAWTs. The authors study the effect of different pitch amplitudes on the power performance ( $C_p$ ) at different tip speed ratios. In order to have the highest  $C_p$ , at low tip speed ratios, the pitch amplitude should be large, and at high tip speed ratios, the pitch amplitude should be small. The authors observe that for any pitch amplitude, the power coefficient is high only for a narrow band of tip speed ratios. This motivates them to change the amplitude of dynamic blade pitching depending on the tip speed ratio in order to sustain maximum power output across a wide range of tip speed ratios. A real turbine in operation will experience variations in the operating tip speed ratio when the wind speed fluctuates. Figure 3.13b shows the resulting pitch strategy for the turbine used in the study. At each tip speed ratio, the pitch amplitude which has the highest  $C_p$  compared to the other pitch amplitudes should be used. As the tip speed ratio increases, the pitch amplitude should decrease. While the authors do not perform optimization, they propose a variable pitch strategy which will result in the highest power extraction possible across tip speed ratios.

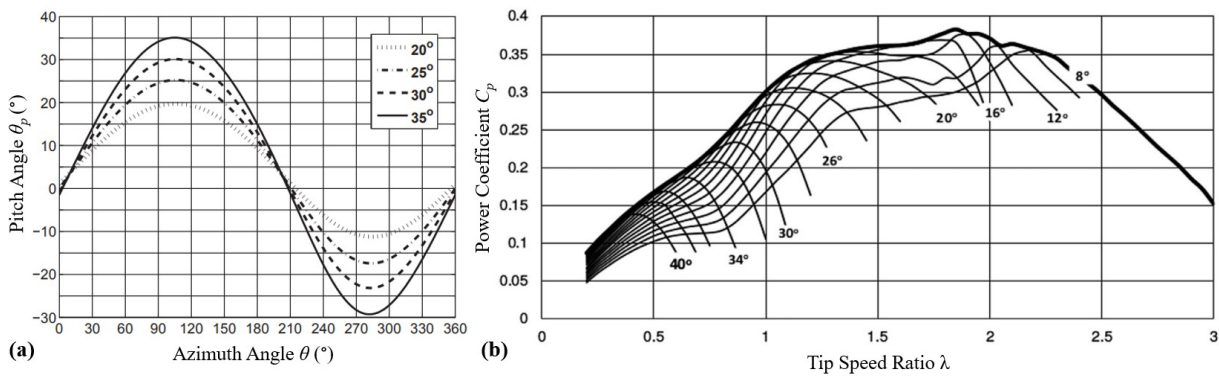


**Figure 3.13:** (a) Collective variable pitch law developed by Jain and Abhishek [26] for several pitch amplitudes. Note that Jain and Abhishek [26] use the opposite pitch sign convention as used in this study. (b) The relationship between  $C_p$  and tip speed ratio for different pitch amplitudes, leading to the pitch strategy that maximizes power output over a range of tip speed ratios (bold line). Figure modified from [26].

### *Individual Pitch*

The most optimal pitch law can be achieved by actively pitching each blade individually. This requires individual actuators for each blade [11]. So while individual pitch control results in the best power performance, power is also required for the pitch actuation. Benedict *et al.* [11] contend that active individual variable blade pitching is complicated, but VAWTs with such capability have been built (e.g. by LeBlanc and Ferreira [14], Le Fouest and Mulleners [5], and Liang *et al.* [12]). In this section, we present many individual active variable blade pitch strategies that are derived in diversified manners. Most of the studies focus on increasing the power coefficient, but a few near the end of the section introduce other objectives.

Staelens *et al.* [18] use three different variable pitch modifications with the goal of increasing a VAWT's power output. The authors add a "local angle of attack correction" at each azimuth position, which represents blade pitching, in order to achieve a more favorable effective angle of attack locally. The DMST model is used. The first modification keeps the effective angle of attack slightly less than the blade static stall angle throughout the revolution (Figure 3.14). The power output increases significantly (for high wind speeds), but the strategy involves large sudden changes in pitch which are physically impossible. In the second modification, the effective angle of attack is set to the stall angle when the geometric angle of attack is greater than the stall angle. This change smoothens the angle of attack correction value, tangential force, and torque coefficient, especially at  $\theta = 0^\circ$  and  $180^\circ$ , but slightly decreases the power output compared to the first modification. Additionally, the angle of attack correction function still has some

discontinuities which may be difficult to implement physically. The third modification makes the local angle of attack correction a smooth, continuous function: a sinusoid whose amplitude is the maximum difference between the local geometric angle of attack and the stall angle, calculated when the former exceeds the latter. This method of setting the sinusoid's amplitude results in a few occurrences of dynamic stall throughout the blade's rotation, which could be avoided by decreasing the sinusoid's amplitude. The third modification has lower power output than the first two modifications, but it is still higher than the case without variable pitching. Importantly, this last modification is practically feasible to implement.

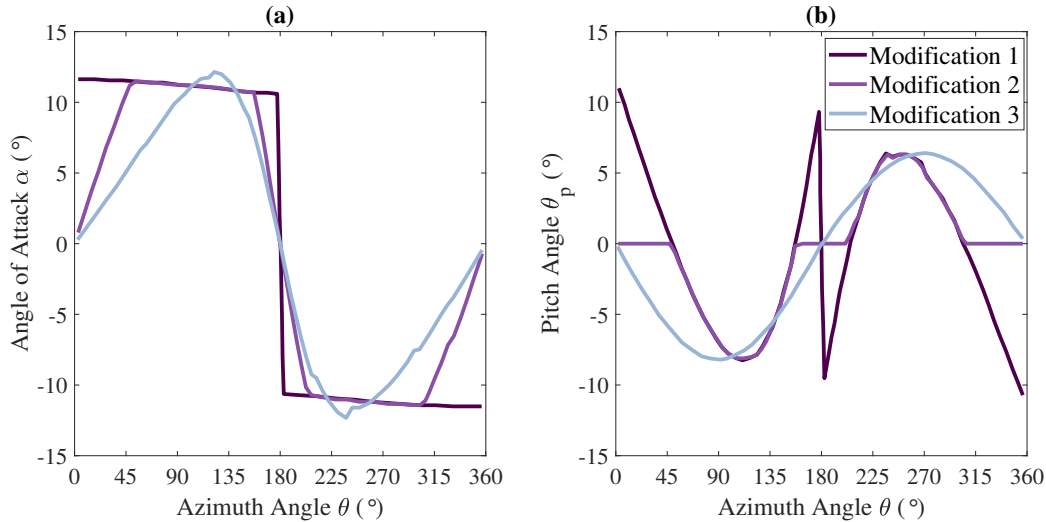


**Figure 3.14:** Three variable pitch laws developed by Staelens *et al.* [18], with increasing smoothness. (a) The effective angle of attack, and (b) the pitch angle. Figure modified from [18].

Recall that Lazauskas [16] investigated two self-acting stabilized pitch controls—passive pitch controls (see Figure 3.11). Recall also that the pitch sign convention used in that study is opposite to the one used here: positive pitch is when the leading edge rotates outward. Lazauskas [16] also optimized a sinusoidal pitch system, using the DMST model. The sinusoidal forced pitch system takes the form of a first-order harmonic:  $\theta_p = A_0 + A_1 \sin \theta$ . The author found that, when the tip speed ratio is three,  $C_p$  is maximized when  $A_0 = 6^\circ$  and  $A_1 = 3^\circ$ , but notes this makes  $\theta_p$  unexpectedly positive at all azimuths (including on the downwind side when  $\theta_p$  is expected to become negative). In terms of the pitch convention used in this study, this means that the leading edge is pitched outward during the whole rotation when it is expected to be pitched inward during the downwind part.

Paraschivoiu *et al.* [9] optimized a variable pitch function of the form  $\theta_p = x_1 \cos \theta + x_2 (\sin \theta)^{x_3}$  (with the opposite pitch sign convention as used in this study).  $x_1$ ,  $x_2$ , and  $x_3$  are the optimization variables. The objective function is to minimize  $\frac{1}{Power}$ , which amounts to maximizing the turbine's power performance. The power is optimized via a genetic algorithm. DMST including dynamic stall is used. The resulting optimal solution is  $x_1 = 2.403$ ,  $x_2 = 1.798$ , and  $x_3 = 3.009$ . The corresponding optimal blade pitch curve, shown in Figure 3.15, has two periods of relatively constant pitch angle in the upwind half and downwind half, respectively, and a maximum amplitude of around  $\pm 2^\circ$ . The authors also compare a sinusoidal variable pitch law with amplitude of  $4^\circ$ , which is the maximum difference between the geometric angle of attack and the static stall angle. The sinusoidal pitch law increases the power output, but only up to a certain wind speed, after which there is a rapid drop-off. The optimal solution for the (non-sinusoidal) pitch law has a high  $C_p$  for the one operating condition (tip speed ratio, or equivalently, wind speed) it was optimized for. However, the optimal pitch variation does not perform well in off-design conditions (other tip speed ratios, or wind speeds). The high power coefficient only holds for a small range of tip speed ratios around the optimization point. Elsewhere, the turbine's efficiency is lower than the zero-pitch case, especially at higher wind speeds. The authors note that these higher wind speeds rarely occur, so the impact may be insignificant, but it is still important to note the limitations of the optimized pitch function. Therefore, the authors optimize the pitch function for wind speeds up to the rated wind speed to improve the turbine's overall efficiency. They achieve almost a 30% increase in annual energy production with this pitch strategy.

After testing their cycloidal pitch law (see the previous section on *Collective Pitch*), Hwang *et al.* [20] investigated improving the power performance of their turbine even more by using individual blade pitch control. They performed

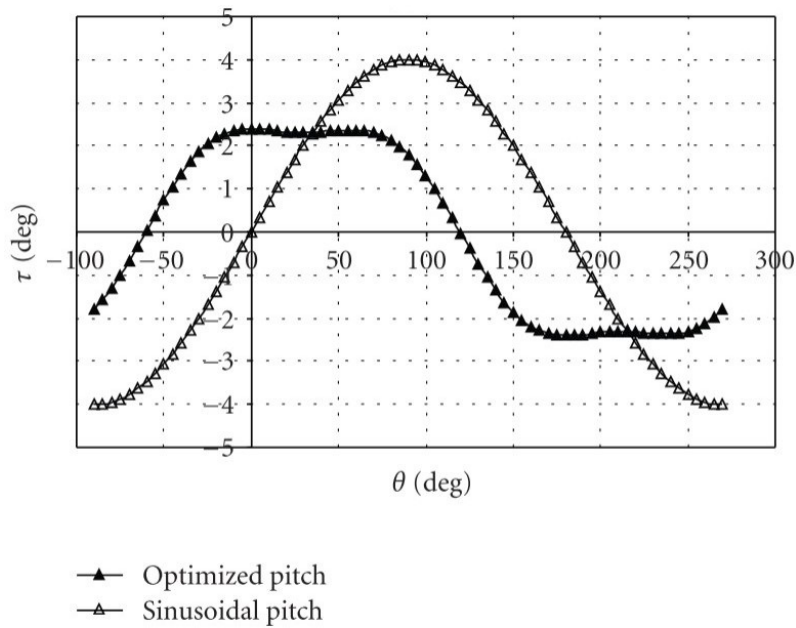


**Figure 3.15:** Optimal variable pitch law developed by Paraschivoiu *et al.* [9]. Note that  $\tau$  is the pitch angle ( $=\theta_p$ ). Note that Paraschivoiu *et al.* [9] use the opposite pitch sign convention as used in this study. Figure from [9].

a numerical optimization using CFD. The objective function is to maximize  $C_p$ . The optimization is done in four steps, with the range of selectable pitch angles becoming narrower in each step. The pitch curve is defined by a set of twelve points at different azimuthal positions (six points in the first step). A genetic algorithm is used to find the optimal pitch curve. The results for four different tip speed ratios are shown in Figure 3.16. Note that the authors use the opposite pitch sign convention than we use: positive pitch is when the leading edge rotates outward. The optimal pitch curve is different for each tip speed ratio. As the tip speed ratio increases, the magnitude of the pitch angle decreases. The magnitude of the pitch angle is also larger upwind than it is downwind. The individual pitch control achieves a 25% improvement in  $C_p$  compared to the cycloidal (collective) pitch law, which already had a 70% improvement compared to zero pitch.

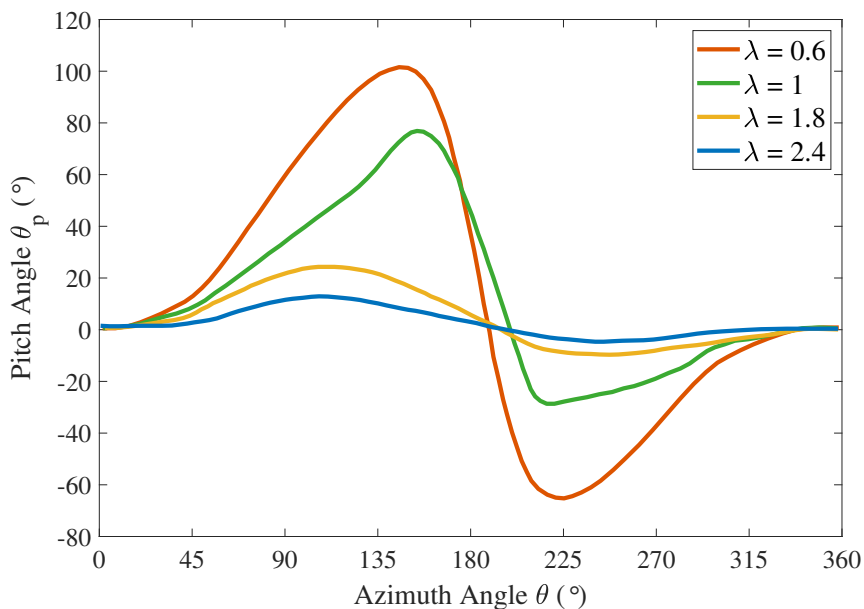


**Figure 3.16:** Variable pitch law developed by Hwang *et al.* [20]. Note that the opposite pitch sign convention is used. Figure modified from [20].

Zhang *et al.* [21] use a numerical procedure based on the DMST model to find an individual active variable pitch control law that maximizes the power output. The resulting pitch kinematics is shown in Figure 3.17a. The variable pitch law improves the tangential force coefficient in the upwind region, specifically, by widening the azimuthal range where  $C_t$  is high. As a consequence, the total tangential force coefficient throughout one revolution is twice as large as that with zero pitch, and the power coefficient  $C_p$  is also greatly improved. However, in the downwind region,  $C_t$  with variable pitch is worse than with zero pitch. Therefore, the blade pitch is set to zero in the downwind half (while it still varies in the upwind half), in what the authors call the optimum individual active variable pitch law (Figure 3.17b).

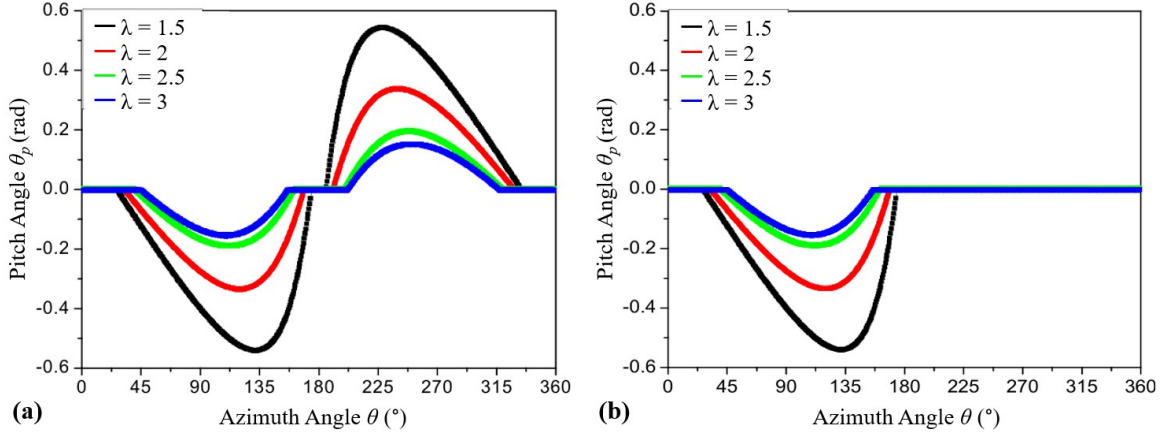


**Figure 3.17:** Variable pitch control law developed by Zhang *et al.* [21] (a) for maximum power output, and (b) optimum. Figure modified from [21].

Liang *et al.* [12] used a similar individual variable pitch curve to Zhang *et al.* [21] (see Figure 3.17a), which depends on the static stall angle but is not optimized. Liang *et al.* [12] analyzed the effect of the pitch curve at several tip speed ratios ( $\lambda = 1.5, 2, 2.5,$  and  $3$ ) using CFD. The turbine with variable pitch has a significantly higher power coefficient than a turbine with fixed zero pitch. With variable pitch, the upwind azimuthal region with high tangential force coefficient widens compared to with zero pitch. This occurs for all tip speed ratios, so the authors conclude that their variable pitch control expands the effective operating region of tip speed ratio. The variable pitch law reduces or avoids dynamic stall and flow separation. It is also favorable for structural design because it decreases the magnitude of the normal force coefficient and the blade pitching moment coefficient. The total torque coefficient of the rotor with variable pitch is much higher than with zero pitch for all the tip speed ratios and across wind speeds ( $V_\infty = 2-14$  m/s). The best effect is when  $\lambda = 1.5$ , for which the torque coefficient is 2.5 times larger with variable pitch than with zero pitch. For  $\lambda = 1.5$ , the authors conducted a vibration analysis, considering the aerodynamic normal force and assuming it is uniformly distributed on the blade. Their variable pitch control law reduces the deformation of the blade compared to zero pitch. However, with variable pitch, the acceleration of the blade mid-span (in the direction perpendicular to the chord) is much higher than with zero pitch, because the blade pitch angle changes frequently.

Recall that Guo *et al.* [19] already found that a fixed pitch angle of  $\theta_p = -1^\circ$  is optimal (see Section 3.5.1). Afterward, the authors investigate variable pitch control to further improve the  $C_p$ . Recall that the method is CFD. To optimize the variable blade pitch control, Guo *et al.* [19] use the results from the fixed pitch angles, instead of using a genetic algorithm optimizer, which according to the authors is computationally expensive and a complex process. The variable pitch law is a step function. In different azimuthal ranges of the rotor, the pitch angle is set to the optimal pitch angle from the fixed-pitch study. In the upwind region ( $\theta = 0^\circ-135^\circ$ ), this is  $\theta_p = 3^\circ$ . However, in order to avoid large steps in the pitch angle,  $\theta_p$  is set to  $1^\circ$ , which has similar blade torque as when  $\theta_p = 3^\circ$ . In the downwind region ( $\theta = 135^\circ-360^\circ$ ), the pitch angle is set to different angles in six cases:  $\theta_p = 4^\circ, 3^\circ, 2^\circ, 0^\circ, -1^\circ,$  or  $-2^\circ$ . All of the variable pitch cases improve  $C_p$  with respect to the fixed pitch angle case that matches the pitch angle in the downwind region. The cases with  $\theta_p = 2^\circ, 0^\circ, -1^\circ,$  and  $-2^\circ$  in the downwind region improve  $C_p$  with respect to the optimal fixed pitch angle of  $\theta_p = -1^\circ$ . The greatest improvement is when  $\theta_p = -2^\circ$  downwind. The  $C_p$  in this case is 0.402, which is a 12% improvement over the  $\theta_p = -1^\circ$  fixed-pitch case and a 17% improvement over the zero-pitch case. Therefore, the optimal variable pitch law is when the pitch angle is  $\theta_p = 1^\circ$  upwind (from  $\theta = 0^\circ-135^\circ$ ) and  $\theta_p = -2^\circ$  downwind (from  $\theta = 135^\circ-360^\circ$ ), which is shown in Figure 3.18. Since the step in  $\theta_p = 1^\circ$  to  $\theta_p = -2^\circ$  is large, the authors use several intermediate sub-steps to lessen disturbances in the flow field and aid in numerical convergence.

The variable pitch strategy leads to higher  $C_p$  than fixed pitch.

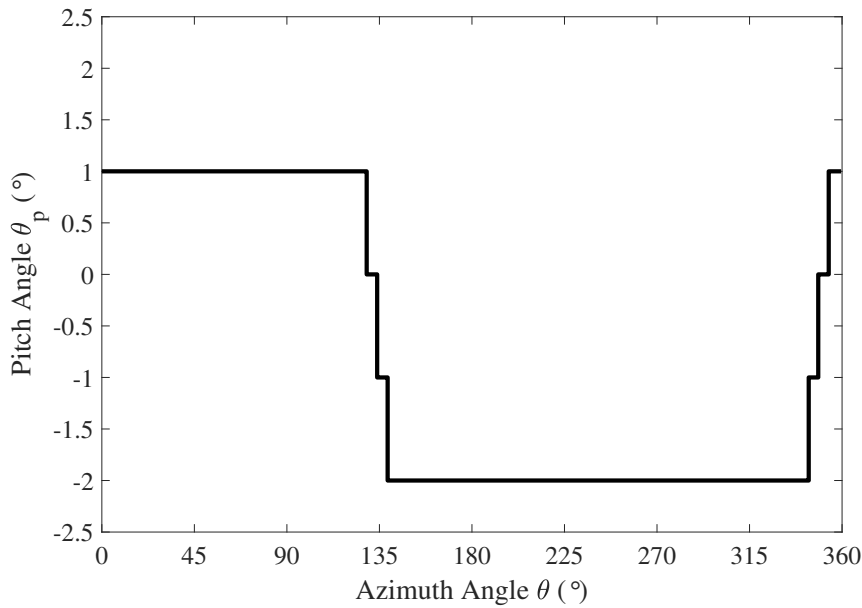


**Figure 3.18:** Variable pitch control law developed by Guo *et al.* [19].  $\theta_p = 1^\circ$  upwind and  $\theta_p = -2^\circ$  downwind. Figure modified from [19].

Abbaszadeh *et al.* [22] found an optimal individual active pitch law using an experimental method. The experiments were conducted in water, and the turbine model was not a complete VAWT but a single blade which was driven in a way so as to simulate the rotation of a VAWT. In the optimization routine, the objective is to maximize the integrated tangential force coefficient. The tangential force is related to power. It can be maximized by controlling the angle of attack so as to have high lift and low drag, and avoiding dynamic stall. The authors find the optimal angle of attack trajectory, instead of optimizing the pitch angle directly. The pitch angle is the difference between the optimal angle of attack,  $\alpha$ , and the geometric angle of attack,  $\alpha_g$  ( $\alpha = \alpha_g + \theta_p$ ). The geometric angle of attack is the original angle of attack when there is zero pitch, given by  $\alpha_g = \tan^{-1}\left(\frac{\sin\theta}{\lambda + \cos\theta}\right)$ . The authors define the optimal angle of attack trajectory  $\alpha$  with a spline consisting of five points. The two end points, corresponding to  $\theta = 0^\circ$  and  $360^\circ$ , are fixed to zero. The remaining three points  $x_1$ ,  $x_2$ , and  $x_3$  are decision variables which are varied in the optimization scheme. A full-factorial optimization approach with hardware-in-the-loop is used to find the optimal spline parameters. Figure 3.19 shows the original angle of attack, optimal angle of attack, and optimal pitch law. Adding the variable blade pitch angle changes the angle of attack in several ways. Firstly, the maximum and minimum angles of attack are smaller. Secondly, there is a shift in the azimuthal locations of the maximum, zero-crossing, and minimum angle of attack. Thirdly, the change in angle of attack is less steep. The optimal pitch law leads to an improvement of 122% in the tangential force coefficient ( $C_t' \approx 0.333$ ) compared to the zero-pitch case. The optimal pitch law also leads to a significant decrease in the drag force compared to the zero-pitch case. There is also a small decrease in the lift force, but the reduction is not as much compared to the drag force.

Abbaszadeh *et al.* [22] optimized the angle of attack for one turbine design and operating condition. The authors demonstrate that VAWTs can be characterized by two values: the tip speed ratio and the reduced frequency. This means that by varying just two parameters, one can study the effect of different turbine designs and operating conditions on the optimal blade pitch. According to the authors, their methodology is fast, simple, and inexpensive so it can easily be used to find the optimal blade pitch for different turbine designs and/or operating conditions. However, in the study, the authors did not repeat the experiment with different tip speed ratio and reduced frequency to reveal how the turbine design and/or operating condition impact the optimal blade pitch angle.

Rainone *et al.* [23] devised a variable pitch law that focuses on achieving the best effective angle of attack at each azimuth position. Their goal was to develop a methodology that is versatile to operating condition and which is computationally efficient. So that the turbine geometry and operating conditions could be easily changed, the authors made an automatic procedure that takes as input the turbine airfoil, radius, and operating conditions and outputs the variable pitch law. In the procedure, the pitch angle is found from the desired angle of attack at eight equally-spaced

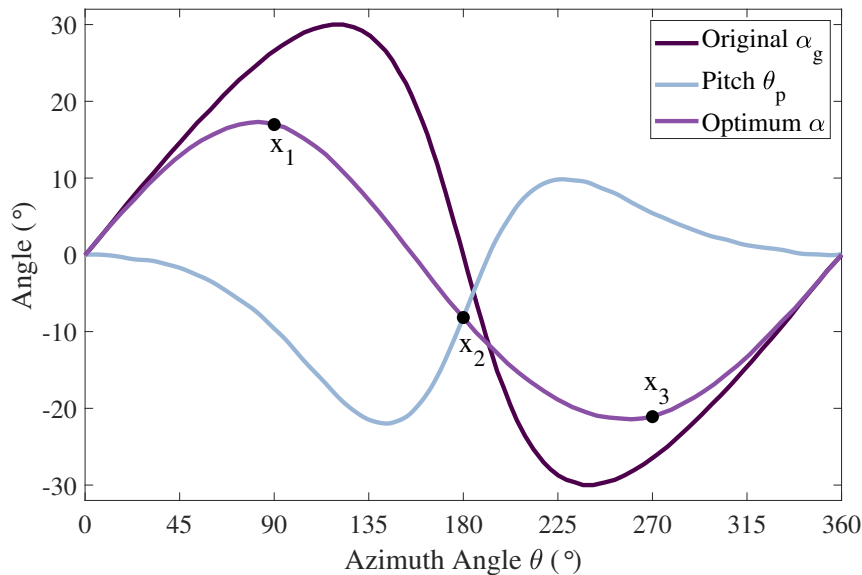


**Figure 3.19:** Variable pitch control law developed by Abbaszadeh *et al.* [22], created by optimizing the angle of attack spline  $\alpha$  compared to the original geometric angle of attack  $\alpha_g$ . Figure modified from [22].

azimuthal positions. The desired effective angle of attack ( $\alpha_{eff}$ ) maximizes the steady aerodynamic efficiency of the airfoil (when  $\frac{C_l}{C_d}$  is maximum, or the tangent line to the  $C_l$ - $C_d$  curve). The lift and drag coefficients (static airfoil polars) are computed using XFOIL, which uses a panel method, given the airfoil shape, Reynolds number, and Mach number at the azimuthal position. The pitch angle for each azimuthal position is calculated as the difference between the effective angle of attack and geometric angle of attack,  $\theta_p = \alpha_{eff} - \alpha_g$ , where the geometric angle of attack is  $\alpha_g = \tan^{-1}\left(\frac{\sin \theta}{\lambda + \cos \theta}\right)$ . Given the blade starts at angle  $\alpha_g$ , it has to rotate by  $\theta_p$  in order for the blade to operate at an angle of attack of  $\alpha_{eff}$ . Lastly, a cubic spline is fit between the eight pitch angles in order to determine the variable pitch law. In the above calculations, the induced velocity is neglected. The authors highlight that their method does not involve optimization, which makes it more versatile to different wind conditions.

Figure 3.20 shows the variable pitch law defined via Rainone *et al.* [23]'s methodology for the turbine analyzed in their study. The blade pitches outward in the upwind half and inward in the downwind half. The authors also ran a

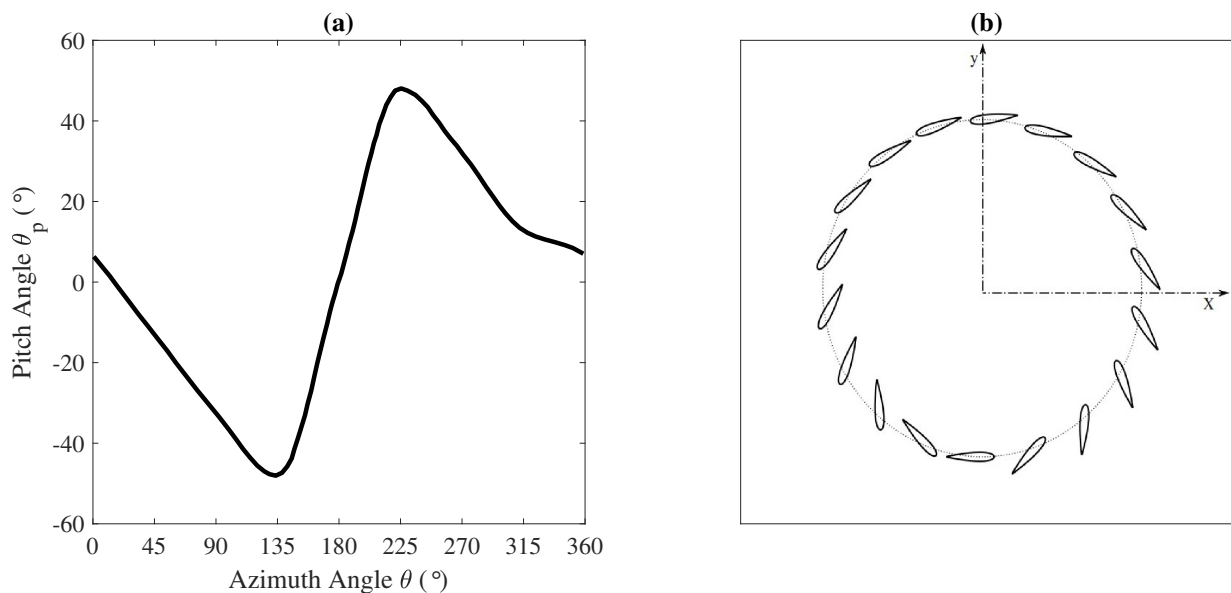


**Figure 3.20:** (a) Variable pitch law developed by Rainone *et al.* [23]. (b) Blade orientations during the revolution. Figure modified from [23].

CFD simulation (2D URANS) to analyze the effect of their pitch strategy. They found that the variable pitch law delays dynamic stall—there is no sudden loss in the instantaneous torque coefficient around  $\theta = 60^\circ$ - $80^\circ$ . The flow is attached to the airfoil except for  $\theta = 170^\circ$ - $210^\circ$ , whereas for the zero-pitch case, the flow is unattached for a much longer range, making the torque coefficient close to zero. The authors also conclude that the  $\alpha_{eff}$  is not optimal, because for dynamic polars, the maximum aerodynamic efficiency occurs at a larger angle of attack than for the static airfoil. Therefore, the maximum instantaneous torque coefficient is achieved in the zero-pitch case. However, the overall average torque coefficient is higher with variable pitch. The average torque coefficient and power coefficient increased with variable pitch compared to with zero pitch, so the pitch strategy improves the turbine performance.

Houf [24] considered more than one objective in their master's thesis on VAWT active pitch control. The objectives are: 1) power maximization, while not increasing thrust (to decrease the cost of energy), 2) power minimization (for power control in the full load region when the rated power should not be exceeded), and 3) thrust minimization, while maintaining power (to decrease the loading on the blades and increase their (fatigue) life). The objectives are considered as single objectives in three separate optimization problems, not simultaneously in a multi-objective optimization problem. The author uses the modified linear AC model. They use sequential quadratic programming to solve the optimization problems, and ran the optimization routine with various tip speed ratios and rotor solidities. The achievable improvement in all three objectives depends on both the tip speed ratio and rotor solidity. The author describes two different optimization approaches. First, the author finds the optimal load-forms  $Q_n$  (for an ideal rotor), then calculates the necessary pitch curves to obtain each load-form. Following Madsen *et al.* [41], the optimal load-form  $Q_n$  approaches a uniform distribution. Houf [24] finds that the corresponding pitch curves oscillate rapidly between positive and negative angles. Importantly, high pitch rates occur, which may make the pitch curves practically infeasible.

Then, in their direct pitch optimization approach (which has realistic flow conditions and geometry), the author uses a tenth-order Bezier curve for the pitch curve, with constraints on the pitch range. The Bezier curve is made to be periodic with a continuity constraint at  $\theta = 0^\circ$  and  $360^\circ$ , however, it is not smooth at the transition, which is a limitation of the selected pitch function. With blade pitching, there is limited possible improvement in maximizing  $C_p$  ( $\sim 1\%$  increase), because the zero-pitch turbine has an efficiency already close to the Betz limit. Yet, using optimal pitch widens the tip speed ratio operating range where the  $C_p$  is high. On the other hand, the pitch optimizer is very effective at alleviating power, with a possible power reduction of 100% for some conditions. This is because for low tip speed ratios, blade pitching pushes the blade (farther) into the stall region, thus increasing drag and decreasing power; and for high tip speed ratios, blade pitching decreases the angle of attack in the upwind region, thus reducing lift and torque (power). The pitch curves are close to a sinusoid, and they cause a decrease in loading almost throughout the entire rotor revolution. In all of the optimization cases, the optimal pitch curves have different shapes depending on the tip speed ratio. For the same tip speed ratio, the pitch curve has relatively similar shape across the solidities, but with a different scaling. Some sample pitch functions (for  $\lambda = 4$ ) are shown in Figure 3.21.

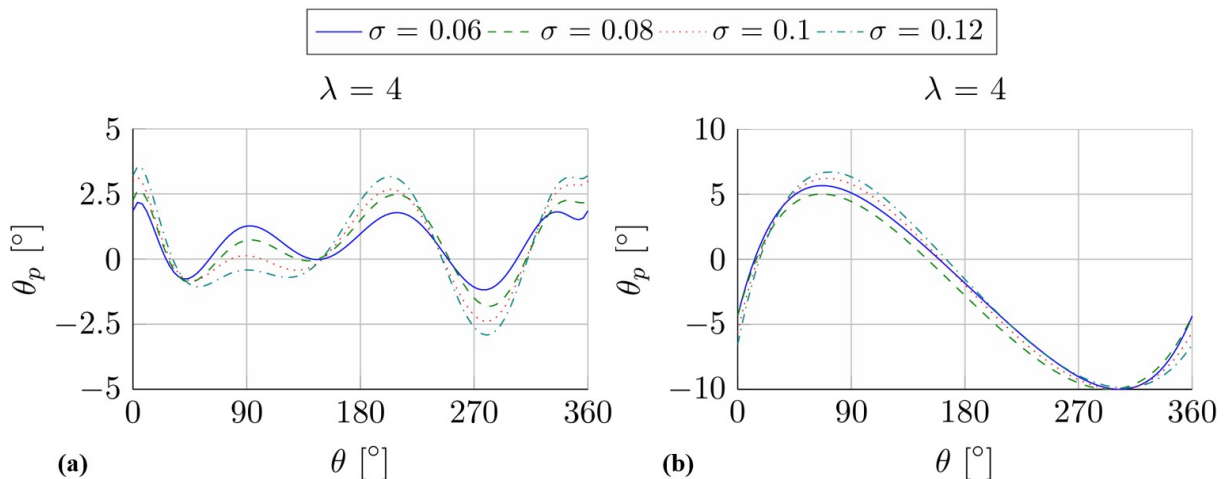


**Figure 3.21:** Example variable pitch curves developed by Houf [24] for the objective of (a) maximizing power or (b) minimizing power. Results are shown for a tip speed ratio of 4 and various solidities. Houf [24] also optimizes at other tip speed ratios, which yields different shapes of the pitch curve. Note that the opposite pitch sign convention is used. Figure from [24].

Houf [24] added dynamic stall to their AC model using a simplified form of the Beddoes-Leishman model. The author compares the unsteady optimization to the steady optimization. There is a phase shift in the pitch curves with the unsteady curves lagging behind the steady curves. This happens because the unsteady aerodynamic loads are delayed compared to the steady ones. The phase shift becomes less when the tip speed ratio and solidity are lower. The author also observes that in the unsteady optimization, the region from  $\theta = 0^\circ$ - $120^\circ$  is the only region of power increase. Including unsteady aerodynamics makes maximizing  $C_p$  and minimizing  $C_T$  more difficult (the potential increase in  $C_p$  is even less with unsteady effects), while minimizing  $C_p$  is easier than with the steady model. It is important to note that including the dynamic stall model significantly increases the computation time of the optimization algorithm. However, it does account for real aerodynamic phenomena that occur for VAWTs.

Erfort *et al.* [13] used a sinusoidal pitch function with the main goal of reducing the rotor torque ripple. Torque ripple is when the torque which is transmitted to the power train varies in time, and it can lead to poor power quality and an over-designed power train. The authors use the DMST model for VAWTs. The airfoil polars are generated using XFOIL, and during the optimization run, the lift and drag coefficients are read from a look-up table based on the Reynolds number and angle of attack, from a range of polars pre-generated in XFOIL. The pitch law is sinusoidal:  $\theta_p = A_1 \sin(\theta w + \phi_1)$ . It prescribes each blade's pitch angle individually, though the authors indicate that it can be implemented with a mechanism (collective pitch).  $A_1$ ,  $w$ , and  $\phi_1$  are the amplitude, frequency, and phase angle of the pitch angle, respectively, and are the decision variables whose optimal values are found in the optimization routine. The optimization routine uses a breeder genetic algorithm in series with the gradient-based modified method of feasible directions. The authors have two objectives: to minimize the torque ripple while maximizing the power coefficient ( $C_p$ ). This is a multi-objective optimization problem, however, the authors turn it into a single-objective optimization problem by turning the  $C_p$  objective into a constraint (see Section 4.1 on the  $\epsilon$ -constraint method). They constrain  $C_p$  to be above a certain value, so then the only remaining objective is to minimize the torque fluctuations. The authors run several cases with different values of the constraint on  $C_p$  which leads to different solutions. The authors were able to maintain the zero-pitch  $C_p$  value while reducing the torque ripple by almost 4%. They could also achieve a 10% reduction in torque ripple, but at the cost of almost a 10% decrease in  $C_p$ . Figure 3.22a shows the reduction in torque ripple for different values of the  $C_p$  constraint. When  $C_p$  is higher, there is less reduction in torque ripple. Figure 3.22b shows the corresponding pitch functions for three combinations of  $C_p$  and torque ripple

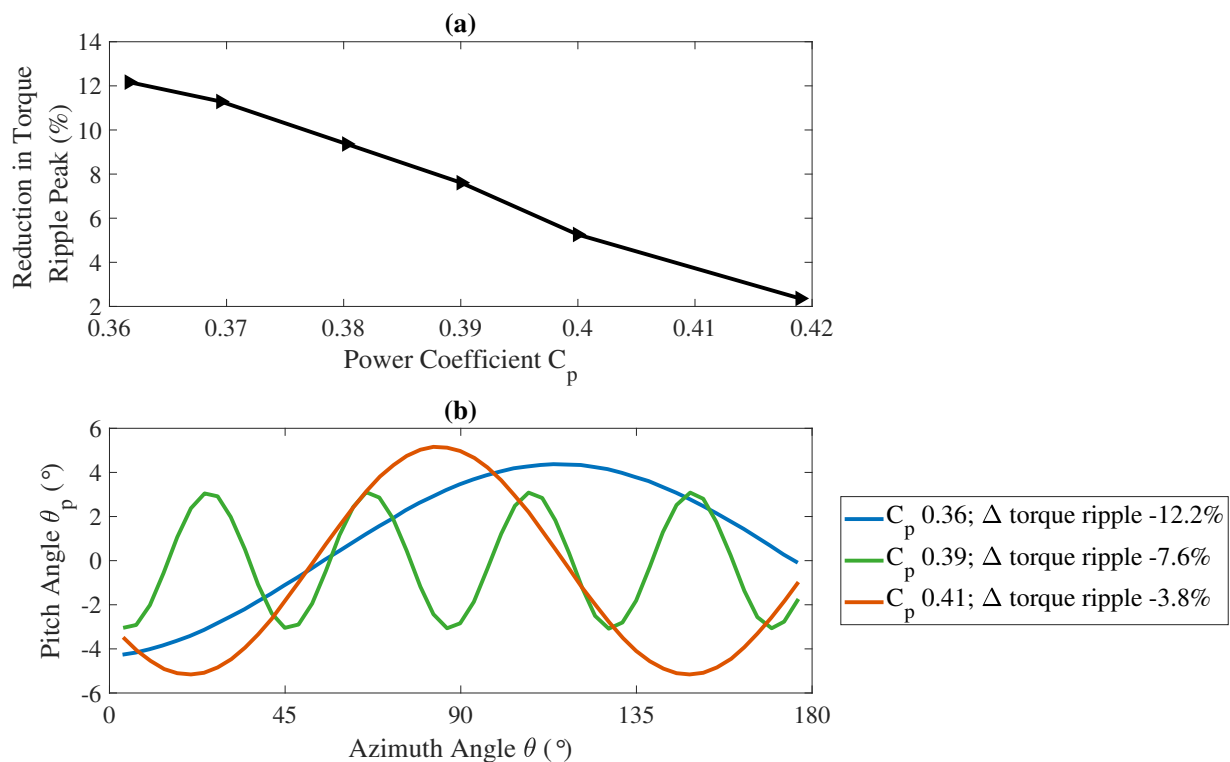


**Figure 3.22:** (a) The relationship between  $C_p$  and reduction in torque ripple. (b) Three examples of sinusoidal pitch laws developed by Erfort *et al.* [13], for different combinations of  $C_p$  and torque ripple reduction. Figure modified from [13].

reduction. The authors conclude that there is no correlation between the amplitude or frequency and the reduction in torque ripple achievable.

Le Fouest and Mulleners [5] conducted experiments on a single-bladed VAWT in water to find the optimal individual pitch law with two objectives in mind: to maximize  $C_p$  and to minimize aerodynamic load fluctuations (quantified by the standard deviation of the blade pitching moment,  $\sigma(M_Z)$ ). The power calculation already subtracts the power consumed by the pitch actuation. Using strain gages, the authors were able to measure the blade normal force, tangential force, and pitching moment. They also measured the flow velocity using PIV. The authors consider two operating conditions: the “on-design” condition with moderate tip speed ratio ( $\lambda = 3.2$ ) and the “off-design” condition with low tip speed ratio ( $\lambda = 1.5$ ). The pitch law is a third-order sinusoid:  $\theta_p = A_0 + \sum_{i=1}^3 A_i \sin(i\Omega t + \phi_i) = A_0 + \sum_{i=1}^3 A_i \sin(i\theta + \phi_i)$ . Note that the frequency is the turbine’s rotational frequency. The decision variables are the offset  $A_0$ , amplitudes  $A_i$ , and phase shifts  $\phi_i$ , for  $i = 1, 2, 3$ . The authors use a genetic algorithm optimizer, with 60 individuals per generation, and using the generational distance as the convergence criterion. Since there are two objectives, the result is a set of Pareto-optimal solutions (see Section 4.2.1 for further explanation), shown in Figure 3.23a for the on-design condition. In the optimal pitch curves the authors found, both objectives could be achieved at the same time. They found pitch curves which could increase the  $C_p$  three times compared to zero pitch for both the on- and off-design conditions. In the on-design condition, the  $C_p$  could be increased up to 2.3 times the zero-pitch case while not increasing the load fluctuations. In the off-design condition, the load fluctuations could be decreased by 77% while maintaining the power coefficient. In general, a larger increase in  $C_p$  corresponds with a lower reduction (or even an increase) in  $\sigma(M_Z)$ . The authors found that for both the on- and off-design conditions, the average  $C_p$  in the upwind region is approximately the same across the Pareto-optimal solutions but the largest difference is in the downwind region.

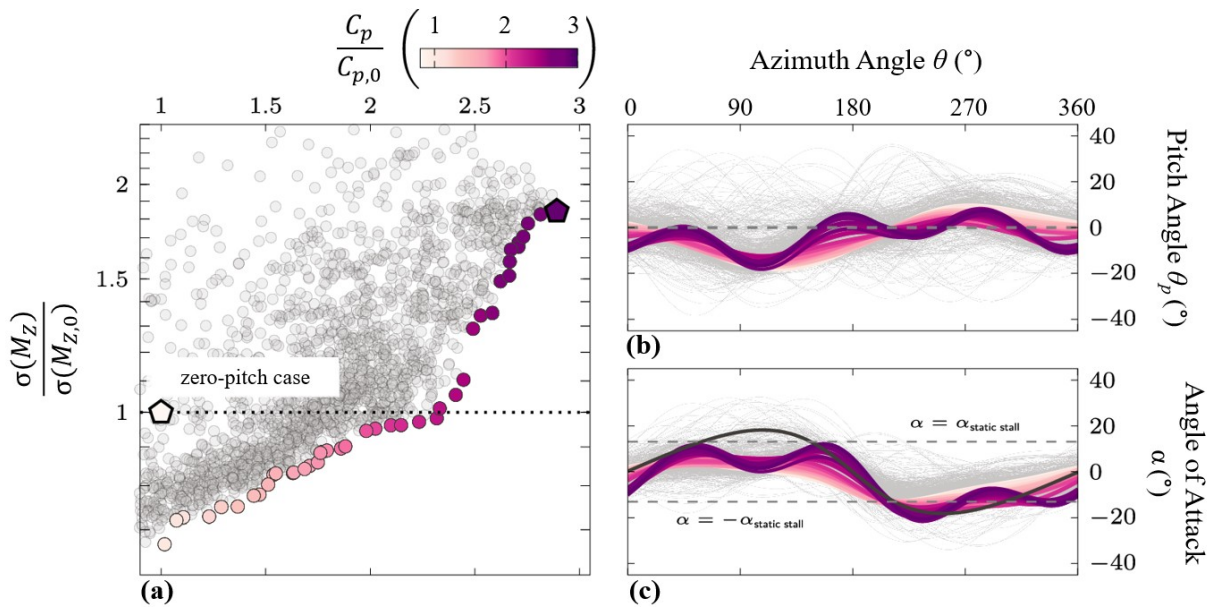


**Figure 3.23:** (a) Solutions to the two-objective optimization problem in Le Fouest and Mulleners [5] shown in the objective space, for the on-design condition ( $\lambda = 3.2$ ). Axes are normalized by the zero-pitch values. The Pareto-optimal front is shown in color. (b) The variable pitch curves. They are third-order sinusoids. (c) The angle of attack. The black curve is the angle of attack for the zero-pitch case. Figure modified from [5].

For the off-design condition, the Pareto-optimal solutions involve pitching outward in the upwind half and pitching inward in the downwind half so that the blade’s effective angle of attack is decreased. As compared to the zero-pitch case, which experiences deep dynamic stall and flow separation, the optimal pitch functions lead to more favorable angles of attack and better control the stall vortex. Pitching the blade outward upwind delays the formation and shedding of the leading-edge stall vortex and delays flow separation in the upwind region. When the blade pitches inward in the downwind region, the stall vortex is shed to the side of the rotor, which avoids blade-vortex interaction. This, combined with the rapid inward pitch maneuver which decreases the effective angle of attack, leads to flow reattachment and more power production in the downwind region.

The optimal pitch functions for the on-design condition are quite different from those for the off-design condition. The amplitude of the pitch functions is lower for the on-design condition than for the off-design condition. Additionally, there are two general shapes of the Pareto-optimal pitch curves: one which resembles a simple sinusoid and one which has three peaks (see Figure 3.23b). The former is associated with lower power coefficients and load fluctuations. The latter is associated with higher power coefficients and load fluctuations. The pitch curves which yield the highest increases in  $C_p$  lead to increases in load fluctuations compared to the zero-pitch case. The pitch functions which reduce the load fluctuations do so by decreasing the effective angle of attack in the downwind region, which also leads to less power production. The pitch functions which increase the power coefficient make the period during which the effective angle of attack is beyond the static stall angle shorter compared to the zero-pitch case, which aids flow reattachment in the downwind region. Since there is little to no flow separation downwind, and because the effective angle of attack is large (but still below the static stall angle), a downwind leading-edge vortex can form, which leads to more power production in the downwind region.

### 3.5.3. Pitch Control Strategies

Evidently, many pitch control strategies have been used in the literature with various goals in mind, original methods of derivation, and resulting in different turbine performance and other conclusions. Here, we summarize the main takeaways from the literature review of VAWT blade pitching, with a particular emphasis on the important conclusions for the remainder of this study.

- Pitch angle affects not only turbine averaged loading, such as  $C_p$  and  $C_T$ , but also instantaneous blade loading.
- A small fixed negative (outward) pitch offset is optimal among fixed pitch angles and can increase the power performance compared to zero pitch.
- Variable pitching can increase  $C_p$  further compared to fixed pitch.
- Most studies find that a negative (outward) pitch angle is favorable in the upwind region and a positive (inward) pitch angle is favorable in the downwind region.
- Large positive (fixed) pitch angles lead to stall in the second half of the upwind half. Large negative (fixed) pitch angles lead to stall in the middle of the downwind half.
- The pitch angle should be limited between an upper and lower bound beyond which stall occurs, leading to a drop in power. The upper and lower bounds do not have to be of the same magnitude. The bounds depend on the specific turbine geometry and operating conditions under consideration.
- Keeping the angle of attack just below the static stall angle requires jumps in pitch angle which are not physically possible.
- The pitch kinematics should be a smooth, continuous function which is physically implementable. There should not be any large jumps in the pitch angle. Large jumps in pitch angle also lead to intense disturbances in the flow field.
- The pitch curve should be continuous and smooth at  $\theta = 0^\circ$  and  $360^\circ$ .
- A first-order sinusoid is most likely not sufficient to represent the optimal pitch angle. Higher-order harmonics need to be added.
- Many studies optimize (maximize) only  $C_p$ .
- The optimal variable pitch law depends on the tip speed ratio, especially the pitch amplitude. The pitch amplitude should decrease as the tip speed ratio increases.
- A pitch law is optimized for a specific turbine geometry and operating condition, so it is not necessarily generalizable or widely applicable to other turbine geometries and/or operating conditions.
- It is useful to integrate across tip speed ratio and/or wind speed to attain the overall maximum power of a turbine in varying site wind conditions.
- It is possible to develop efficient pitch angle optimization methodologies in which the turbine design and operating condition can easily be changed so as to allow for pitch optimization at other conditions.
- The optimal pitch angle can be derived by first finding an optimal effective angle of attack and then computing  $\theta_p = \alpha_{eff} - \alpha_g$ , where  $\alpha_g$  is the geometric angle of attack.
- The DMST model has been used in many VAWT pitch studies in the past, however, it is not very accurate. Additionally, CFD is commonly used, but it is computationally expensive.
- The variable pitch law can be optimized using a genetic algorithm, especially when the problem is non-linear

and has multiple competing objectives.

- The pitch strategy should differ depending on what region of the operating curve the turbine is in, because the objective also changes (i.e. partial load vs. full load region).
- Individual blade dynamic pitching is more complicated and energy-consuming than other strategies, but enables the most control and best power outcomes.
- Even if a pitch law schedules the blades' pitch angle according to azimuth,  $\theta$ , a VAWT can still be insensitive to the incoming wind direction when the wind direction is measured and the pitch adjusted accordingly (shifted azimuthally).

# 4

## Multi-Objective Optimization

Multi-objective optimization is a useful tool in real-world problems when an optimal decision has to be made considering more than one factor. Single-objective optimization can leave out important aspects and over-simplify reality. In single-objective optimization, the goal is to find a single optimal solution. In a multiple-objective optimization problem (MOOP), we want to optimize multiple objectives simultaneously [42]. These objectives are also often conflicting with each other, so multi-objective optimization results in a set of (many) optimal trade-off solutions—solutions that are better in one objective but worse in others. The user then has to decide which trade-off solution is preferred. The trade-off solutions are called Pareto-optimal solutions, and the goal of multi-objective optimization is not only to converge to the Pareto-optimal solutions, but also to maintain a good distribution (diversity) of these solutions. When an optimization problem has two to three objective functions, it is called a multi-objective problem, and when it has more than three objective functions, it is called a many-objective problem [33]. There are differences in the ways these two classes of problems are solved. In this chapter, we look at the different ways single-, multi-, and many-objective optimization problems are solved. First, in Section 4.1, we describe classical multi-objective optimization methods and why they are not suitable for the present study. Then, Section 4.2 provides background on the type of algorithm we do use to perform optimization: genetic algorithms. Section 4.3 elaborates on the specific genetic algorithm used in this study. Lastly, Section 4.4 outlines some methods for analyzing the performance of the algorithm after the optimization problem has been solved.

### 4.1. Classical Multi-Objective Optimization Methods

In classical approaches to solving MOOPs, the multiple objectives are turned into a single objective. Two classical multi-objective optimization methods are the weighted sum and the  $\epsilon$ -constraint method [42]. In the weighted sum method, a scalarizing technique is applied to condense the multiple objective functions into a single objective function. Each objective is multiplied by a weight, which is specified by the user, then the objectives are added together [42]. The single objective function is then minimized. A key to this method is determining the weight of each objective function, which is based on the relative importance of each objective. This determination is highly subjective. The optimization procedure leads to a single solution, with a trade-off among the objectives already built-in through the weighting. The trade-off solution is also sensitive to the weight vector chosen—a different set of weights will lead to a different trade-off solution. The weighted sum method is simple, but there is much subjectivity in the selection of the weights, which controls the outcome of the optimization.

Another classical multi-objective optimization method is the  $\epsilon$ -constraint method. This method also turns a MOOP into a single-objective optimization problem, but by keeping only one of the objective functions and treating the rest of the objective functions as constraints [42]. That is, the remaining objective functions  $f_m$  are reformulated as constraints of the form  $f_m \leq \epsilon_m$ , where  $\epsilon_m$  is some user-specified upper bound. The method leads to one solution, which is sensitive to the choice of  $\epsilon$ —a different set of  $\epsilon_m$  will lead to a different solution. Both the classical weighted sum and  $\epsilon$ -constraint multi-objective optimization methods could be used to solve our optimization problems, but due to the high level of subjectivity and single resulting solution, we turn to genetic algorithms instead.

### 4.2. Genetic Algorithms

Genetic algorithms are a type of multi-objective evolutionary algorithm. They can efficiently find multiple Pareto-optimal solutions to a MOOP in one simulation run [42]. Genetic algorithms are population-based. An individual in the population is a vector,  $\mathbf{x}$ , of the decision variables [5]. An individual is also referred to as a chromosome, and the

decision variables are called genes, so that a vector of genes (decision variables) makes up a chromosome (individual). A set of individuals make up a population. Each generation is a population, at a specific time, and the next generation is created from the previous generation using different methods depending on the specific genetic algorithm.

In general, there are three operations to create the next generation (offspring) from the previous generation (parents): cloning, crossover, and mutation [5]. Cloning is when a Pareto-optimal individual in the parent population also becomes a member of the offspring population. In crossover, or recombination, a new individual, or child, is created as a combination of two parents' decision variables. Crossover can be implemented in different ways. For example, a weighted average of the two parents can be taken to create the new vector of decision variables [5], or, the variables past a certain point in the decision variable vector can be exchanged between the two parents to create two new individuals [43]. Before crossover, the parents have to be chosen in a process called selection. Two types of selection are random selection and tournament selection [43]. In random selection, two parents are randomly chosen from the parent population. Binary tournament selection is a type of selection meaning two individuals (hence binary) are randomly chosen and competed/compared against each other. The one with a better rank, or non-domination level, wins and is selected to be a parent [43]. Binary tournament selection leads to faster convergence than randomly selecting parents. Lastly, mutation is when some of the decision variables in an (highly-ranked) individual's vector are randomly changed [5]. The other decision variables are unchanged.

There are many different types of genetic algorithms, each with their own variations, but the basic steps are as follows. First, an initial population is created (randomly). Then, each individual is evaluated based on the objective function(s). The individuals in the population are ranked with respect to each other, for example using the concept of dominance (see Section 4.2.1). Next, the offspring population is created from the parent population. Often, some sort of selection operator is applied to select the parents. Then the offspring are created using the crossover and mutation operations. The next generation is populated and the process continues, creating new generations in turn, until a termination criterion is met. There are several types of termination criteria, including: a number of total function evaluations, a number of generations, the run time, convergence in the decision variable space, or convergence in the objective function space [42], [43]. The output of the genetic algorithm is the optimal solution/individual in the case of single-objective problems, or the Pareto-optimal front in the case of multi- and many-objective problems.

In this study, we focus on non-dominated sorting genetic algorithms. The non-dominated sorting genetic algorithm II (NSGA-II) is a widely-applied multi-objective optimization algorithm [42]. NSGA-II is best used for two- and three-objective optimization problems. The non-dominated sorting genetic algorithm III (NSGA-III) is designed to solve many-objective optimization problems, and it does not scale down well to single-objective optimization problems [33]. Since in this study we have cases where there are one, two, or three objectives, we use a different, but related, algorithm: the unified non-dominated sorting genetic algorithm III (U-NSGA-III). Theoretically, NSGA-II could be used to solve the single-, two-, and three-objective optimization problems in this study. However, U-NSGA-III was specifically designed to be a unified algorithm to efficiently solve single-, multi-, and many-objective optimization problems [33]. Using U-NSGA-III in this study also makes the methodology generalizable to adding more objectives. Additionally, genetic algorithms are applicable to the optimization problems in this study, instead of gradient-based optimization methods, because according to Le Fouest and Mulleners [5], it is difficult to solve problems with a large, non-linear design space and multiple competing objectives with gradient-based methods.

### 4.2.1. The Concept of Non-dominance

In multi- and many-objective optimization problems, since we are considering more than one objective, we cannot strictly say that one solution is better than another in the same way that we can in single-objective optimization problems—in a single-objective minimization problem, the best solution is the one with the lowest objective value. In MOOPs, we use the concept of non-dominance to express this comparison between solutions. A solution  $\mathbf{x}_1$  dominates another solution  $\mathbf{x}_2$  if  $\mathbf{x}_1$  is no worse than  $\mathbf{x}_2$  in all objectives and  $\mathbf{x}_1$  is strictly better than  $\mathbf{x}_2$  in at least one objective [42]. There are a couple of properties to note about domination:

- If  $\mathbf{x}_1$  dominates  $\mathbf{x}_2$ , then  $\mathbf{x}_2$  does not dominate  $\mathbf{x}_1$ .
- If  $\mathbf{x}_1$  does not dominate  $\mathbf{x}_2$ , then  $\mathbf{x}_2$  does not necessarily dominate  $\mathbf{x}_1$ .
- If  $\mathbf{x}_1$  dominates  $\mathbf{x}_2$ , and  $\mathbf{x}_2$  dominates  $\mathbf{x}_3$ , then  $\mathbf{x}_1$  dominates  $\mathbf{x}_3$  (i.e. domination is transitive).

If we have two solutions,  $\mathbf{x}_1$  and  $\mathbf{x}_2$ , and  $\mathbf{x}_1$  does not dominate  $\mathbf{x}_2$  and  $\mathbf{x}_2$  does not dominate  $\mathbf{x}_1$ , then we say that the solutions are non-dominated with respect to each other [42]. When we find a set of such non-dominated solutions from a larger set of solutions, it is called a non-dominated set [42]. To find the non-dominated set, we compare all possible pairs of solutions in the whole solution set to find which solutions are non-dominated with respect to

each other. Any solution in the non-dominated set is not dominated by any solution in the whole set of solutions. Any solution outside the non-dominated set is dominated by some solution in the non-dominated set. When the solution set under consideration is the entire search space, then the non-dominated set is called the Pareto-optimal set. The non-dominated set is used in many multi-objective evolutionary algorithms, and an algorithm for finding the non-dominated set is outlined by Deb [42]. However, we are more interested in sorting the entire solution set into a sequence of non-dominated fronts. Solutions in the first front are not dominated by any solution in the whole solution set, solutions in the second front are only dominated by solutions in the first front, and so on. An algorithm to perform such non-dominated sorting is [42]:

1. For each solution  $\mathbf{x}_i$  in the solution set:
  - Calculate the number of solutions which solution  $\mathbf{x}_i$  dominates. This is called its domination count,  $n_i$ .
  - Make the set  $S_i$  which is the set of solutions which solution  $\mathbf{x}_i$  dominates.
2. If a solution's domination count is zero,  $n_i = 0$ , then solution  $\mathbf{x}_i$  is in the first non-dominated front.
  - For each of these solutions  $\mathbf{x}_i$ , reduce the domination count  $n_j$  of all solutions  $\mathbf{x}_j$  in the set  $S_i$  by one.
3. If for any solution  $\mathbf{x}_j$ , its domination count  $n_j$  becomes zero, then solution  $\mathbf{x}_j$  is in the second non-dominated front.
4. The process is repeated with every solution in the second non-dominated front to find the third non-dominated front, and so on, until all solutions are classified in a front.

This non-dominated sorting method is used in NSGA-II, NSGA-III, and U-NSGA-III. It is depicted in Figure 4.1.

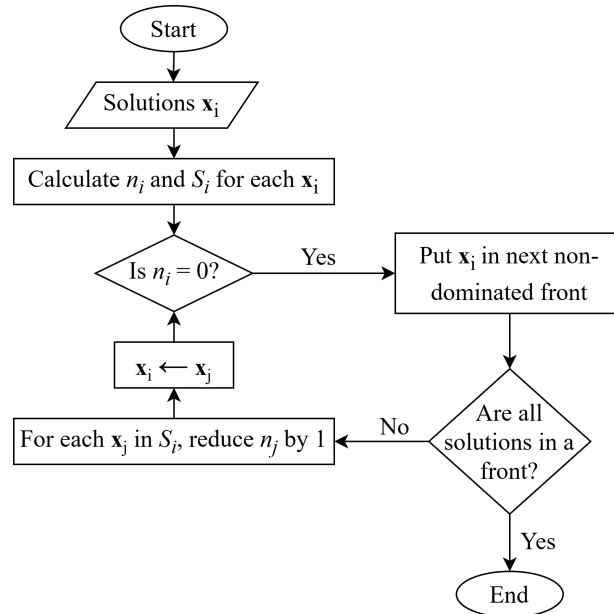


**Figure 4.1:** Flowchart of the non-dominated sorting algorithm.

### 4.3. U-NSGA-III

In this study, the unified non-dominated sorting genetic algorithm III (U-NSGA-III) is used. This algorithm was developed by Seada and Deb [33] to create one, unified algorithm that can be used for single-, multi-, and many-objective optimization problems. Older single- and multi-objective optimization algorithms do not scale up for many-objective problems, and vice versa, many-objective optimization algorithms do not scale down for single- or multi-objective problems [33]. This creates the need for a unified optimization algorithm that can solve all three types of problems. U-NSGA-III is such an algorithm that “automatically degenerates” into an efficient algorithm for single-, multiple-, and many-objective optimization problems simply based on the number of specified objective functions [33]. The advantage of a unified optimization algorithm is that it allows for one-time implementation in a computer code. Since in this study we have single-, two-, and three-objective optimization problems, we use U-NSGA-III throughout for consistency.

U-NSGA-III is based on the many-objective genetic optimization algorithm NSGA-III [33]. Therefore, we first describe NSGA-III then explain the modifications to it that yield U-NSGA-III. NSGA-III is meant for solving optimization problems with 3 to 15 objectives. Since the number of non-dominated solutions increases dramatically as the number of objectives (dimensions) increases, NSGA-III uses pre-defined reference directions to guide its search [33]. The reference directions are used to maintain diversity in the population, and at the end of the optimization procedure, there is expected to be one Pareto-optimal solution for each reference direction. The steps in the NSGA-III algorithm are [33]:

1. Make  $H$  well-distributed  $M$ -dimensional reference points on a unit hyperplane.
  - $H$  is the number of reference points, which is also the number of desired optimal solutions at the end.
  - The reference points should be well-distributed so that the set of optimal solutions are also well-distributed.
  - A unit hyperplane means that it intersects each axis in the objective function space at a value of one.
2. Make a random initial population of size  $N_{pop}$ , where  $N_{pop}$  is the smallest multiple of four which is greater than  $H$ .
3. Call the parent population  $P_t$ . Perform non-dominated sorting on  $P_t$ .
4. Make an empty set,  $P_{t+1}$ , which is the next generation.
5. Make the offspring  $O_t$  by recombination and mutation of the parent population  $P_t$ .
  - The parents are randomly chosen. This is because there is expected to be one individual per reference point, so a binary tournament selection would compete individuals from different reference points against each other.
  - This means that there is no selection pressure on  $P_t$  when choosing parents.
  - Except, selection is performed if and only if at least one potential parent is infeasible. In that case, when two individuals are compared, the feasible one is selected to be a parent over the infeasible one. If both individuals are infeasible, then the less-violating one is selected.
6. Make the new set  $R_t$  which is the combination of  $P_t$  and  $O_t$ .  $R_t$  is of size  $2N_{pop}$ .
7. Perform non-dominated sorting on  $R_t$  to get the non-dominated fronts.
8. Add the non-dominated fronts one at a time, in order, to the next generation  $P_{t+1}$  until a complete front cannot be added without the size of  $P_{t+1}$  exceeding  $N_{pop}$ .
  - Call the last front that could not be fully accommodated in  $P_{t+1}$  as  $F_l$ .
  - Delete all other fronts below  $F_l$ .
9. Choose  $K$  solutions from  $F_l$ , where  $K$  is the difference between  $N_{pop}$  and the size of  $P_{t+1}$ , via a niche-preserving operator.
  - (a) First normalize the objectives of members of  $P_{t+1}$  and  $F_l$ .
  - (b) For each member  $\mathbf{x}$  of  $P_{t+1}$  and  $F_l$ , associate the reference point  $\pi(\mathbf{x})$  with it, which is the closest reference point to  $\mathbf{x}$ .
    - $\pi(\mathbf{x})$  is the closest reference point to  $\mathbf{x}$ .
    - $d(\mathbf{x})$  is the perpendicular distance between  $\mathbf{x}$  and the reference line of  $\pi(\mathbf{x})$ .
  - (c) For each reference point, compute its niche count, which is the number of members  $\mathbf{x}$  associated with it.
  - (d) Choose  $K$  members from  $F_l$ , one at a time, based on niching—choose members associated with least- or un-represented reference points in  $P_{t+1}$ —and add them to  $P_{t+1}$ .
10. The output is  $P_{t+1}$ , the next generation.
11. Iterate from Step 3, finding the next generation and so on, until the termination criterion is met.

Seada and Deb [33] emphasize that NSGA-III does not require any additional parameters, and constraints can be handled also without introducing a new parameter.

NSGA-III has many similarities with the popular multi-objective optimization algorithm NSGA-II, such as the non-dominated sorting algorithm, making a combined population  $R_t$  of the parents and offspring, and filling the new generation one non-dominated front at a time [33]. While NSGA-II is not used in this study, the workings of the algorithm are relevant, so the reader is referred to Appendix A for further details.

With NSGA-III as a basis, U-NSGA-III is now conceived by making a few modifications. These modifications

address some of the issues that arise when applying NSGA-III to single- and multi-objective optimization problems, such as the small population size, absence of selection pressure, and inapplicability of the niching and normalization operations [33]. The modifications are:

- The population size  $N_{pop}$  is detached from  $H$ , instead of being the smallest multiple of four which is greater than  $H$ .  $N_{pop}$  is still greater than or equal to  $H$ , and it should still be a multiple of four. For single-objective problems,  $H$  is always one, but now  $N_{pop}$  can be chosen to be much larger. For many-objective problems, since  $H$  is already quite large,  $N_{pop}$  can still be chosen to be the smallest multiple of four which is greater than  $H$ , and  $N_{pop}/H \approx 1$ .
- Selection pressure is introduced by using the niche-based tournament selection operator, instead of randomly choosing parents. The niche-based tournament selection operator compares two individuals and selects one to be a parent. If the individuals have different associated reference points, then one is chosen randomly. Otherwise, if they are associated with the same reference point, then the one with the better non-dominated rank is selected. Otherwise, if they are associated with the same reference point and are in the same non-dominated front, then the one with the smaller distance to the reference direction is selected. This selection process creates a mating population,  $P'_t$ , which is used to create the offspring  $O_t$  via recombination and mutation of parents in the mating population  $P'_t$ . For single- and multi-objective problems, since  $N_{pop} > H$ , there will be more than one population member associated with each reference direction, so the niche-based tournament selection operator selects among them. For single-objective problems, the niche-based tournament selection operator becomes equivalent to normal binary tournament selection, where the individual with the better objective value wins. For many-objective problems, usually  $N_{pop}/H \approx 1$ , so individuals have different associated reference points, so the niche-based tournament selection operator degenerates into random selection of parents.

U-NSGA-III is also capable of handling constraints [33]. Figure 4.2 shows a flowchart of the algorithm. For multi-objective problems, U-NSGA-III is the same as NSGA-II except for 1) the niche-based selection operator, and 2) U-NSGA-III only finds  $H$  well-distributed Pareto-optimal solutions (while the other  $N_{pop} - H$  solutions in the final population are not necessarily well-distributed) whereas in NSGA-II, all  $N_{pop}$  Pareto-optimal solutions in the final population are well-distributed [33]. For three and more objectives, U-NSGA-III is the same as NSGA-III [33].

### 4.3.1. Reference Directions

The U-NSGA-III algorithm requires the specification of a set of reference directions. There are multiple methods for creating those reference directions, but here we focus on the commonly-used Das-Dennis approach [44], [45]. The Das-Dennis approach creates  $H$  reference points that are equally-spaced on the unit simplex. By connecting each point to the origin, we get the reference directions. The number of reference points is determined by the parameter  $P_H$ .  $P_H$  is the number of partitions that there are along each objective axis. If there are  $P_H$  partitions, then there are  $P_H + 1$  points along each axis. The points are uniformly spaced. The total number of reference points/directions, based on  $P_H$ , is given in Equation 4.1 [44].  $M$  is the number of objectives, and  $C$  is the choose operator. Note that this restricts  $H$  to certain values based on  $M$  and  $P_H$ , i.e. an arbitrary number of reference points/directions cannot be created.

$$H = C_{P_H}^{M+P_H-1} \quad (4.1)$$

$P_H$  must be greater than  $M$  in order for there to be reference points in the interior of the unit simplex. The disadvantage of the Das-Dennis approach arises in high-dimensional problems (large  $M$ ) [44]. As the dimensionality increases, the total number of reference points  $H$  explodes. Additionally, more and more points lie on the boundaries instead of in the interior of the unit simplex. This issue can be addressed by using multiple layers of Das-Dennis points, but this method is not explained here because it is not expected to be necessary in this study since  $M$  is not too large.

## 4.4. Post-Optimization Analysis

When the optimization procedure is complete and the (set of) optimal solution(s) has been obtained, it is important to perform post-optimization analysis. The optimization results should be analyzed for convergence and diversity [42]. Deb [42] suggests several approaches for this. For example, one could run several  $\epsilon$ -constraint optimization problems with different values of  $\epsilon$  and compare the solutions to the genetic algorithm solutions. However, we will not perform such analysis because it involves defining and executing extra optimization problems. Or, one could plot the initial population alongside the optimal solutions to show the level of optimization done by the genetic algorithm, which is a simple visualization done in this study. We expect good diversity of the optimal solutions because of the use of reference directions. Even so, we will also check the diversity visually using the plot of the Pareto front.

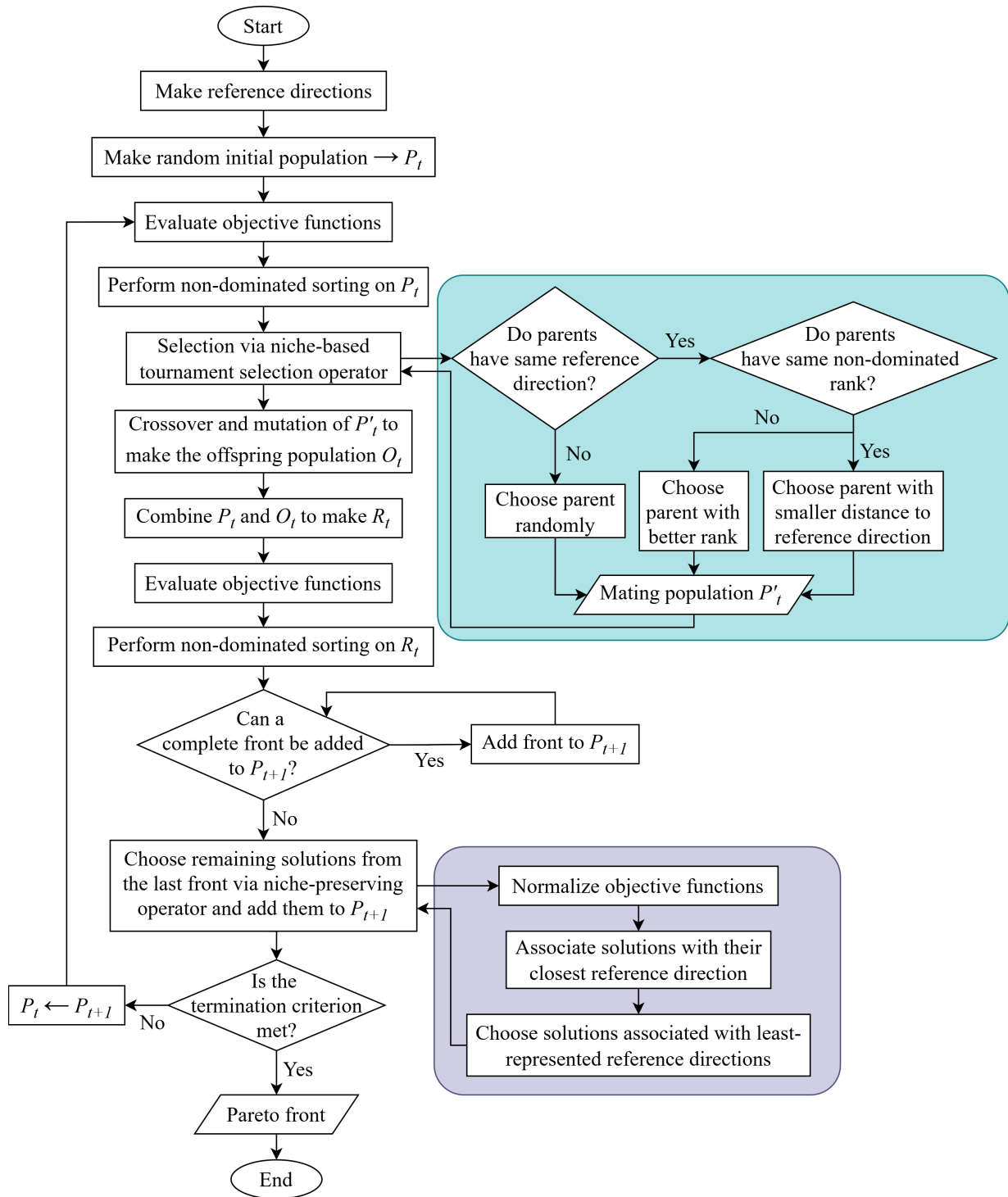


**Figure 4.2:** Flowchart of the U-NSGA-III algorithm.

Additionally, the hypervolume is a performance metric which is commonly used to measure the extent of both convergence and diversity of the solution set [42]. The hypervolume represents the space (area in 2D, or volume in 3D) which is dominated by the set of optimal solutions with respect to some reference point. Figure 4.3 shows how this space is identified when there are two objectives. The objectives should first be normalized before calculating the hypervolume [43]. The goal is to maximize the hypervolume, as this means that the optimal solutions which were found by the algorithm better approximate the Pareto-optimal front. The hypervolume can be easily calculated for two or three objectives. However, it is computationally expensive to calculate the hypervolume when there are more

than three objectives, but there are approximate methods to estimate the hypervolume when there are more objectives [42], [43].

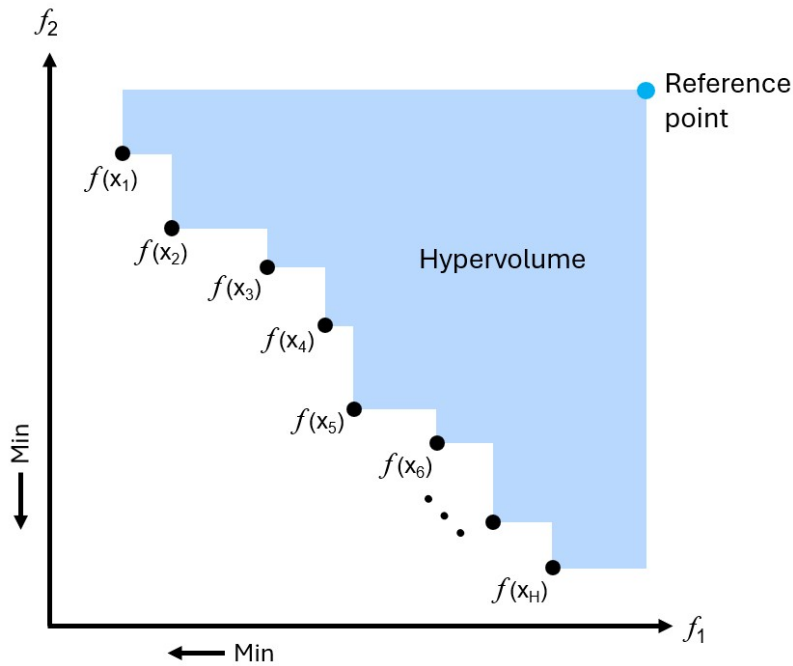


**Figure 4.3:** Graphical depiction of the hypervolume for two dimensions.

The change in the objective space can also be used to study the convergence of the optimization algorithm. The approach depends on the number of objectives. For a single objective, we can look at the convergence of the value of that single objective between generations. The difference in the objective function value should become small for many consecutive generations near the end of the simulation, meaning that the algorithm has converged. When there are more objectives, we can calculate the generational distance, as Le Fouest and Mulleners [5] did to measure the convergence of their two-objective optimization problem. The generational distance is the average distance in the objective space between the Pareto-optimal solutions and the Pareto-optimal solutions of the previous generation [5]. If the Pareto front is known i.e. for some theoretical/test problem, then the generational distance can measure the difference between the Pareto-optimal solutions found by the genetic algorithm and the true Pareto-optimal front [43]. However, if the Pareto front is not known (as is the case in this study), it can be approximated using the Pareto front from the last generation. Then the generational distance is calculated with respect to this final solution set to analyze the convergence of the algorithm to the final solution set. The aim is to minimize the generational distance. When the generational distance is small for many consecutive generations, the algorithm has converged.

Lastly, once multiple trade-off solutions are obtained, the user has to decide on which single optimal solution to use [42]. The approaches for doing this are outside the scope of this study, and the decision is left to the user. An “innovization” study can also be performed, which involves finding properties that are common among multiple trade-off solutions [42], and could be valuable from a practical standpoint.

# Part II

## Methodology

## VAWT Model Implementation

Due to the accuracy and low computational requirement of the AC model [7], [8], [28], [37], [38], it is used to model VAWTs in this study. The 2D AC model was already explained in detail in Section 3.4. The present chapter focuses on the implementation of the model in a computer code. Section 5.1 describes how the AC model is implemented in discrete form, including the inputs, calculations, and outputs of the actuator cylinder function. We briefly mention some limitations of the model. Then, Section 5.2 justifies the selection of the reference turbine used in this study and outlines its specifications.

### 5.1. 2D Actuator Cylinder Model Implementation

This section describes the numerical implementation of the 2D actuator cylinder model in a computer code. It is based on the master's thesis by Li [39] and a paper by Cheng *et al.* [8].

The input data to the model specify the turbine's geometry and operating conditions. The inputs are: the number of blades, tip speed ratio, blade chord length, rotor radius, freestream wind speed, airfoil polars ( $C_l$  and  $C_d$  as a function of  $\alpha$ , depending on the airfoil shape and Reynolds number), and pitch angle.

First, the AC is discretized into  $N_{el}$  equal-sized sections. Each section covers the azimuthal range:

$$\Delta\theta = \frac{2\pi}{N_{el}} \quad (5.1)$$

Here, a value of  $N_{el} = 72$  is used, so  $\Delta\theta = 5^\circ$ . For each section, there is a control point,  $\theta_i$ , which is set to be at the midpoint of the section. All points in the section are assumed to have the same properties as at the control point, i.e. the loading  $Q_n$  and  $Q_t$  are assumed to be piecewise constant. The control points are located at the azimuthal positions given by:

$$\theta_i = (i - 1/2)\Delta\theta = (2i - 1)\pi/N_{el} \text{ for } i = 1, 2, \dots, N_{el} \quad (5.2)$$

Li [39] makes two important notes regarding this discretization method. The first is that the angles  $\theta = 0^\circ$  and  $\theta = 180^\circ$ , which are the transitions between the upwind and downwind halves of the rotor, are not control points. The second is that every control point on the upwind side has a corresponding control point on the downwind side which has the same  $y$ -value.

Using this discretization method, the integral parts of the induced velocities in Equation 3.29 are written as:

$$\begin{aligned} w_x(x, y) &= -\frac{1}{2\pi} \sum_{i=1}^{N_{el}} Q_{n,i} \int_{\theta_i - \frac{1}{2}\Delta\theta}^{\theta_i + \frac{1}{2}\Delta\theta} \frac{-(x + \sin\theta) \sin\theta + (y - \cos\theta) \cos\theta}{(x + \sin\theta)^2 + (y - \cos\theta)^2} d\theta \\ &\quad - \frac{1}{2\pi} \sum_{i=1}^{N_{el}} Q_{t,i} \int_{\theta_i - \frac{1}{2}\Delta\theta}^{\theta_i + \frac{1}{2}\Delta\theta} \frac{-(x + \sin\theta) \cos\theta - (y - \cos\theta) \sin\theta}{(x + \sin\theta)^2 + (y - \cos\theta)^2} d\theta \\ w_y(x, y) &= -\frac{1}{2\pi} \sum_{i=1}^{N_{el}} Q_{n,i} \int_{\theta_i - \frac{1}{2}\Delta\theta}^{\theta_i + \frac{1}{2}\Delta\theta} \frac{-(x + \sin\theta) \cos\theta - (y - \cos\theta) \sin\theta}{(x + \sin\theta)^2 + (y - \cos\theta)^2} d\theta \\ &\quad + \frac{1}{2\pi} \sum_{i=1}^{N_{el}} Q_{t,i} \int_{\theta_i - \frac{1}{2}\Delta\theta}^{\theta_i + \frac{1}{2}\Delta\theta} \frac{-(x + \sin\theta) \sin\theta + (y - \cos\theta) \cos\theta}{(x + \sin\theta)^2 + (y - \cos\theta)^2} d\theta \end{aligned} \quad (5.3)$$

Any evaluation point  $(x, y)$  on the cylinder can be written as:

$$x = -\sin(\theta) \quad (5.4)$$

$$y = \cos(\theta) \quad (5.5)$$

when the cylinder is normalized to a radius of 1.

However, when the induced velocities are calculated at the control points, a singularity in Equation 5.3 occurs because the denominator becomes zero. To address the singularity problem, the control points are moved slightly inside or outside the cylinder surface. This is implemented by multiplying the  $(x, y)$  evaluation coordinate by a factor  $f$  which is slightly below or above 1 to move the coordinate inside or outside the cylinder, respectively. Here, a value of  $f = 0.999$  is used, so the control points are moved inside the cylinder. Note that this also has implications on the expression of the induced velocity  $w_x$  because now the control points are inside the cylinder, so for all control points, the  $*$  terms in Equation 3.29 need to be included. There are no control points in front of the cylinder nor in the wake.

Now the evaluation control points, indexed by  $j = 1, 2, \dots, N_{el}$ , are written as:

$$x_j = -f \sin(\theta_j) = f \cdot x \quad (5.6)$$

$$y_j = f \cos(\theta_j) = f \cdot y \quad (5.7)$$

When calculating the induced velocity at control point  $j$ , the influence of all the other control points  $i = 1, 2, \dots, N_{el}$  on the evaluation control point  $j$  are accounted for (see the summation in Equation 5.10) [8]. We introduce the influence coefficients  $I_{wx}$  and  $I_{wy}$ :

$$I_{wx,i,j} = \int_{\theta_i - \frac{1}{2}\Delta\theta}^{\theta_i + \frac{1}{2}\Delta\theta} \frac{-(x_j + \sin\theta) \sin\theta + (y_j - \cos\theta) \cos\theta}{(x_j + \sin\theta)^2 + (y_j - \cos\theta)^2} d\theta \quad (5.8)$$

$$I_{wy,i,j} = \int_{\theta_i - \frac{1}{2}\Delta\theta}^{\theta_i + \frac{1}{2}\Delta\theta} \frac{-(x_j + \sin\theta) \cos\theta - (y_j - \cos\theta) \sin\theta}{(x_j + \sin\theta)^2 + (y_j - \cos\theta)^2} d\theta$$

The influence coefficients only depend on the geometry and are independent of loading and time [8], [39]. Therefore, they only need to be computed once in the execution of the code.

The integral in Equation 5.8 is discretized and calculated numerically as in Equation 5.9. The angular section  $\theta_i - \frac{1}{2}\Delta\theta$  to  $\theta_i + \frac{1}{2}\Delta\theta$  is divided into  $N_s$  sub-sections. Here,  $N_s = 1000$  is used.

$$I_{wx,i,j} = \sum_{k=1}^{N_s} \frac{-(x_j + \sin\theta_k) \sin\theta_k + (y_j - \cos\theta_k) \cos\theta_k}{(x_j + \sin\theta_k)^2 + (y_j - \cos\theta_k)^2} \Delta\theta_k \quad (5.9)$$

$$I_{wy,i,j} = \sum_{k=1}^{N_s} \frac{-(x_j + \sin\theta_k) \cos\theta_k - (y_j - \cos\theta_k) \sin\theta_k}{(x_j + \sin\theta_k)^2 + (y_j - \cos\theta_k)^2} \Delta\theta_k$$

Now the induced velocity at evaluation control point  $j$  is:

$$w_{x,j} = -\frac{1}{2\pi} \left( \sum_{i=1}^{N_{el}} Q_{n,i} I_{wx,i,j} + \sum_{i=1}^{N_{el}} Q_{t,i} I_{wy,i,j} \right) - (Q_{n,N_{el}+1-j})^* - (Q_{t,N_{el}+1-j} \frac{y_j}{\sqrt{1-y_j^2}})^* \quad (5.10)$$

$$+ (Q_{n,j})^{**} - (Q_{t,j} \frac{y_j}{\sqrt{1-y_j^2}})^{**}$$

$$w_{y,j} = -\frac{1}{2\pi} \left( \sum_{i=1}^{N_{el}} Q_{n,i} I_{wy,i,j} - \sum_{i=1}^{N_{el}} Q_{t,i} I_{wx,i,j} \right)$$

Since  $f < 1$ , all the control points are inside the cylinder so the cylinder is only crossed once (on the upwind side) for all points. Only the  $*$  terms in Equation 5.10 are included. In discrete form, the  $*$  terms become as written in Equation 5.11. Notice that the index is different depending on if the control point  $j$  is on the upwind or downwind half. If the control point is on the downwind half ( $j > \frac{N_{el}}{2}$ ), the point of concern is the one across from it on the

upwind side with the same  $y$ -value. This control point is given by the index  $N_{el} + 1 - j$ . Figure 5.1 shows this relationship between the indices.

$$\begin{aligned} \text{Upwind } (j \leq N_{el}/2): & - (Q_{n,j})^* - (Q_{t,j} \frac{y_j}{\sqrt{1-y_j^2}})^* \\ \text{Downwind } (j > N_{el}/2): & - (Q_{n,N_{el}+1-j})^* - (Q_{t,N_{el}+1-j} \frac{y_j}{\sqrt{1-y_j^2}})^* \end{aligned} \quad (5.11)$$

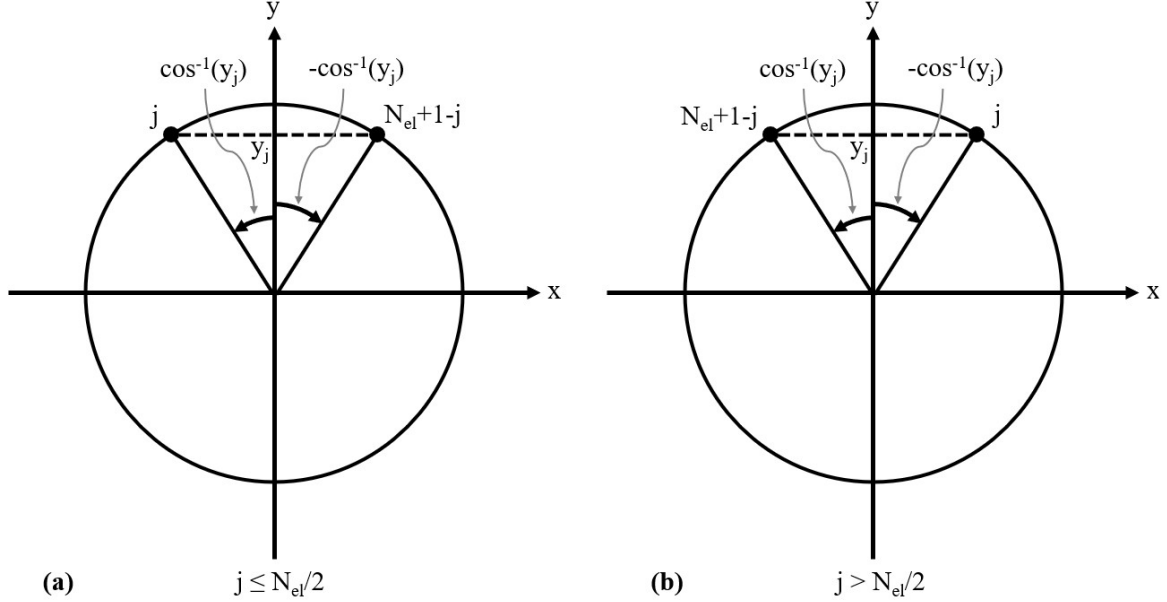


**Figure 5.1:** Control point indices in the AC model when (a)  $j \leq N_{el}/2$  and (b)  $j > N_{el}/2$ . Control points  $j$  and  $N_{el} + 1 - j$  are directly across from each other on the cylinder (one upwind, one downwind) and have the same  $y$ -value.

In the case that  $f > 1$ —which is not used in this study—the expression of Equation 5.10 is slightly different. The control points are moved outside the cylinder, so now they will be either in front of the cylinder or in the wake. For  $j \leq \frac{N_{el}}{2}$ , the control point is in front of the cylinder, so neither \* nor \*\* terms are included. For  $j > \frac{N_{el}}{2}$ , the control point is in the wake of the cylinder, so both the \* and \*\* terms are included. The \* term with index  $N_{el} + 1 - j$  for  $Q_n$  and  $Q_t$  corresponds to the first crossing of the cylinder in the upwind half. When  $j > \frac{N_{el}}{2}$ , the control point indexed by  $N_{el} + 1 - j$  is the corresponding control point on the upwind side of the cylinder with the same  $y$ -value as control point  $j$ . The \*\* terms in Equation 5.10 represent the second cylinder crossing, on the downwind side. When  $j > \frac{N_{el}}{2}$ , this index  $j$  for  $Q_n$  and  $Q_t$  simply matches with the evaluation control point index  $j$ .

The velocities and loading at the control points are calculated iteratively. The relative wind velocity at the control point is:

$$\vec{V}_{rel} = \vec{V}_{\infty} + \vec{V}_{ind} + \vec{V}_{rot} \quad (5.12)$$

where  $\vec{V}_{\infty}$  is the freestream velocity,  $\vec{V}_{ind}$  is the induced velocity, and  $\vec{V}_{rot}$  is the rotational velocity. The induced velocity is calculated using Equation 5.10. The rotational speed is equal to  $V_{rot} = \Omega R$ .

The  $x$  and  $y$  wind speed components are given by:

$$V_x = V_{\infty}(1 + w_x) + \Omega R \cos \theta \quad (5.13)$$

$$V_y = V_{\infty} w_y + \Omega R \sin \theta \quad (5.14)$$

The normal and tangential wind speeds are given by:

$$V_n = V_x \sin \theta - V_y \cos \theta \quad (5.15)$$

$$V_t = V_x \cos \theta + V_y \sin \theta \quad (5.16)$$

The relative wind speed (magnitude of the relative wind velocity) is then:

$$V_{rel} = \sqrt{V_n^2 + V_t^2} = \sqrt{V_x^2 + V_y^2} \quad (5.17)$$

Now the inflow angle,  $\varphi$ , can be calculated based on the relative wind speed components:

$$\varphi = \tan^{-1}\left(\frac{V_n}{V_t}\right) \quad (5.18)$$

And the angle of attack,  $\alpha$ , is:

$$\alpha = \varphi + \theta_p \quad (5.19)$$

where  $\theta_p$  is the pitch angle. Recall that the convention used in this study is that a positive pitch angle is when the leading edge is pointing inward.

With knowledge of the angle of attack, the appropriate lift ( $C_l$ ) and drag ( $C_d$ ) coefficients can be found. These coefficients depend on the angle of attack, the airfoil, and the Reynolds number. A table of  $\alpha$ ,  $C_l$ , and  $C_d$  values is input to the code, so given  $\alpha$ ,  $C_l$  and  $C_d$  can be looked up in the table and using interpolation.

The normal and tangential load coefficients are obtained by a projection of lift and drag:

$$C_n = C_l \cos \alpha + C_d \sin \alpha \quad (5.20)$$

$$C_t = C_l \sin \alpha - C_d \cos \alpha \quad (5.21)$$

Next, the lift ( $F_L$ ) and drag ( $F_D$ ) forces are calculated for each control point:

$$F_L(\theta) = \frac{1}{2} \rho V_{rel}^2(\theta) c C_l(\alpha) \quad (5.22)$$

$$F_D(\theta) = \frac{1}{2} \rho V_{rel}^2(\theta) c C_d(\alpha) \quad (5.23)$$

where  $\rho$  is the air density and  $c$  is the airfoil chord length.

Then, the normal and tangential forces are calculated as:

$$F_n(\theta) = F_L(\theta) \cos \alpha + F_D(\theta) \sin \alpha = \frac{1}{2} \rho V_{rel}^2(\theta) c C_n \quad (5.24)$$

$$F_t(\theta) = F_L(\theta) \sin \alpha - F_D(\theta) \cos \alpha = \frac{1}{2} \rho V_{rel}^2(\theta) c C_t \quad (5.25)$$

The nondimensional, time-averaged normal and tangential loads  $Q_n(\theta)$  and  $Q_t(\theta)$  are now calculated:

$$Q_n(\theta) = \frac{B}{2\pi R \rho V_\infty^2} (F_n(\theta) \cos \theta_p - F_t(\theta) \sin \theta_p) \quad (5.26)$$

$$Q_t(\theta) = -\frac{B}{2\pi R \rho V_\infty^2} (-F_n(\theta) \sin \theta_p + F_t(\theta) \cos \theta_p) \quad (5.27)$$

Then the induced velocities  $w_x$  and  $w_y$  are calculated from Equation 5.10. The modified linear correction term  $k_a$  is taken into account. First, the thrust coefficient is calculated as:

$$C_T = \int_0^{2\pi} (Q_n(\theta) \sin \theta + Q_t(\theta) \cos \theta) d\theta \quad (5.28)$$

Then, the induction factor  $a$  is calculated using Equation 3.32 (repeated in Equation 5.29).  $k_a$  is calculated according to Equation 3.33 (repeated in Equation 5.30). Finally,  $w_x$  and  $w_y$  are multiplied by  $k_a$ .

$$a = k_3 C_T^3 + k_2 C_T^2 + k_1 C_T + k_0 \quad (5.29)$$

$$k_a = \begin{cases} \frac{1}{1-a} & a \leq 0.15 \\ \frac{1}{1-a} (0.65 + 0.35e^{-4.5(a-0.15)}) & a > 0.15 \end{cases} \quad (5.30)$$

The above process is iterated until  $w_x$  and  $w_y$  converge. In the process, a relaxation factor is implemented which yields a weighted average of the induced velocities from the previous iteration and the current iteration in order to aid with the convergence. The calculation is deemed to converge when the difference between the induced velocities from the current iteration and previous iteration is below some tolerance (here,  $1 \times 10^{-7}$  is used).

Lastly, the power coefficient is calculated:

$$C_p = \frac{1}{2\pi} \int_0^{2\pi} \frac{B(F_t \cos(-\theta_p) + F_n \sin(-\theta_p))\Omega R}{\frac{1}{2}\rho(2R)V_\infty^3} d\theta \quad (5.31)$$

The function returns the thrust coefficient, power coefficient, and the following parameters as a function of the azimuth angle  $\theta$ :  $\alpha$ ,  $C_l$ ,  $C_d$ ,  $V_{rel}$ ,  $C_n$ ,  $C_t$ ,  $F_n$ ,  $F_t$ ,  $Q_n$ , and  $Q_t$ . The 2D AC model is implemented in Python, in a code originally written by Bruce LeBlanc, and modified by the author for use in this study.

### 5.1.1. Model Limitations

As discussed in Section 3.3 and evidenced in the AC model validation (Section 7.2), the 2D AC model has several limitations, most notably aerodynamic phenomena which are not modeled. The AC model does not include dynamic stall, flow curvature, dynamic inflow, blade-vortex interaction, or the effect of the tower and struts [4], [8], [37]. Additionally, since we use the 2D AC model, only a 2D cross section of the rotor is considered (at the mid-span of the blades) and blade tip effects are not included. Many of these phenomena can be integrated into the AC model by adding models designed for each of the specific phenomena [4], [8], [24], [28], [30], [37]. Including these aerodynamic effects are recommended future improvements of the model, but they are outside the scope of the present study. Lastly, the AC is a quasi-steady model so it does not evolve in time and represents time-averaged blade forces.

## 5.2. Reference Turbine

To the author's knowledge, there is no reference H-rotor VAWT with complete experimental and numerical performance and load data. Several turbines from the literature were investigated in order to select an appropriate turbine for use in this study. We use a reference turbine which is based on the Sandia National Laboratories (Sandia, or SNL) 34-meter  $\Phi$ -rotor VAWT [32] to perform the pitch optimization.

There were several considerations when choosing a reference turbine, namely:

- The turbine size, with a preference for larger turbines with higher Reynolds number so the airfoil polars are more accurate. Small wind-tunnel-scale turbines (used in both experimental and numerical studies) were mostly avoided because they have low Reynolds numbers and thus the airfoil polars calculated by XFOIL are inaccurate [46]. Melani *et al.* [46] found that at low Reynolds numbers, the airfoil polars calculated by XFOIL do not match experimental data, either in the pre- or post-stall region, possibly because XFOIL cannot model the laminar separation bubbles properly. Therefore, it is difficult to procure accurate airfoil polars for low Reynolds numbers. On the other hand, when the Reynolds number is not too low ( $Re \geq 140,000$ ), XFOIL's polars match experimental data, at least in the linear region, because transition and separation phenomena are less pertinent and the flow is stable [46].
- The availability of published power and load data, with a preference toward numerical data over experimental data, so that our AC model could be validated. Blade-level load data per azimuth is particularly desired because rotor-averaged parameters including  $C_p$  and  $C_T$  are not sufficient for validation [38]. Ferreira and Scheurich [47] found that the same power coefficient can be obtained for a VAWT with different azimuthal blade loading distributions. Furthermore, numerical data is preferred as it is complicated to compare our numerical results to experimental results because there are uncertainties in the experimental measurements and the AC model does not capture several physical phenomena which do occur in experiments. For example, the AC does not model dynamic stall. Additionally, the absence of modeling blade-vortex interaction and tower shadow can lead to different results than experiments especially in the loading downwind. It is important to have data with which to validate the base case (zero pitch) model first before performing pitch optimization.
- The rotor shape, with a preference for H-rotors. With an H-rotor, the rotor radius does not change in the vertical direction. Additionally, compared to  $\Phi$ -rotors, H-rotors have been more common in the past decade [3].
- Whether the turbine exists in the real world, is an experimental model, or was invented for purely theoretical (numerical) use. An existing turbine is preferred so that our study has more practical implications. Using a large-scale turbine which has proven to work and could be used on a commercial scale would also make the present study more relevant.

Most of the turbines considered in the literature review (Section 3.5) and validation of the 2D AC model (Section 7.2) do not meet these criteria. For example, the turbines used in De Tavernier [4] and De Tavernier and Ferreira [30] are non-existent, small turbines with idealized airfoil polars (sinusoidal or linear lift coefficient and zero drag). LeBlanc and Ferreira [14] and LeBlanc and Ferreira [15] used an experimental turbine, so it is hard to compare our numerical results to their experimental results. Their turbine is also of wind-tunnel scale with a low Reynolds number, which means the airfoil polars calculated using XFOIL, which would be used in our numerical model, are inaccurate [46]. Le Fouest and Mulleners [5] also use a small experimental turbine. Most of the authors from Section 3.5 use a small turbine, whether their study is experimental or numerical. Such as Rezaeiha *et al.* [6] who use a 1-meter diameter fictitious VAWT in their numerical (CFD) study. However, there is extensive load data published, which was used to validate our AC model, as well as airfoil polars for their turbine. We also considered the T1-turbine, which is a full-scale (200 kW, 26-m diameter) H-rotor turbine built by Vertical Wind AB, in collaboration with Uppsala University, in 2010 in Sweden [35], [48]. However, published (numerical) blade load data could not be found to compare our baseline modeling case to. Ultimately, we selected the Sandia 34-m turbine as the reference turbine because it is a large, real-life turbine which was used for research and it is well-documented with numerical load and performance data available.

The Sandia 34-m turbine was built in the late 1980s by Sandia National Laboratories in the United States [3]. It was used for research purposes but was decommissioned in 1998. The turbine's rated power is 500 kW [32]. It is a  $\Phi$ -rotor with two aluminum blades. The chord length and airfoil shape vary along the blade [32]. Near the blade root, the chord length is 1.22 m and the airfoil is the NACA 0021 airfoil. In the mid-section of the blade, the chord length is 0.91 m and the airfoil is SNL 0018/50. In the sections in between, the chord length is 1.07 m and the airfoil is also SNL 0018/50. The SNL 0018/50 airfoil is part of a family of airfoils designed specifically for VAWTs [32]. It is symmetric and has the same relative thickness as the NACA 0018 airfoil, but the thickest point is closer to the trailing edge compared to the NACA 0018 airfoil [49]. The leading edge of the SNL 0018/50 airfoil is less-rounded than the NACA 0018 airfoil, and near the trailing edge, the SNL 0018/50 airfoil is curved slightly inward (reflex). Figure 5.2 shows the shape of the SNL 0018/50 airfoil as compared to the NACA 0018 one. The SNL 0018/50 airfoil achieves natural laminar flow for approximately 50% of the chord of the airfoil [49]. We retrieve the SNL 0018/50 airfoil polars from QBlade [31]. QBlade has several turbine model files available for download, and we downloaded the model for the Sandia 34-m turbine, which includes the airfoil polar data. The airfoil polars from QBlade are already extended to cover the  $360^\circ$  range of angle of attack using the extrapolation method of Montgomerie [50]. Figure 5.3 shows these airfoil polars.

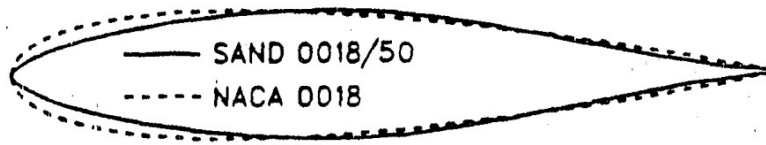


**Figure 5.2:** The SNL 0018/50 airfoil shape compared to the NACA 0018 airfoil. Figure from [49].

The rated power of 500 kW is achieved at a rated wind speed of 12.5 m/s and rotational speed of 37.5 rpm (3.927 rad/s), making the tip speed ratio 5.27 [32]. This means that the chord-based Reynolds number is  $4.05 \times 10^6$ . However, the airfoil polars available for the SNL 0018/50 airfoil in QBlade only go up to  $Re = 1 \times 10^6$ . These polars were also not generated using XFOIL, but were procured from elsewhere. We were also unable to recreate the polars in XFOIL using the corresponding airfoil shape and Reynolds number. Therefore, accurate airfoil polars for the SNL 0018/50 airfoil cannot be generated for higher Reynolds numbers (e.g.  $4.05 \times 10^6$ ) using XFOIL. In order to have an accurate airfoil polar input, we therefore limit our operating condition so that the Reynolds number equals  $1 \times 10^6$ . Figure 5.4a shows various combinations of the tip speed ratio and freestream velocity which satisfy this  $Re = 1 \times 10^6$  limit. Common tip speed ratios for VAWTs in the literature are 2 to 4 [4]–[6], [14]–[16], [19], [20]. We therefore look in this range of tip speed ratios and find a compromise between  $\lambda$ ,  $V_\infty$ , and  $C_p$ . Figure 5.4a clearly shows that a lower tip speed ratio corresponds to a higher freestream wind speed, which is favorable. However, Figure 5.4b shows that these low tip speed ratios also result in low power coefficients. In order to still obtain a reasonable power coefficient for the base case, we choose the operating conditions of a tip speed ratio of  $\lambda = 4$  and freestream wind speed of  $V_\infty = 4.0659$  m/s. This is admittedly a low wind speed, but we are constrained by the  $1 \times 10^6$  Reynolds number, and would like a reasonable base case power coefficient, which depends on the tip speed ratio.

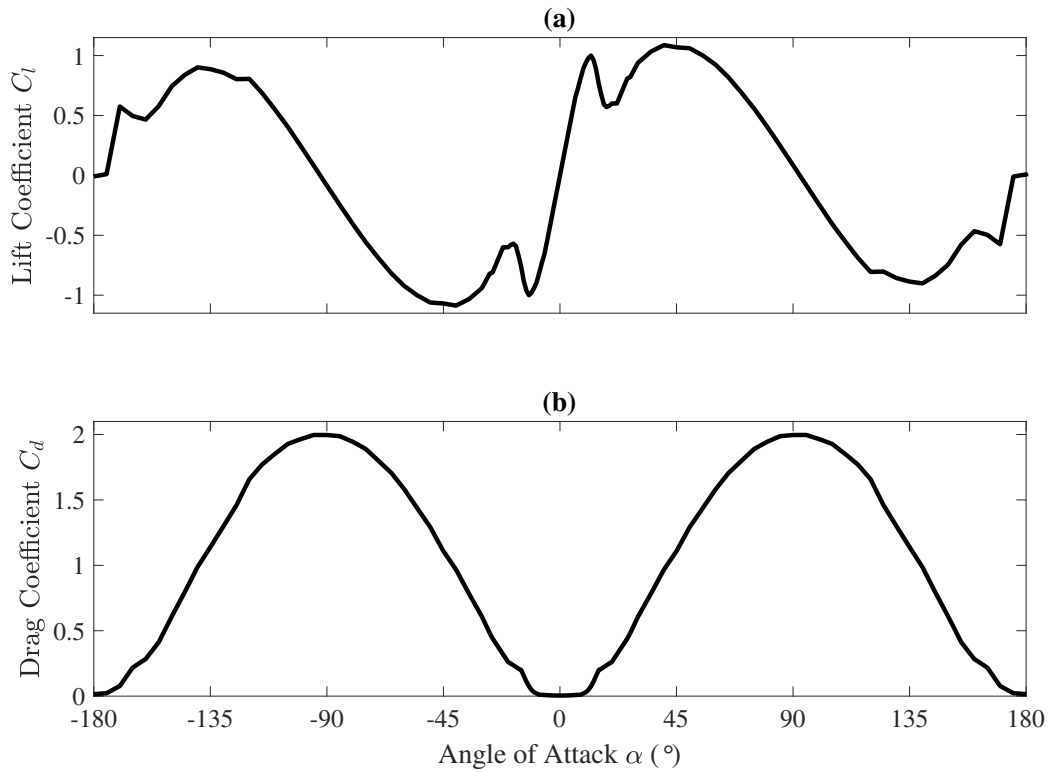


**Figure 5.3:** The airfoil polars of the SNL 0018/50 airfoil from QBlade [31] for  $Re = 1 \times 10^6$ . (a) The lift coefficient and (b) the drag coefficient.

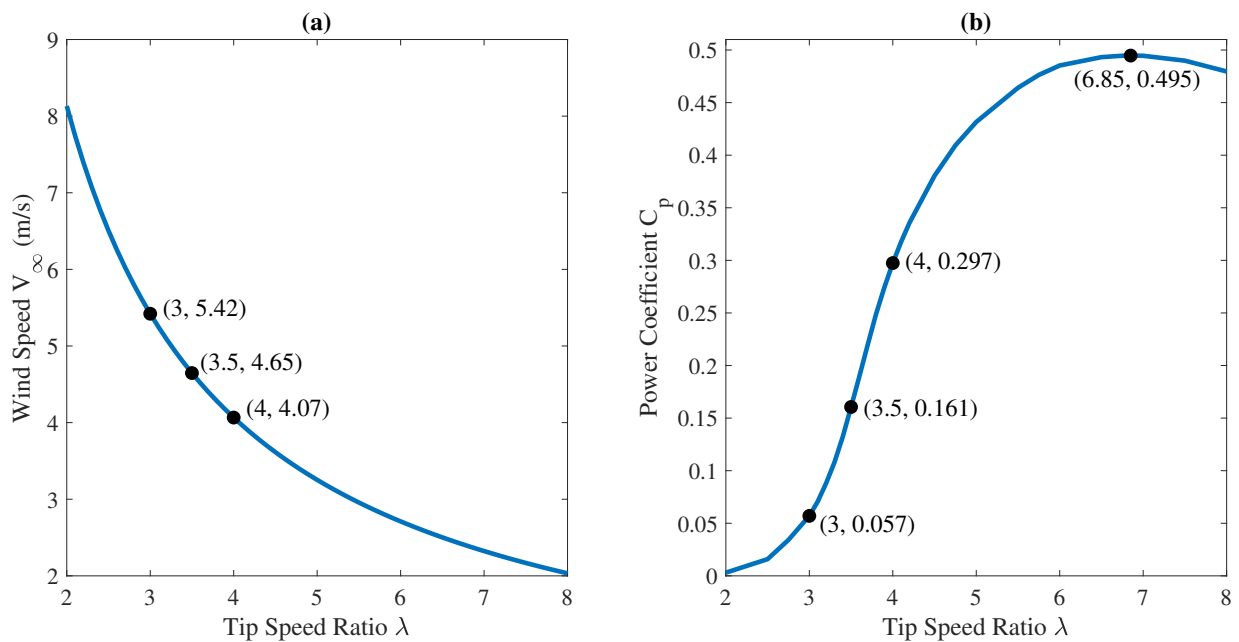


**Figure 5.4:** (a) Combinations of tip speed ratio and freestream wind speed which meet the  $Re = 1 \times 10^6$  operating condition. (b) Power coefficient of the turbine at those tip speed ratios, calculated using the 2D AC model.

The power coefficient for the base case (with zero pitch), calculated using the AC model, is  $C_p = 0.297$ . It should be noted that  $\lambda = 4$  is usually at the upper end of the efficient operating range for VAWTs [5]. However, data published by Ashwill [32] show that the optimal tip speed ratio for the Sandia 34-m turbine is a little above 6, depending on the rotational speed. They made measurements of the turbine operating at different rotational speeds. At 28 rpm (2.93

rad/s), the maximum power coefficient ( $C_p = 0.409$ ) occurs at  $\lambda = 6.34$ . At 34 rpm (3.56 rad/s), the maximum power coefficient ( $C_p = 0.401$ ) occurs at  $\lambda = 6.12$ . At 38 rpm (3.98 rad/s), the maximum power coefficient ( $C_p \approx 0.38$ ) occurs around  $\lambda \approx 6.1$ , but there is not enough data for this case [32]. Note that all of these conditions correspond to a Reynolds number greater than we have airfoil polar data for ( $Re \geq 3 \times 10^6$ ). Using the AC model, we found that for our operating condition— $\lambda = 4$  and  $V_\infty = 4.0659$  m/s corresponds to  $\Omega = 9.26$  rpm (0.97 rad/s)—the peak power coefficient occurs at  $\lambda = 6.85$  (see the  $C_p$ - $\lambda$  curve in Figure 5.4b). This is unusually high for VAWTs, but inline with the data from Ashwill [32].

The Sandia 34-m turbine meets our conditions of being a large, real-life turbine with full numerical load and performance data. However, it does come with a few drawbacks which require modifications in our model inputs. First of all, the Sandia 34-m turbine is a  $\Phi$ -rotor, whereas we consider an analogous H-rotor. This can be seen as extracting the mid-section of the  $\Phi$ -rotor and ignoring the curvature of the 3D blade around it, or extending the blades into a straight-bladed H-rotor with the same properties and diameter as the mid-section. The method we use in this study is a 2D model in any case. Therefore, we input the geometrical parameters at the mid-section of the blade: SNL 0018/50 airfoil, chord length of 0.91 m, and radius of 16.774 m (diameter of 33.548 m) [31], [32]. It should also be noted that the Sandia 34-m turbine has two blades, while three blades is more common for H-rotors. Three-bladed turbines have less fluctuations in the turbine loads and power (torque) [6]. However, we keep two blades so that the rotor solidity is consistent. The number of blades comes into play when the rotor loading  $Q_n$  and  $Q_t$  are calculated in the AC model. The effect of having two vs. three blades is explored in Chapter 9. Lastly, accurate airfoil polars are available only up to a Reynolds number of  $1 \times 10^6$ . Consequently, we set the input operating condition to  $\lambda = 4$  and  $V_\infty = 4.0659$  m/s as previously discussed, which is not the condition at the rated wind speed and rated power. The Sandia 34-m turbine properties are summarized in Table 5.1.

**Table 5.1:** Specifications of the Sandia 34-meter reference turbine and the modifications made for this study [32].

Parameter	Sandia 34-m	Present Study
Rated power	500 kW	
Rotor type	$\Phi$	H
Number of blades	2	2
Diameter	Various, max 34 m	33.548 m
Chord length	0.91, 1.07, 1.22 m	0.91 m
Rotor height	42.5 m	42.5 m
Blade length	54.5 m	42.5 m
Airfoil	NACA 0021, SNL 0018/50	SNL 0018/50
Wind speed	12.5 m/s rated wind speed	4.0659 m/s freestream wind speed
Tip speed ratio	Various, 5.27 at rated power	4
Reynolds number	4,050,000 at rated power	1,000,000

# Multi-Objective Optimization Implementation

In this study, we optimize the pitch function for multiple objectives. This chapter outlines the implementation of the multi-objective optimization problem. First, Section 6.1 explains the functional form of the pitch angle which will be used in the subsequent optimization. It is a third-order sinusoid. Next, Section 6.2 defines the optimization problem, including the decision variables, objective functions, and constraints. Section 6.3 defines the optimization algorithm we use, including its important parameters. We use the U-NSGA-III algorithm for all optimization cases, for consistency and generalizability. Finally, Section 6.4 describes the termination criterion, execution of the optimization problems, and post-optimization analysis. For the computational implementation, we use the multi-objective optimization library in Python called pymoo [43].

## 6.1. Functional Form of the Pitch Angle

Several functional forms of pitch angle have already been tested in the literature. For example, a sinusoid [16], sinusoid with varying frequency [13], and sinusoid with three harmonics [5]; a step function [19]; a spline which is directly optimized [22] or a spline which is fit to pre-calculated optimal pitch angles [23]; and a 10th-order Bezier curve [24]. The goal of this chapter is to establish the functional form of the pitch angle, as a function of azimuth angle  $\theta$ , that will be used in the optimization problems.

Scheduling the pitch angle as a function of the azimuth angle is a type of active variable pitch. We use active variable pitch control because it can achieve higher power efficiencies than fixed pitch or passive variable pitch systems [11], [19]. Particularly, we use individual active variable pitch so as not to be constrained by a collective pitch linkage mechanism. With a collective pitch mechanism, the blade pitch angle is limited to the kinematics prescribed by the physical mechanism, so the optimal pitch angle cannot be realized at every azimuthal angle [23]. Individual blade pitch offers more flexibility in finding the optimal pitch angles. Individual pitch does, however, require individual actuators for each blade and input power to these actuators [11]. While implementing individual variable pitch may sound complicated, LeBlanc and Ferreira [14] and Le Fouest and Mulleners [5] have built experimental turbines with mechanical systems that can achieve individual variable pitch. Collective pitch linkage mechanisms also come with their own weaknesses: high maintenance and susceptibility to failure [22].

Having established that individual variable blade pitching will be used, we now derive a functional form for the pitch angle. Considering the objective to maximize power, it has already been tried by Staelens *et al.* [18] to keep the effective angle of attack relatively constant just below the static stall angle throughout the revolution. This leads to an unsmooth and practically infeasible pitch kinematics (see Figure 3.14). Additionally, De Tavernier *et al.* [51] used the conclusion from Madsen *et al.* [41] that the maximum power coefficient is obtained when the normal load distribution approaches a uniform distribution upwind and a uniform distribution downwind, at a different constant. De Tavernier *et al.* [51] translate this to a constant bound circulation distribution in the upwind and downwind halves, respectively, with a jump at  $\theta = 0^\circ$  and  $180^\circ$ . The angle of attack needed to achieve such circulation can be realized by using variable pitch. The resulting pitch angle which maximizes  $C_p$  has large jumps and corners in the pitch angle (see Figure 7.11), which are practically infeasible. The authors note that constraints could be applied to the pitch rate and magnitude to make the pitch profile feasible. Houf [24] also followed the conclusion from Madsen *et al.* [41] that the ideal load-form ( $Q_n$  curve) should approach a uniform distribution. The author found optimal load-forms and derived the required pitch profiles to produce them. The resulting pitch curves may not be feasible because they have large pitch rates. However, directly putting constraints on the pitch profile before carrying out optimization to make the pitch profile feasible is not possible with this optimization method. The method also considers an ideal

rotor with an infinite number of blades and zero tangential loading.

Considering the objective of minimizing load fluctuations (standard deviation of the normal load), we can see this as trying to flatten the normal load curve. For example, we could flatten it to zero by subtracting an equivalent curve, the mirror image of  $Q_n$  over the x-axis. Therefore, we would like to approximate the shape of the  $Q_n$  curve with some functional form. This functional form can also be applied to the pitch angle, because the pitch angle serves to change the local effective angle of attack. The angle of attack, in turn, is related to the lift coefficient. This  $C_l$ - $\alpha$  relationship is roughly linear (up to stall). Finally, the lift force is the major contributor to the normal force on the blade.

We use the normal force curve of the Sandia 34-m turbine, at our operating conditions, at the mid-section, as the base case (see Figure 6.1). We use the curve fitting function in Matlab [52] to fit multiple functional curves to the  $Q_n$  curve. It was found that of the many model types in the fitting library, the polynomial model, sum of sines model, and Fourier model fit best. The difference between the sum of sines model and Fourier model is as follows. The Fourier function takes the form  $Q_n = A_0 + \sum_{i=1}^n (A_i \cos(iw\theta) + B_i \sin(iw\theta))$  while the sum of sines model has the form  $Q_n = \sum_{i=1}^n A_i \sin(B_i\theta + C_i)$ . So, the Fourier function has a constant intercept term  $A_0$  while the sine model does not; and the sine model includes a phase shift while the Fourier model achieves the same purpose with a sum of sines and cosines. In addition, as can be seen from the equations, the sine model does not require the sine functions to have periodic frequencies, while the Fourier function does. That is,  $B_i$  in the sum of sines model can be determined independently, whereas the frequencies in the Fourier model are always a multiple of  $w$ . Since the theory behind the two functional forms is the same, we will combine them and refer to them collectively as the “sinusoidal function”. Sinusoidal functions are continuous and smooth, which make them good candidates for a pitch function which is practically feasible to implement.

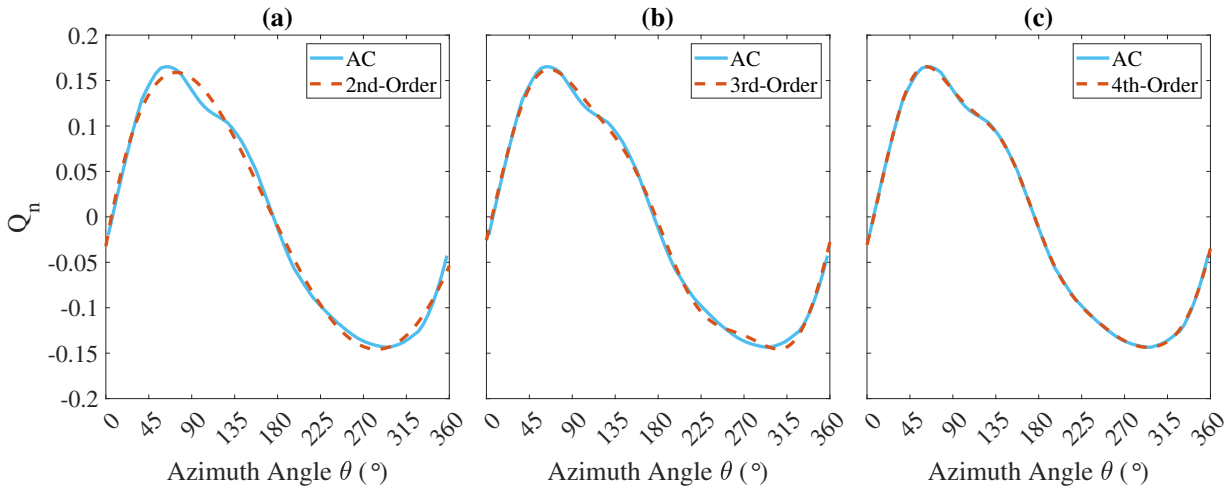


**Figure 6.1:** Normal load curve of the Sandia 34-m turbine for  $0^\circ$  pitch generated by the AC model, with a Fourier function fit with increasing number of harmonics: (a) second-order, (b) third-order, and (c) fourth-order.

A good fit of the sinusoidal function to the  $Q_n$  curve can be achieved with order three or higher. The third-order sinusoidal function, as shown in Figure 6.1b, is able to represent the trend in the  $Q_n$  curve sufficiently well without over-fitting it. The R-squared value is 0.998 and the root mean squared error is 0.0047 (unitless). Figure 6.1 compares second-, third-, and fourth-order sinusoidal fits. It can be seen that the third-order sinusoid fits better than the second-order sinusoid. The second-order sinusoid does not have sufficient degrees of freedom to capture the shape of the  $Q_n$  curve. The fourth-order sinusoid is able to match the  $Q_n$  curve very well, however, this can be seen as over-fitting. Over-fitting of models includes using more terms than are necessary [53]. Having more harmonics than is necessary makes the optimization problem more complex without any benefit in performance compared to a simpler model. It could even lead to worse performance. We avoid over-fitting because it restricts the pitch curve in the optimization problem to be of a specific functional form based on the fit to one dataset. Instead, we would just like to be able to capture the general shape of the curve, to allow more generality of the optimal pitch function. A fourth-order sinusoid is not necessary because a similar quality of fit can be obtained with a third-order sinusoid, which is a simpler function. Additionally, a higher-order sinusoidal pitch function engenders more decision variables in the optimization problem. It was found that the computation time of the optimization code increases significantly as the functional order increases. It was also found that more generations were needed to achieve convergence of the

optimization algorithm when the order was higher. With these practicalities in mind, a third-order sinusoidal pitch function is selected.

Le Fouest and Mulleners [5] also use a third-order sinusoid for the pitch function, inspired by Strom *et al.* [54]. Le Fouest and Mulleners [5] argue that three harmonics can bring about a pitch function which can change the angle of attack where needed (when the angle of attack is exceptionally high), in terms of large enough gradients of the pitch angle and adequate phase shift of the pitch function. At the same time, pitch functions with higher harmonics could introduce undesirable high-frequency vibrations. This corroborates our choice for a third-order sinusoidal pitch function. It should also be noted that the angle of attack and loading of a VAWT is periodic with the rotational frequency of the turbine, and any periodic function can be written as a (infinite) sum of sinusoids, which is known as a Fourier series. This further substantiates our choice of a sinusoidal function for the pitch function, even if we are truncating the series to three terms.

The functional form of the pitch angle used in this study is:

$$\theta_p = A_0 + A_1 \sin(\theta w + \phi_1) + A_2 \sin(2\theta w + \phi_2) + A_3 \sin(3\theta w + \phi_3) \quad (6.1)$$

This function combines aspects of the sum of sines and Fourier models in Matlab. Namely, we use an intercept  $A_0$ , we express the equation as a sum of sines only with phase shifts (no cosines), and we require the frequencies to be harmonic (multiples of  $w$ ). This yields 8 decision variables: the intercept/pitch offset  $A_0$ ; amplitudes  $A_1$ ,  $A_2$ , and  $A_3$ ; phase shifts  $\phi_1$ ,  $\phi_2$ ,  $\phi_3$ ; and frequency multiplier  $w$ . In order for the pitch function to be the same from revolution to revolution of the turbine, it must be continuous at  $\theta = 0^\circ$  and  $360^\circ$ . This effectively constrains  $w$  to be an integer.

A similar goodness-of-fit to the  $Q_n$  curve can be obtained with a ninth-degree polynomial (see Figure 6.2). However, the polynomial functional form was not selected because a similar fit and curve shape can be achieved with a lower-order sinusoidal function. The ninth-degree polynomial has more decision variables than the third-order sinusoid, which adds computational burden to the optimization code. Additionally, an extra constraint would have to be imposed to make the pitch angle smooth at the transition from  $\theta = 0^\circ$  to  $360^\circ$  so that it is feasible to implement. On the other hand, a sinusoidal function which meets the continuity constraint is automatically also smooth. Thus, we only consider the sinusoidal pitch function.

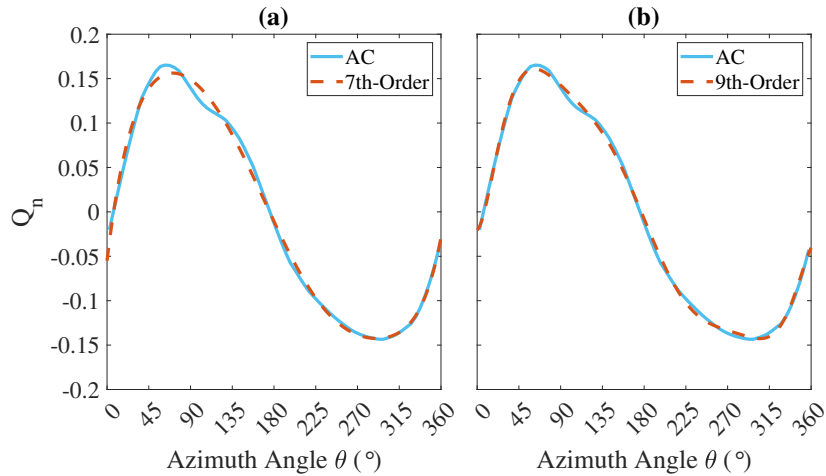


**Figure 6.2:** Normal load curve of the Sandia 34-m turbine for  $0^\circ$  pitch generated by the AC model, with a polynomial function fit: (a) seventh-order and (b) ninth-order.

The coefficients in the function obtained by curve fitting are not relevant, because those will be the optimization variables. Furthermore, they will be optimized for the pitch function, while we fit to the normal force curve, with the relation between pitch angle and normal force explained earlier. The purpose of the curve fitting study was to elucidate that a third-order sinusoidal function should be used as the functional form of the pitch angle in the optimization problems.

## 6.2. Optimization Problem Definition

### 6.2.1. Decision Variables

Now, we define the optimization problem. This includes specifying the number of decision variables, which depends on the functional form of the pitch angle. In Section 6.1, we established that the pitch angle,  $\theta_p$ , will be a third-order sinusoidal function (Equation 6.2).

$$\theta_p = A_0 + A_1 \sin(\theta w + \phi_1) + A_2 \sin(2\theta w + \phi_2) + A_3 \sin(3\theta w + \phi_3) \quad (6.2)$$

This yields eight decision variables:

1.  $A_0$ , the intercept, or pitch offset, in degrees.
2.  $A_1$ , the amplitude of the first harmonic, in degrees.
3.  $A_2$ , the amplitude of the second harmonic, in degrees.
4.  $A_3$ , the amplitude of the third harmonic, in degrees.
5.  $\phi_1$ , the phase shift of the first harmonic, in degrees.
6.  $\phi_2$ , the phase shift of the second harmonic, in degrees.
7.  $\phi_3$ , the phase shift of the third harmonic, in degrees.
8.  $w$ , the frequency multiplier, unitless.

Most authors (e.g. [5], [9], [16]) do not consider the frequency  $w$  as a decision variable, it is simply set to one. For example, Le Fouest and Mulleners [5] consider sinusoids with the same frequency as the rotational frequency of the turbine ( $w = 1$ ), to enforce periodicity. However, we do not know what the optimal frequency is, so we retain  $w$  as a decision variable. In control studies for HAWTs such as Munters and Meyers [55], the sinusoidal frequency is a changing parameter in the optimization. Furthermore, the functional form of the pitch angle, as determined in Section 6.1, was based on curve-fitting in Matlab. In this process, the frequency of the sinusoids was left as a free parameter. We enforce periodicity with a continuity constraint at  $\theta = 0^\circ$  and  $360^\circ$ , as discussed shortly (Section 6.2.3). This effectively constrains  $w$  to be an integer. In Chapter 8, it is found that the optimal value of  $w$  is always one, but it is still important to include the frequency as a decision variable because the optimal frequency is not known *a priori*.

The decision variables are given upper and lower bounds. These are shown in Table 6.1. The bounds are motivated by observations of optimal pitch magnitudes in the literature (see Section 3.5), as well as the bounds used by Le Fouest and Mulleners [5] for a third-order sinusoidal pitch function. The amplitude bounds of the sine functions are set to allow exploration of a large search space, while restraining the pitch angle from causing the effective angle of attack to be very large. Large angles of attack lead to low efficiency and high stress on the blades [5]. Additionally, the amplitude bound decreases as the order of the sinusoid increases; as such, the optimization algorithm does not search for a high amplitude of the higher-frequency terms, because such a pitch actuation would require more power [5]. The bounds on the phase shifts allow exploration of the full possible range of phase shifts. The bounds are different for the different harmonics because of their respective periodicity (e.g. a second-order sinusoid repeats twice per revolution, while a third-order sinusoid repeats three times per revolution).

**Table 6.1:** Upper and lower bounds on the decision variables.

Variable	Lower Bound	Upper Bound
$A_0$	$-10^\circ$	$10^\circ$
$A_1$	$-25^\circ$	$25^\circ$
$A_2$	$-15^\circ$	$15^\circ$
$A_3$	$-10^\circ$	$10^\circ$
$\phi_1$	$-180^\circ$	$180^\circ$
$\phi_2$	$-90^\circ$	$90^\circ$
$\phi_3$	$-60^\circ$	$60^\circ$
$w$	0	7.64

The upper bound on the frequency variable,  $w$ , is aimed at avoiding high frequency pitch oscillations, which are not favorable from a physical perspective (e.g. loads on the blades, pitch actuation mechanism and power consumption).

The upper bound on  $w$  is inspired by sinusoidal pitch control for HAWTs. Frederik *et al.* [56] investigate various types of pitch control, including periodic dynamic induction control, which is realized through a sinusoid with nondimensional frequency given by the Strouhal number,  $St = 0.25$ . This optimal Strouhal number was found by Munters and Meyers [55], who considered thrust coefficient control for HAWTs. Frederik *et al.* [56] note that it has not yet been explained physically why this is the optimal frequency. Supposing that the optimal frequency for HAWTs also applies to VAWTs, we also consider an optimal Strouhal number of 0.25. The Strouhal number is defined as  $St = \frac{f_e D}{V_\infty}$ , where  $f_e$  is the frequency in Hz,  $D$  is the rotor diameter in meters, and  $V_\infty$  is the freestream wind speed in m/s. Considering the Sandia 34-m turbine (see Section 5.2), this means that the optimal pitch frequency would be  $f_e = \frac{St \cdot V_\infty}{D} = \frac{0.25(4.0659 \text{ m/s})}{33.548 \text{ m}} = 0.0303 \text{ Hz}$  (0.19 rad/s or 1.82 rpm). The rotational frequency of the Sandia 34-m turbine is 0.97 rad/s (9.26 rpm). This yields a frequency multiplier of  $0.97/0.19 = 5.09$ . We apply a factor of 1.5 to this to set the upper bound of  $w$ , which becomes 7.64. Note that since  $w$  is an integer, this could be equivalently set to any number slightly above 7.

Overall, the approach to the decision variable bounds is to allow exploration of a large search space, to avoid excluding any potentially-optimal solutions. After the optimization problems were solved, we checked whether the optimal solutions are far from the bounds. If they are far from the bounds, it means we did not over-constrain the problem. For the single-objective and three-objective problems, all of the optimal decision variables are far from their respective bounds. However, for the two-objective case,  $\phi_1$  is close to  $180^\circ$  and  $\phi_2$  is close to  $90^\circ$  for some solutions. Therefore, we studied the effect of shifting the bounds from  $0^\circ$ - $360^\circ$  for  $\phi_1$  and  $0^\circ$ - $180^\circ$  for  $\phi_2$ , and the solutions obtained were equivalent.

### 6.2.2. Objective Functions

The next step in defining the optimization problem is specifying the number of objective functions and defining what the objective function(s) are. The number of objective functions is one to three, depending on the optimization case. There are three optimization cases, with increasing numbers of objectives. In the simplest case, Case 1, the single objective is to maximize the turbine efficiency, represented by the power coefficient,  $C_p$ . This is a common objective for VAWT pitch control in the literature (e.g. [9], [16], [19]–[22], [25]). However, maximizing the power coefficient is not the only important consideration for VAWTs.

Therefore, we successively add more objectives to elucidate the optimal pitch control to achieve different goals. Pitch control can also help reduce load fluctuations and torque fluctuations. The former is unfavorable from a blade structural and fatigue lifetime point of view [5], [24]. The latter is unfavorable from a power quality and drivetrain design point of view [13]. Therefore, the second objective we add is to minimize the fluctuations in rotor normal force, quantified by the standard deviation in the nondimensionalized normal force from the AC model,  $\sigma(Q_n)$ . The standard deviation is a measure of how much a quantity varies about its mean. Note that  $Q_n$  includes the force from all the blades, but the difference is only a factor of  $B$ , which does not affect the optimization problem. In this case, we are still trying to maximize  $C_p$ , so we have a two-objective optimization problem. We call this Case 2.

Then, we add minimizing the rotor torque fluctuations as the third objective. The torque from one blade is equal to its tangential force times the rotor radius. The torque used in the optimization problem is calculated at the rotor level, that is, summing the torque across the blades, because this is the torque experienced by the drivetrain and generator. In the AC model, the force  $Q_t$  already represents the tangential force of all the blades. Therefore, we quantify torque fluctuations as the standard deviation  $\sigma(Q_t)$ . Note that this should be multiplied by the rotor radius and dimensionalized to get the true rotor torque, but these constants do not impact the optimization problem. This is a three-objective optimization problem, which is referred to as Case 3.

Table 6.2 summarizes the objectives, and how they are built up one at a time. In the optimization code, the objective function(s) are defined by calling the Actuator Cylinder function (see Section 5.1) and defining the objective function(s) for each optimization case based on the AC model's outputs. For example, extracting the  $C_p$  value and the standard

**Table 6.2:** Optimization cases.

Objective	Case 1	Case 2	Case 3
Maximize $C_p$	✓	✓	✓
Minimize $\sigma(Q_n)$		✓	✓
Minimize $\sigma(Q_t)$			✓
Number of objectives	1	2	3

deviation of  $Q_n$ . Every objective function has to be written as a minimization, so the objective of maximizing  $C_p$  is written as minimizing  $-C_p$ .

### 6.2.3. Constraints

Lastly, we specify the number of (equality and inequality) constraints. In this study, there are no equality constraints, and every problem has at least one inequality constraint. The inequality constraint that is applied to all the optimization cases ensures that the pitch angle is continuous at  $\theta = 0^\circ$  and  $360^\circ$ . Since equality constraints can be too strict, most algorithms in pymoo cannot handle them efficiently [43]. Therefore, we implement the continuity constraint as an inequality constraint with a small tolerance for the difference between  $\theta_p(0^\circ)$  and  $\theta_p(360^\circ)$ . Since the pitch function is a sinusoid, it will also be differentiable/smooth.

More inequality constraints are added depending on the optimization case. For the two-objective case, it is required that  $C_p$  is larger than the base case (zero pitch)  $C_{p,0}$  and that the normal load fluctuations are less than those of the base case:

$$-C_p + C_{p,0} \leq 0 \quad (6.3)$$

$$\sigma(Q_n) - \sigma(Q_{n,0}) \leq 0 \quad (6.4)$$

where the 0 index denotes the base case. We add these constraints because we are only interested in solutions which improve the operation of the turbine compared to the base case. We would like to increase the turbine's power coefficient while not compromising its structural integrity, and, we would like to decrease the fluctuations the turbine experiences in structural loads without sacrificing power generation. If a solution decreases  $C_p$  or increases normal load fluctuations compared to the base case, it is not useful from an operational point of view. The constraints allow us to limit the search space to interesting solutions. From a computational perspective, these constraints were necessary to avoid the optimal solutions which were obtained which decrease  $C_p$  compared to the base case. The optimization algorithm continued to search for solutions in that region, which hindered the convergence of the algorithm. With these two additional constraints, there are three inequality constraints total. A similar constraint on  $C_p$  could be added for the single-objective (maximize  $C_p$ ) case, but it is not necessary given there is only one direction (the  $C_p$  axis) to search along. The optimization algorithm has no problem finding solutions which increase  $C_p$  compared to the base case. For the three-objective case, a fourth inequality constraint is added for a similar purpose: we are only interested in solutions which decrease the torque fluctuations compared to the base case. The two constraints from the two-objective case are also applied, and the fourth constraint is:

$$\sigma(Q_t) - \sigma(Q_{t,0}) \leq 0 \quad (6.5)$$

Note that adding these constraints can be confused with the classical  $\epsilon$ -constraint multi-objective optimization method (see Section 4.1). However, we are still using a genetic algorithm to solve the MOOPs, because importantly, there are still multiple objectives. The problems are not being turned into single-objective problems. Using the  $\epsilon$ -constraint method for example for the two-objective optimization case would result in a single solution with the maximum  $C_p$  but with normal load fluctuations just below the base case value. Other solutions which improve  $C_p$  over the base case and reduce the load fluctuations more compared to the base case would only be found if the value of  $\epsilon$  is sequentially changed, and the optimization problem is re-solved, in order to get multiple solutions. Our (constrained) genetic algorithm finds many Pareto-optimal solutions that do not violate the constraints at once.

## 6.3. Optimization Algorithm and Parameters

Next, we define the optimization algorithm which is used and its parameters. We use the unified non-dominated sorting genetic algorithm III (U-NSGA-III) for all optimization cases (see Section 4.3). Since we have problems ranging from one to three objectives, this provides consistency in the optimization method. Furthermore, using U-NSGA-III makes the methodology more flexible to adding more objectives. More objectives can be added easily in future research without changing the algorithm implementation. We would not be limited to three objectives, as would be the case if, for example, NSGA-II were used because NSGA-II does not scale up well to many-objective problems [33].

We use many of the default parameters for U-NSGA-III in pymoo [43]. The optimal parameters used in a genetic algorithm depend on the problem [57] and they "interact in a complex way" [58], meaning that the optimal values of the parameters also depend on each other. Moreover, the parameters can impact the solution of the genetic algorithm. Finding the optimal parameters is generally challenging and computationally expensive. Performing parameter optimization would involve an extensive study which is outside the scope of the present study. Instead,

we set parameter values based on the literature. Furthermore, while dynamic parameters—that is, parameters that vary during the optimization run—can improve the performance of the genetic algorithm [57]–[59], we use static parameters which are defined at the beginning of the optimization code, and do not change, for simplicity. The basic parameters we need to determine are: population size, crossover probability, crossover distribution index, mutation probability, mutation distribution index, and the number of generations.

### Population Size

We set the population size to  $N_{pop} = 100$ , which is a moderate population size. The population size needs to be large enough for the genetic algorithm to find good solutions. A larger population size leads to higher accuracy of the solution generated by the genetic algorithm [58]. That is, it is more likely to find the optimum solution for a single-objective problem or a better Pareto-optimal front for multi-objective problems. Therefore, a larger population size is favorable. However, a larger population also means an increase in computation time. A larger population also slows the convergence of the genetic algorithm, requiring a higher number of generations to reach convergence. In an extensive literature review on genetic algorithm parameters done by Hassanat *et al.* [58], a population size of 50 or 100 was common. A few studies use other population sizes below 50 (small) and some other studies use a population size of multiple hundreds (large), while one study went up to  $N_{pop} = 4000$ . In other literature studies of VAWT pitch control which utilize a genetic algorithm, the population size is on the smaller side. Li *et al.* [25] used  $N_{pop} = 20$ ; Hwang *et al.* [20] used  $N_{pop} = 32$ ; Le Fouest and Mulleners [5] used  $N_{pop} = 60$ ; and Paraschivoiu *et al.* [9] used  $N_{pop} = 100$ . In order to strike a balance between accuracy and computation time, we choose to use a moderate population size of  $N_{pop} = 100$ . This is at the upper end of other VAWT pitch control literature, but ensures that we will obtain optimal solutions while still being computationally manageable. Additionally, the population size should be a multiple of four [33], which  $N_{pop} = 100$  satisfies. We decide to specify the population size in the optimization algorithm because the default in pymoo is a population size equal to the number of reference directions [43]. Specifying the population size allows us to define the population based on the literature and keep it consistent across the optimization cases. Lastly, the number of offspring is set to the default, making it equal to the population size. Thus, the population size remains the same from generation to generation.

### Selection, Crossover, and Mutation

The sampling technique used to make the initial population at the beginning of the simulation is the default float random sampling. As the name implies, the individuals are generated by randomly sampling a floating point number for each variable. After the initial generation, the crossover and mutation operations help create the next generation. Both operations should be used because it leads to better results than the use of only one operator [58]. The parents are selected via tournament selection, which is the default in pymoo and part of the U-NSGA-III algorithm as explained in Section 4.3.

Crossover between two parents to create offspring can be executed in several different ways. For example, point crossover, uniform crossover, and simulated binary crossover [43]. We use the default simulated binary crossover (SBX) for U-NSGA-III in pymoo. SBX is based on single-point crossover for binary variables [60], in which the bits beyond the selected crossover point in the decision variable vector are switched between the two parents, creating two offspring [58]. SBX “simulates the operation” which is performed for binary-valued variables onto real-valued variables [60]. SBX requires two parameters: a crossover probability,  $p_c$ , and a crossover distribution index,  $\eta_c$  [61]. The crossover probability determines how likely it is for crossover to occur between two parents [58]. A high crossover probability means it is more likely for crossover to occur, so new individuals will be created from the parents, which generally promotes diversity and exploration of the search space. However, the effect of crossover on diversity, fitness, and convergence depends on the diversity of the parent population [62], [63]. A low crossover probability means it is less likely for crossover to occur, so it is more likely that the parents remain unchanged into the next generation. In Hassanat *et al.* [58]’s literature review, a crossover probability of 0.8 or 0.9 was common. Deb and Agrawal [64] apply SBX with a crossover probability of 0.9. With the literature as guidance, we adopt a value of  $p_c = 0.9$ .

The crossover distribution index in SBX,  $\eta_c$ , defines the probability distribution used to create the offspring [59], [61]. It controls the spread of the offspring solutions around the parent solutions. It can be any non-negative value. A large value of  $\eta_c$  makes the distribution narrower, meaning the offspring are kept near the parents [59], [61], [64]. A small value of  $\eta_c$  allows the offspring to be far from the parents. Deb and Agrawal [60] use values of  $\eta_c$  from 2 to 5, which according to the authors are moderate values of  $\eta_c$ . The default value of  $\eta_c$  in pymoo for the U-NSGA-III algorithm is 30, which is relatively high. To strike a balance in the spread of the offspring, we choose  $\eta_c = 5$ . This is the upper end of Deb and Agrawal [60]’s range, but considerably below the default pymoo value.

The mutation of an individual can also be implemented in several different ways. For example, random mutation, Gaussian mutation, or polynomial mutation [65]. We use the default polynomial mutation (PM) for U-NSGA-III in pymoo. PM perturbs the value of a parent’s decision variable(s) in the vicinity of the parent’s value, according to a polynomial probability distribution, in order to create a new offspring [65]. PM requires two parameters: a mutation probability,  $p_m$ , and a mutation distribution index,  $\eta_m$ . The mutation probability determines how likely it is for an individual to be mutated. A high mutation probability means it is more likely for mutation to occur. Mutation helps maintain the diversity of the population and avoid local optima [58], [65]. However, a mutation probability that is too high turns the genetic algorithm into a random search. A low mutation probability means it is less likely for mutation to occur, so it is more likely that an individual is unchanged into the next generation. A low mutation probability results in less exploration of the search space. In the literature, a low mutation probability is common. For example, 0.01-0.1 in Hassanat *et al.* [58]’s literature review.  $p_m = 0.001$  is also used by some authors. Hassanat *et al.* [58] reference a study by Schlierkamp-Voosen [66] in which a mutation probability of  $p_m = 1/n_{var}$  is suitable, where  $n_{var}$  is the number of decision variables. This corroborates with Deb and Deb [65]’s study where  $p_m$  equals  $0.5/n_{var}$  to  $1.5/n_{var}$ . Therefore, using the guideline  $p_m = 1/n_{var}$ , since there are 8 decision variables, we have  $p_m = 1/8 = 0.125$ , which we round down to  $p_m = 0.1$ , considering the practice that  $p_m$  is usually small.

The mutation distribution index in PM defines the probability distribution used to create the mutated offspring. It controls how far away a decision variable can be perturbed from the parent’s value. It can be any non-negative value. A larger value of  $\eta_m$  makes the distribution narrower, meaning the variable is perturbed less far from the parent [64]. A higher  $\eta_m$  was found to lead to faster convergence. A small value of  $\eta_m$  means the variable can be perturbed farther from the parent. Deb and Deb [65] reference a study by Deb and Agrawal [64] in which a suitable  $\eta_m$  is 20-100 for most problems, but this could not be independently verified in the source. The default value in pymoo is  $\eta_m = 20$ . In their own study, Deb and Deb [65] found that  $\eta_m$  from 100-150 is suitable. Therefore, we choose the middle value of  $\eta_m = 100$  for our study.

Table 6.3 summarizes the parameters used in the implementation of U-NSGA-III as discussed above: the population size, crossover probability, crossover distribution index, mutation probability, and mutation distribution index.

**Table 6.3:** Parameters used in the genetic algorithm for all optimization cases.

Parameter	Value
Population size	100
Crossover probability	0.9
Crossover distribution index	5
Mutation probability	0.1
Mutation distribution index	100

### Number of Generations

The number of generations is an important parameter in genetic algorithms. It can be determined by the termination criterion, or it can be the termination criterion itself. In general, a larger number of generations is preferred to ensure accuracy of the solution. In this study, we do not use the number of generations as the termination criterion. Instead, the final number of generations used is determined by a termination criterion in the objective space, as discussed in Section 6.4. The number of generations differs among the optimization cases (Table 6.4). As the number of objectives increases, more generations are needed before the simulation converges. For the single-objective case, the number of generations is 89. For the two-objective case, the number of generations is 200. For the three-objective case, the number of generations is 396. For comparison, Hwang *et al.* [20] only used 15 generations for their genetic algorithm. Le Fouest and Mulleners [5] found convergence based on the generational distance after 17 and 27 generations (for the off- and on-design conditions, respectively) but ran the optimization algorithm for some generations longer. Li *et al.* [25] used 50 generations and showed that the optimization converged. Paraschivoiu *et al.* [9] used 1,500 generations, which is a very large number. Thus, the number of generations used in this study are significantly higher than those used by Hwang *et al.* [20], Le Fouest and Mulleners [5], and Li *et al.* [25], but much less than the number of generations used by Paraschivoiu *et al.* [9]. However, we are confident that we do not need more generations to obtain better solutions because the number of generations was determined based on convergence in the objective space. Since there are 100 individuals per generation, this results in 8,900, 20,000, and 39,600 total function evaluations for the single-, two-, and three-objective optimization cases, respectively.

**Table 6.4:** Number of generations and function evaluations for each optimization case.

Parameter	Case 1	Case 2	Case 3
Number of generations	89	200	396
Total function evaluations	8,900	20,000	39,600

### Reference Directions

Next we define the reference directions. In the case that there is only one objective, then there is only one reference direction, which is defined as the vector  $\mathbf{1}$ . Otherwise, we use the Das-Dennis approach to create the reference directions (see Section 4.3.1) [44], [45]. In the Das-Dennis approach, we change the parameter  $P_H$  (the number of partitions) according to the optimization case. The number of partitions differs based on the optimization case because the optimization cases have different numbers of objectives, and the number of resulting reference directions,  $H$ , depends on the number of objectives and the number of partitions, according to Equation 4.1 [44]. We also keep in mind that the population size  $N_{pop}$  must be greater than  $H$ . For multi-objective problems (2-3 objectives), generally  $N_{pop}/H > 1$ , whereas for many-objective problems (4+ objectives), generally  $N_{pop}/H \approx 1$  [33]. Recall that  $H$  is also the number of optimal solutions which will be generated by the genetic algorithm.

With the above in mind, we determine  $P_H$  for each optimization case. For the two-objective case, we use  $P_H = 59$  so that there are  $H = 60$  reference directions. This is based on a parameter study of  $P_H$  where we executed the two-objective optimization case with different numbers of reference directions and evaluated the hypervolume (the area dominated by the optimal solutions). Ideally, the hypervolume would converge to a maximum value as the number of reference directions increases. However, as seen in Figure 6.3, the hypervolume increases at a decreasing rate until  $H = 60$ . From  $H = 70$  to 90 reference directions, the hypervolume is unstable. The maximum number of reference directions there can be is  $H = 100$  (the population size). However, it is not desired to obtain 100 solutions because 100 solutions is too many. Obtaining too many optimal solutions is not beneficial from a practical standpoint, because ultimately, one optimal solution (pitch function) must be implemented. When comparing the solutions with  $H = 60$  vs.  $H = 100$  reference directions, the Pareto front is similar. The percent difference in the hypervolume between  $H = 60$  and  $H = 100$  reference directions is only 0.21%. Thus, the solution space can be equally-well represented with 60 solutions/reference directions, and there is no gain from finding more solutions. Visually,  $H = 60$  also provides a good density of the Pareto front. From this analysis, we choose  $H = 60$  reference directions. For the three-objective optimization case, we set  $P_H$  so that  $H$  is relatively the same, within the constraints of Equation 4.1. Therefore, we use  $P_H = 10$  partitions, so that there are  $H = 66$  reference directions.

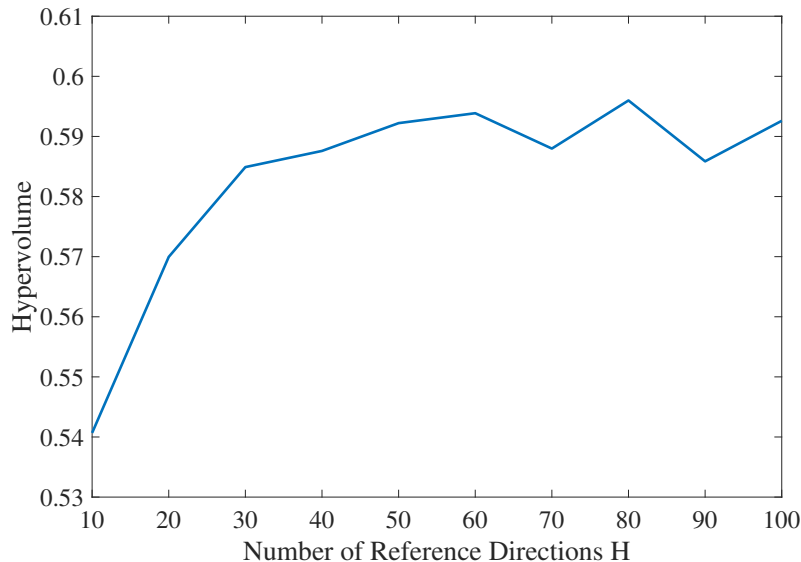


**Figure 6.3:** Parameter study to determine the number of partitions,  $P_H$ , and therefore the number of reference directions,  $H$ . The two-objective optimization case was run with  $H = 10, 20, 30, 40, 50, 60, 70, 80, 90$ , and 100.

## 6.4. Optimization Problem Execution and Analysis

When the optimization problem is solved, the optimization algorithm needs a termination criterion. The termination criterion can be defined in many different ways. For example, based on the number of total function evaluations, number of generations, run time of the optimization code, or convergence in the decision variable space or objective function space (for example using the generational distance as done by Le Fouest and Mulleners [5]) [43]. We use a termination criterion based on convergence in the objective space. In the single-objective case, the value of  $C_p$  is used to determine convergence, while in the multi-objective cases, since there is no single objective value, the hypervolume is used to determine convergence. For each generation, the change in  $C_p$  or hypervolume is calculated as a percentage relative to the previous generation. Once the percent change in  $C_p$  or hypervolume is less than 0.01% for five consecutive generations, the optimization procedure is ended. Since the hypervolume cannot be directly used as the termination criterion in pymoo, the optimization code was run for many generations and the termination criterion was applied thereafter to determine the last generation. This resulted in 89, 200, and 396 generations to convergence for the single-, two-, and three-objective optimization cases, respectively. The convergence plots for each optimization case are shown in Chapter 8 and they confirm that the termination criterion yields converged results because there is very little change in the  $C_p$  or hypervolume for many generations near the end of the simulation.

Finally, the optimization (minimization) problem can be solved. pymoo returns the optimization results which include the optimum decision variables and objective function values, which can then be plotted and analyzed. We also analyze the performance of the optimization algorithm considering several indicators. First, we look at the constraint violation and when a feasible solution is first found. For the single-objective case, we look at the convergence of the objective value ( $C_p$ ) between generations. When the difference in  $C_p$  becomes small for many consecutive generations, we can be confident that the algorithm has converged (this is also the termination criterion).

For the two- and three-objective optimization cases, we do a visual check of the Pareto front to see that it covers the objective space well and there is good diversity in the solutions. By plotting the initial population alongside the Pareto front in several generations over time and the final Pareto front, we can see the effectiveness of the optimization algorithm in finding better solutions. We also calculate the hypervolume for our multi-objective cases. The hypervolume is the area/volume dominated by the optimal solution set and it represents both convergence and diversity of the solution set [42]. The hypervolume should be maximized, meaning the optimal solution set dominates as much of the objective space as possible. We also look at the change in hypervolume between consecutive generations to make sure the algorithm converged (this is the termination criterion). Lastly, we calculate the generational distance in the multi-objective cases, which is the average distance in the objective space between two Pareto fronts from different generations. Since we do not know the true Pareto front for our optimization problems, we approximate it using the Pareto front in the last generation and calculate the generational distance of each generation with respect to the last generation [43]. We also calculate the generational distance between two consecutive generations [5]. These values provide a picture of how the Pareto front changes over time and how the algorithm converges toward the final solution set. The generational distance should be minimized, meaning there is little remaining change in the Pareto front near the end of the simulation.

# Part III

## Results

## 2D Actuator Cylinder Model Validation

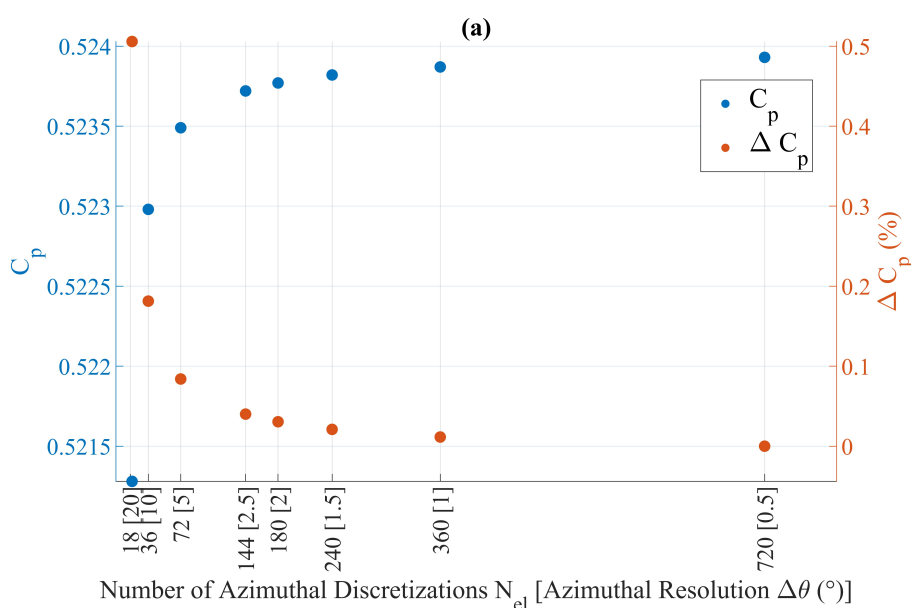
The 2D Actuator Cylinder model implementation was detailed in Chapter 5. This chapter presents the sensitivity analysis of the AC model to several implementation choices, in Section 7.1. Then, in Section 7.2, we verify the model implementation and validate that the AC model can represent VAWT loading. In the analysis, we use case studies with zero pitch, fixed non-zero pitch, and variable pitch. An AC model, a vortex model, a CFD model, and an experiment from the literature are used for comparison.

### 7.1. Model Sensitivity

There are several parameters and settings that have an effect on the model output. This section compares execution of the 2D AC model with these various parameters/settings and outlines the version of the model used in the remainder of this study. In the analysis, the inputs to the model are those used in De Tavernier [4]: 2 blades, radius of 1 m, chord length of 0.1 m, incoming wind speed of 1 m/s, and tip speed ratio of 3. The lift and drag coefficients are  $C_l = 2\pi \sin \alpha$  and  $C_d = 0$ . The pitch angle is zero.

#### Azimuthal Resolution

In the AC model implementation, the actuator cylinder is discretized into  $N_{el}$  sections. This determines the resolution of the model.  $N_{el}$  is inversely proportional to how many degrees is covered in each section,  $\Delta\theta$ . A high  $N_{el}$  means a high azimuthal resolution and a small  $\Delta\theta$ . Figure 7.1 shows the impact of the azimuthal resolution on the power and thrust coefficients. As  $\Delta\theta$  decreases,  $C_p$  becomes marginally larger and  $C_T$  becomes marginally smaller. The values converge asymptotically. Looking at the right axes, which show the percent change in  $C_p$  and  $C_T$ , it is clear that the azimuthal resolution negligibly changes the results. The difference in  $C_p$  between  $\Delta\theta = 5^\circ$  ( $N_{el} = 72$ ) and  $\Delta\theta = 0.5^\circ$  ( $N_{el} = 720$ ) is only 0.084% and that of  $C_T$  is only 0.11%. Furthermore, Figure 7.2 shows the angle of attack, normal



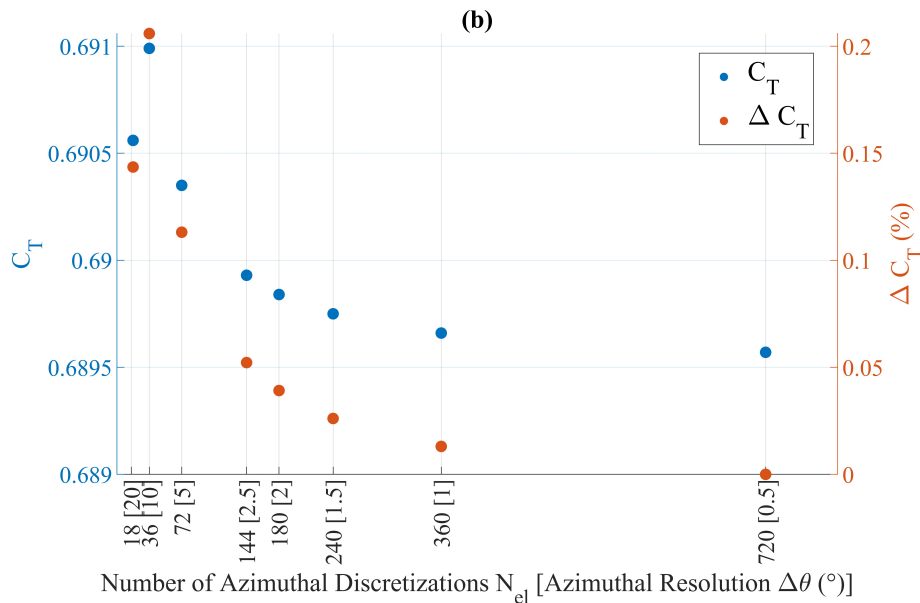


**Figure 7.1:** Azimuthal resolution sensitivity study conducted for the AC model considering eight different discretization levels. (a) Power coefficient  $C_p$  and (b) thrust coefficient  $C_T$ . The right y-axis shows the percent error with respect to  $\Delta\theta = 0.5^\circ$  ( $N_{el} = 720$ ).

force, and tangential force for different values of  $\Delta\theta$ . A limited number of  $\Delta\theta$  are shown for clarity of the figure, since the curves mainly overlap. Other than  $\Delta\theta = 20^\circ$  ( $N_{el} = 18$ ), the results are indistinguishable.  $\Delta\theta = 20^\circ$  has too low of an azimuthal resolution so that corners in the curves are clearly visible. Thus, a discretization of at least  $\Delta\theta = 10^\circ$  ( $N_{el} = 36$ ) should be used.

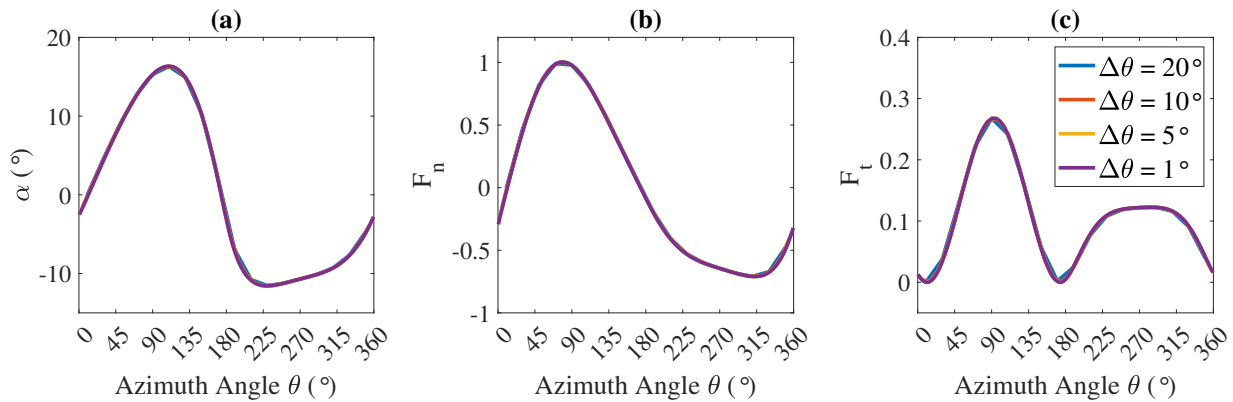


**Figure 7.2:** Azimuthal resolution sensitivity study conducted for the AC model considering eight different discretization levels. (a) Angle of attack, (b) normal force, and (c) tangential force. A limited number of  $\Delta\theta$  are shown for clarity of the figure.

Based on this analysis, an azimuthal resolution of  $\Delta\theta = 5^\circ$  ( $N_{el} = 72$ ) is used in this study. Other authors, including Li [39], Madsen *et al.* [7], and Cheng *et al.* [8] use  $\Delta\theta = 10^\circ$  ( $N_{el} = 36$ ). This value produces results that line up well with those with higher discretizations. We choose to use one level of discretization higher in order to provide a finer azimuthal resolution. This is important because it may be optimal to change the pitch angle more frequently than every  $10^\circ$  around the cylinder. Furthermore, a finer azimuthal resolution is not used considering computation time and the optimization which will be performed. When  $\Delta\theta = 10^\circ$ , the model takes around 0.25 seconds to run (using the Intel i7-1255U processor with speed 1.7 GHz) which is indeed very favorable for optimization in which the model is repeatedly executed. When  $\Delta\theta = 5^\circ$ , the run time is approximately 1 second, which is still manageable for optimization. For  $\Delta\theta = 2.5^\circ$ , each run takes approximately 3.9 seconds, and for  $\Delta\theta = 1^\circ$ , it takes approximately 34.4

seconds—so decreasing  $\Delta\theta$  will make the optimization routine take increasingly longer and longer to run (Figure 7.3). Lastly, it was found that if  $\Delta\theta$  is too small, it leads to issues with the model convergence because the control points are too close together.

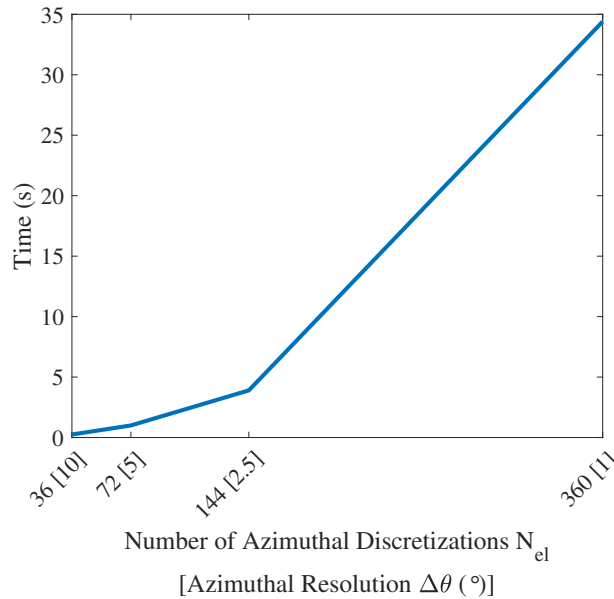


**Figure 7.3:** Computation time of the AC model depending on the azimuthal resolution.

#### Modified Linear Solution and Tangential Force Term

In Section 5.1, we used settings in the AC model based on work from Cheng *et al.* [8]. Namely, 1) the inclusion of the blade tangential force in the calculation of the induced velocities, and 2) an additional correction to  $k_a$  in the modified linear solution for high induction factors. We now study the effect of those implementation choices. Figure 7.4 shows this comparison.

The largest difference between the new modified linear solution (Equation 3.33) [8] and the simple  $k_a = \frac{1}{1-a}$  [7] factor is in the angle of attack and forces in the downwind region. The calculation for  $k_a$  from Cheng *et al.* [8] for  $a > 0.15$  makes the correction factor  $k_a$  smaller than when  $k_a = \frac{1}{1-a}$ . Thus, the modified linear induced velocities are also smaller. Considering the velocity triangle in the downwind region, a smaller induced velocity makes the angle of attack larger (more negative). A larger angle of attack increases the lift coefficient,  $C_l$ , so the normal force and tangential force are also greater. Since the tangential loading increases, the power also increases. Cheng *et al.* [8] adjusted the  $k_a$  factor because they observed that at high tip speed ratios, the simple modified linear solution

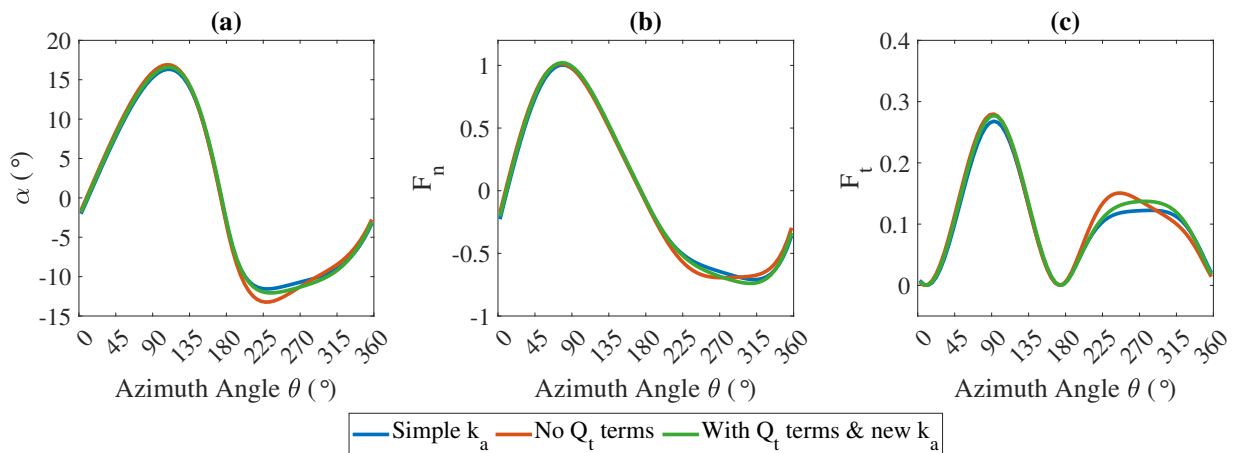


**Figure 7.4:** Effect of including the tangential load terms and/or new modified linear correction  $k_a$  from Cheng *et al.* [8] in the AC model. (a) Angle of attack, (b) normal force, and (c) tangential force.

from Madsen *et al.* [7] underestimates the power coefficient. Using Cheng *et al.* [8]'s new  $k_a$ , the power coefficient increases by 5.5% for the case shown in Figure 7.4. So, the new  $k_a$  factor achieves the desired result. The tip speed ratio in the present case is three, which is not too high, which is probably why only a small difference in Figure 7.4 is observed. While the difference is small, the new modified linear solution from Cheng *et al.* [8] (Equation 3.33) is used in this study because it is more accurate compared to the full (linear and non-linear) solution of the AC, especially for high tip speed ratios.

Whether or not the blade tangential force is included in the calculation of the induced velocities has a greater effect than which equation for  $k_a$  is used. In Figure 7.4, the effect is again particularly seen in the downwind region. The upwind region with and without the  $Q_t$  terms match well, which is also what Cheng *et al.* [8] found. Including the tangential load terms makes the average normal and tangential forces in the downwind region a little smaller. This is in agreement with what Cheng *et al.* [8] observed. We also observe a shift in the loading between  $\theta = 225^\circ$  and  $315^\circ$  azimuth angle. Including the tangential load terms decreases the angle of attack in the downwind region from about  $\theta = 180^\circ$ - $270^\circ$  which decreases the lift and drag forces, and so also the magnitude of the normal and tangential forces. In the downwind region after  $\theta = 270^\circ$ , the angle of attack with the inclusion of the tangential load terms is slightly larger than that without the tangential load terms. Accordingly, the normal and tangential forces are also larger with the tangential load terms than without. The overall net reduction in loading leads the power coefficient  $C_p$  to decrease by 1.13% for this case compared to excluding the  $Q_t$  terms. We conclude that the effect of including the tangential loads when calculating the induced velocities is small and mostly evident in the downwind region. For the remainder of this study, the  $Q_t$  terms are included because it is the more complete formulation and does not add to computational cost.

### Control Point Shifting

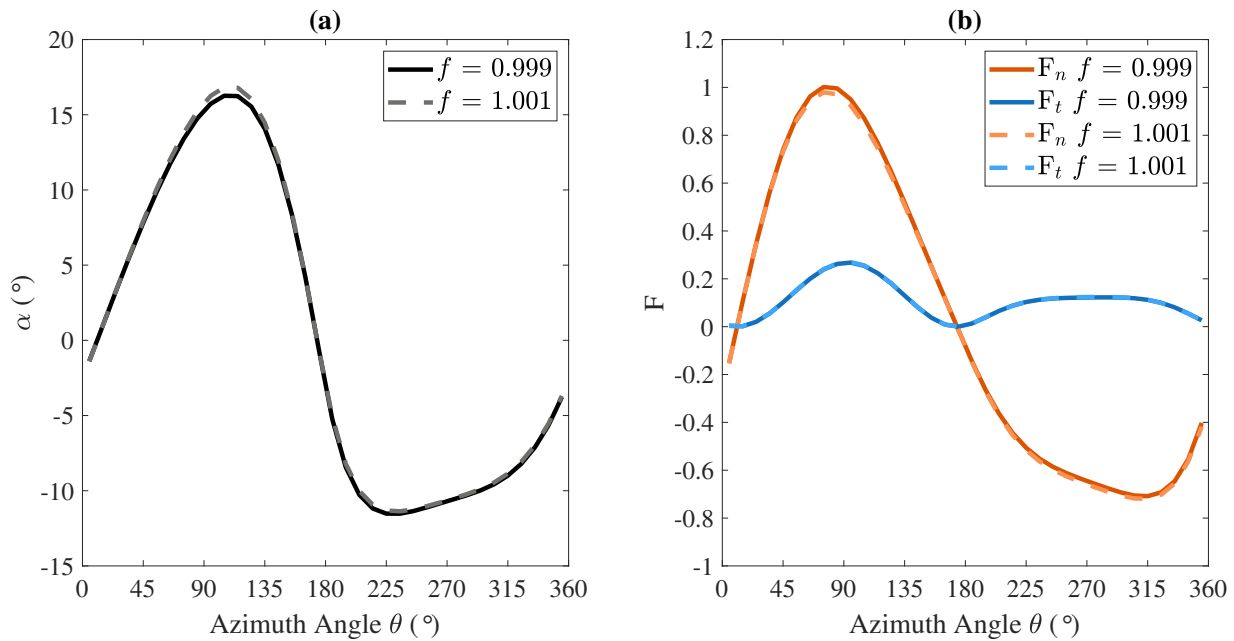
The scaling factor  $f$  is used to move the control points slightly outside ( $f > 1$ ) or inside ( $f < 1$ ) the actuator cylinder to deal with singularity issues in Equation 5.3 (see Section 5.1). Whether the control points are outside or inside the cylinder determines which extra terms are added in the linear solution to the AC (Equation 3.29). Li [39] uses  $f > 1$ , so the control points are just outside the cylinder. However, in the model implementation used here, this leads to a complication because the contribution of the tangential load terms is included. When the control points are outside the cylinder, and  $N_{el}$  is sufficiently large, then the y-value (absolute value) of the control points near the top and bottom of the cylinder is greater than 1. This causes issues in Equation 3.29 because it makes the square root  $\sqrt{1 - y^2}$  not a real number. To avoid this issue, we move the control points inside the cylinder by setting  $f = 0.999$ .

Figure 7.5 shows the forces and angle of attack calculated by the AC model with  $f > 1$  and  $f < 1$ . In this case,  $N_{el} = 36$  so that all control points have a real solution. There are a few points where the curves differ slightly. In the angle of attack, there is a small difference in the upwind region. When  $f = 1.001$ , the control point is in front of the cylinder so no extra loading terms are added in the induced velocity. The induced velocity is therefore smaller, which changes the relative velocity  $V_{rel}$  such that  $\alpha$  is larger, compared to when  $f = 0.999$ .

Looking at the normal force, when  $f = 1.001$ , the normal force in the upwind region is slightly less than when  $f = 0.999$ . This is because when  $f = 1.001$ , the control points are in front of the cylinder so the flow has not yet crossed the actuator surface and no extra loading terms are added. In the downwind region, the normal force when  $f = 1.001$  is slightly greater (more negative) than when  $f = 0.999$ . When the control point is outside the cylinder ( $f = 1.001$ ) as opposed to inside, the actuator cylinder is crossed for a second time and the wake terms need to be added. When the actuator cylinder is crossed, more energy is extracted from the flow and more force is put on the blade.

The tangential force is the same throughout the revolution. In the middle of the upwind and downwind regions, the tangential force is aligned with the y-direction, which has the same calculation for the induced velocity no matter  $f$  and the region (in front, inside, or in the wake). Near the top and bottom of the cylinder, the tangential force is aligned with the x-direction, and the normal and tangential forces,  $Q_n$  and  $Q_t$ , are relatively small, so the addition of the \*\* terms has no noticeable effect. This makes sense because the points at the top and bottom of the cylinder are not technically in the wake region.

With respect to the power and thrust coefficients, when  $f = 1.001$ ,  $C_p$  increases by 0.633% and  $C_T$  decreases by 0.272%, compared to  $f = 0.999$ . These are very small differences. Overall, when comparing the results for  $f = 0.999$  and  $f = 1.001$ , the differences are small, so the choice of  $f$  should not impact the pitch angle optimization.



**Figure 7.5:** Sensitivity of the AC model to the scaling factor  $f$  used to shift the control points slightly inside ( $f = 0.999$ ) or outside ( $f = 1.001$ ) the cylinder. (a) Angle of attack and (b) normal and tangential forces. The model was run with  $N_{el} = 36$ .

In Section 5.1, we implemented a relaxation factor in the code to aid with convergence. To confirm that our choice of 0.3 does not impact the results, we ran several test cases. We varied the relaxation factor from 0, 0.05, 0.1, 0.3, 0.5, 0.7, 0.9, and 0.95, and tested both a moderate and high value of  $N_{el}$ . There is no effect on the model's solution, as long as the relaxation factor is not 1. The power coefficient  $C_p$ , thrust coefficient  $C_T$ , angle of attack  $\alpha$ , normal force  $F_n$ , and tangential force  $F_t$  are exactly the same. There is also no discernible trend on the computation time with changing relaxation factor.

### 7.1.1. Final Model Settings

In summary, the 2D AC model as used in this study has the following features:

- Azimuthal discretization  $N_{el} = 72$  ( $\Delta\theta = 5^\circ$ )
- $f = 0.999$  (control points inside the cylinder)
- Tangential force terms included when calculating the induced velocities
- New modified linear solution from Cheng *et al.* [8] (Equation 3.33)

## 7.2. Model Verification and Validation

In order to verify that the AC model was implemented correctly in the computer code, results are compared to several cases in the literature. Cases are also presented to validate whether the 2D AC model is an accurate representation of reality (e.g. if the loads calculated from the model are what a real VAWT blade experiences). The analysis is done considering zero pitch, fixed non-zero pitch, and variable pitch. The final model settings in Section 7.1.1 are used in the model verification and validation, unless explicitly mentioned otherwise. Recall also from Section 5.1.1 that the AC model does not model dynamic stall, flow curvature, or blade-vortex interaction.

### 7.2.1. Zero Pitch

First, we will look at the very simple case with no pitching of the blades. Figure 7.6 compares the output of the 2D AC model implemented in this study to results from De Tavernier [4]. The set-up is for a 2-bladed turbine with a radius of 1 m and chord length of 0.1 m. Its rotational speed is 3 rad/s and the incoming wind velocity is 1 m/s. Thus, the tip speed ratio is 3. The lift and drag polars are  $C_l = 2\pi \sin \alpha$  and  $C_d = 0$ . In the AC model, the modified linear solution is calculated using  $k_a = \frac{1}{1-a}$ , instead of Cheng *et al.* [8]'s version with the adapted  $k_a$  factor for large induction factors (Equation 3.33), although elsewhere in De Tavernier [4], the version from Cheng *et al.* [8] is used.

As can clearly be seen in Figure 7.6, the output from our model matches De Tavernier [4]’s. This therefore verifies that the 2D AC model code was implemented correctly.

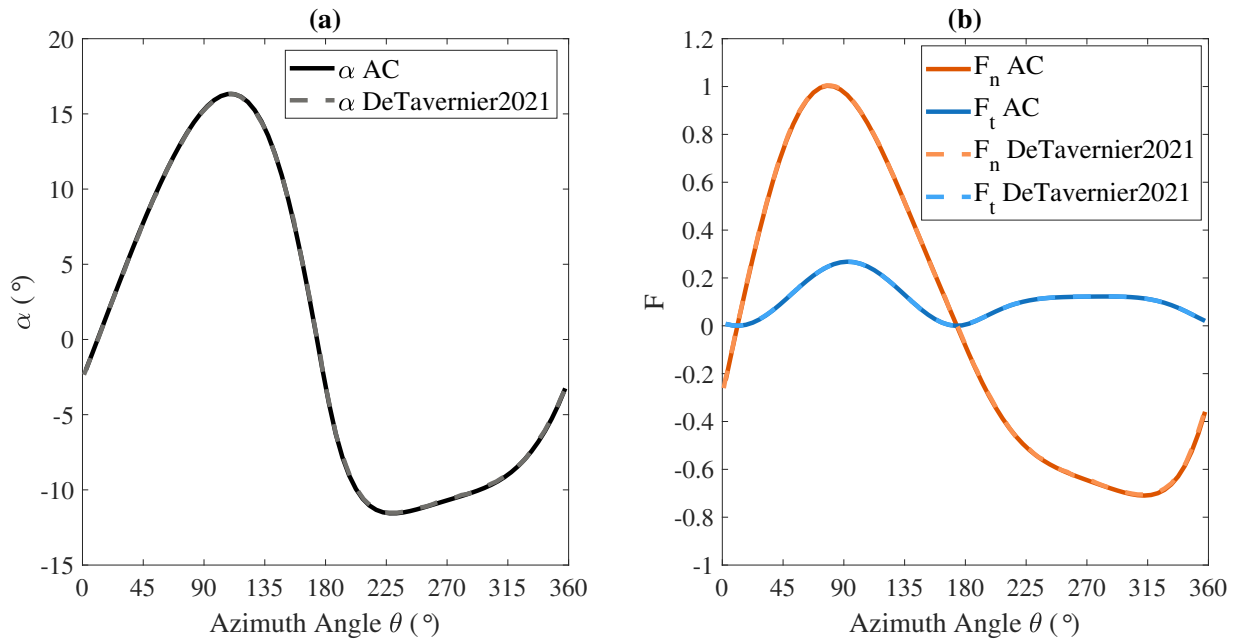


**Figure 7.6:** AC model compared to AC model results in De Tavernier [4]. (a) Angle of attack and (b) normal and tangential forces for  $0^\circ$  constant pitch.  $B = 2$ ,  $R = 1$  m,  $c = 0.1$  m,  $\lambda = 3$ , and  $V_\infty = 1$  m/s. The airfoil polars are  $C_l = 2\pi \sin \alpha$  and  $C_d = 0$ .

De Tavernier and Ferreira [30] also present results from the 2D AC model with zero pitch angle. The turbine radius is 1 m and the rotor solidity is 0.1. Assuming that the turbine has 3 blades, this yields a chord length of 0.0667 m. While the number of blades is not explicitly mentioned, it is assumed from the figures in [30] that  $B = 3$ . In the end, the results ( $Q_n$  and  $Q_t$ ) are normalized by the number of blades so this assumption does not affect the model verification. Additionally,  $V_\infty$  is not specified by the authors, but the results are also normalized by  $V_\infty$ , so this similarly does not affect the model verification. A value of  $V_\infty = 1$  m/s is assumed to execute the AC model. The tip speed ratio is 3. The airfoil polars are  $C_l = 1.1 \cdot 2\pi\alpha$  and  $C_d = 0$ , which are different from the previously-analyzed case in De Tavernier [4]. The 2D AC model is run without the inclusion of the tangential force terms and without the modified linear correction  $k_a$  from Cheng *et al.* [8]. However, the authors imply that both the tangential force terms and the modified linear correction from Cheng *et al.* [8] are used. The authors use  $N_{el} = 42$ , but we continue to use  $N_{el} = 72$  to verify that the model implementation used in this study can reproduce results from other studies. As was shown in Section 7.1, this difference in  $N_{el}$  has negligible impact on the results. Figure 7.7 shows the results from our AC model implementation compared to the results from De Tavernier and Ferreira [30], with respect to the angle of attack, normal loading, and tangential loading. We again see very good agreement and this verifies that the AC model is implemented correctly and that it can be applied accurately with slightly different model settings than the previously-discussed case from De Tavernier [4].

We validate the AC model against numerical results from a vortex model implemented in QBlade. We do so using the base case (zero pitch) Sandia 34-m turbine used for the pitch optimization in this study (see Section 5.2). QBlade is a software that implements a free wake vortex model, and they have model files for several wind turbines available for download [31]. We downloaded the Sandia 34-m VAWT file and ran the simulation corresponding to our operating conditions ( $\lambda = 4$ ,  $V_\infty = 4.0659$  m/s) in QBlade. We ran the aerodynamic model only (e.g. excluding the turbine structural model), and dynamic stall was not modeled, to be consistent with the AC model. The QBlade model considers the 3D  $\Phi$ -shaped rotor, and we extracted the angle of attack and force data at the mid-span. The AC model uses the corresponding turbine inputs at the mid-span: 2 blades, chord of 0.91 m, radius of 16.774 m, and the SNL 0018/50 airfoil polars for  $Re = 1 \times 10^6$  downloaded from QBlade. Figure 7.8 shows the comparison between the models’ calculations. The AC model corresponds relatively well with QBlade. The AC model captures the trends in the angle of attack and forces. The values of the angle of attack throughout the upwind half match very well. The models also have similar peaks (maxima/minima) in the loading. The main difference in the angle of attack is

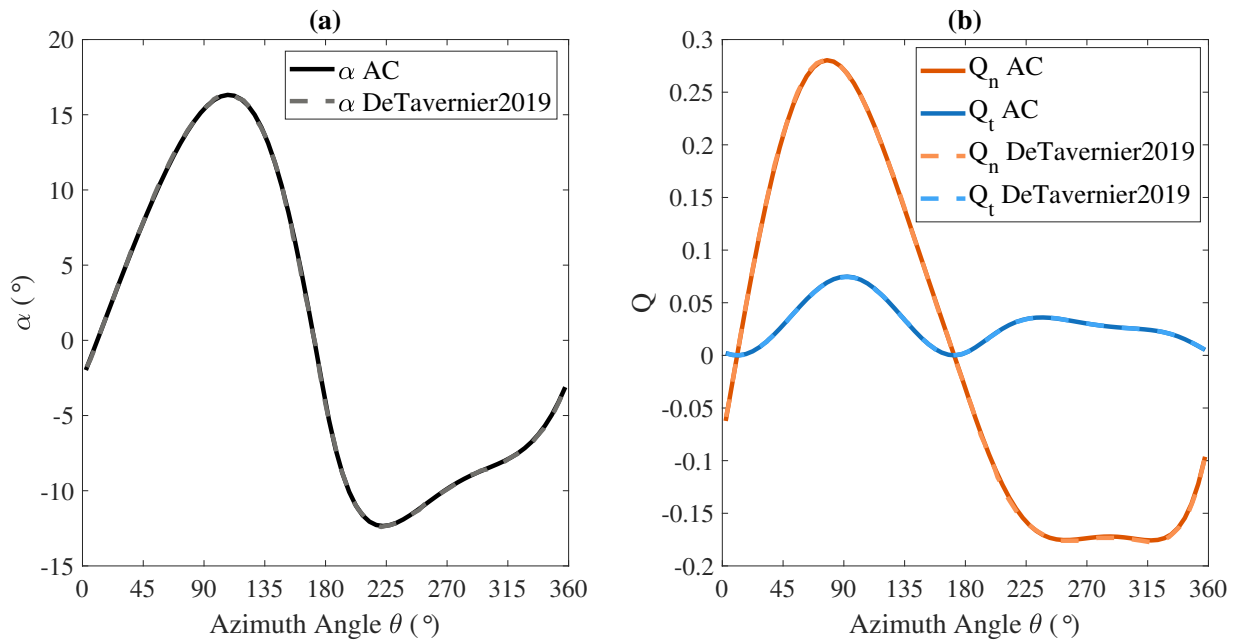


**Figure 7.7:** AC model compared to AC model results in De Tavernier and Ferreira [30]. (a) Angle of attack and (b) normal and tangential forces for  $0^\circ$  constant pitch.  $B = 3$ ,  $R = 1$  m,  $c = 0.0667$  m,  $\lambda = 3$ , and  $V_\infty = 1$  m/s. The airfoil polars are  $C_l = 1.1 \cdot 2\pi\alpha$  and  $C_d = 0$ .

downwind. This is most likely because in the downwind half, the flow field, and therefore the angle of attack, is influenced by the passage of the blade in the upwind half. The flow field calculated by QBlade and the AC model are different because the induced velocities are calculated in different ways. QBlade also considers a 3D flow field whereas the AC model is 2D. The differences in the forces are not major and can be expected considering two different models were used. This validates the use of the AC model in the present study.

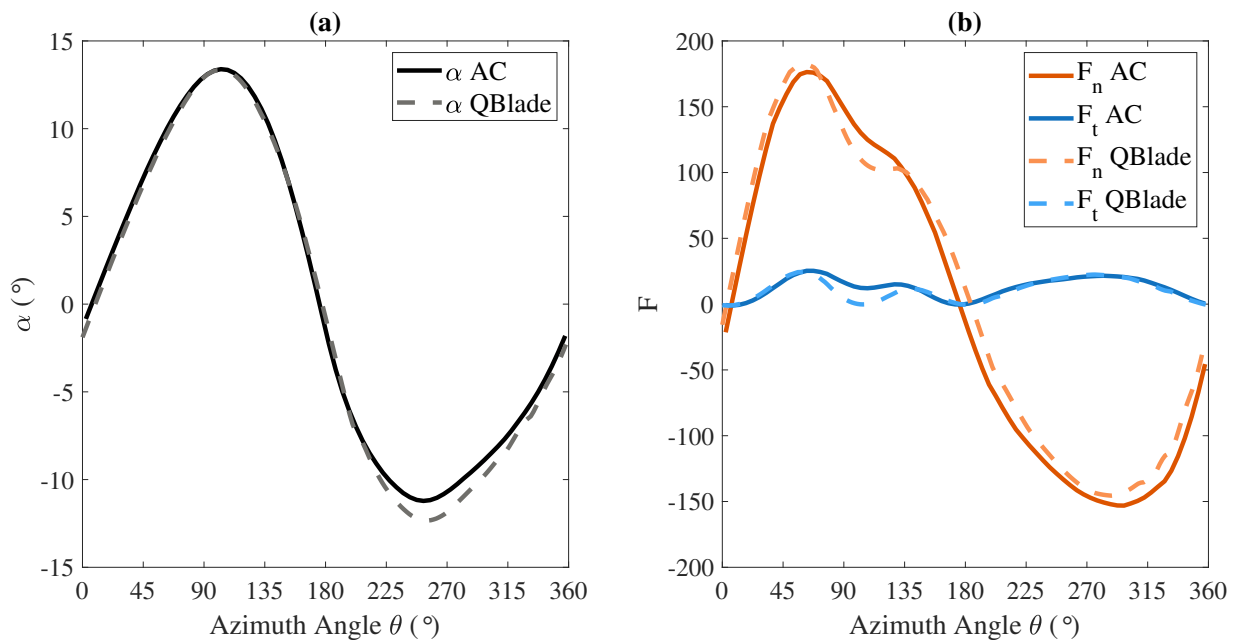


**Figure 7.8:** AC model compared to results for the Sandia 34-m turbine generated in QBlade (free wake vortex model) [31]. (a) Angle of attack and (b) normal and tangential forces for  $0^\circ$  constant pitch.  $B = 2$ ,  $R = 16.774$  m,  $c = 0.91$  m,  $\lambda = 4$ , and  $V_\infty = 4.0659$  m/s. The Reynolds number is  $1 \times 10^6$  and the corresponding SNL 0018/50 airfoil polars are from QBlade [31].

Figure 7.9 shows the comparison of the 2D AC model to an experiment by LeBlanc and Ferreira [14]. The authors used particle image velocimetry (PIV) to measure the flow velocity field around a VAWT and used those measurements to calculate the normal and tangential blade forces. The experiment was conducted for three constant pitch angle cases ( $0^\circ$ ,  $5^\circ$ , and  $-5^\circ$ ) and measured at six azimuthal positions (three upwind and three downwind). Figure 7.9 compares the  $0^\circ$  pitch case. The experimental VAWT has two NACA 0021 blades, a diameter of 1.48 m, height of 1.508 m, and chord length 0.075 m. The turbine is operated at a tip speed ratio of 4 with incoming wind speed of 4 m/s. The airfoil polars used in the 2D AC model execution are calculated using XFOIL for a NACA 0021 airfoil and Reynolds number 80,000.

The results from the AC model in Figure 7.9 show similar trends in loading to the experimental data while overestimating the normal load in the downwind half. The tangential force coefficient in particular lines up well. The tangential force is mostly positive and peaks near  $\theta = 90^\circ$  in the upwind region. According to LeBlanc and Ferreira [14], the calculated tangential load is sensitive to accurately measuring the thin wake of the airfoil, though we see good agreement between the results. Regarding the normal load, in the downwind region, it is negative and relatively consistent. It has a lower magnitude than it does upwind because the relative wind velocity is lower downwind. The normal load in the upwind region is similar to the experimental results. It is positive and first increases then decreases after  $\theta = 90^\circ$  as the blade retreats from the incoming wind. In Figure 7.9, we notice that the peak in the normal load calculated by the AC model is a little higher and shifted earlier than the peak normal load from the experiment. This could be due to the fact that the  $C_l$ - $\alpha$  curve from XFOIL is too steep so the lift and normal forces would be overestimated. Since the experiment is conducted at a low Reynolds number, the airfoil polars obtained from XFOIL are inaccurate [46], as explained further in Appendix B. Therefore, the unreliable polars used as input to the AC model impact the AC forces shown in Figure 7.9.

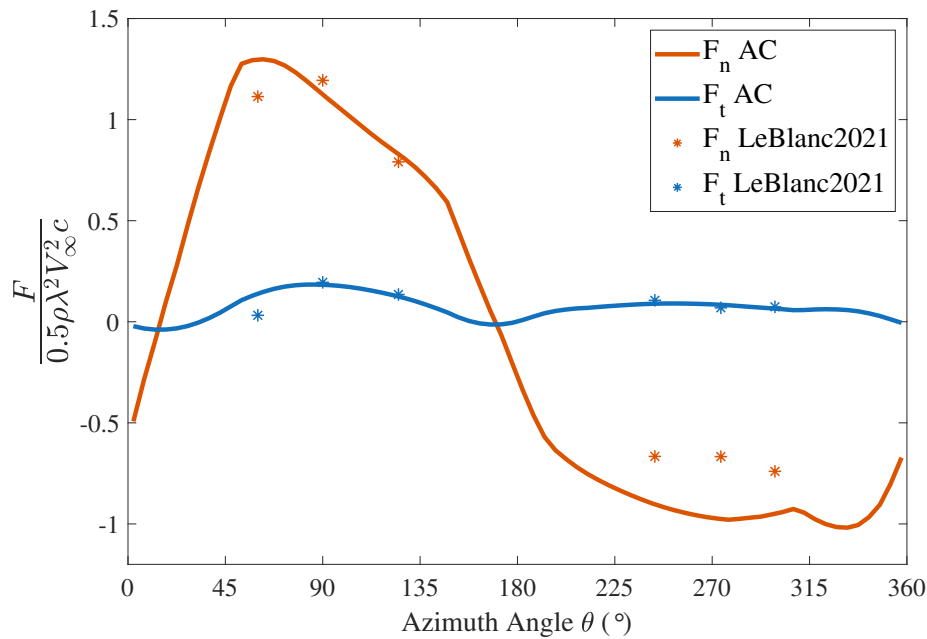


**Figure 7.9:** AC model compared to PIV experimental results in LeBlanc and Ferreira [14]. Normal and tangential force coefficients for  $0^\circ$  constant pitch.  $B = 2$ ,  $D = 1.48$  m,  $c = 0.075$  m,  $\lambda = 4$ , and  $V_\infty = 4$  m/s. The Reynolds number is 80,000 and the airfoil is NACA 0021.

The largest difference between the experimental and model results is in the normal loading downwind. The AC model overpredicts the normal force coefficient. This is likely because the AC model does not model blade-vortex interaction nor tower shadow, which do occur in the experiment and impact the inflow conditions downwind and thus the force on the blade. The difference can also be due to the fact that the airfoil polars used for the AC model overestimate the lift coefficient in the linear region, thus resulting in a greater lift force and so also a greater normal force. There is a corner in the normal loading predicted by the AC near  $\theta = 310^\circ$ . This is because there is also a corner (sudden change) in the angle of attack at this position due to the change in relative velocity.

In addition, small errors in the experimental data could be introduced when the blade forces are calculated from the

flow velocity field. Firstly, LeBlanc and Ferreira [14] found that the load calculations have a small sensitivity to the selected boundary surface used for the calculations (the tangential load is more sensitive than the normal load). Secondly, when the blade forces are calculated, the flow acceleration is approximated with a numerical differentiation of the velocity field using two azimuth positions which are close to each other. These two factors could lead to some small inaccuracies in the experimental data which we are comparing to.

### 7.2.2. Fixed Pitch

Modeling VAWT behavior with non-zero pitch is central to the present study. This section analyzes the adequacy of the 2D AC model for non-zero pitch angles, though the pitch angle is still kept constant throughout the turbine rotation. Due to a lack of fixed pitch offset cases using the AC model in the literature to compare to, our AC model implementation is validated against another modeling technique: CFD. Rezaeiha *et al.* [6] use CFD to model a VAWT with fixed pitch angles from  $-7^\circ$  to  $3^\circ$ . Their turbine has three blades that are NACA 0015 airfoils with a chord length of 0.0575 m. The turbine is 1 m tall and 1 m in diameter. The incoming wind speed is 7 m/s and the tip speed ratio is 4. We compare the fixed pitch angles of  $0^\circ$ ,  $2^\circ$ , and  $-2^\circ$ ; because the authors found that a pitch angle of  $\theta_p = -2^\circ$  is the optimal, and we would like to compare both a positive and negative pitch offset to zero pitch. In the 2D AC model execution, instead of using the airfoil polars generated by XFOIL for the corresponding airfoil shape and Reynolds number, we use the lift and drag coefficients for the static airfoil at the given Reynolds number which are also presented by Rezaeiha *et al.* [6]. This is because the Reynolds number is low and using the authors' polars yields more congruous results.

In Figure 7.10, the angle of attack and normal force coefficient from the AC model and Rezaeiha *et al.* [6] are compared for the different fixed pitch offsets. The general shape of the angle of attack and normal load curves between the CFD model and the AC model are the same, except a bump in the downwind half predicted by the AC model whereas the CFD results are more monotonic. The most notable difference between the two models is that the CFD results are shifted up compared to the AC model. This is most likely attributed to flow curvature—because the blades rotate about a vertical axis, they experience a curved inflow, which is implicitly modeled in CFD [4] but not modeled by the AC. According to De Tavernier *et al.* [28], this effect is represented by an additional angle of attack. Indeed, the angle of attack from the CFD model is shifted up compared to the AC model. Also, the normal force curve is translated upward due to the flow curvature effect [26], [28], which is also seen in Figure 7.10. It is more positive in the upwind region and less negative in the downwind region. Therefore, the increase in the magnitude of the normal force downwind modeled by the AC is likely due to the absence of flow curvature effects. Additionally, CFD

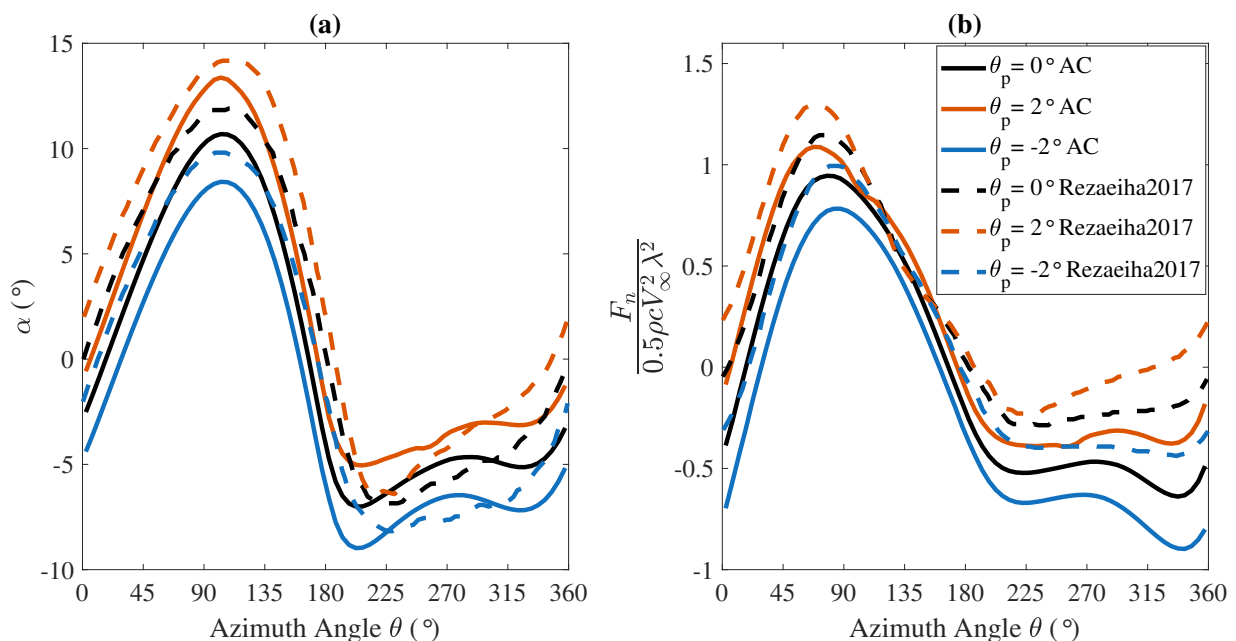


**Figure 7.10:** AC model compared to CFD results in Rezaeiha *et al.* [6]. (a) Angle of attack and (b) normal force coefficient for  $0^\circ$ ,  $2^\circ$ , and  $-2^\circ$  fixed pitch.  $B = 3$ ,  $D = 1$  m,  $c = 0.0575$  m,  $\lambda = 4$ , and  $V_\infty = 7$  m/s. The Reynolds number is 115,000 and the airfoil is NACA 0015; the corresponding airfoil polars are from [6].

implicitly models the blade-vortex interaction [4] which leads to very different inflow conditions in the downwind half compared to the AC model which does not capture blade-vortex interaction.

Furthermore, just as Rezaeiha *et al.* [6] found, a positive pitch angle results in a higher angle of attack and normal load coefficient throughout the revolution. Oppositely, a negative pitch angle results in a lower angle of attack and normal load coefficient throughout the revolution (i.e.  $\theta_p = -2^\circ$  has the smallest angle of attack and load in the upwind region and largest angle of attack and load in the downwind region). The AC model results in Figure 7.10 do show this trend. There is no shift in the instantaneous normal load between the upwind and downwind halves, as Rezaeiha *et al.* [6] also observed.

As for the power coefficient,  $C_p$ , there is a significant difference between the CFD model and the AC model results (only 1% difference for  $\theta_p = 0^\circ$ , but 27% for  $\theta_p = 2^\circ$ ). Most notably, Rezaeiha *et al.* [6] found that the optimal pitch offset of  $\theta_p = -2^\circ$  increases  $C_p$  by 6.6% compared to  $0^\circ$  pitch. However, the AC model actually predicts a decrease in  $C_p$  of 2.8% from  $0^\circ$  to  $-2^\circ$  pitch. This large difference in  $C_p$  is explained by the difference in loading between the models (see Figure 7.10), mostly due to flow curvature and the airfoil polars used. The difference in the thrust coefficient,  $C_T$ , between the two models is smaller (1-6%) and the relative ordering of  $C_T$  with respect to pitch angle is the same.

There could also be some small errors in the CFD results which should be taken into consideration. Rezaeiha *et al.* [6] state that the results depend on the model set-up, such as the domain and grid construction, and the number of turbine revolutions before data sampling—though thorough sensitivity analyses were conducted. Also recall that we used the static airfoil polars from Rezaeiha *et al.* [6], while the authors also present dynamic airfoil polars for different pitch angle offsets, which are different from the static polars. However, the dynamic polars were not used in order to facilitate repeated executions of the AC model with different fixed pitch values and to avoid the complexity of accounting for the hysteresis in the lift and drag coefficients for the dynamic airfoils. Thus, the airfoil polars used in the AC model are not exactly correct and could be the source for some of the discrepancies observed in the loading. According to Rezaeiha *et al.* [6], applying the static airfoil polars to a VAWT results in incorrect loads on the blades.

Overall, given the differences between the two models as described above, we believe the AC model is suitable to represent the load trends with fixed pitch offsets. The differences can be mostly attributed to the neglect of flow curvature in the AC model.

We also compared the 2D AC model to an experiment by LeBlanc and Ferreira [15] which used strain gages to measure the blade normal force for several fixed pitch offsets. There is much uncertainty in those experimental results, so the full comparison is left to Appendix B.

### 7.2.3. Variable Pitch

Finally, we verify the 2D AC model when the blade pitch is variable, which is how the model is used in the remainder of this study. In De Tavernier [4], there is a case where the pitch angle varies as shown in Figure 7.11. The turbine has two blades and a solidity of 0.1. There are several assumed parameters that are not given in [4], but do not have an effect on the results because of nondimensionalization. These are that the radius is 1 m and the freestream velocity is 1 m/s. Given this radius, the solidity, and the number of blades, the chord length is 0.1 m. The tip speed ratio is 4. The airfoil polars are simply  $C_l = 2\pi\alpha$  and  $C_d = 0$ . When running the AC model, we leave out the tangential force

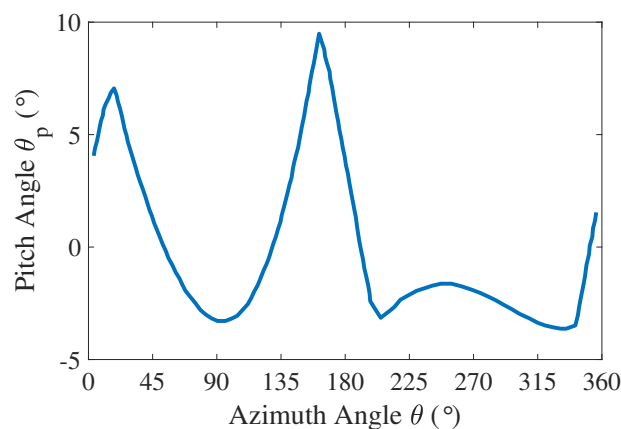


**Figure 7.11:** The varying pitch angle used in De Tavernier [4].

terms and the modified linear solution from Cheng *et al.* [8]. Figure 7.12 compares our AC model to the results in De Tavernier [4]. The angle of attack and normal force line up very well, thereby verifying that we are able to model dynamic pitch with our 2D AC implementation.

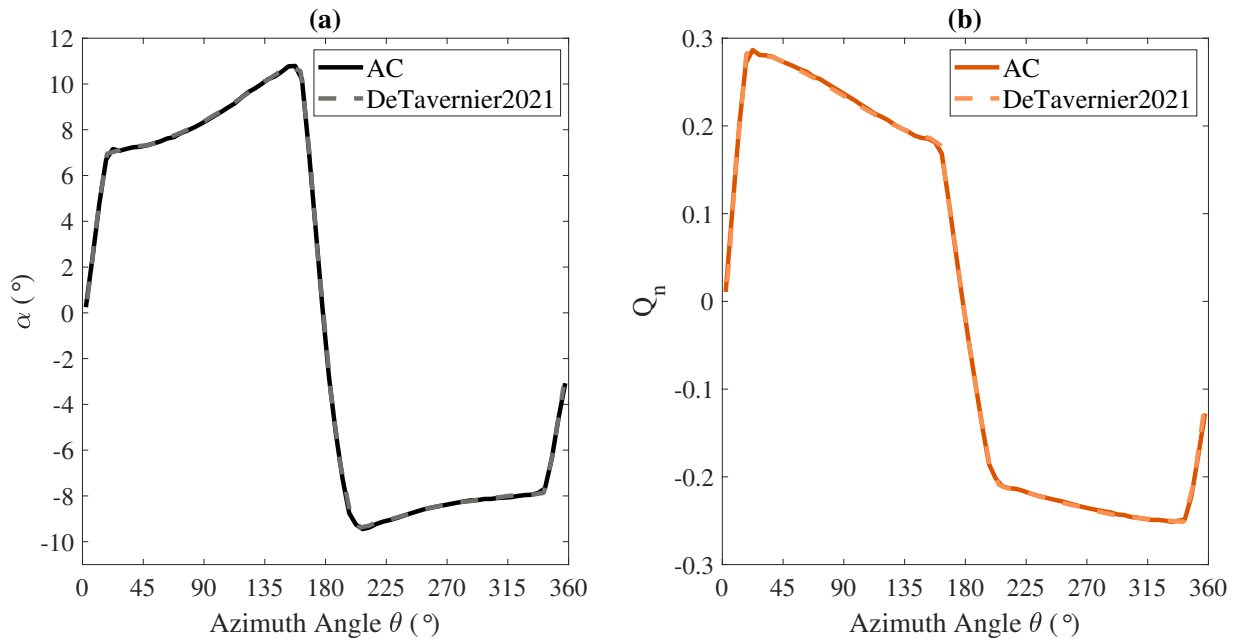
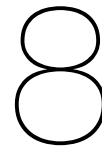


**Figure 7.12:** AC model compared to AC model results in De Tavernier [4]. (a) Angle of attack and (b) normal force for dynamic pitch.  $B = 2$ ,  $R = 1$  m,  $c = 0.1$  m,  $\lambda = 4$ , and  $V_\infty = 1$  m/s. The airfoil polars are  $C_l = 2\pi\alpha$  and  $C_d = 0$ .



# Optimal Pitch Results

This chapter presents the optimization results for the single-, two-, and three-objective optimization problems. The optimal pitch functions are analyzed to understand how they increase the power coefficient, reduce the rotor normal load fluctuations, and/or reduce the rotor torque fluctuations. First, we establish the base case for comparison in Section 8.1. Sections 8.2, 8.3, and 8.4 discuss the results of the single-, two-, and three-objective optimization cases, respectively. Several optimal solutions are selected as case studies for further analysis. Then, we compare the results across the optimization cases with different numbers of objectives in Section 8.5. Section 8.6 discusses some physical implications of the optimal pitch functions. Lastly, Section 8.7 highlights the key conclusions about the optimal pitching strategies found in this study.

## 8.1. Base Case

In this chapter, all results are compared to the base case in which the pitch angle is zero throughout the entire rotor revolution. In the base case, the power coefficient of the turbine is  $C_p = 0.297$ . The thrust coefficient is  $C_T = 0.478$ . The standard deviation in the normal force and tangential force are 0.111 and 0.007, respectively. These values are unitless because  $Q_n$  and  $Q_t$  are unitless. The quantities are used to represent the fluctuations in normal force and the fluctuations in torque, respectively.

As will be elaborated on in subsequent sections, the angle of attack in the base case exceeds the static stall angle of the airfoil,  $\alpha_{ss} = 12^\circ$ , in the upwind region from approximately  $\theta = 80^\circ$  to  $125^\circ$  (see Figure 8.2b). Static stall occurs, which causes a significant drop in the normal and tangential loads, as well as the power coefficient in the upwind region. In the region where the angle of attack is high, above the static stall angle, flow separation likely occurs. The flow reattaches later on when the angle of attack decreases again, and the loading on the blades recovers.

## 8.2. Single Objective: Maximize $C_p$

In the single-objective optimization case, the objective is to maximize the efficiency of the turbine:  $C_p$ . Historically, VAWTs have lower power efficiencies than HAWTs, and pitch control has been identified as a method to increase VAWTs' efficiency and thus overall power generation [5], [8]–[14], [18]–[20], [23], [24], [27]. First, we confirm that the optimization algorithm has converged to the optimal solution by looking at the change in  $C_p$ . Then, we analyze the characteristics of the optimal solution.

### 8.2.1. Post-Optimization Analysis

In order to confirm the convergence of the single-objective case, we look at the change in  $C_p$  with generation. Recall that convergence in  $C_p$  was used as the termination criterion for the optimization algorithm, so we expect that the  $C_p$  does not change much near the end of the simulation. Figure 8.1 shows this convergence in the objective space. A feasible solution was first found after six generations.  $C_p$  converges asymptotically, and is quite flat for the last 40 or so generations. Therefore, we can be confident that the algorithm has converged.

### 8.2.2. Optimization Results

The optimal pitch function which maximizes  $C_p$  that was found by the optimization algorithm has a power coefficient of 0.349, which is a 17.3% increase in  $C_p$  compared to the base case (Table 8.1). When analyzing the optimization results, we look at six quantities as a function of azimuthal angle, as shown in Figure 8.2. These are the pitch angle ( $\theta_p$ ), angle of attack ( $\alpha$ ), blade normal force coefficient ( $C_n$ ), blade tangential force coefficient ( $C_t$ ), power coefficient

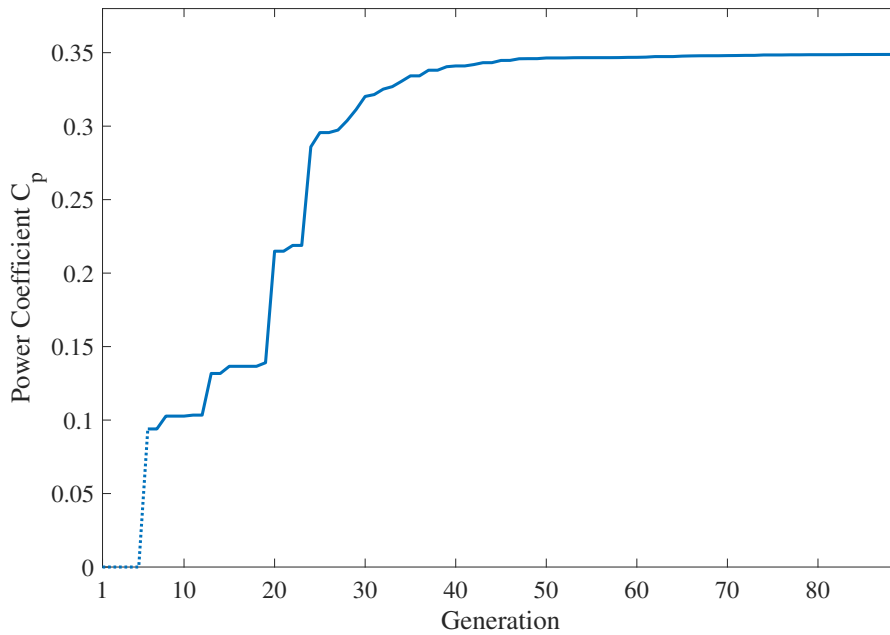


**Figure 8.1:** Evolution of the maximum power coefficient across generations. The simulation is ended after 89 generations when the convergence criterion is met. The dotted line shows when no feasible solution was yet found.

**Table 8.1:** Power and thrust coefficients in the single-objective optimization case.

Pitch Function	$C_p$	$C_T$
Zero pitch	0.297	0.478
Optimal pitch	0.349	0.476

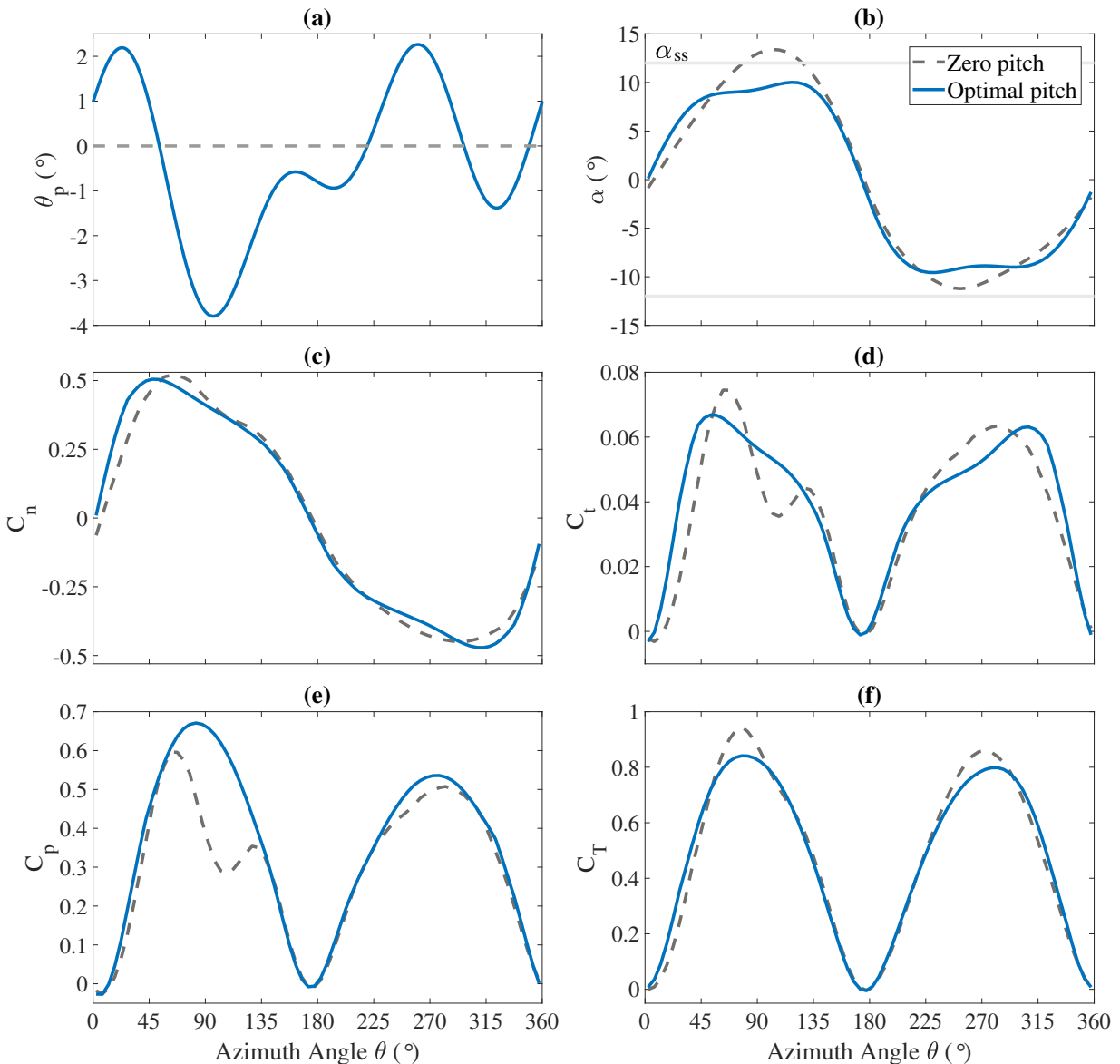
( $C_p$ ), and thrust coefficient ( $C_T$ ). In Figure 8.2, the top row is on the airfoil level, the middle row is on the blade level, and the bottom row is on the rotor level.

Figure 8.2a shows the optimal pitch curve. In the upwind half, the pitch angle initially increases to a maximum of  $2.19^\circ$ , then it decreases into negative values, with a minimum of  $-3.79^\circ$ . At the beginning of the downwind half, the pitch angle is still slightly negative, but in the middle of the downwind half, it is positive, with a peak of  $2.26^\circ$ . The pitch angle decreases below zero again before the end of the downwind half, then becomes positive again as the blade heads back into the upwind half. By focusing on different azimuth ranges, it becomes clear how this pitch curve improves the power coefficient of the turbine.

In the first part of the upwind region, from approximately  $\theta = 0^\circ$  to  $50^\circ$ , the pitch angle is positive. This increases the angle of attack in this azimuthal region compared to the base case (Figure 8.2b), and thus also the normal and tangential blade forces (Figures 8.2c and d). The angle of attack in the base case is small in this region, leading to lower loads and power extraction. By pitching the blade slightly inward at the very beginning of the upwind region, the angle of attack and blade forces are increased so that slightly more power is extracted from the wind.

The next azimuthal region of interest is from  $\theta \approx 50^\circ$  to  $140^\circ$ . In this region, the pitch angle is negative. This decreases the angle of attack with respect to the base case, which is beneficial because otherwise, the angle of attack exceeds the static stall angle when there is zero pitch. This is shown in Figure 8.2b where a horizontal line marks the static stall angle at  $\alpha_{ss} = 12^\circ$ . Static stall is associated with a decrease in lift force and increase in drag force. Thus, when the blade stalls in the base case, there is a pronounced decrease in the blade loads and in the power production. This is most visible in the tangential load curve (Figure 8.2d) and power coefficient curve (Figure 8.2e) around  $\theta = 67.5^\circ$ . Pitching the blade outward decreases the angle of attack so that it remains below the static stall limit. This results in increased power production in the upwind half. In Figure 8.2f, we see that the thrust coefficient of the optimal pitch solution is less than that of the base case in the middle of the upwind region. This is in agreement with the higher power coefficient because the base case thrust coefficient actually exceeds the optimal thrust coefficient according to the Betz limit,  $C_T = 8/9$ . The thrust coefficient with optimal pitch is closer to  $8/9$  than the base case

thrust coefficient, meaning the efficiency is higher.



**Figure 8.2:** Optimal solution which maximizes  $C_p$ . (a) The optimal pitch function, (b) angle of attack, (c) blade normal force coefficient, (d) blade tangential force coefficient, (e) power coefficient, and (f) thrust coefficient as a function of azimuthal angle. The forces are normalized by  $\frac{1}{2}\rho(2R)V_\infty^2$ . Values are compared to the base case with zero pitch (dashed gray line).

In the region from  $\theta \approx 140^\circ$  to  $220^\circ$ , the pitch angle is a small negative value, and the angle of attack, blade forces, power coefficient, and thrust coefficient are very close to the base case. This is a region of low forces and power generation in any case. We find that blade pitching is not used to increase power production in this range.

From  $\theta \approx 220^\circ$  to  $300^\circ$ , the pitch angle is positive, which decreases the magnitude of the angle of attack (Figure 8.2b). While the angle of attack in the base case does not exceed the static stall angle in this region, the decreased angle of attack improves the aerodynamic efficiency of the blade. That is, the aerodynamic efficiency of the SNL 0018/50 airfoil is better (higher  $\frac{C_l}{C_d}$  ratio) at  $\alpha = 9^\circ$  (with pitch) compared to  $\alpha = 11^\circ$  (without pitch). Blade pitching keeps the angle of attack relatively constant near  $\alpha = 9^\circ$  for an extended period in the downwind half. So in this region, we also see a slightly higher  $C_p$  compared to the base case (Figure 8.2e).

In the rest of the downwind region, from  $\theta \approx 300^\circ$  to  $350^\circ$ , the pitch angle is again slightly negative. This increases

the angle of attack compared to the base case, and the normal and tangential loads are again slightly higher (Figures 8.2b, c, and d). The concept is the same as the  $0^\circ$ - $50^\circ$  azimuth region where a small increase in the angle of attack (with an outward pitching maneuver this time because we are in the downwind region) can lead to higher loads and power extraction.

Other than the changes in magnitude of the load curves with azimuth angle which were previously mentioned, we observe other changes in the load curves with optimal pitching compared to zero pitch. In Figures 8.2c and d, we can see that the peaks in the forces are shifted between the two cases. In the upwind region, the peak in normal and tangential force is more upwind compared to the base case. This is expected because in this azimuthal range, the pitch angle is positive, which according to LeBlanc and Ferreira [15] leads the loads to shift earlier in the rotation. Likewise, in the downwind region, the peak normal and tangential forces are shifted more downwind. The pitch angle is negative at this moment, which shifts the loading later in the rotation [15]. Additionally, the peak normal and tangential loads upwind with optimal pitching are slightly less than those in the base case. However, the average loads (normal and tangential) in the upwind half with optimal pitching are greater than without pitching. In the downwind half, the peak normal load is greater while the peak tangential load is slightly less than the base case. Again, the average normal and tangential loads in the downwind half are greater with optimal pitching than without. There is a symmetry in the loading between the upwind and downwind halves, with the upwind magnitude being slightly greater than that downwind, similar to De Tavernier *et al.* [51]. This symmetry is likely due to the fact that the pitch control strives to maximize the rotor power both upwind and downwind. The load curve is also relatively flat compared to the base case. This shape aids in maximum power extraction [41]. There are no dramatic drops in the load profiles which would indicate flow separation. The flow is most likely attached to the blade throughout most of the revolution because the angle of attack does not exceed the static stall angle and there are no dramatic drops in the forces or power coefficient.

Looking at the  $C_p$  curve, in Figure 8.2e, we see that the biggest impact of the optimal pitch on  $C_p$  is a significant increase in the  $C_p$  upwind, particularly in the range where the base case exceeded the static stall angle. In the downwind region, there is also a small increase in  $C_p$ . Throughout the revolution, the power coefficient is hardly below zero, whether there is pitching or not. The optimal pitch function causes two significant regions of power extraction in the upwind and downwind halves, respectively. The average power coefficient is larger upwind than it is downwind, meaning more power is extracted in the upwind pass compared to the downwind pass, as is expected for a VAWT.

### 8.3. Two Objectives: Maximize $C_p$ and Minimize $\sigma(Q_n)$

In the two-objective optimization case, in addition to maximizing the turbine's efficiency,  $C_p$ , we also aim to minimize the normal load fluctuations. Reducing load fluctuations can mitigate the structural burden on the blades and rotor, and lessen their fatigue [5], [24]. Before discussing the optimization results, we ensure that we have satisfactory convergence and diversity of the final solution set.

#### 8.3.1. Post-Optimization Analysis

In order to analyze the convergence of the simulation, we study several performance metrics. First, as an illustration of convergence, Figure 8.3 shows the optimal solution set for several generations. It also shows the initial population, which, when compared to the final solution set, shows the extent of optimization done by the algorithm. The final solution set is very different from the initial population, highlighting the effectiveness of the genetic algorithm: the final solution set is a clear Pareto-optimal front with higher  $C_p$  and lower  $\sigma(Q_n)$  values than the random initial population. There is also good diversity in the final solution set. The sequential Pareto fronts show the progress made by the algorithm in finding better solutions from generation to generation. The Pareto front is successively pushed farther to the lower right. Additionally, more non-dominated solutions are found as the algorithm proceeds. Comparing the 70th, 100th, and 200th generations, most of the progress made is at the ends of the Pareto front, while the middle of the Pareto front is essentially the same. Between the 150th generation (not pictured due to clarity of the figure) and 200th generation, there is visually very little change in the Pareto front. Since the Pareto front is similar for many generations before the end of the simulation, we are confident that the final solution at the 200th generation is converged.

To analyze the convergence quantitatively, we calculate the hypervolume and generational distance. Figure 8.4 shows the hypervolume across generations. The hypervolume is calculated with respect to the  $(C_p, \sigma(Q_n))$  point of the base case. This is the (1, 1) point in Figure 8.6. In order to calculate the hypervolume, a reference point must be specified. We use the  $C_p$  and  $\sigma(Q_n)$  of the base case as the reference point because we are only interested in solutions which

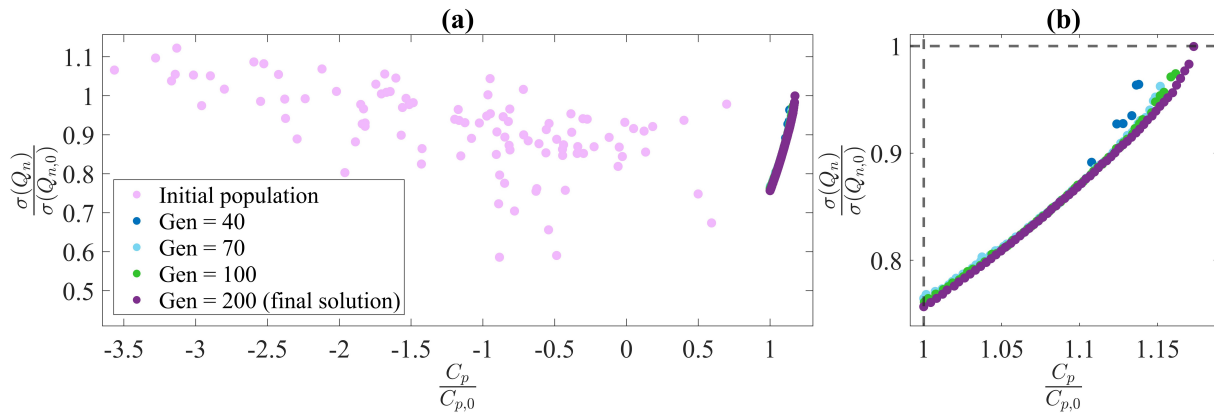


**Figure 8.3:** (a) Evolution of the Pareto front across generations in the two-objective case, along with the initial population; with (b) zoomed in on the region of interest.

improve both objectives compared to the base case (this is also enforced by the constraints on the objective values). Such a feasible solution was first found after 16 generations, shown by the dashed gray line in Figure 8.4. In Figure 8.4a, the value of the hypervolume itself shows a converging pattern. It asymptotically approaches a maximum value of around 0.57. It does not appear to change much after about the 160th generation. The change in hypervolume between consecutive generations is of greater interest, which is shown in Figure 8.4b. The change in hypervolume was used as the termination criterion for the optimization. The change in hypervolume decreases over time. Near the end of the simulation, the hypervolume changes very little from generation to generation. This means that the area dominated by the Pareto front is not changing much, so we can be confident that our final solutions are optimal.

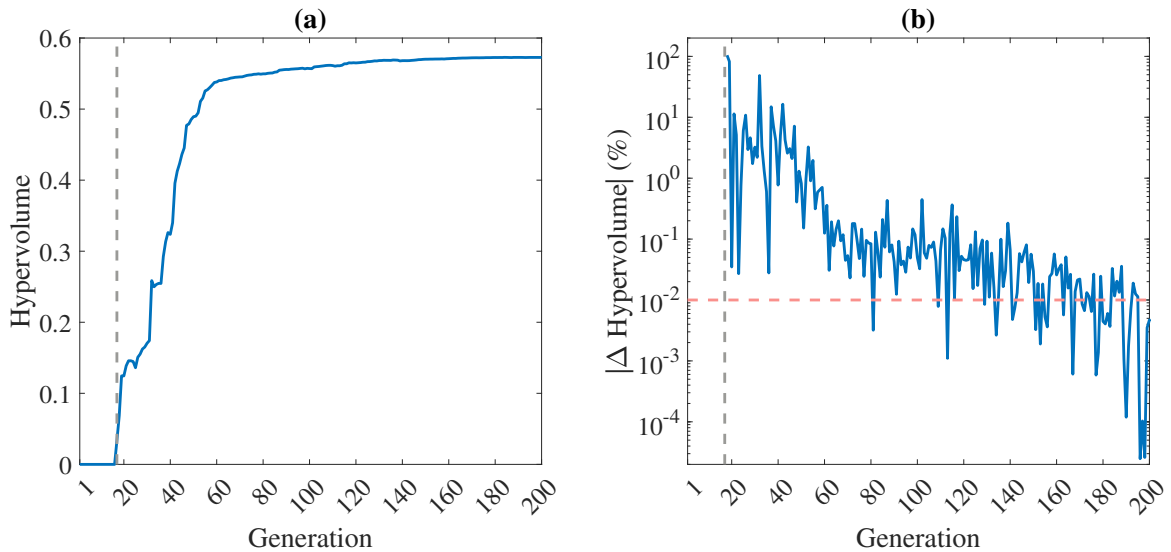


**Figure 8.4:** (a) The hypervolume across generations and (b) the change in hypervolume between two successive generations. The simulation is ended after 200 generations when the convergence criterion is met. The dashed red line shows the threshold used for the termination criterion. The dashed vertical line shows when a feasible solution is first found.

Figure 8.5a shows the generational distance between two consecutive generations. The generational distance clearly decreases over time. This means that the average distance between the Pareto fronts from one generation to the next is becoming smaller. Since the algorithm is terminated after 200 generations based on the termination criterion, Figure 8.5b shows the generational distance of every generation with respect to this final generation in order to analyze the progress in converging toward the final solution set. The generational distance from the 200th generation becomes smaller over time. The generational distance is relatively flat and near zero for the last 40 or so generations. This means there is very little change in the Pareto front between these generations. Therefore, we feel confident that the algorithm has converged.

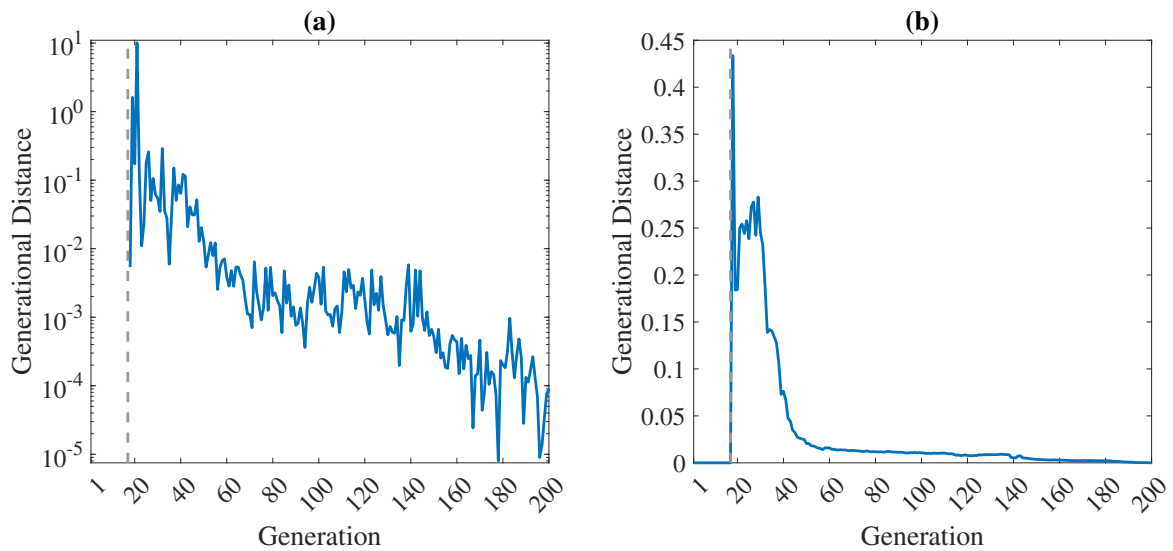


**Figure 8.5:** The generational distance (a) between two successive generations and (b) with respect to the 200th generation. The dashed vertical line shows when a feasible solution is first found.

### 8.3.2. Optimization Results

The optimal solutions for the two-objective case are shown in Figure 8.6. The colors represent the same individual across plots. Due to the constraints on the objective function values, all of the solutions obtained achieve both

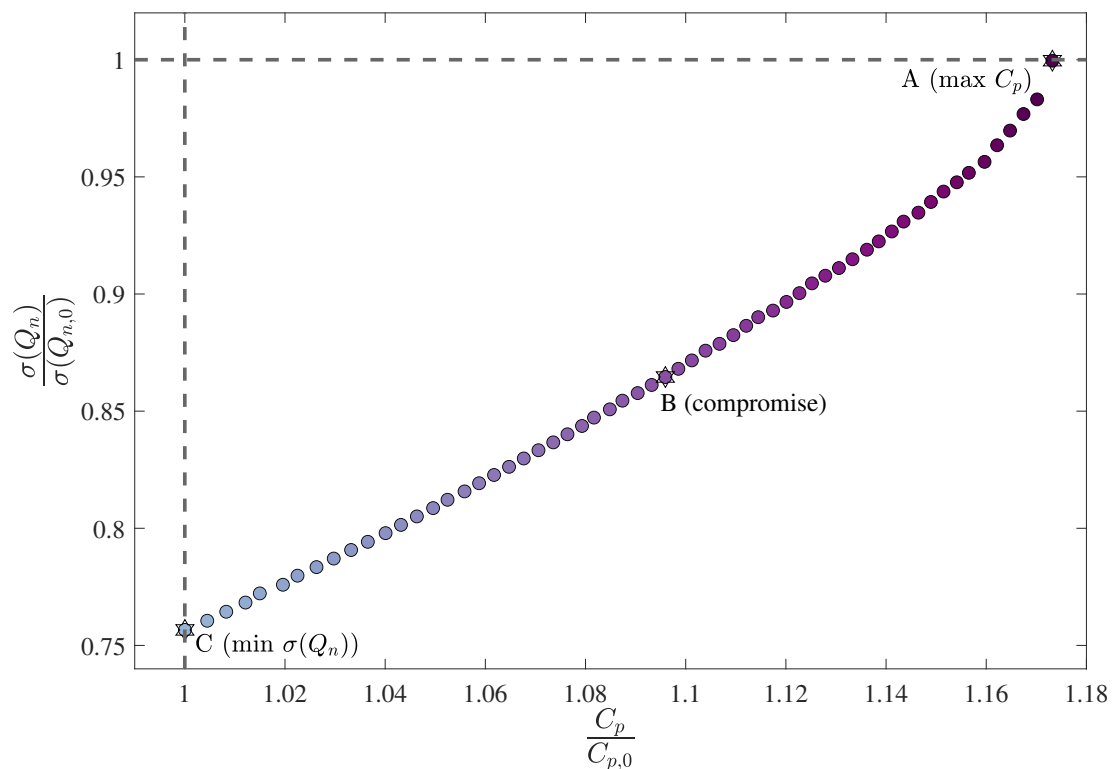


**Figure 8.6:** The Pareto-optimal front for the two-objective optimization case: maximize  $C_p$  and minimize  $\sigma(Q_n)$ . Solution A increases  $C_p$  the most, while maintaining normal load fluctuations. Solution C decreases normal load fluctuations the most, while maintaining power efficiency. Solution B is a compromise, which achieves some improvement in both objectives at the same time. The color of the solutions is sorted from high  $C_p$  (dark purple) to low  $C_p$  (blue). The axes are normalized with respect to the base case and the dashed lines show unity.

objectives at the same time: they increase  $C_p$  while decreasing the normal load fluctuations, with respect to the base case. At the ends of the Pareto front, the base case  $C_p$  can be maintained while decreasing  $\sigma(Q_n)$  by 24.3%; and the base case  $\sigma(Q_n)$  can be maintained while increasing  $C_p$  by 17.3%. As expected, the general trend in Figure 8.6 is that attempting to decrease the load fluctuations also results in a decrease in  $C_p$ .

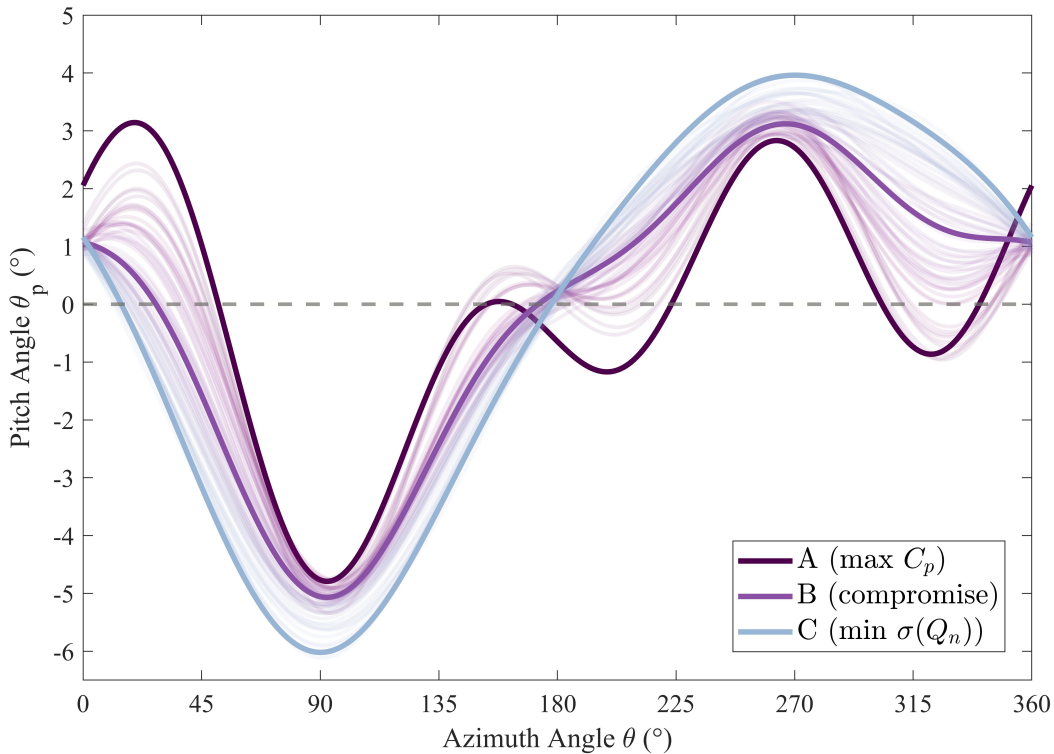


**Figure 8.7:** The optimal pitch functions for the two-objective optimization case. Solution A increases  $C_p$  the most, while maintaining normal load fluctuations. Solution C decreases normal load fluctuations the most, while maintaining power efficiency. Solution B is a compromise, which achieves some improvement in both objectives at the same time.

Figure 8.7 shows all the optimal pitch functions. In general, the pitch angle is negative upwind and positive downwind, as expected. The solutions with higher  $C_p$  (and higher load fluctuations) have lower amplitude and more oscillations. The solutions with lower  $C_p$  (and lower load fluctuations) have higher amplitude and resemble a first-order sinusoid more. Le Fouest and Mulleners [5] also found that pitch curves which maximize  $C_p$  have more oscillations and pitch curves which minimize load fluctuations (blade pitching moment in their case) resemble simple sinusoids. As the load fluctuations decrease, the maximum amplitude of the pitch function increases. Figure 8.8a shows this where low  $C_p$  (low load fluctuations) solutions have high magnitude of  $A_1$ , and vice versa, high  $C_p$  (high load fluctuations) have low magnitude of  $A_1$ . The contribution of the second and third harmonics is shown in Figure 8.8b and c. The solutions with high  $C_p$  (high load fluctuations) have higher values of  $A_2$  and  $A_3$ . As such, they have more contribution from the higher-order terms, which is also evident in the oscillating pitch functions in Figure 8.7. These solutions have a pitch function which is more varying in order to adjust the angle of attack at each azimuthal position to the optimal for extracting as much power as possible. The range in  $A_1$  among the solutions is the largest, followed by the range in  $A_3$ , while  $A_2$  has a very small range. As for the other decision variables, there is no pattern in  $A_0$  across the solutions, though  $A_0$  is always negative, and the frequency variable,  $w$ , is always one. This means that the amplitude of the first and third harmonics of the pitch function are the most important in determining the  $C_p$  and normal load fluctuations: a low  $A_1$  and high  $A_3$  lead to high  $C_p$  and high load fluctuations.

Figure 8.8d shows the effect of pitch angle on the maximum angle of attack (upwind) and the corresponding trend with the objective functions. The pattern with the minimum angle of attack (downwind) is the inverse. All of the solutions have a peak angle of attack below the static stall angle ( $\alpha_{ss} = 12^\circ$ ), which means static stall is avoided, unlike in the base case. The magnitude of the maximum angle of attack is higher when higher  $C_p$  (higher load fluctuations) is

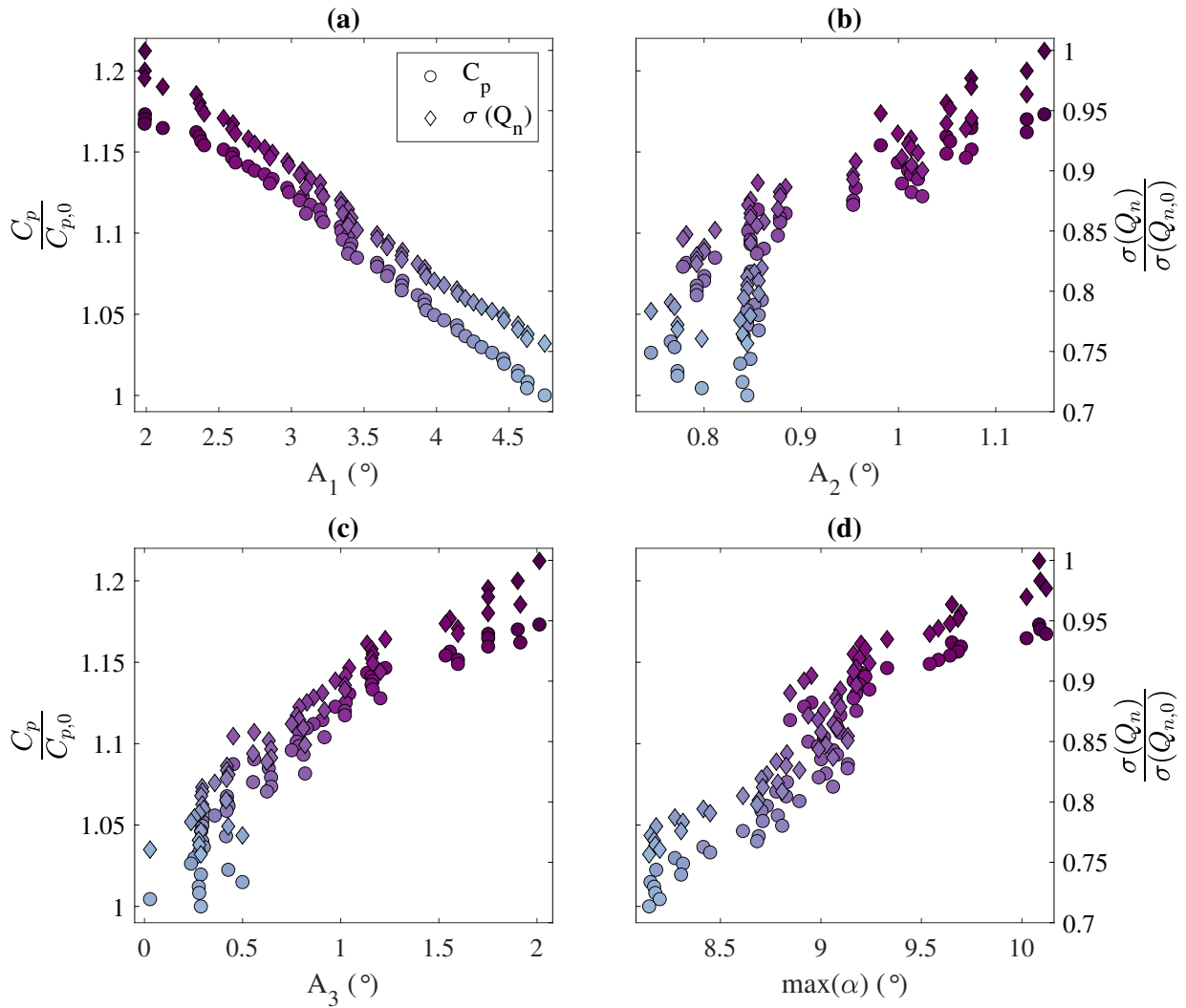


**Figure 8.8:** The trend in the optimal values of the decision variables with the objective functions. (a) Amplitude of the first harmonic ( $A_1$ ), (b) amplitude of the second harmonic ( $A_2$ ), and (c) amplitude of the third harmonic ( $A_3$ ). (d) The trend in the maximum angle of attack with the objective functions.

obtained. This makes sense because, in the pre-stall region, a higher angle of attack leads to a higher lift coefficient, and higher overall forces on the blades. Conversely, the solutions with lower  $C_p$  (lower load fluctuations) have lower maximum angles of attack because they have higher pitch amplitudes. In brief, the large pitch angles significantly decrease the angle of attack, and therefore, the loading on the blades also decreases. This is the effect of the second objective—the normal load curve is flattened toward the mean so that the normal load standard deviation is minimized. The load fluctuations are low because the load does not reach a very high amplitude, but rather stays at low amplitudes close to the mean. However, the consequence of this is lower power generation because the loads on the blades are lower.

Figure 8.6 labels a few individuals in the Pareto front which we will consider as case studies. Solution A achieves the highest  $C_p$  while not increasing the normal load fluctuations compared to the base case. Solution B achieves both an increase in  $C_p$  and a reduction in normal load fluctuations compared to the base case—it is a compromise between the two objectives. Solution C maintains  $C_p$  compared to the base case while reducing normal load fluctuations the most. Table 8.2 compares the power and thrust coefficients of the optimal solutions to the base case. As the power coefficient decreases, so too does the thrust coefficient. All of the optimal solutions have a thrust coefficient which is less than the base case.

**Table 8.2:** Power and thrust coefficients in the two-objective optimization case.

Pitch Function	$C_p$	$C_T$
Zero pitch	0.297	0.478
Solution A (max $C_p$ )	0.349	0.467
Solution B (compromise)	0.326	0.418
Solution C (min $\sigma(Q_n)$ )	0.297	0.372

**Solution A: Maximum  $C_p$** 

Solution A is similar to the optimal solution obtained for the single-objective optimization problem in which the only goal was to maximize  $C_p$ . Analysis of how this pitch function shape changes the angle of attack and loads in different azimuth ranges in order to maximize  $C_p$  is already discussed in Section 8.2. Solution A and the optimal solution to Case 1 have essentially the same  $C_p$ , a 17.3% increase compared to the base case. The difference between the solutions is that solution A does not increase the normal load fluctuations while the optimal solution to Case 1 increases the standard deviation of the normal load by 1.44% compared to the base case. Therefore, the solutions are compared in Section 8.5.

**Solution C: Minimum  $\sigma(Q_n)$** 

Solution C decreases  $\sigma(Q_n)$  by 24.3% while maintaining the  $C_p$  of the base case. The pitch function, shown in Figure 8.9a, resembles more of a simple sinusoid, with less third-order contribution. The pitch angle is mostly negative (outward pitching) upwind and positive (inward pitching) downwind. However, it is not symmetric between the upwind and downwind halves—the maximum magnitude of the pitch angle is greater in the upwind half than in the downwind half. The pitch angle reaches  $-6^\circ$  upwind and  $4^\circ$  downwind which means the pitch mechanism needs to have a range of motion spanning these  $10^\circ$ . The amplitude of the pitch angle is also larger than that of solution A and the optimal solution to Case 1 which maximize  $C_p$ . The solution C pitch angle decreases the angle of attack compared to the base case almost throughout the entire revolution, as shown in Figure 8.9b. The angle of attack is well below the static stall angle and it peaks close to the airfoil's maximum aerodynamic efficiency point at  $\alpha = 8^\circ$  both in the upwind and downwind regions. The magnitude of the normal force (Figure 8.9c) is significantly less than the base case—it is flattened toward the mean, which makes sense given the second objective of minimizing the standard deviation of normal force. A new feature in the normal blade force curve, which has not been seen in the previously-analyzed cases, is that the maximum normal load downwind is greater than the maximum normal load upwind. Usually, the upwind peak in normal force is greater than the downwind peak. The tangential blade force of solution C, in Figure 8.9d, is also overall lower than the base case. Notably, solution C's peak in tangential force is higher downwind than it is upwind. The average tangential force downwind is also greater than the one upwind. Therefore, we conclude that in order to minimize the normal load fluctuations while maintaining  $C_p$ , the loading on the blades is shifted more toward the downwind half of the revolution. This happens because, in the base case, the peak normal load upwind is greater than the peak downwind. This large load contributes to load fluctuations of a high magnitude, which are undesired. In order to decrease the load fluctuations (decrease the standard deviation of the normal load), the large loads upwind are decreased. At the same time, power generation must be maintained, and therefore the loading in the downwind half is increased. In Figure 8.9e, the peak  $C_p$  is still larger upwind than it is downwind. Importantly, the average  $C_p$  of the base case can be maintained because, while the force magnitudes are overall lower, there is no static stall in the upwind region. Lastly, the peak magnitude in  $C_T$  of solution C is greater downwind than upwind (Figure 8.9f). The average thrust coefficient is also greater downwind. Therefore, both on a blade and rotor level, the loading is shifted downwind in order to minimize the normal load fluctuations.

**Solution B: Compromise**

Solution B achieves both objectives at the same time: a 9.59% increase in  $C_p$  and 13.5% decrease in  $\sigma(Q_n)$  compared to the base case. The pitch function is shown in Figure 8.9a. It has less fluctuations than solution A which maximizes  $C_p$ , but contributions of the second and third harmonics are still visible. The maximum pitch amplitude of solution B is higher than that of solution A but smaller than that of solution C. Like solution C, which minimizes the normal load fluctuations, the pitch angle is mostly negative in the upwind region and positive in the downwind region. The maximum magnitude of the pitch angle is also greater in the upwind half than in the downwind half. The blade pitches outward in the upwind region and inward in the downwind region in order to decrease the angle of attack in each respective region. This is shown in Figure 8.9b where the angle of attack for solution B is less than the angle of attack for the base case for almost the entire revolution. Solution B's angle of attack is also smaller than the angle

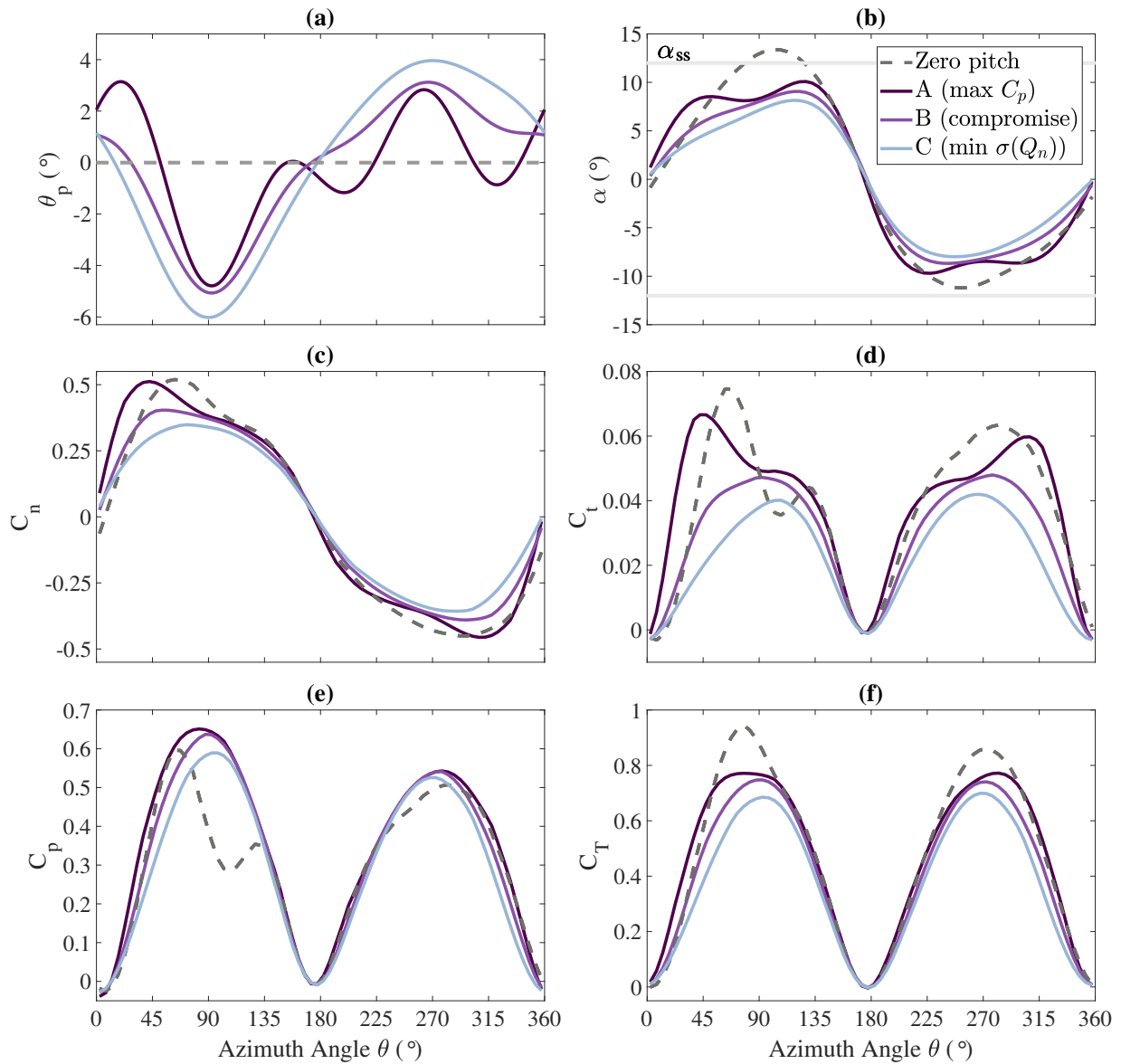


**Figure 8.9:** Example solutions to the two-objective optimization problem. Solution A increases  $C_p$  the most, while maintaining normal load fluctuations. Solution C decreases normal load fluctuations the most, while maintaining power efficiency. Solution B is a compromise, which achieves some improvement in both objectives at the same time. (a) The optimal pitch function, (b) angle of attack, (c) blade normal force coefficient, (d) blade tangential force coefficient, (e) power coefficient, and (f) thrust coefficient as a function of azimuthal angle. The forces are normalized by  $\frac{1}{2}\rho(2R)V_\infty^2$ . Values are compared to the base case with zero pitch (dashed gray line).

of attack for solution A throughout most of the revolution due to the more negative pitch angle upwind and more positive pitch angle downwind. The angle of attack is greater than that of solution C throughout the revolution due to the lower pitch amplitudes of solution B. The pitch function decreases the maximum angle of attack in the upwind region so that the static stall angle is not exceeded, as was also seen for the Case 1 optimal solution and Case 2 solutions A and C. As previously discussed, this increases power production in the upwind region. At the same time, the angle of attack is still relatively high and around the maximum aerodynamic efficiency point of the airfoil ( $\alpha = 8^\circ$ ). Therefore, the net power coefficient is still high, but the lower angle of attack leads to smaller normal loads compared to the base case.

The magnitude of the normal load is decreased during most of the revolution compared to the base case and solution A (Figure 8.9c). The maximum and minimum peaks in the normal load coefficient are also smaller than in the base case and solution A. The result is that the normal force throughout the revolution is closer to the mean, which makes

the standard deviation in normal force smaller, as desired in the second objective. However, the magnitude of the normal load is still greater than that of solution C, due to the smaller pitch angles, so the normal load fluctuations are higher than they are in solution C. The tangential force is also mostly lower than in the base case and solution A throughout the revolution, but it is larger than the tangential force in solution C (Figure 8.9d). The relative decrease in the normal and tangential forces of solution B with respect to the base case is greater in the upwind half compared to the downwind half. Hence, relatively speaking, the loading for solution B is shifted downwind. Adding the second objective targets reducing the normal force upwind in order to minimize the standard deviation of normal force. While the magnitude of the blade normal and tangential forces are lower than the base case, the blade pitch helps redirect the force in the direction tangential to the rotor, leading to higher  $C_p$ . Thus, optimal blade pitching allows the blade normal and tangential forces, and their standard deviations, to be lower, because the pitch angle helps redirect the force in the tangential direction thus leading to high torque and power.

The power coefficient, in Figure 8.9e, is higher than the base case in the middle of the upwind and downwind halves. In the middle part of the upwind region, the  $C_p$  is significantly higher than the base case  $C_p$  because the base case experienced stall in this region while solution B does not. The  $C_p$  is also greater than the base case downwind. Comparing solutions A, B, and C, there is a successive decrease in the power coefficient in the upwind half, while in the downwind half, the power coefficients are more similar. Thus, the second objective targets lowering the loading and power generation upwind compared to downwind. The average  $C_p$  of solution B is lower than the  $C_p$  of solution A, but both power coefficients are higher than solution C and the base case with zero pitch. Solution B can still achieve close to a 10% increase in  $C_p$  without requiring a pitch mechanism which is able to pitch frequently.

## 8.4. Three Objectives: Maximize $C_p$ , Minimize $\sigma(Q_n)$ , and Minimize $\sigma(Q_t)$

The third objective which is added is to minimize the rotor torque fluctuations, quantified by the standard deviation in the tangential load  $Q_t$ . Reducing the torque fluctuations improves the power quality and the loading on the drivetrain [13]. First, we analyze the optimization results for convergence and diversity. Then, we discuss the optimization results.

### 8.4.1. Post-Optimization Analysis

We again use the hypervolume and generational distance to analyze the convergence and diversity of the optimization results. Figure 8.10a shows the hypervolume across generations. The hypervolume uses the  $(C_p, \sigma(Q_n), \sigma(Q_t))$  point of the base case as the reference point, meaning it represents the volume dominated by the optimal solution set which improves all three objectives compared to the base case. A feasible solution was first found after 26 generations. The hypervolume rapidly expands for the first 80 generations. Thereafter, it oscillates around a value of 0.26, but

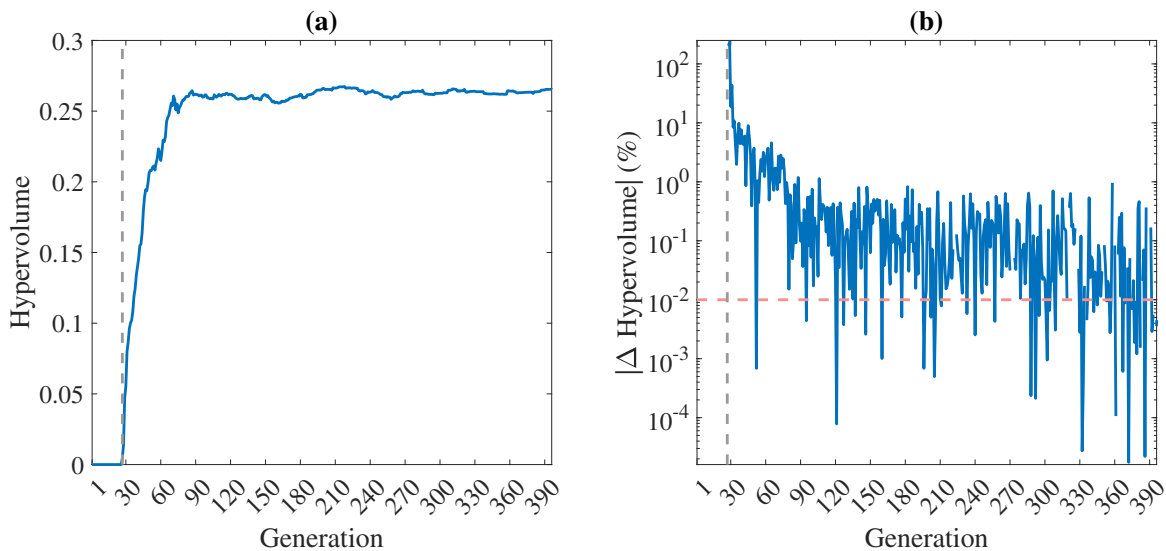


**Figure 8.10:** (a) The hypervolume across generations and (b) the change in hypervolume between two successive generations. The simulation is ended after 396 generations when the convergence criterion is met. The dashed red line shows the threshold used for the termination criterion. The dashed vertical line shows when a feasible solution is first found.

the changes are small. The hypervolume is relatively flat, but it does not monotonically increase to an asymptote because in each generation, the optimal points in the Pareto front shift slightly, which can sometimes lead to a small decrease in the hypervolume. However, we are more interested in the change in the hypervolume between successive generations. This is shown in Figure 8.10b. Recall that the change in hypervolume was used as the termination criterion for the optimization. The change in hypervolume decreases over time. The small change in hypervolume from generation to generation means that the volume dominated by the Pareto front remains relatively consistent, so we can be confident that we have found a set of optimal solutions which cannot be improved appreciably more.

Figure 8.11a shows the generational distance between two consecutive generations. The generational distance decreases over time, signaling that the change in the Pareto front gets smaller as the generations progress. Since there is little change in the Pareto front near the end of the simulation, we can be confident that the algorithm has converged. Figure 8.11b shows the generational distance of every generation with respect to the 396th (final) generation. The generational distance from the 396th generation becomes smaller over time. The solution set gradually progresses toward the final solution set.

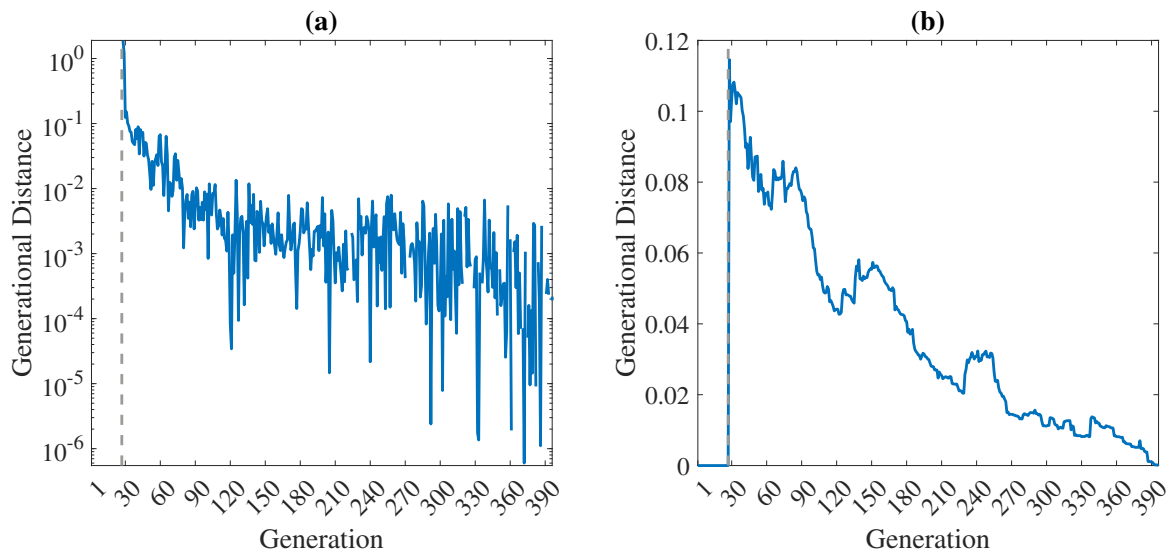
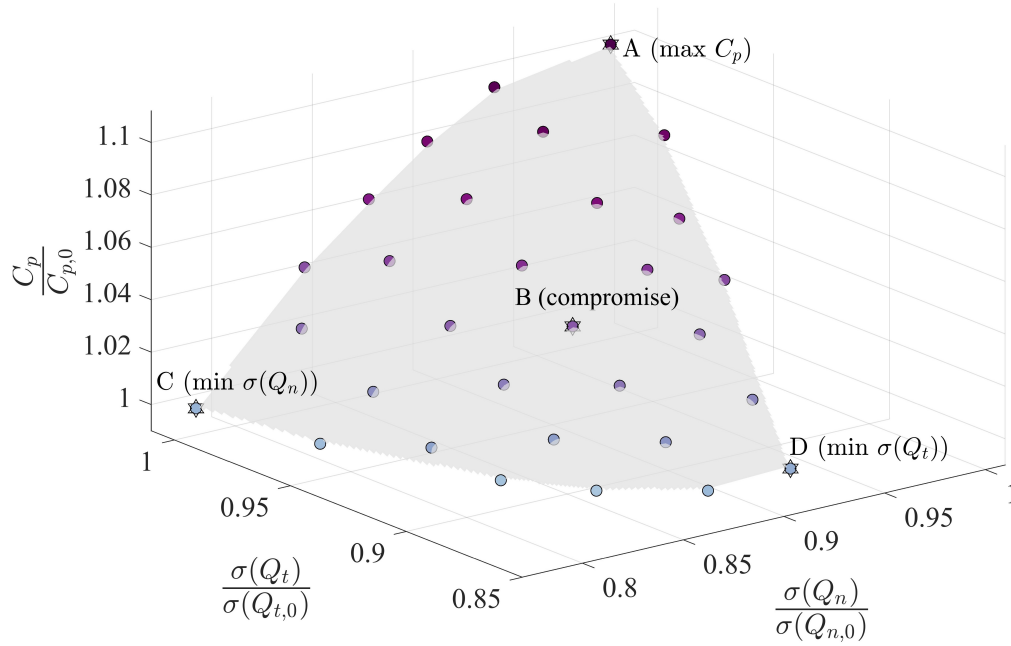


**Figure 8.11:** The generational distance (a) between two successive generations and (b) with respect to the 396th generation. The dashed vertical line shows when a feasible solution is first found.

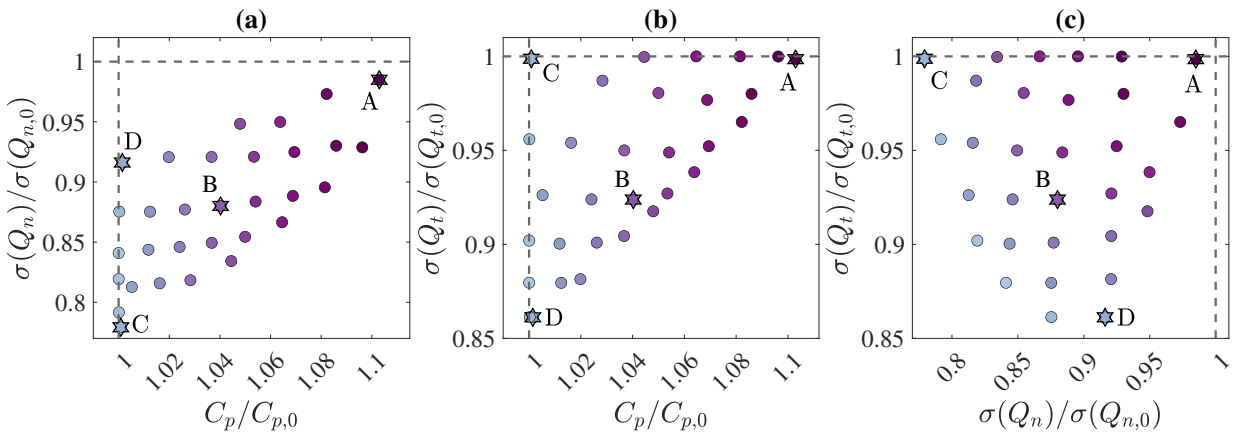
### 8.4.2. Optimization Results

Figure 8.12 shows the optimal solutions obtained for the three-objective optimization case. Since there are three objectives, the Pareto front is in 3D. The Pareto front is also shown in 2D in Figure 8.13 where the Pareto front is projected onto each pair of axes ( $\sigma(Q_n)$  vs.  $C_p$ ,  $\sigma(Q_t)$  vs.  $C_p$ , and  $\sigma(Q_t)$  vs.  $\sigma(Q_n)$ ). It is evident that the three objectives are all conflicting because in each 2D plot, an improvement in one objective comes with a worsening of the other objective. There are no solutions that achieve the best improvement for all three objectives simultaneously. Additionally, the individuals on the outer-most front in one 2D plot are not the same individuals which are on the outer-most front of another 2D plot. With three objectives, the maximum attainable  $C_p$  is 0.328, or a 10.3% increase over the base case. The greatest reduction in normal force fluctuations that can be achieved while maintaining the  $C_p$  of the base case is 22.1%. The greatest reduction in torque fluctuations that can be achieved while maintaining the  $C_p$  of the base case is 13.9%. Compared to the two-objective case, the relative improvements in  $C_p$  and  $\sigma(Q_n)$  are smaller. The  $C_p$  can now be increased by 10.3% compared to 17.3% in the two-objective case.  $\sigma(Q_n)$  can now be decreased by 22.1% compared to 24.3% in the two-objective case. Figure 8.14 shows that the Pareto front in the  $C_p$ - $\sigma(Q_n)$  plane is not pushed as far out as in the two-objective case. Therefore, adding the third objective to minimize rotor torque fluctuations does affect the attainable improvement in the other two objectives.

Figure 8.15 shows the optimal pitch functions obtained. Most of the solutions in the Pareto front have a similar shape of the pitch function: third-order sinusoids. All of the solutions have negative pitch angles in the middle of the upwind region and positive pitch angles in the middle of the downwind region. The main difference among the solutions lies in the variations in the amplitudes of the pitch functions. As an exception, solution C, which achieves the lowest normal load fluctuations, has a less-oscillating pitch function, which was also seen in Case 2 for solutions with lower normal load fluctuations.



**Figure 8.12:** The Pareto-optimal front for the three-objective optimization case: maximize  $C_p$ , minimize  $\sigma(Q_n)$ , and minimize  $\sigma(Q_t)$ . Solution A increases  $C_p$  the most, while maintaining normal load and torque fluctuations. Solution C decreases normal load fluctuations the most, while maintaining power efficiency and torque fluctuations. Solution D decreases torque fluctuations the most, while maintaining power efficiency and with a slight reduction in normal load fluctuations. Solution B is a compromise, which achieves some improvement in all objectives at the same time. The color of the solutions is sorted from high  $C_p$  (dark purple) to low  $C_p$  (blue). The axes are normalized with respect to the base case.



**Figure 8.13:** The Pareto-optimal front for the three-objective optimization case: maximize  $C_p$ , minimize  $\sigma(Q_n)$ , and minimize  $\sigma(Q_t)$ . (a) The Pareto front in the  $C_p$ - $\sigma(Q_n)$  plane, (b) in the  $C_p$ - $\sigma(Q_t)$  plane, and (c) in the  $\sigma(Q_n)$ - $\sigma(Q_t)$  plane. Solution A increases  $C_p$  the most, while maintaining normal load and torque fluctuations. Solution C decreases normal load fluctuations the most, while maintaining power efficiency and torque fluctuations. Solution D decreases torque fluctuations the most, while maintaining power efficiency and with a slight reduction in normal load fluctuations. Solution B is a compromise, which achieves some improvement in all objectives at the same time. The color of the solutions is sorted from high  $C_p$  (dark purple) to low  $C_p$  (blue). The axes are normalized with respect to the base case and the dashed lines show unity.

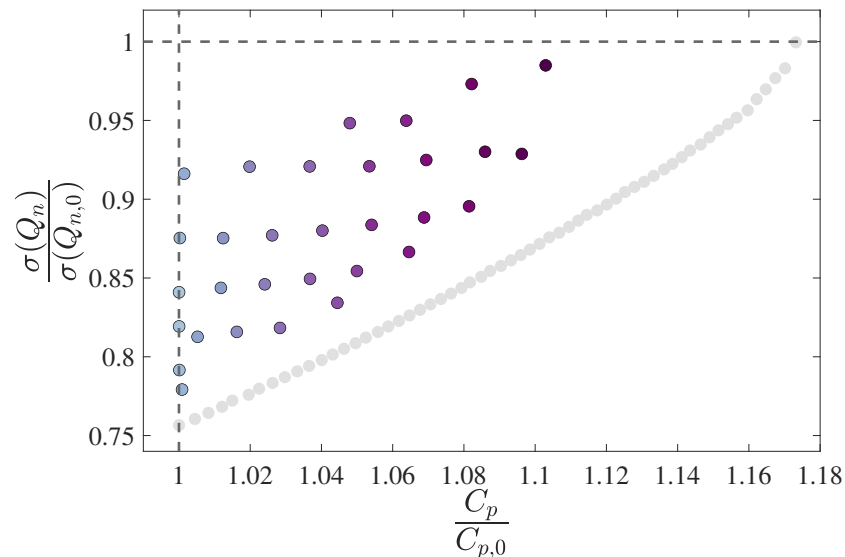


**Figure 8.14:** The Pareto-optimal front in the  $C_p$ - $\sigma(Q_n)$  plane for the three-objective optimization case vs. the two-objective optimization case (gray points). The three-objective case does not achieve as high  $C_p$  or as low normal load fluctuations as the two-objective case. The axes are normalized with respect to the base case and the dashed lines show unity.

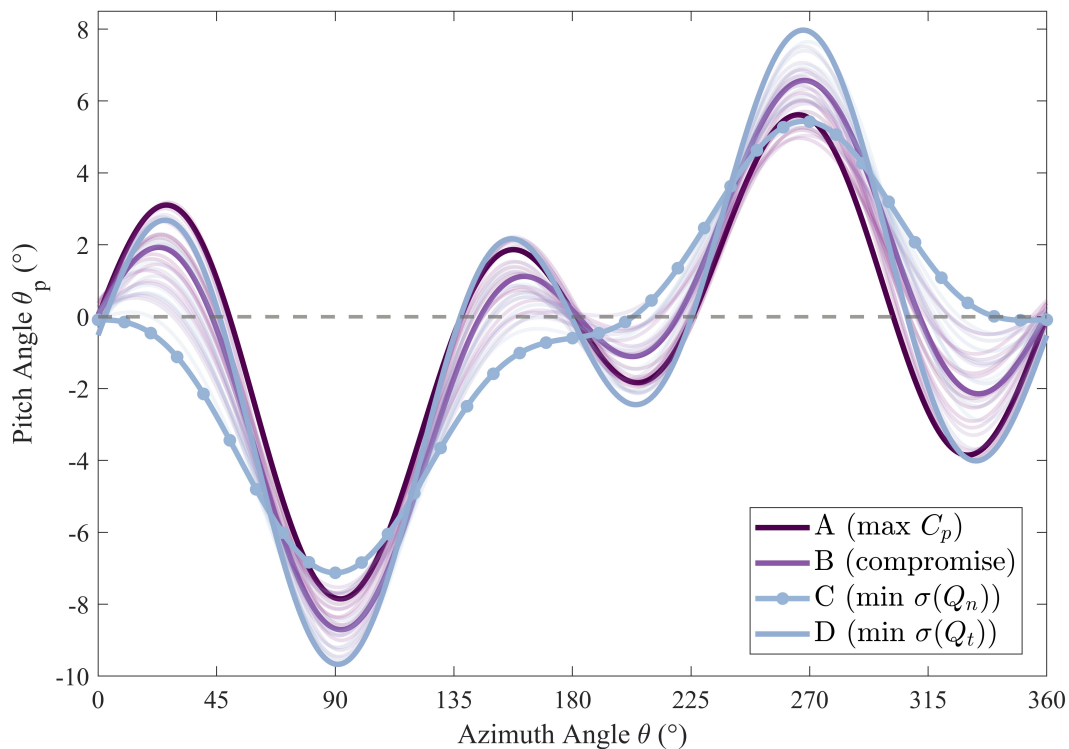


**Figure 8.15:** The optimal pitch functions for the three-objective optimization case. Solution A increases  $C_p$  the most, while maintaining normal load and torque fluctuations. Solution C decreases normal load fluctuations the most, while maintaining power efficiency and torque fluctuations. Solution D decreases torque fluctuations the most, while maintaining power efficiency and with a slight reduction in normal load fluctuations. Solution B is a compromise, which achieves some improvement in all objectives at the same time.

As was done for the two-objective optimization case, we look at the trends in the decision variables with the objective functions. Since there are many variables and objectives, there are many resulting combinations of one variable and one objective, which are summarized in Table 8.3. A positive correlation means that the objective function increases as (the magnitude of) the decision variable increases. A negative correlation means that the objective function decreases as (the magnitude of) the decision variable increases. There can also be no correlation between the two. A strong correlation means that there is a clear trend line between the objective function and the decision variable while a weak correlation means that the trend is visible but less definite.

**Table 8.3:** The trends in the optimal values of the decision variables with the objective functions for the three-objective optimization case.

Variable	$C_p$	$\sigma(Q_n)$	$\sigma(Q_t)$
$ A_0 $	None	None	None
$ A_1 $	Negative (strong)	Negative (strong)	None
$ A_2 $	Positive (weak)	Positive (strong)	None
$ A_3 $	None	Positive (strong)	Negative (weak)

Firstly, solutions with a high power coefficient and high normal load fluctuations have a lower amplitude of  $A_1$ . This was also observed for the two-objective optimization case. These solutions also tend to have a higher value of  $A_2$ , the amplitude of the second harmonic, as was also the case for Case 2. However, from Figure 8.15, it appears that the maximum amplitude of the pitch function should not be too large in order to minimize the normal load fluctuations. This is in contradiction with the solutions in Case 2, where the solutions with lower load fluctuations had larger pitch amplitudes (see Figure 8.7). However, these observations are in relation to the other solutions in the optimal solution set. The pitch functions in Case 3 generally have higher amplitudes than those in Case 2. On an absolute level, the pitch functions which minimize the normal load fluctuations in Case 2 and Case 3 have similar amplitudes:  $-6^\circ/-7^\circ$  upwind and  $4^\circ/5^\circ$  downwind. Secondly, the amplitude of the third harmonic,  $A_3$ , is only correlated with normal load and torque fluctuations. In Case 2, a large  $A_3$  was associated with high  $C_p$  and high  $\sigma(Q_n)$ . Now, in Case 3, there is no correlation between  $A_3$  and  $C_p$ . This makes sense because, as can be seen in Figure 8.15, most of the optimal pitch functions have strong oscillatory behavior, even though their power coefficients vary.  $A_3$  is still correlated with the normal load fluctuations in that solutions with a lower  $A_3$  have lower normal load fluctuations. From these trends, we conclude that the contribution of the third harmonic, via  $A_3$ , is in fact not a good predictor of  $C_p$ . Rather, the overall maximum amplitude of the pitch function is better correlated with  $C_p$  in that lower amplitudes are associated with higher power coefficients. We also conclude that the degree of oscillations in the pitch function is more important for determining the normal load fluctuations. In order to minimize the normal load fluctuations, the variation in pitch angle should be minimized, and instead the pitch function should resemble more of a first-order sinusoid that pitches outward upwind and inward downwind.

There is also a trend that more oscillatory pitch functions, with higher  $A_3$ , have lower torque fluctuations. However, the torque fluctuations are not correlated with the other decision variables. Therefore, we can only conclude that frequent variations in pitch are useful for minimizing the torque fluctuations. Even so, from Figure 8.15, it also appears that pitch functions with the largest magnitude in the middle of the upwind and downwind regions lead to lower torque fluctuations.

Lastly, there is no trend in the objective function values with the offset  $A_0$ , though  $A_0$  is always a small negative number; and the frequency variable,  $w$ , is always one. While not a decision variable, we also study the correlation between the objective functions and the maximum/minimum angle of attack. The maximum angle of attack is positively correlated with the normal load fluctuations: an increase in the maximum angle of attack is associated with higher normal load fluctuations. This was also the case in Case 2 where it was explained how lower maximum angles of attack lead to lower loading, so the normal force curve can be flattened toward the mean. The maximum angle of attack is weakly negatively correlated with the torque fluctuations, indicating that it is favorable to keep the maximum angle of attack high in order to reduce torque fluctuations, which is in contrast to the second objective (minimizing normal load fluctuations). The maximum angle of attack is not correlated with  $C_p$ . The maximum angle of attack amplitude for all the Case 3 solutions is below the static stall angle ( $\alpha_{ss} = 12^\circ$ ), which means static stall is avoided.

Figure 8.12 labels four individuals in the Pareto front which we will consider as case studies. Solution A has the highest  $C_p$  while slightly reducing the normal load fluctuations and maintaining the torque fluctuations compared to the base case. Solution B achieves an increase in  $C_p$ , a reduction in normal load fluctuations, and a reduction in

torque fluctuations compared to the base case—it is a compromise among all three objectives. Solution C reduces the normal load fluctuations the most, while maintaining  $C_p$  and torque fluctuations. Solution D reduces the torque fluctuations the most, while also reducing the normal load fluctuations some and maintaining  $C_p$ . The power and thrust coefficients of the solutions are summarized in Table 8.4. Figure 8.16 shows the pitch function, angle of attack, blade normal force coefficient, blade tangential force coefficient, power coefficient, and thrust coefficient as a function of azimuth for these four solutions.

**Table 8.4:** Power and thrust coefficients in the three-objective optimization case.

Pitch Function	$C_p$	$C_T$
Zero pitch	0.297	0.478
Solution A (max $C_p$ )	0.328	0.438
Solution B (compromise)	0.309	0.394
Solution C (min $\sigma(Q_n)$ )	0.298	0.372
Solution D (min $\sigma(Q_t)$ )	0.298	0.390

#### Solution A: Maximum $C_p$

Solution A achieves the highest  $C_p$  (10.3% over the base case) without increasing the normal load or torque fluctuations compared to the base case. There is a small reduction in  $\sigma(Q_n)$  (1.51%) and essentially no reduction in  $\sigma(Q_t)$ . However, at least solution A does not increase the torque fluctuations compared to the base case, in contrast to the Case 1 optimal solution which achieves a 17.3% increase in  $C_p$ , but increases  $\sigma(Q_t)$  by 18.3% compared to base case. This comparison between solution A and the Case 1 optimal solution is further explored in Section 8.5.

Solution A's pitch function is shown in Figure 8.16a, compared to the base case. The shape is similar to that of the Case 1 optimal solution which maximizes  $C_p$ . The blade initially pitches inward from  $\theta \approx 0^\circ$ - $50^\circ$ , then extensively outward from  $\theta \approx 50^\circ$ - $135^\circ$ , slightly inward from  $\theta \approx 135^\circ$ - $180^\circ$ , slightly outward from  $\theta \approx 180^\circ$ - $225^\circ$ , then significantly inward from  $\theta \approx 225^\circ$ - $300^\circ$ , and finally outward from  $\theta \approx 300^\circ$ - $360^\circ$ . The blade pitch angle causes two main differences in Figures 8.16b, c, and d compared to the base case: 1) a decrease in the angle of attack, normal force coefficient, and tangential force coefficient in the middle of the upwind and downwind regions, and 2) an increase in those variables near the transitions between the upwind and downwind regions (in the azimuthal ranges around  $\theta = 0^\circ$  and  $180^\circ$ ). Because the pitch angle is positive at the beginning of the upwind region and negative at the end of the downwind region, the peak normal and tangential forces are shifted more upwind in the upwind half and more downwind in the downwind half respectively, as expected [15]. Comparing the power coefficient to the base case in Figure 8.16e, solution A avoids static stall in the upwind region. Additionally, there is a slight increase in  $C_p$  compared to the base case at the beginning of the upwind half and end of the downwind half. This also occurred in the optimal solution to Case 1, where an initial positive pitch angle from approximately  $\theta = 0^\circ$  to  $50^\circ$ , and likewise, a negative pitch angle from approximately  $\theta = 300^\circ$  to  $350^\circ$ , led to a small increase in the angle of attack, loads, and power extraction in this azimuthal range (see Section 8.2). These small increases in  $C_p$  contribute to making the average  $C_p$  of solution A higher than that of the base case, but the main factor is the prevention of static stall in the upwind region and the periods of sustained, high  $C_p$  in the middle of the upwind and downwind regions (from approximately  $\theta = 60^\circ$  to  $110^\circ$  and  $\theta = 240^\circ$  to  $300^\circ$ ). In fact, the average power coefficient is approximately the same in the upwind and downwind halves, meaning there is about equal power extraction upwind and downwind. The pattern in  $C_T$  (Figure 8.16f) is similar to  $C_p$ , as formerly described. The magnitude of the loading ( $C_n$ ,  $C_t$ ,  $C_p$ , and  $C_T$ ) of solution A is higher compared to the other Case 3 solutions, which makes sense given that this solution achieves the highest  $C_p$ . At the same time, the higher peaks in the normal force coefficient and power coefficient make its normal load fluctuations and torque fluctuations higher compared to the other Case 3 solutions.

#### Solution C: Minimum $\sigma(Q_n)$

Solution C achieves the largest reduction in normal force fluctuations, 22.1% lower than the base case. It has the same power coefficient and torque fluctuations as the base case. The pitch angle is shown in Figure 8.16a. The blade pitches outward for essentially the whole upwind half and inward for essentially the whole downwind half, with a larger pitch amplitude in the upwind half. Solution C has a relatively low pitch amplitude compared to the other Case 3 solutions, and it also has fewer oscillations. The angle of attack is significantly less than the base case throughout most of the revolution (Figure 8.16b). The angle of attack peaks near the airfoil maximum aerodynamic efficiency point ( $\alpha = 8^\circ$ ) and the static stall angle is not exceeded. The angle of attack and force coefficients for

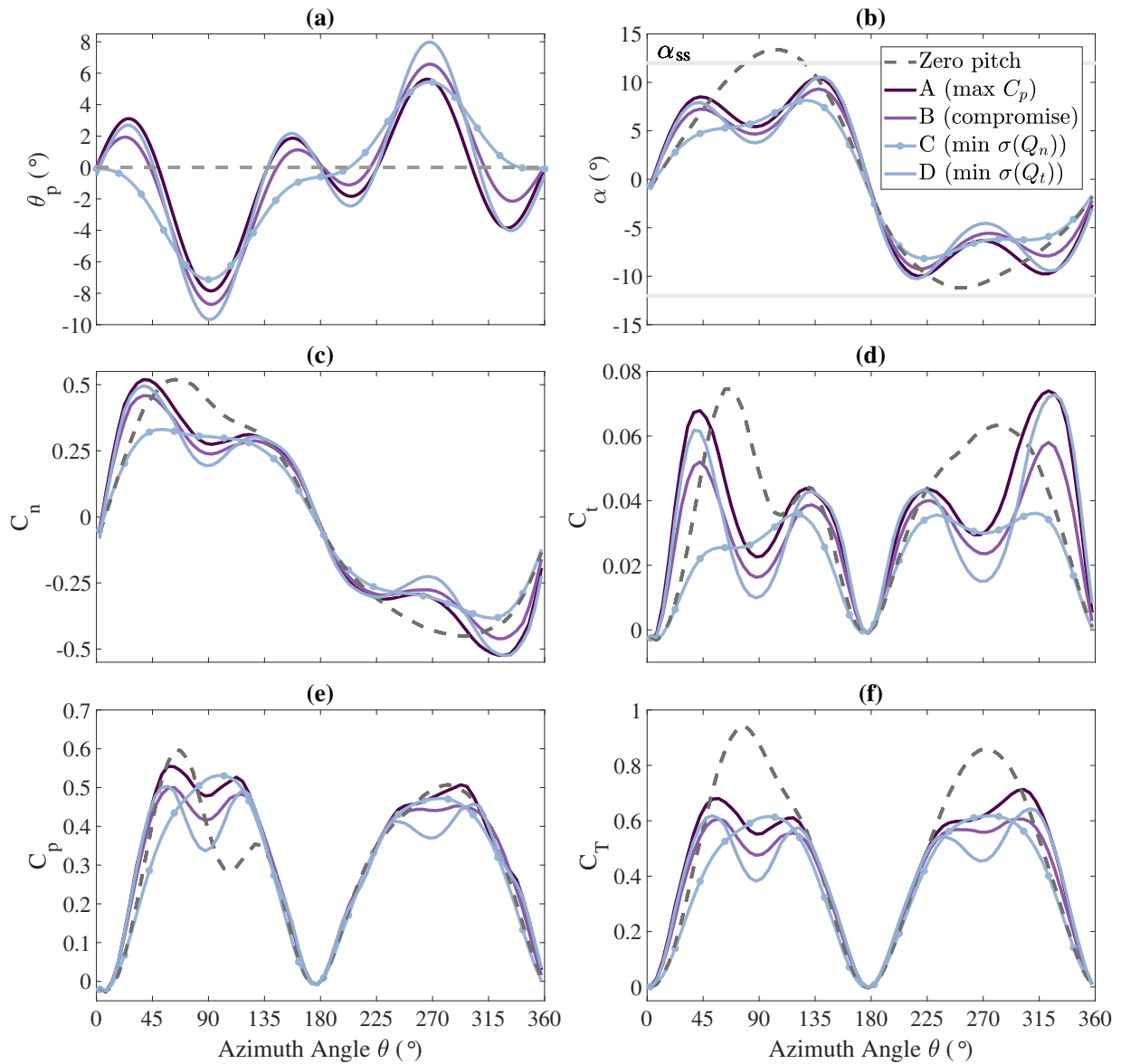


**Figure 8.16:** Example solutions to the three-objective optimization problem. Solution A increases  $C_p$  the most, while maintaining normal load and torque fluctuations. Solution C decreases normal load fluctuations the most, while maintaining power efficiency and torque fluctuations. Solution D decreases torque fluctuations the most, while maintaining power efficiency and with a slight reduction in normal load fluctuations. Solution B is a compromise, which achieves some improvement in all objectives at the same time. (a) The optimal pitch function, (b) angle of attack, (c) blade normal force coefficient, (d) blade tangential force coefficient, (e) power coefficient, and (f) thrust coefficient as a function of azimuthal angle. The forces are normalized by  $\frac{1}{2}\rho(2R)V_\infty^2$ . Values are compared to the base case with zero pitch (dashed gray line).

solution C are relatively flat compared to the other Case 3 solutions. The normal and tangential force coefficients are also significantly less than in the base case for most of the revolution (Figure 8.16c and d). The lower magnitudes of normal force mean the normal force is flattened toward the mean, and therefore the standard deviation in normal force is smaller, as desired by the second objective. The peak and average normal force is larger downwind than it is upwind. This was also seen in the Case 2 solution C, which had the lowest normal load fluctuations, reaffirming that in order to minimize the normal load fluctuations, the blade loading is shifted toward the downwind half. Similarly, for the power coefficient, shown in Figure 8.16e, even though the peak  $C_p$  in the upwind half is greater than the peak  $C_p$  in the downwind half, the average  $C_p$  is larger in the downwind half. The average thrust coefficient downwind is also larger than it is upwind, while the peak thrust coefficient is about the same upwind and downwind (Figure 8.16f).

Therefore, more energy is extracted from the wind in the downwind half compared to the upwind half. The maximum  $C_p$  for solution C is lower than that of the base case both in the upwind and downwind halves. Yet, the average power coefficient is maintained because in solution C, static stall does not occur in the upwind half. The lower peaks in  $C_p$  also help maintain the torque fluctuations compared to the base case. However, compared to solutions B and D, which decrease the torque fluctuations below the base case level, solution C does not have a dip in  $C_p$  in the middle of the upwind and downwind regions. Instead, solution C has higher, narrower peaks in  $C_p$  compared to solutions B and D, meaning the torque fluctuations are not reduced.

#### **Solution D: Minimum $\sigma(Q_t)$**

Solution D achieves the greatest reduction in rotor torque fluctuations ( $\sigma(Q_t)$ ) while maintaining the  $C_p$  of the base case. The decrease in  $\sigma(Q_t)$  is 13.9%. There is also some decrease in  $\sigma(Q_n)$  (8.38%). We will analyze the results in azimuthal sections to best understand how the pitch function achieves the objectives: first the middle of the upwind and downwind regions, then around the top and bottom of the AC.

In the middle of the upwind and downwind regions, the pitch function has a large amplitude (Figure 8.16a). In fact, solution D has the largest range in pitch angle among the Case 3 solutions: the pitch angle is near  $-10^\circ$  upwind and  $8^\circ$  downwind. The large pitching action in these azimuthal ranges causes a large decrease in the angle of attack (Figure 8.16b). Correspondingly, there is a large dip in the blade normal force and tangential force (Figure 8.16c and d). The power coefficient and thrust coefficient also decrease in the middle of the upwind and downwind regions (Figure 8.16e and f). The base case turbine also experienced a drop in  $C_p$  in the upwind region, but it was for a different reason. When there was zero pitch, stall occurred, but for solution D, the power coefficient is intentionally decreased in this region in order to reduce normal load and torque fluctuations. The maximum  $C_p$  of solution D is less than the base case in both the upwind and downwind halves. Yet, the average  $C_p$  is maintained because the average  $C_p$  upwind is greater than the base case, due to the absence of stall, while the average  $C_p$  downwind is less than the base case, due to the inward pitching maneuver. The torque fluctuations are decreased by decreasing the peaks in torque compared to the base case (best seen in the  $C_p$  curve, Figure 8.16e).

Near the top and bottom of the AC, in the ranges around  $\theta = 0^\circ$  and  $180^\circ$ , the relatively large pitch angle of solution D (Figure 8.16a) impacts the turbine loading. The blade is pitched inward in the upwind half and outward in the downwind half in these azimuthal ranges, so the magnitude of the angle of attack increases (Figure 8.16b). There is also an increase in the blade normal and tangential forces compared to the base case (Figure 8.16c and d). The difference is more pronounced at the top of the AC than at the bottom. The associated slight increases in  $C_p$  and  $C_T$  near the top of the AC are visible in Figure 8.16e and f.

In conclusion, by increasing the rotor torque where it was low (the top and bottom) and decreasing it where it was high (the middle of the upwind and downwind regions), the optimal pitch function D is able to decrease the standard deviation in torque, yet maintain the power output, compared to the base case. In particular, the average power coefficient is maintained by avoiding stall in the upwind region and extracting a little more power around the top of the AC. As for the normal load fluctuations, while there are still high peaks in normal load near the top of the AC, the substantial reductions in normal load in the middle of the upwind and downwind regions make the overall standard deviation of the normal load lower than the base case (8.38% reduction in  $\sigma(Q_n)$  compared to the base case). The peak and average blade loads of solution D are larger downwind than they are upwind; therefore, the loading is shifted relatively more downwind.

#### **Solution B: Compromise**

Solution B is an example pitch function which achieves a compromise among all three objectives. Such a solution could be of interest to implement in order to realize benefits in power output, normal load fluctuations, and torque fluctuations at the same time. With solution B, there is a 4.03% increase in  $C_p$  compared to the base case, a 12.0% decrease in  $\sigma(Q_n)$ , and a 7.62% decrease in  $\sigma(Q_t)$ . Solution B has a similar pitch function shape to solutions A (highest  $C_p$ ) and D (lowest  $\sigma(Q_t)$ ), but with different amplitudes (Figure 8.16a). In the middle of the upwind and downwind regions, solution B's pitch amplitude is larger than that of solution A but smaller than that of solution D. As such, the reduction in the angle of attack, normal force coefficient, and tangential force coefficient in the middle of the upwind and downwind regions is also in between solutions A and D (Figures 8.16b, c, and d). Reducing the forces in these regions leads to lower normal load fluctuations and torque fluctuations. As can be seen in Figure 8.16e, this also leads to a compromise-value of  $C_p$ , which is not as high as solution A, but greater than solution D. Importantly, solution B increases the average  $C_p$  compared to the base case because the outward pitching motion in the middle of the upwind region prevents static stall.

Around the top and bottom of the AC, solution B has the smallest pitch amplitude compared to solutions A and D.

Therefore, it has the smallest angle of attack, normal force coefficient, and tangential force coefficient of the three solutions in these azimuthal ranges (Figures 8.16b, c, and d). Solution B's maximum normal and tangential force coefficients in the upwind and downwind regions are smaller than those of the base case, with the exception of the downwind peak in the normal force coefficient, which is slightly above that of the base case. This is in contrast to solution A, which has higher peaks in normal force compared to the base case, and a higher  $C_p$  than solution B, but also higher normal load fluctuations than solution B. By reducing the maximum normal force experienced and decreasing the force in the middle of the upwind and downwind regions, the standard deviation of the normal force is less than that of the base case.

Additionally, for solution B, the peak in normal and tangential forces are larger downwind than they are upwind. The average normal and tangential forces are also greater downwind than upwind. And the average power coefficient is greater downwind than it is upwind. Thus, in order to reduce the load fluctuations, the pitch function shifts the loading downwind. It is also interesting to note that the power coefficient is held relatively constant for an extended period in the downwind half ( $\theta \approx 240^\circ$  to  $300^\circ$ ) (Figure 8.16e). It is beneficial for the generator to have such constant input.

## 8.5. Comparison Across Optimization Cases

Having obtained and analyzed solutions for the single-, two-, and three-objective optimization cases, we observe some similarities and differences among them. For example, the solution that maximizes  $C_p$  changes when the second objective of minimizing normal load fluctuations is added, but its shape remains relatively the same. It changes again when the third objective of minimizing torque fluctuations is added. This section compares optimal solutions across the optimization cases and further explores the effects of adding more objectives on the optimization results.

### 8.5.1. Maximizing $C_p$

The objective of maximizing  $C_p$  is always an objective in all three optimization cases. The resulting solutions which achieved the maximum  $C_p$  all have similar shapes and fluctuations in the pitch function (the inward-outward-inward-outward motion). But, their magnitudes of pitch angle are different. Adding more objectives changes the optimal pitch function when the solution also needs to minimize the normal load fluctuations, and in the three-objective case, also minimize the torque fluctuations.

#### Case 1 Optimal Solution Compared to Case 2 Solution A

Solution A of the two-objective optimization case (Case 2) achieves the greatest increase in  $C_p$  above the base case (17.3%) while maintaining the normal load fluctuations. Solution A has essentially the same  $C_p$  as the optimal solution to the single-objective optimization case (Case 1). However, the Case 1 optimal solution increases the normal load fluctuations by 1.44% compared to the base case. Therefore, in this section, we focus on the difference between solution A and the optimal solution to Case 1 to explain why solution A does not increase the normal load fluctuations while the optimal solution to Case 1 does (albeit by a small amount).

While the pitch functions of solution A and the Case 1 optimal solution have a similar shape, solution A has higher-magnitude maxima and minima in the pitch angle than the Case 1 optimal solution, except for in the last portion of the downwind region (Figure 8.17a). From approximately  $\theta = 0^\circ$  to  $50^\circ$ , the more positive pitch angle of solution A compared to the Case 1 optimal solution increases the angle of attack and loads slightly (Figures 8.17b, c, and d). The peak normal load increases slightly, which is counterintuitive to the second objective of decreasing the standard deviation of normal load. However, there are decreases in normal load elsewhere—particularly in the middle of the upwind half from  $\theta \approx 50^\circ$  to  $110^\circ$ —which help decrease the overall standard deviation in normal load. From  $\theta \approx 50^\circ$  to  $110^\circ$ , the more negative pitch angle decreases the angle of attack and normal and tangential loads compared to the Case 1 optimal solution. This also leads to a small decline in  $C_p$  in this region (Figure 8.17e). At the bottom of the AC ( $\theta \approx 140^\circ$  to  $220^\circ$ ), the solutions show very similar behavior. Finally, in the downwind half, solution A's peak normal and tangential loads are smaller than the Case 1 optimal solution's because the pitch angle and angle of attack are less negative.

Thus, the impacts on the normal load of adding the second objective are: higher normal load peak upwind, lower normal load in the middle of the upwind and downwind regions, and lower normal load peak downwind; so, when averaged, the standard deviation in normal load is smaller while the  $C_p$  is approximately the same compared to the Case 1 optimal solution. By adding the second objective to minimize normal load fluctuations, approximately the same  $C_p$  can be achieved as the single-objective case (maximizing  $C_p$ ), but adding the second objective ensures that the normal load fluctuations do not increase with respect to the base case. This is important because if one only

focuses on maximizing  $C_p$ , the optimal pitch strategy comes with an increase in the normal load fluctuations which could compromise the structural integrity of the turbine.

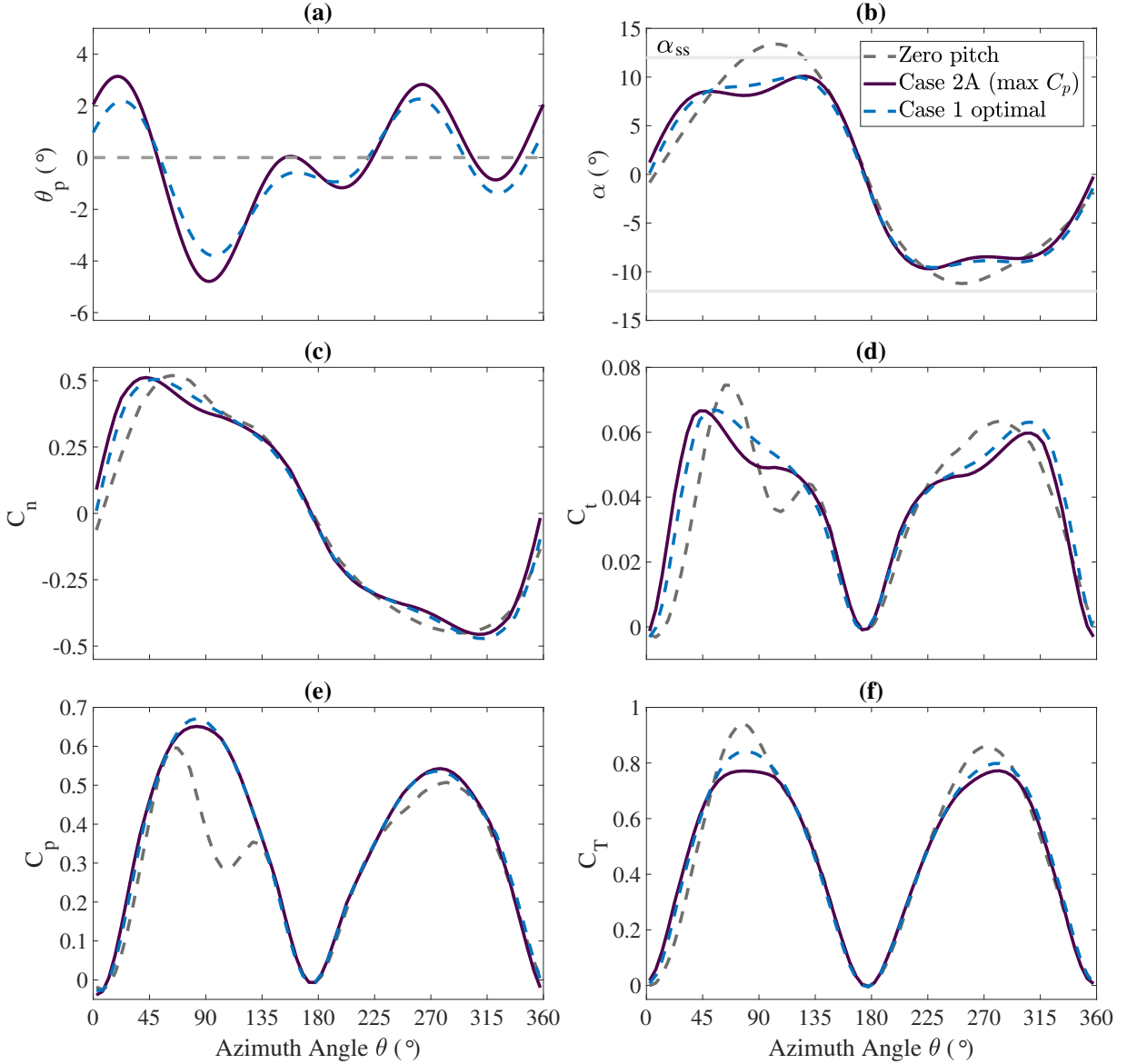


**Figure 8.17:** Case 1 optimal solution and Case 2 solution A, which achieve the maximum  $C_p$ . The Case 1 optimal solution increases the normal load fluctuations compared to the base case while Case 2 solution A does not. (a) The optimal pitch function, (b) angle of attack, (c) blade normal force coefficient, (d) blade tangential force coefficient, (e) power coefficient, and (f) thrust coefficient as a function of azimuthal angle. The forces are normalized by  $\frac{1}{2}\rho(2R)V_\infty^2$ . Values are also compared to the base case with zero pitch (dashed gray line).

#### Case 1 Optimal Solution Compared to Case 3 Solution A

Compared to the Case 1 optimal solution, solution A of the three-objective optimization case (Case 3) has a lower average  $C_p$ , but it does not increase the normal load or torque fluctuations compared to the base case. Recall that the Case 1 optimal solution increases  $C_p$  by 17.3% compared to the base case, but also increases normal load fluctuations by 1.44%, and torque fluctuations by 18.3%. Solution A increases  $C_p$  by 10.3% while decreasing the normal load fluctuations by 1.51% and maintaining the torque fluctuations of the base case. Therefore, we compare the pitch functions to understand how they lead to an increase in  $\sigma(Q_n)$  and  $\sigma(Q_t)$  for the Case 1 optimal solution but not for solution A.

The pitch function of solution A has similar oscillations to the Case 1 optimal solution. The difference in the pitch

functions is that solution A has greater pitch amplitudes (Figure 8.18a). The larger pitch angles are key to increasing the  $C_p$  while maintaining the normal load and torque fluctuations compared to the base case. The angle of attack of solution A is lower than that of the Case 1 optimal solution in the middle of the upwind and downwind regions, but it is slightly larger near the top and bottom of the AC (Figure 8.18b). Looking at Figure 8.18c, solution A has higher peaks in normal loading than the Case 1 optimal solution, both upwind and downwind, which does not help in decreasing the load fluctuations. However, these regions are important for increasing  $C_p$  while maintaining torque fluctuations (Figure 8.18e). At the same time, the average normal force coefficient of solution A in the upwind half is less than that of the Case 1 optimal solution, and it is about the same downwind as the Case 1 optimal solution, due to the relative decrease in loading in the middle of the upwind and downwind regions. So, overall, the standard deviation of the normal force is smaller for solution A.

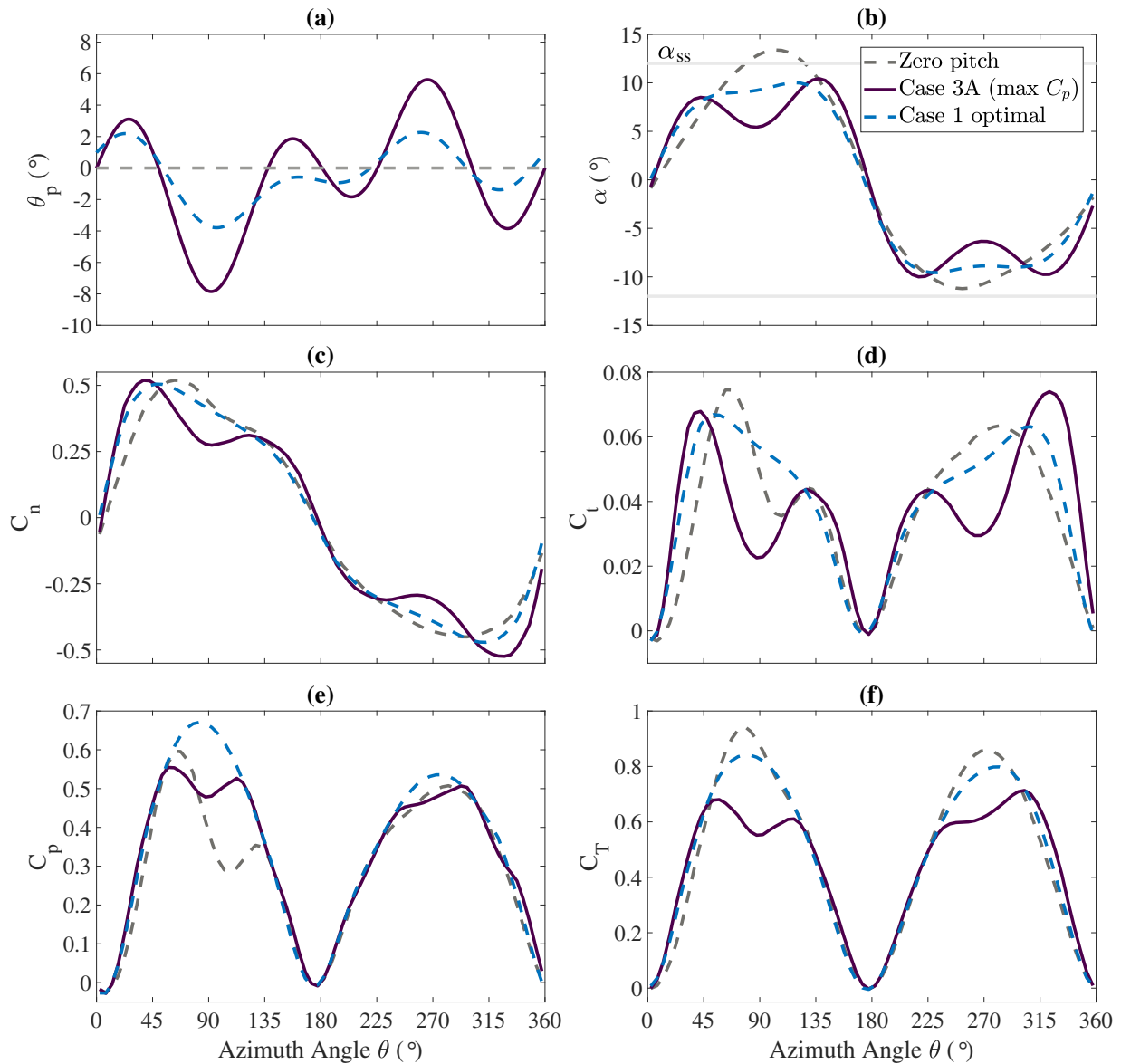


**Figure 8.18:** Case 1 optimal solution and Case 3 solution A, which achieve the maximum  $C_p$ . The Case 1 optimal solution increases the normal load and torque fluctuations compared to the base case while Case 3 solution A does not. (a) The optimal pitch function, (b) angle of attack, (c) blade normal force coefficient, (d) blade tangential force coefficient, (e) power coefficient, and (f) thrust coefficient as a function of azimuthal angle. The forces are normalized by  $\frac{1}{2}\rho(2R)V_\infty^2$ . Values are also compared to the base case with zero pitch (dashed gray line).

As for the torque fluctuations, the Case 1 optimal solution has high peaks in  $C_p$  (a representation of torque) in the upwind and downwind regions, centered around  $\theta = 90^\circ$  and  $270^\circ$ , respectively (Figure 8.18e). These peaks mean there is more power extraction, but they also increase the standard deviation of the torque. Additionally, the average  $C_p$  is higher upwind than downwind. In contrast, the  $C_p$  curve of solution A is flatter (with a dip in the upwind region) in the middle of the upwind and downwind regions, from approximately  $\theta = 60^\circ$  to  $110^\circ$  and  $\theta = 240^\circ$  to  $300^\circ$ . Solution A still maintains a relatively high  $C_p$  in the middle of the upwind and downwind regions, just not as high as the Case 1 optimal solution, which makes its standard deviation of torque smaller. It does, however, come with some sacrifice in power extraction compared to the Case 1 optimal solution. The average  $C_p$  of solution A is about the same upwind and downwind. Therefore, there is more equality in power production between the upwind and downwind halves. Visually, in Figure 8.18e, the peaks in  $C_p$  are more equal compared to those of the Case 1 optimal solution. The power generation in solution A is more spread out in order to minimize the torque fluctuations.

### 8.5.2. Minimizing $\sigma(Q_n)$

Both the two-objective and three-objective optimization problems have minimizing the rotor normal load fluctuations as an objective. However, their solutions which obtain the minimum  $\sigma(Q_n)$  differ because the three-objective case considers rotor torque fluctuations. In this section, we compare the solutions which achieve the lowest normal load fluctuations in each optimization case: the two-objective problem (solution 2 C), and the three-objective problem (solution 3 C). Solution 2 C decreases  $\sigma(Q_n)$  by 24.3% compared to the base case and solution 3 C decreases  $\sigma(Q_n)$  by 22.1%. Both solutions have the same  $C_p$  as the base case. However, solution 2 C increases the torque fluctuations by 12.2% compared to the base case while solution 3 C maintains the same torque fluctuations as the base case. Therefore, we analyze the two pitch functions to understand why one leads to an increase in torque fluctuations, while the other does not, and what leads to the small difference in normal load fluctuations between them. It is important to consider the third objective, because when only maximizing  $C_p$  and minimizing the normal load fluctuations, there is an unfavorable increase in torque fluctuations.

The 2 C and 3 C pitch functions are shown in Figure 8.19a. Both pitch angles are mostly negative upwind (outward pitching) and positive downwind (inward pitching). The functions are not as oscillatory as some of the other pitch functions seen (such as the ones which maximize  $C_p$ ), but solution 2 C has more of a simple-sinusoidal shape than solution 3 C. Solution 3 C has a larger contribution of the third harmonic than 2 C. The maximum amplitude of pitch angle is greater in solution 3 C than 2 C, and this occurs in the middle of the upwind and downwind regions. However, near the top and bottom of the AC, solution 2 C has larger pitch angles than 3 C. These differences in magnitudes between the solutions are more pronounced in the downwind half. In the upwind half, the pitch angles are similar.

The angle of attack in the upwind half is similar between solutions 2 C and 3 C (Figure 8.19b). There are some small differences caused by the difference in pitch angle: solution 3 C has a small dip in the angle of attack in the middle of the upwind region and its angle of attack is slightly higher than that of 2 C at the very beginning and end of the upwind half. The differences in angle of attack are more sizeable in the downwind half. The angle of attack of solution 3 C is smaller than that of 2 C in the middle of the downwind half, and larger than that of 2 C near the beginning and end of the downwind half. This pattern in angle of attack is also seen in the normal and tangential force coefficients (Figure 8.19c and d).

The normal force coefficients of both solutions are significantly lower than the base case (Figure 8.19c). As previously observed for both solutions 2 C and 3 C, minimizing the normal load fluctuations shifts the loading on the rotor toward the downwind half in relation to the upwind half. Comparing the two solutions, the normal force coefficient is similar between them in the upwind half. In the upwind half, the normal force coefficient of solution 3 C peaks sooner than that of 2 C and it starts decreasing later than 2 C. 3 C's normal force coefficient is held flatter in the upwind region than that of 2 C, but overall at a lower magnitude. Thus, the normal load is more spread out across the upwind region. Solution 3 C has a slightly lower peak in the normal force coefficient in the upwind half, but in the downwind half, it has a noticeably higher peak in the normal force coefficient. The upwind peak in 3 C's normal force is shifted upwind compared to 2 C and the downwind peak is shifted downwind compared to 2 C due to the relative pitch angles in these regions. The spreading out of the normal force in solution 3 C also occurs in the downwind half, but the force coefficient is less flat than it is in the upwind region. From  $\theta \approx 300^\circ$  to  $360^\circ$ , there is a significant region where solution 3 C's normal force coefficient is larger than that of 2 C. The higher overall normal load fluctuations of solution 3 C compared to 2 C is most likely due to this region.

Comparing the torque and power of the two solutions (Figure 8.19e), solution 2 C clearly has higher peaks in  $C_p$  in the middle of the upwind and downwind regions than solution 3 C. These high peaks lead to an increase in the torque fluctuations. On the other hand, solution 3 C has a slightly larger  $C_p$  than solution 2 C near the top and bottom of

the AC; this is most visible at the end of the downwind half. Thus, solution 3 C spreads out the power generation, effectively flattening the peaks in  $C_p$ , and therefore it has lower torque fluctuations than solution 2 C. Recall that for both solutions 2 C and 3 C, a shift in the power and thrust coefficients towards the downwind half was observed, in order to minimize the normal load fluctuations.

In conclusion, while there are many small differences between solutions 2 C and 3 C, the critical region is at the end of the downwind region ( $\theta \approx 300^\circ$  to  $360^\circ$ ), where solution 3 C has a smaller pitch angle than 2 C, and so a larger angle of attack and forces. This increases the normal load fluctuations compared to 2 C. It also increases the rotor torque so that the power generation is more spread out, so that overall, the average power coefficient between the two solutions is the same, while solution 3 C has lower torque fluctuations.

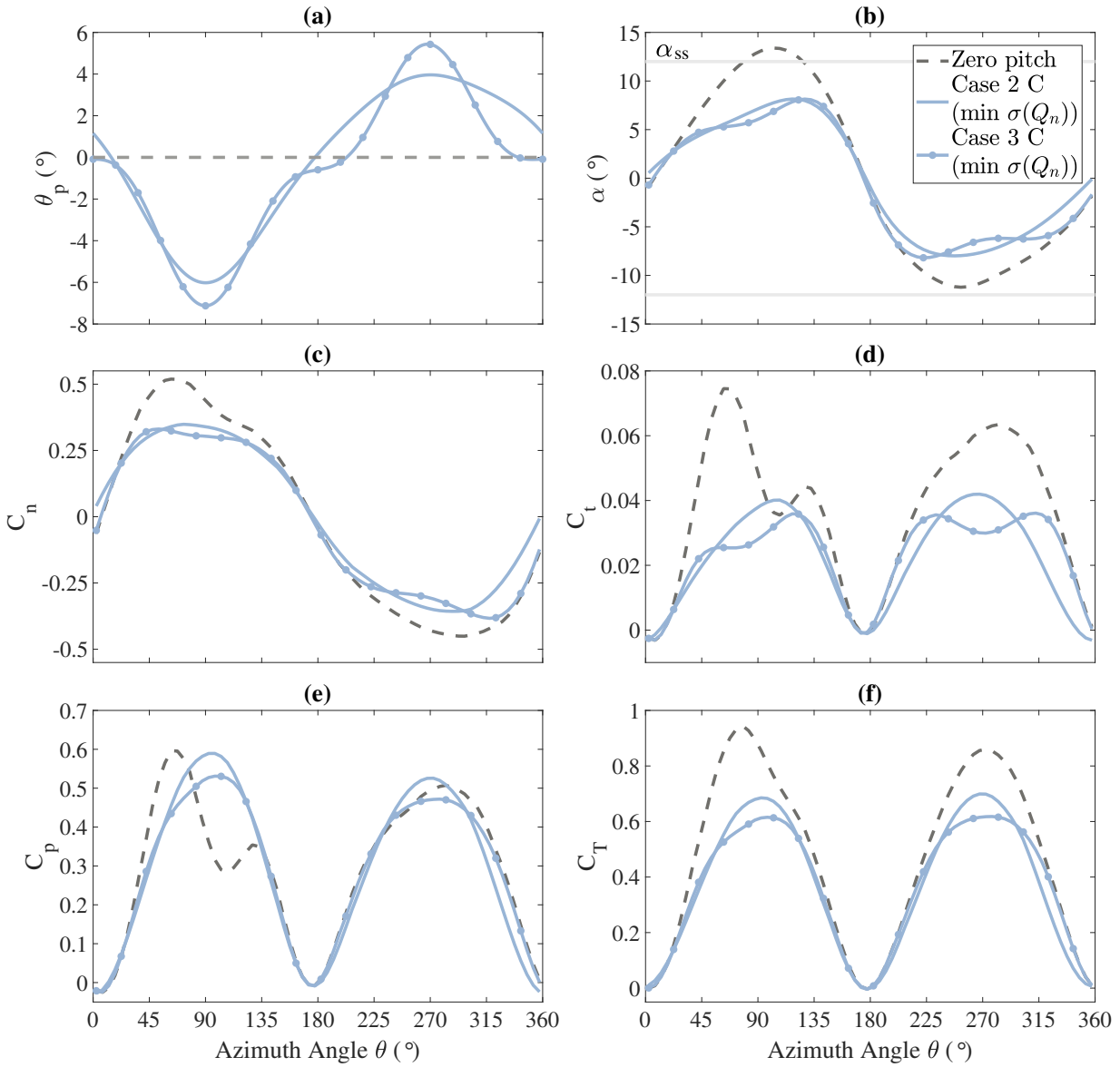


**Figure 8.19:** Case 2 solution C and Case 3 solution C, which achieve the minimum normal load fluctuations. Case 2 solution C increases the torque fluctuations compared to the base case while Case 3 solution C does not. (a) The optimal pitch function, (b) angle of attack, (c) blade normal force coefficient, (d) blade tangential force coefficient, (e) power coefficient, and (f) thrust coefficient as a function of azimuthal angle. The forces are normalized by  $\frac{1}{2}\rho(2R)V_\infty^2$ . Values are also compared to the base case with zero pitch (dashed gray line).

## 8.6. Physical Implications of the Pitching Motion

We have obtained many pitch functions that will improve a turbine's performance in theory. Before concluding which pitch strategies are the best, we briefly analyze the physical implications of applying the pitch functions to a turbine. In particular, a pitch mechanism needs to be fabricated which can actually realize the desired pitch function. The two requirements of such a pitch mechanism we explore here are the pitch angle range and the rate of pitching.

The pitch function determines the range in pitch angles that the pitch mechanism needs to be able to reach. The solution which requires the largest range capability of the pitch mechanism is Case 3 solution D, which has the minimum torque fluctuations. It requires a total range of  $17.6^\circ$ . Given the pitch angle ranges of some experimental turbines in the literature which have been built [5], [11], this is a very achievable pitch range. In general, the solutions which maximize  $C_p$  require a lower range of pitch motion. The Case 1 optimal solution has the lowest overall pitch range,  $6.06^\circ$ . Comparing the Case 1 optimal solution, Case 2 solution A, and Case 3 solution A, the maxima and minima in the pitch angle increase. This means that the pitch mechanism needs to be able to reach a larger range of pitch angles if it is also desired to decrease the rotor normal load and torque fluctuations. Furthermore, in Case 2, solution C, which minimizes the normal load fluctuations, has the largest pitch range. Thus, in order to minimize the normal load fluctuations, a larger pitch range is required. Solution 3 C has a larger pitch range than solution 2 C. So, a pitch mechanism capable of covering a large range of motion is needed if we also have the goal of minimizing torque fluctuations.

The pitch function also requires the pitch mechanism to change the pitch angle at a certain rate. Some pitch functions are more varying and require more pitch action while others do not. The solutions which maximize  $C_p$  in each optimization case (Case 1 optimal solution, Case 2 solution A, Case 3 solution A) have pitch angles which are continuously varying, and the pitch mechanism needs to be able to execute this motion. Pitch functions which are more oscillatory are more demanding on the pitch mechanism. On the other hand, solutions that minimize the normal load fluctuations are less varying. In Case 2, solution C ( $\min \sigma(Q_n)$ ), has a smaller pitch gradient than solution A ( $\max C_p$ ). This means the pitch mechanism does not need to pitch very quickly. In Case 3, solution C ( $\min \sigma(Q_n)$ ) also has the least variations and smallest pitch gradient. Lastly, the solution which has the smallest torque fluctuations, Case 3 solution D, is continuously varying and has the largest pitch gradient of all the solutions. Therefore, minimizing the torque fluctuations requires a greater pitch rate and a pitch mechanism which can pitch quickly. The required rate of pitching also has implications on the energy consumption of the pitch actuation.

## 8.7. Pitch Optimization Key Conclusions

The key conclusions with regards to the multi-objective optimization cases are:

- All three objectives of maximizing  $C_p$ , minimizing rotor normal load fluctuations, and minimizing rotor torque fluctuations are conflicting. An improvement in one objective worsens the other two objectives. There are always trade-offs involved among the solutions.
- It is possible to find solutions which achieve both/all three objectives simultaneously. There are many compromise solutions which achieve some amounts of improvement in all the objectives.
- It is important to consider the second and third objectives. Only maximizing  $C_p$  leads to an increase in unfavorable normal load and torque fluctuations. Adding more objectives affects the optimization results. The optimal pitch function(s) changes when the solution also needs to minimize the normal load fluctuations and/or minimize the torque fluctuations.
- Adding the third objective to minimize torque fluctuations reduces the attainable improvements in  $C_p$  and normal load fluctuations compared to the two-objective case.

The important observations concerning the optimal pitch functions and their effects on the objectives are:

- For the majority, the blade pitches outward in the upwind region and inward in the downwind region.
- The maximum pitch angle in the upwind half is greater than that in the downwind half, most likely because the base case angle of attack is larger upwind than downwind.
- Outward pitching in the upwind region decreases the angle of attack so that it does not exceed the static stall angle. Static stall is avoided which significantly increases power generation ( $C_p$ ) upwind. Avoiding static stall is useful for maintaining  $C_p$  when more objectives are added.
- Blade pitching keeps the angle of attack near the maximum aerodynamic efficiency point of the airfoil in the middle of the upwind and downwind regions.

- The optimal frequency of the pitch function,  $w$ , is always 1.
- The pitch functions which maximize  $C_p$  and/or minimize the torque fluctuations are continuously varying. They have a high contribution of the second- and/or third-order term.
- Slight inward pitching at the beginning of the upwind region and slight outward pitching at the end of downwind region increase the power extraction ( $C_p$ ) in these regions.
- The pitch functions which have higher power coefficients have lower maximum pitch amplitudes. The amplitude increases when the second and third objectives are added (to maintain normal load and torque fluctuations).
- The pitch functions which minimize the normal load fluctuations are less oscillating. They have lower contribution from the third-order harmonic and resemble more a first-order sinusoid. The blade pitches outward for essentially the whole upwind half and inward for essentially the whole downwind half. There are no smaller peaks near the transitions between the upwind and downwind halves, unlike in other solutions (which maximize  $C_p$  and/or minimize the torque fluctuations). The pitch functions have relatively low gradients.
- The pitch functions which have lower normal load fluctuations reduce the magnitude of the angle of attack, normal load, and tangential load during most of the revolution compared to the base case. Therefore, the normal load curve is flattened toward the mean so the standard deviation is smaller. The blade pitch helps redirect the forces in the direction tangential to the rotor, so the  $C_p$  can be maintained or slightly increased.
- The aforementioned reduction in the angle of attack and blade loads is targeted toward the upwind region as compared to the downwind region. The pitch functions which have lower normal load fluctuations have higher relative loading and power extraction downwind compared to upwind. They shift the loading on the blades and rotor toward the downwind half.
- The pitch functions which minimize the torque fluctuations have large maximum pitch amplitudes, large ranges in pitch angle, and large pitch gradients.
- The pitch functions which minimize the torque fluctuations have large pitch angles in the middle of the upwind and downwind regions, which cause a significant decrease in the angle of attack, normal force, tangential force, power coefficient, and thrust coefficient in the middle of the upwind and downwind regions.
- The pitch functions which minimize the torque fluctuations increase the angle of attack, loads, power coefficient, and thrust coefficient around the transitions between the upwind and downwind regions (top and bottom of the AC), with a greater effect around  $\theta = 0^\circ$ .
- From the above two points, the pitch functions which minimize the torque fluctuations spread out the blade loading and rotor torque in the revolution. The peaks in  $C_p$  in the upwind and downwind regions are lower and wider than in other solutions—the power generation is spread out.

The optimal objective function values obtained are:

1. In the single-objective optimization problem,  $C_p$  can increase by 17.3% compared to the base case. However, the normal load fluctuations increase by 1.44% and the torque fluctuations increase by 18.3%.
2. In the two-objective optimization problem,  $C_p$  can increase by 17.3% compared to the base case without increasing the normal load fluctuations. The normal load fluctuations can be reduced by 24.3% while maintaining the base case  $C_p$ .
3. In the three-objective optimization problem,  $C_p$  can increase by 10.3% compared to the base case without increasing the normal load fluctuations or torque fluctuations. The normal load fluctuations can decrease by 22.1% compared to the base case while maintaining the  $C_p$  and torque fluctuations. The torque fluctuations can decrease by 13.9% while maintaining the  $C_p$  and normal load fluctuations of the base case.

## Optimal Pitch Under Different Operating Condition and Turbine Design

In the previous chapter, pitch optimization was performed for one turbine geometry at one operating condition. Real turbines in operation experience different operating conditions, such as varying incoming wind speed. It is also useful for a pitch control strategy to be applicable to different turbine design parameters and sizes. Therefore, in this chapter, we study how generalizable the optimal pitch results from the previous chapter are. In particular, we study the effect of pitch with different tip speed ratios in Section 9.1 and with a different number of blades in Section 9.2.

### 9.1. Different Operating Condition: Tip Speed Ratio

In Chapter 8, optimal pitch functions were presented for the case when the tip speed ratio is 4. We now investigate whether those optimal pitch functions are applicable to a turbine operating at other tip speed ratios. This is important because it is impracticable to perform optimization for every single operating condition from a computational standpoint. We particularly consider Case 3 solution A, which is the solution that achieved the highest  $C_p$  without increasing normal load or torque fluctuations in the three-objective optimization case. We apply the optimal pitch function and execute the AC model with different tip speed ratios. The freestream wind velocity is adjusted so that the Reynolds number remains  $Re = 1 \times 10^6$ . Figure 9.1 shows the power and thrust coefficients with the optimal pitch function and without (with zero pitch) for several tip speed ratios. The optimal pitch function does not lead

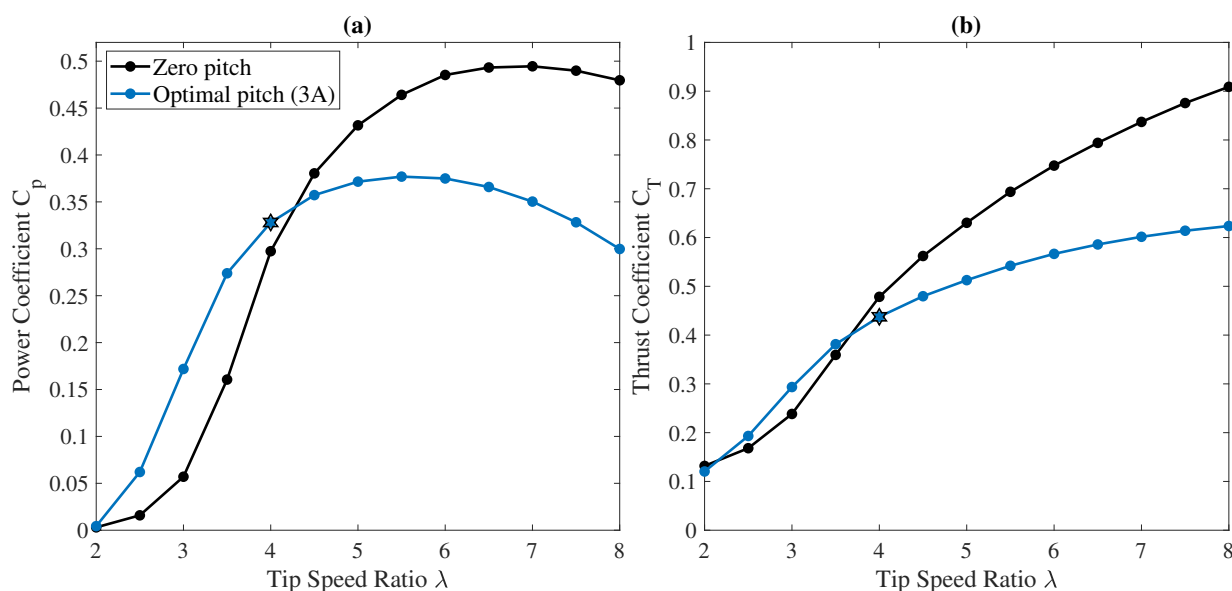


**Figure 9.1:** (a) Power coefficient and (b) thrust coefficient across tip speed ratios when the Case 3 solution A pitch function is applied, compared to the case with zero pitch. The pitch function maximized  $C_p$  without increasing normal load or torque fluctuations when  $\lambda = 4$ . The marker indicates the optimization condition.

to an improvement in  $C_p$  outside of a small range of tip speed ratios ( $\lambda = 2-4$ ). For higher tip speed ratios above 4, the optimal pitch function performs significantly worse than the zero-pitch case. Paraschivoiu *et al.* [9] and Jain and Abhishek [26] also found that the optimal pitch curve leads to a high  $C_p$  for only a narrow range of tip speed ratios. When  $\lambda \geq 4$ , the thrust coefficient with optimal pitch is less than the thrust coefficient with zero pitch. The optimal pitch function does lead to lower normal load and torque fluctuations when  $\lambda \geq 4$ , but this is inconsequential because the  $C_p$  is lower than when there is zero pitch. We conclude that the optimal pitch function found for one tip speed ratio operating condition may only be applied in a narrow range of tip speed ratios. Therefore, to account for the full range of operating tip speed ratios, multiple optimization procedures should be performed.

We now aim to understand what the optimal pitch function is for higher tip speed ratios above  $\lambda = 4$ . Considering Figure 9.1a, the maximum  $C_p$  when the Case 3 solution A pitch function is applied occurs at a tip speed ratio of  $\lambda = 5.5$ . Therefore, we re-solve the the optimization problem with this different operating condition:  $\lambda = 5.5$  and  $V_\infty = 2.957$  m/s (so the Reynolds number is still  $1 \times 10^6$ ). We only consider the three-objective optimization problem. The optimal pitch functions found when  $\lambda = 5.5$  are considerably different from the optimal pitch functions when  $\lambda = 4$ . For example, Figure 9.2 shows the pitch functions which maximize  $C_p$  (solution 3 A) at each tip speed ratio. The pitch function for  $\lambda = 5.5$  has significantly lower pitch amplitudes than the pitch function for  $\lambda = 4$ . The range in pitch angle is only  $3.04^\circ$  when  $\lambda = 5.5$  compared to  $13.47^\circ$  when  $\lambda = 4$ . When  $\lambda = 5.5$ , the minimum pitch angle is  $\theta_p = -1.57^\circ$  and it occurs around  $\theta = 90^\circ$  azimuth. The minimum pitch angle when  $\lambda = 4$  also occurs around  $\theta = 90^\circ$ , but it is much larger,  $\theta_p = -7.85^\circ$ . In both cases, the blade pitches outward in the middle of the upwind region, but when  $\lambda = 5.5$ , a large outward pitching maneuver is no longer necessary because the base case angle of attack is smaller and does not exceed the static stall angle, hence, blade pitch is not used to avoid static stall in the middle of the upwind region. The maximum pitch angles are also very different ( $\theta_p = 1.47^\circ$  vs.  $5.62^\circ$ ), but notably, they occur at very different azimuth angles. The maximum pitch angle when  $\lambda = 5.5$  occurs around  $\theta = 0^\circ$  while the maximum pitch angle when  $\lambda = 4$  occurs around  $\theta = 270^\circ$ . In fact, around  $\theta = 270^\circ$ , in the middle of the downwind region, the pitch angle is positive when  $\lambda = 4$ , but it is slightly negative when  $\lambda = 5.5$ . The outward pitching in the middle of the downwind region when  $\lambda = 5.5$  increases the angle of attack so the airfoil operates closer to its maximum aerodynamic efficiency point, thus leading to an increase in the loads and power coefficient in the downwind half. We also notice that the pitch functions have different periodicity: when  $\lambda = 4$ , there are three oscillations in the pitch function during one revolution, while when  $\lambda = 5.5$ , there are only two oscillations. So, not only the pitch amplitudes differ, but the curve shape is fundamentally not the same. The difference in the optimal pitch functions is likely due to the fact that at higher tip speed ratios, the rotational effects are more significant. The rotational velocity component is more dominating compared to the freestream wind velocity. Therefore, the variations in angle of attack are smaller so smaller adjustments in pitch angle are needed in order to attain the best performance of the airfoil. It should also be noted that when  $\lambda = 5.5$ , since the base case  $C_p$  is already quite high (0.464), only a 2.67% increase in  $C_p$  can be

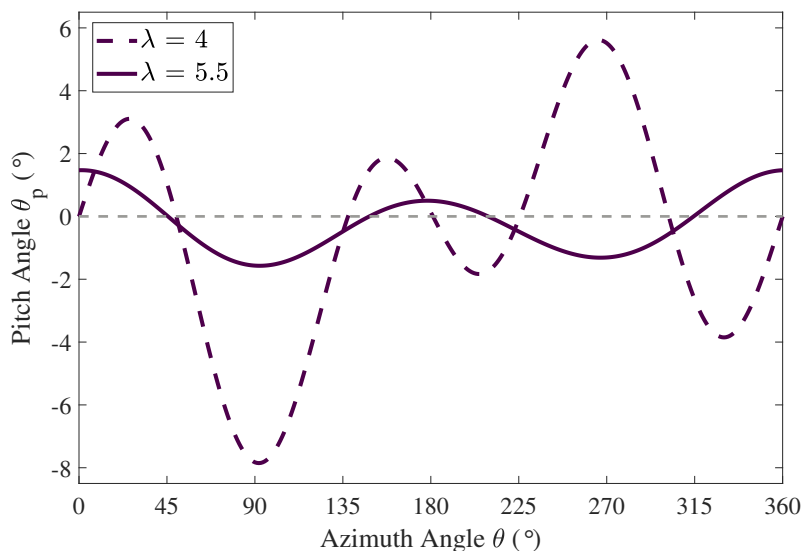


**Figure 9.2:** The optimal pitch functions for two different tip speed ratios: 4 and 5.5. The solutions are the three-objective optimization case solution A, which increases  $C_p$  the most, while maintaining normal load and torque fluctuations.

achieved with solution 3 A. Due to the second and third objectives, the pitch function still serves to even out the loading between the upwind and downwind halves.

Other authors have also found that the optimal pitch function depends on the tip speed ratio. Kiwata *et al.* [17], Benedict *et al.* [11], Hwang *et al.* [20], Jain and Abhishek [26], and Le Fouest and Mulleners [5] concluded that the pitch amplitude should be lower when the tip speed ratio is higher. We also observe that the pitch amplitude is lower when  $\lambda = 5.5$ , which is higher than  $\lambda = 4$ . When the tip speed ratio is low, the blade's angle of attack can be quite large in some azimuth ranges so it is more prone to stall. That is likely why large pitch amplitudes are needed, to decrease the angle of attack to avoid stall. Additionally, for different tip speed ratios, using individual variable pitch, Houf [24] obtained optimal pitch curves with different shapes. We also found optimal pitch curves with different shapes at the two different tip speed ratios we studied,  $\lambda = 4$  and 5.5. We conclude that the amplitude and shape of the optimal pitch function should change depending on the tip speed ratio.

To further investigate the applicability of the optimal pitch function for one tip speed ratio to other tip speed ratios, we now apply the Case 3 solution A when  $\lambda = 5.5$  to other tip speed ratios and evaluate the AC model. Again we keep the Reynolds number at  $1 \times 10^6$  and adjust the freestream wind velocity accordingly. The resulting power and thrust coefficients are presented in Figure 9.3, compared to those with zero pitch. We see that applying the Case 3 solution A pitch function to other tip speed ratios does lead to an increase in  $C_p$  over a wide range of tip speed ratios ( $\lambda = 2.5-8$ ). This means that in this case, the pitch function's effectiveness is transferable to other tip speed ratios, leading to an increase in  $C_p$  without the additional computational cost of optimization. However, this pitch function yields sub-optimal results for the other tip speed ratios. For example, the increase in  $C_p$  when  $\lambda = 4$  is not as large as when the original Case 3 solution A is applied (which was optimized for  $\lambda = 4$ ). Additionally, applying the  $\lambda = 5.5$  solution 3 A to other tip speed ratios leads to an increase in the normal load fluctuations compared to the zero-pitch case for all tip speed ratios except  $\lambda = 5.5$ , and an increase in the torque fluctuations for  $\lambda = 3-5$ . Therefore, trade-offs between computational cost and obtaining the optimal pitch functions across the entire operating range of a turbine should be considered in practical implementations of pitch control.

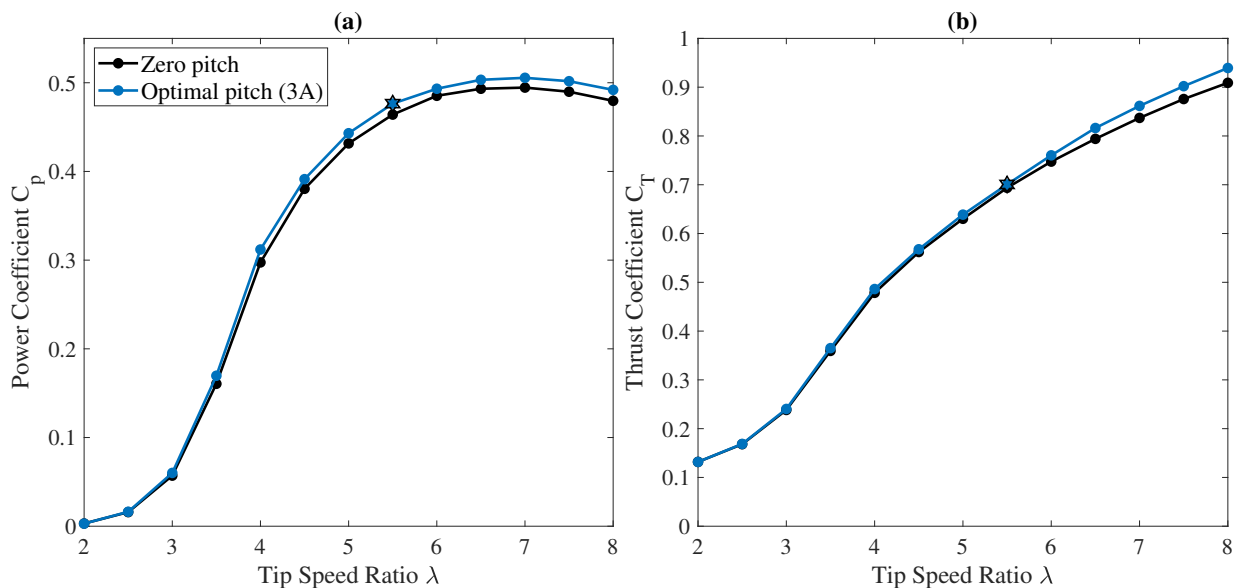


**Figure 9.3:** (a) Power coefficient and (b) thrust coefficient across tip speed ratios when the Case 3 solution A pitch function is applied, compared to the case with zero pitch. The pitch function maximized  $C_p$  without increasing normal load or torque fluctuations when  $\lambda = 5.5$ . The marker indicates the optimization condition.

This section has shown that in some cases, the optimal pitch function found for one operating condition is transferrable to other operating conditions. The pitch function may be applied to other tip speed ratios in a certain range and lead to an increase in  $C_p$ . Yet, it is not optimal for the other operating conditions. The other objectives of minimizing normal load fluctuations and torque fluctuations should also still be considered. However, being able to apply pitch functions across tip speed ratios alleviates the burden of performing optimization at each different operating condition of a turbine.

## 9.2. Different Turbine Design: Number of Blades

The turbine used in this study had two blades to be consistent with the Sandia 34-m turbine design. However, three-bladed VAWTs have less fluctuations in the turbine loads and power (torque) [6], [67]. Therefore, in this section, we explore the effect of using pitch control on a turbine with two vs. three blades. For the three-bladed turbine, we change the chord length to 0.607 m so that the rotor solidity is the same as the original turbine, and the effect of solidity on the turbine performance is removed. The rotor radius is still the same as the original turbine ( $R = 16.774$  m). The operating tip speed ratio and wind speed are also the same as for the original turbine ( $\lambda = 4$  and  $V_\infty = 4.0659$  m/s). Yet, since the chord length is different, the Reynolds number is also different. Now,  $Re = 667,000$ , so we use the SNL 0018/50 airfoil polars for  $Re = 500,000$  from QBlade [31] (the closest Reynolds number with available polars).

Table 9.1 shows the base case (zero pitch) power coefficient, normal load fluctuations, and torque fluctuations for the three-bladed case. The values are similar to those of the two-bladed case. Other authors have found that the average power and thrust coefficients are mostly insensitive to the number of blades, provided that the Reynolds number is sufficiently high, and that the tip speed ratio and rotor solidity are the same [68], [69]. The authors emphasize that the rotor solidity needs to be kept constant in order to make a valid comparison, which we have done. Sakib and Griffith [68] in reality found that for low wind speeds, such as ours, the  $C_p$  of a two-bladed turbine is slightly higher than that of a three-bladed turbine due to the lower Reynolds number of the three-bladed turbine. This may explain the small difference in the power coefficients we see for our turbines in Table 9.1. The largest difference we observe between the three blade and two blade base cases is the blade loading. The blade normal and tangential forces are significantly lower when there are three blades compared to two blades (see Figure 9.4). This is expected, because with three blades, the loading on each blade can be lower while the same total power is extracted. In terms of the range in load amplitude in one revolution, there is approximately a 35% decrease in the load range (maximum – minimum) for the three-bladed case compared to the two-bladed case. Sakib and Griffith [68] also found a significant reduction in the load range and peaks with three vs. two blades (but considering the streamwise and crosswind forces). Rezaeiha *et al.* [69] and Sakib and Griffith [68] also found that the number of blades impacts the distribution of azimuthal loading and power, which we do not observe, due to the time-averaged nature of the AC model. We conclude that the effect of the third blade is a significant reduction in the magnitude of the blade loading with minimal effect on the power generation. The lower blade loading demonstrates that it is beneficial to have three blades as opposed to two.

**Table 9.1:** Objective function values of the base case (zero pitch) with three blades.

Number of Blades	$C_p$	$\sigma(Q_n)$	$\sigma(Q_t)$
2 (original)	0.297	0.111	0.00716
3	0.284	0.107	0.00684

Having established the effect of three vs. two blades with zero pitch, we now investigate the impact of pitch control for a three-bladed turbine. The pitch optimization problem was re-solved for the three-bladed turbine. Only the three-objective problem was solved. The optimal pitch functions obtained are very similar to those obtained for the two-bladed turbine. Figure 9.4 shows the pitch functions which maximize  $C_p$  (solution A), minimize  $\sigma(Q_n)$  (solution C), and minimize  $\sigma(Q_t)$  (solution D). Also shown are the blade normal and tangential force coefficients. Because the optimal pitch curves are very similar, the blade angle of attack is also similar. However, the single-blade normal and tangential forces are significantly lower because the rotor loads are distributed among three blades instead of two. Comparing the effect of the optimal pitch curve on the loads for each turbine (two-bladed vs. three-bladed) to its respective base case reveals that the effect of the pitch function is parallel. That is, the loading with pitch is changed the same way relative to the base case in each azimuthal region.

In terms of the objective functions, the optimal pitch functions achieve very similar changes in  $C_p$ ,  $\sigma(Q_n)$ , and  $\sigma(Q_t)$  between the two-bladed and three-bladed turbines, as exhibited in Table 9.2. For example, the maximum achievable increase in  $C_p$  is 10.3% for the two-bladed turbine and 10.4% for the three-bladed turbine. The maximum decrease in torque fluctuations is 13.9% for the two-bladed turbine and 14.2% for the three-bladed turbine. The relative increase in  $C_p$  and reductions in normal load fluctuations and torque fluctuations are slightly better with three blades. Therefore, performing pitch optimization and using an optimal pitch function does provide a benefit when there are three blades. Since the optimal pitch functions found in the three-blade optimization problem are very similar to those from the two-blade optimization problem, and since the changes in the objective functions are similar, this indicates that the optimal pitch functions found for one number of blades are useful for turbines with a

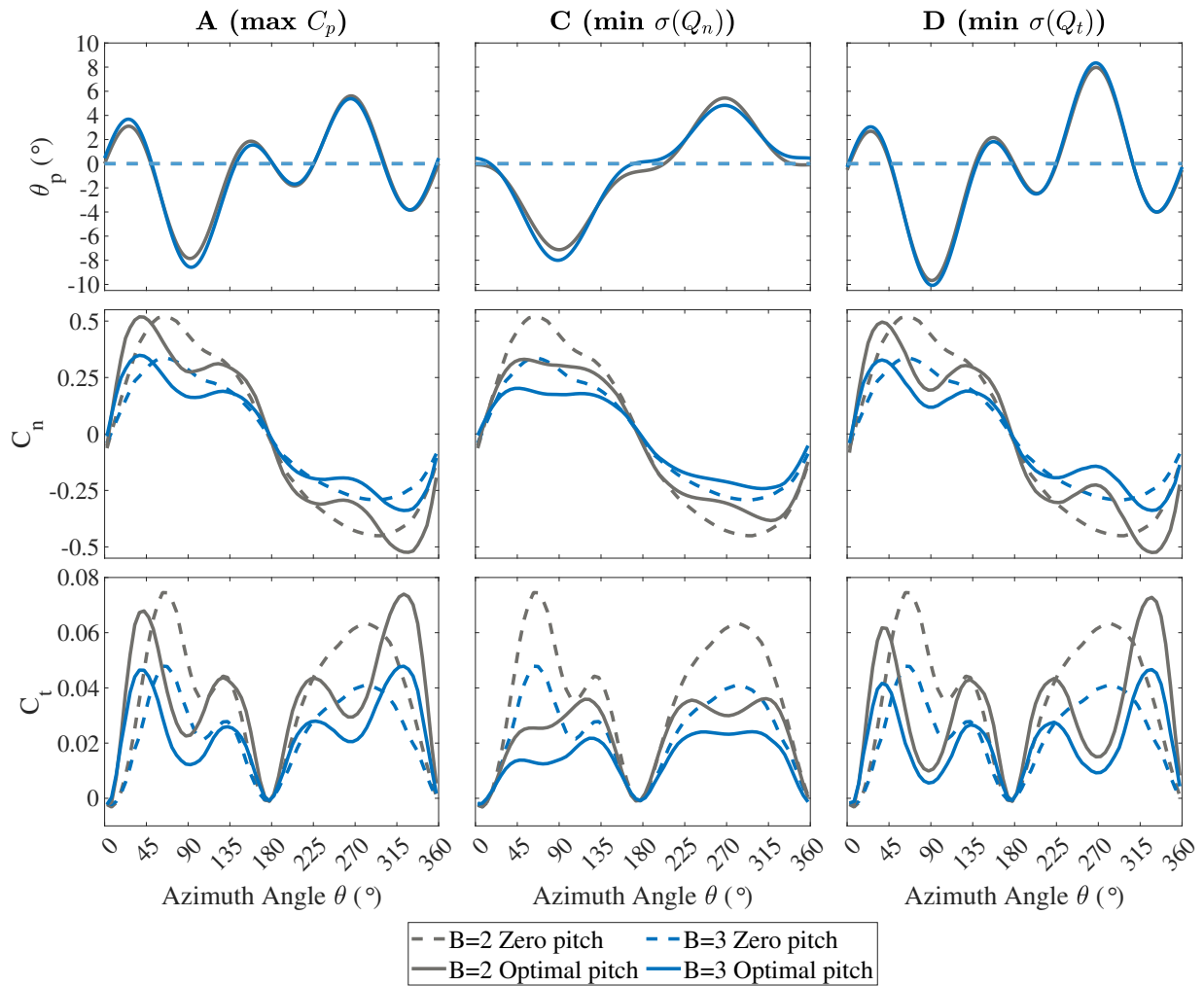


**Figure 9.4:** Solutions to the three-objective optimization problem with 2 vs. 3 blades. Solution A (left column) increases  $C_p$  the most, while maintaining normal load and torque fluctuations. Solution C (middle column) decreases normal load fluctuations the most, while maintaining power efficiency and torque fluctuations. Solution D (right column) decreases torque fluctuations the most, while maintaining power efficiency and with some reduction in normal load fluctuations. The optimal pitch function (top row), the blade normal force coefficient (middle row), and the blade tangential force coefficient (bottom row) as a function of azimuthal angle. The forces are normalized by  $\frac{1}{2}\rho(2R)V_\infty^2$ . Values are also compared to the two- and three-bladed base cases with zero pitch (dashed lines).

**Table 9.2:** Optimal objective function values for two vs. three blades. Values are shown as a percent difference with respect to the respective (three-bladed or two-bladed) base case.

Solution	3 Blades			2 Blades		
	$C_p$	$\sigma(Q_n)$	$\sigma(Q_t)$	$C_p$	$\sigma(Q_n)$	$\sigma(Q_t)$
A (max $C_p$ )	10.4%	-1.60%	-0.16%	10.3%	-1.51%	-0.15%
C (min $\sigma(Q_n)$ )	0.17%	-23.7%	-0.19%	0.09%	-22.1%	-0.13%
D (min $\sigma(Q_t)$ )	0.08%	-9.07%	-14.2%	0.14%	-8.38%	-13.9%

different number of blades (provided that the solidity and operating conditions (except Reynolds number) are the same). This finding may be influenced by the quasi-steady assumption of the AC model and the fact that it considers distributed blade loading across an actuator surface.

We conclude that the number of blades does not significantly impact the optimal pitch functions. The pitch optimization routine has a similar effect with two or three blades. This reveals that even with three blades, for which the base case

load amplitudes are much lower than with two blades, using optimal pitching can still improve the power performance and loading characteristics of the turbine compared to zero pitch. Specifically, blade pitching is useful for reducing the load and torque fluctuations even when there are three blades. Thus, it is still worthwhile to perform (multi-objective) pitch optimization when a VAWT has three blades.

# Part IV

## Conclusion

# 10

## Conclusion

This work aimed to find the optimal active blade pitch control strategy for vertical axis wind turbines to fulfill the simultaneous objectives of maximizing the power generation and minimizing detrimental fluctuations in rotor normal load and torque. The following research sub-questions were addressed:

- *What research related to optimal VAWT blade pitching has been done in the literature?*
- *What is a suitable numerical method to model vertical axis wind turbines?*
- *What functional form should be used to represent the pitch angle? What are the parameters to be optimized?*
- *What multi-objective optimization method is suitable?*
- *What is the optimal pitch function to maximize the power coefficient?*
- *What is the optimal pitch function(s) to maximize the power coefficient and minimize the rotor normal load fluctuations?*
- *What is the optimal pitch function(s) to maximize the power coefficient, minimize the rotor normal load fluctuations, and minimize the rotor torque fluctuations?*
- *How general are the optimal pitch functions? Are they applicable to different turbine designs and operating conditions? How do the optimal pitch functions change when the turbine design or operating condition changes?*

The 2D actuator cylinder (AC) model was used to model VAWTs. This model was selected for a balance between accuracy and computational efficiency. The low computational requirement of the AC model is important when performing optimization because of the many function evaluations involved. The modified linear solution of the AC was implemented in a computer code, which was validated against the literature. The model proved to be insensitive to the azimuthal resolution as long as the number of elements along the cylinder is greater than or equal to 36. We used  $N_{el} = 72$  elements ( $\Delta\theta = 5^\circ$ ) to allow for a finer resolution of pitch angle while keeping the computational time low. The control points along the AC were moved slightly inside the cylinder to avoid singularity issues. Whether the control points are inside or outside the cylinder leads to a very small difference in the solution of the AC, which should not impact the optimization results. The blade tangential force was included in the calculation of the induced velocities—which affects the solution especially in the downwind region—because it is a more complete formulation of the model and does not add computational burden. The limitations of the AC model include the absence of important unsteady aerodynamic phenomena: dynamic stall, flow curvature, dynamic inflow, and blade-vortex interaction. There is also no tower shadow, and no blade tip effects since the model is 2D. Accounting for these aerodynamic effects could impact the pitch optimization results.

The pitch angle optimization was performed considering a single turbine design at a single operating condition. The reference turbine was based on a large, real-life turbine—the Sandia 34-m turbine. It was chosen because there exists detailed documentation and publicly-available load and power data for this turbine. The properties of the turbine at the mid-span were used in the 2D actuator cylinder model. It was assumed that this was a 2D cross-section of an H-rotor, which are the more common type of VAWTs developed today, but the assumption does not affect the modeling. The turbine was operated at a lower wind speed and tip speed ratio than the rated conditions due to a constraint on the Reynolds number. The resulting wind speed is low. But, airfoil polars were only available up to  $Re = 1 \times 10^6$ .

Individual active variable blade pitch control was realized through a third-order sinusoidal function of the blade pitch

angle. This functional form was chosen considering the literature on blade pitch strategies. We investigated individual active variable pitch control because it can lead to a higher power efficiency than fixed pitch or passive variable pitch control, and the optimal pitch angle can be attained at each azimuthal angle without being constrained by a collective pitch mechanism. It was essential to have a pitch function which is continuous and smooth so that it is physically feasible to implement. A third-order sinusoid was arrived at considering the second objective of minimizing the normal load fluctuations. Therefore, a function was fit to the normal load curve. A third-order sinusoidal function could capture the shape of the normal load curve without over-fitting it. It also results in a manageable number of decision variables. There are eight decision variables (an intercept, three amplitudes, three phase shifts, and the frequency multiplier), but while the frequency multiplier was allowed to vary, the optimal frequency multiplier was always found to be one. Continuity of the pitch angle at  $\theta = 0^\circ$  and  $360^\circ$  was enforced. Since the pitch function was in the form of a third-order sinusoid, optimal pitch functions were limited to this functional form.

The unified non-dominated sorting genetic algorithm III (U-NSGA-III) was used to perform the pitch optimization. This algorithm was chosen because it yields multiple solutions, makes the methodology consistent across the optimization cases (with different numbers of objectives), is flexible to adding more objectives without needing to change the algorithm implementation, and because our optimization problems are large, non-linear problems with multiple competing objectives. The parameters used in the U-NSGA-III implementation were determined based on literature. The parameters can impact the solution of the genetic algorithm, but the optimal parameters depend on the optimization problem and are arduous to find. A parameter optimization study was not performed, which could impact the pitch optimization results.

In the optimization problems, the turbine's efficiency was quantified by the power coefficient,  $C_p$ , the rotor normal load fluctuations were quantified by the standard deviation of  $Q_n$ , and the rotor torque fluctuations were quantified by the standard deviation of  $Q_t$ . For the two- and three-objective optimization cases, it was important to constrain the objectives to be better than the base case (zero pitch) values (higher  $C_p$ , lower  $\sigma(Q_n)$ , lower  $\sigma(Q_t)$ ) to limit the search space to interesting/useful solutions. Only solutions which improve the functioning of the turbine compared to the base case were obtained. From a computational perspective, this aided in the convergence of the optimization algorithm because otherwise, the Pareto front continued to expand in unproductive directions. The algorithm was terminated based on convergence in the objective space. The termination criterion proved to ensure good convergence of the optimization results because there was very little change in the objective function values of the solution/Pareto front for many generations near the end of the simulation. Based on the termination criterion, there were 8,900, 20,000, and 39,600 total function evaluations for the single-, two-, and three-objective optimization cases, respectively.

Many pitch functions were found which improve all three objectives compared to the base case with zero pitch. In general, all the optimal pitch functions involve pitching the blade outward in the upwind region and inward in the downwind region, with a greater maximum pitch angle upwind than downwind. Outward pitching in the upwind region decreases the angle of attack so that static stall is avoided, which significantly increases the power generation upwind and is important for maintaining/increasing  $C_p$ .

In order to maximize the power coefficient, the pitch function should have many oscillations: the blade should pitch slightly inward from  $\theta \approx 0^\circ$ - $50^\circ$ , outward from  $\theta \approx 50^\circ$ - $140^\circ$ , slightly inward from  $\theta \approx 140^\circ$ - $180^\circ$ , slightly outward from  $\theta \approx 180^\circ$ - $220^\circ$ , inward from  $\theta \approx 220^\circ$ - $300^\circ$ , and slightly outward from  $\theta \approx 300^\circ$ - $350^\circ$ . The amplitude of the pitch function need not be too large, but it should be increased so that normal load and torque fluctuations do not increase with respect to the base case. The slight pitching around  $\theta = 0^\circ \pm 50^\circ$  increases the power generation in this region.

In order to minimize the normal load fluctuations (while maintaining the power coefficient), the blade should pitch outward for essentially the whole upwind half ( $\theta = 0^\circ$ - $180^\circ$ ) and inward for essentially the whole downwind half ( $\theta = 180^\circ$ - $360^\circ$ ). Such a pitch curve reduces the magnitude of the angle of attack, normal load, and tangential load compared to the base case almost throughout the entire revolution; so that the normal load curve is flattened toward the mean. The loading on the blades and rotor are shifted toward the downwind half compared to the upwind half. While the blade forces are relatively small, the blade pitch helps redirect them in the direction tangential to the rotor, so the power generation can be maintained or slightly increased.

In order to minimize the torque fluctuations (while maintaining the power coefficient and normal load fluctuations), the pitch function should oscillate just as it did for maximizing  $C_p$ —inward-outward-inward-outward-inward-outward—but with a larger amplitude. The pitch function spreads out the blade loading and rotor torque (power generation) over the revolution. Large pitch angles in the middle of the upwind and downwind regions cause a significant decrease in the angle of attack, normal force, tangential force, power coefficient, and thrust coefficient. The pitch function increases these same parameters around the transitions between the upwind and downwind regions,

especially around  $\theta = 0^\circ$ .

It has been shown that blade pitch control can increase the power efficiency, reduce normal load fluctuations, and reduce torque fluctuations (simultaneously). Still, these objectives are conflicting and there are trade-offs among the solutions. It is important to consider all of the objectives because only maximizing  $C_p$  led to an increase in unfavorable normal load and torque fluctuations. Adding objectives changed the optimal pitch function(s).

The optimal objective function values obtained are as follows:

1. In the single-objective optimization problem,  $C_p$  can increase by 17.3% compared to the base case. However, the normal load fluctuations increase by 1.44% and the torque fluctuations increase by 18.3%.
2. In the two-objective optimization problem,  $C_p$  can increase by 17.3% compared to the base case without increasing the normal load fluctuations. The normal load fluctuations can be reduced by 24.3% while maintaining the base case  $C_p$ .
3. In the three-objective optimization problem,  $C_p$  can increase by 10.3% compared to the base case without increasing the normal load fluctuations or torque fluctuations. The normal load fluctuations can decrease by 22.1% compared to the base case while maintaining the  $C_p$  and torque fluctuations. The torque fluctuations can decrease by 13.9% while maintaining the  $C_p$  and normal load fluctuations of the base case.

The optimal pitch functions were found to be applicable to other operating condition and turbine design in some cases. When the optimal pitch function which maximizes  $C_p$  for one tip speed ratio is applied to other tip speed ratios, an increase in  $C_p$  can be realized in some ranges of  $\lambda$ , without the additional computational expense of optimization. Considering all three objectives, obtaining the optimal pitch function(s) for every tip speed ratio should be weighed against the computational requirement of performing optimization. The optimal pitch functions for different tip speed ratios are considerably different, notably a decrease in the pitch amplitude with higher tip speed ratio and a change in the shape of the pitch curve. When the number of blades of the turbine changes from two to three, the optimal pitch functions are very similar to those obtained for the two-bladed turbine, and they achieve very similar changes in the objective functions. The effect of the third blade is a significant reduction in the magnitude of the blade normal and tangential loads, while the optimal pitch curves have a similar effect on the blade loading compared to the zero-pitch case for both the two-bladed and three-bladed turbine. The optimal pitch functions found for one number of blades are useful for turbines with a different number of blades, provided that the solidity and tip speed ratio are the same. Pitch optimization is still beneficial for improving the power efficiency and reducing the normal load and torque fluctuations of a turbine when there are three blades.

Vertical axis wind turbines have two main promising applications in sustainable energy systems: multi-megawatt floating offshore turbines and small-scale urban turbines. Pitch control can address some weaknesses of VAWTs and improve their performance in these applications. The results of this study illuminate the benefits of using active individual variable blade pitching. Implementing an optimal pitch function found in this study can increase the efficiency of the turbine, thereby increasing the overall power generated by the turbine; reduce the normal load fluctuations, which can lengthen the fatigue lifetime; and reduce the torque fluctuations, to improve loading on the drivetrain and improve power quality. Importantly, these objectives can be achieved at the same time. Blade pitching can lead to a significant increase in the power coefficient while not compromising the structural integrity of the turbine. Or, if fatigue is more of a concern, the load fluctuations can be reduced without sacrificing power production. Improving the performance and operation of VAWTs in these ways could make them more viable and attractive on a commercial scale.

# Recommendations

Building off of the pitch control optimization conducted in this study, there are several recommendations to extend and refine the research in the future.

## Recommendation 1

This study focused on the effect of pitch on a single rotor. Meanwhile, many wind turbines do not operate in isolation but are part of a larger wind farm. The wake from one wind turbine impacts the performance of downwind turbines. Usually this impact is detrimental, but for VAWTs, it has been shown that certain rotor configurations in a wind farm can increase the overall farm efficiency [11]. Therefore, it is recommended to study the effect of the optimal pitch functions on the wake development. This could give insight into the impact of a turbine with pitching on a downwind turbine. The pitch function could also be optimized considering the wake recovery as an additional objective. This likely requires a higher-fidelity model than the actuator cylinder to better model the wake. This type of pitch optimization could, for example, maximize the power production of multiple rotors.

## Recommendation 2

Maximizing the power coefficient was an objective in all three optimization cases in this study. The power coefficient was calculated considering the aerodynamic power of the rotor. However, the fact that power is required to pitch the blades was not considered. Therefore, it is recommended to minimize the pitch load duty cycle as an additional objective. The pitch load duty cycle is a measure of how much energy is consumed in the pitch actuation, and is given by  $\int_0^{2\pi} \dot{\theta} C_m d\theta$ , where  $\dot{\theta}$  is the blade pitch rate and  $C_m$  is the airfoil pitching moment coefficient (about the 1/4-chord). This objective should be added because it is important to consider that while blade pitching can have an advantageous impact on turbine power and loads, actuating the blade comes with an energy cost. The objective was not included in the present study because the moment coefficients of the SNL 0018/50 airfoil were not available. Adding the objective would be straightforward using the U-NSGA-III algorithm, but it requires the airfoil moment coefficients, so a different turbine (or at least airfoil) would have to be used. As another approach, the power consumed by the pitching motion can be subtracted from the generated power in the first objective. This is done by Le Fouest and Mulleners [5] who maximize the power coefficient which already includes the power expense of the pitch actuation; the net power is the power generated by the blade minus the power consumed by the pitch actuation, and maximizing it is one objective.

## Recommendation 3

This study used the 2D actuator cylinder model to model VAWTs. This is an accurate model within its assumptions of 2D and quasi-steady conditions, and it is computationally efficient [7], [8], [28], [37]. However, it does have some physical simplifications. These include neglecting dynamic stall, flow curvature, and dynamic inflow. These aerodynamic phenomena can be incorporated with additional corrections to make the AC model more accurate and a better representation of reality [4], [8], [37]. Therefore, it is recommended to improve the AC model implementation used in this study by including models for dynamic stall, flow curvature, and dynamic inflow. Doing so would require a thorough literature review of the existing methods, selecting a method with justification of the choice, implementing it in the computer code, and validating the model. Then the pitch optimization routine can be executed again. We particularly recommend implementing dynamic stall because the optimal pitch functions found in this study involve pitching the blade frequently, so dynamic stall is likely a relevant phenomenon. It should also be considered that adding dynamic stall to the AC model could (significantly) increase the computational requirement of the optimization routine [24].

**Recommendation 4**

In Chapter 9, we explored the effect of pitch control at different tip speed ratios. It is recommended to extend this investigation. As a first step, it would be useful to further investigate the transferability of optimal pitch functions to other tip speed ratios. For example, studying whether the tip speed ratio which was used for optimization is related to the range for which the optimal pitch function is applicable. As a second step, it would be useful to optimize the pitch function considering multiple tip speed ratios. Recognizing that the operating condition of a turbine constantly changes (due to varying incoming wind speed), an objective could be added which maximizes the power coefficient integrated across tip speed ratios. Developing a pitch control strategy which improves the turbine performance over a wide range of tip speed ratios would be valuable because it would yield the overall maximum power output of a turbine in operation.

**Recommendation 5**

The generalizability study of the pitch functions was limited to different tip speed ratios and number of blades. It is recommended to also study other operating conditions and turbine designs. The optimization routine performed in this study could be repeated for different Reynolds numbers, rotor solidities, and airfoils, with the goal of finding a relationship between the optimal pitch function and turbine design and/or operating condition. It should be understood if the optimal pitch functions are applicable to other turbine designs and operating conditions and/or how they change with different turbine designs and operating conditions. We were not able to study the effect of Reynolds number in this study due to a limitation of available airfoil polars.

# References

- [1] T. M. Letcher, “Chapter 1 - why wind energy,” in *Wind Energy Engineering (Second Edition)*, T. M. Letcher, Ed., Second Edition, Academic Press, 2023, pp. 3–10, ISBN: 978-0-323-99353-1. DOI: <https://doi.org/10.1016/B978-0-323-99353-1.00025-6>. [Online]. Available: <https://www.sciencedirect.com/science/article/pii/B9780323993531000256>.
- [2] International Energy Agency. “Wind.” (2024), [Online]. Available: <https://www.iea.org/energy-system/renewables/wind> (visited on 02/17/2025).
- [3] E. Möllerström, P. Gipe, J. Beurskens, and F. Ottermo, “A historical review of vertical axis wind turbines rated 100 kw and above,” *Renewable and Sustainable Energy Reviews*, vol. 105, pp. 1–13, 2019, ISSN: 1364-0321. DOI: <https://doi.org/10.1016/j.rser.2018.12.022>. [Online]. Available: <https://www.sciencedirect.com/science/article/pii/S1364032118308153>.
- [4] D. De Tavernier, “Aerodynamic advances in vertical-axis wind turbines,” Doctoral thesis, Delft University of Technology, Delft, the Netherlands, 2021. DOI: <https://doi.org/10.4233/uuid:7086f01f-28e7-4e1b-bf97-bb3e38dd22b9>. [Online]. Available: <https://repository.tudelft.nl/record/uuid:7086f01f-28e7-4e1b-bf97-bb3e38dd22b9>.
- [5] S. Le Fouest and K. Mulleners, “Optimal blade pitch control for enhanced vertical-axis wind turbine performance,” *Nature Communications*, vol. 15, pp. 1–13, 1 Mar. 2024, ISSN: 2041-1723. DOI: 10.1038/s41467-024-46988-0. [Online]. Available: <https://www.nature.com/articles/s41467-024-46988-0>.
- [6] A. Rezaeiha, I. Kalkman, and B. Blocken, “Effect of pitch angle on power performance and aerodynamics of a vertical axis wind turbine,” *Applied Energy*, vol. 197, pp. 132–150, Jul. 2017, ISSN: 0306-2619. DOI: 10.1016/J.APENERGY.2017.03.128. [Online]. Available: <https://www.sciencedirect.com/science/article/pii/S0306261917303744>.
- [7] H. A. Madsen, T. J. Larsen, U. S. Paulsen, and L. Vita, “Implementation of the actuator cylinder flow model in the hawc2 code for aeroelastic simulations on vertical axis wind turbines,” in *51st AIAA Aerospace Sciences Meeting including the New Horizons Forum and Aerospace Exposition 2013*, Jan. 2013, ISBN: 978-1-62410-181-6. DOI: 10.2514/6.2013-913. [Online]. Available: <https://orbit.dtu.dk/en/publications/implementation-of-the-actuator-cylinder-flow-model-in-the-hawc2-c>.
- [8] Z. Cheng, H. A. Madsen, Z. Gao, and T. Moan, “Aerodynamic modeling of floating vertical axis wind turbines using the actuator cylinder flow method,” *Energy Procedia*, vol. 94, pp. 531–543, Sep. 2016, 13th Deep Sea Offshore Wind R&D Conference, EERA DeepWind’2016, ISSN: 1876-6102. DOI: 10.1016/J.EGYPRO.2016.09.232. [Online]. Available: <https://www.sciencedirect.com/science/article/pii/S1876610216309195>.
- [9] I. Paraschivoiu, O. Trifu, and F. Saeed, “H-darrieus wind turbine with blade pitch control,” *International Journal of Rotating Machinery*, vol. 2009, no. 1, p. 505 343, 2009. DOI: <https://doi.org/10.1155/2009/505343>. eprint: <https://onlinelibrary.wiley.com/doi/pdf/10.1155/2009/505343>. [Online]. Available: <https://onlinelibrary.wiley.com/doi/abs/10.1155/2009/505343>.
- [10] M. Elkhoury, T. Kiwata, and E. Aoun, “Experimental and numerical investigation of a three-dimensional vertical-axis wind turbine with variable-pitch,” *Journal of Wind Engineering and Industrial Aerodynamics*, vol. 139, pp. 111–123, 2015, ISSN: 0167-6105. DOI: <https://doi.org/10.1016/j.jweia.2015.01.004>. [Online]. Available: <https://www.sciencedirect.com/science/article/pii/S0167610515000136>.
- [11] M. Benedict, V. Lakshminarayan, J. Pino, and I. Chopra, “Aerodynamics of a small-scale vertical-axis wind turbine with dynamic blade pitching,” *AIAA Journal*, vol. 54, no. 3, pp. 924–935, 2016. DOI: 10.2514/1.J052979. eprint: <https://doi.org/10.2514/1.J052979>. [Online]. Available: <https://doi.org/10.2514/1.J052979>.

- [12] Y. Liang, L. Zhang, E. Li, and F. Zhang, "Blade pitch control of straight-bladed vertical axis wind turbine," *Journal of Central South University*, vol. 23, no. 5, pp. 1106–1114, May 2016. DOI: 10.1007/s11771-016-0360-0. [Online]. Available: <https://doi.org/10.1007/s11771-016-0360-0>.
- [13] G. Erfort, T. W. von Backström, and G. Venter, "Reduction in the torque ripple of a vertical axis wind turbine through foil pitching optimization," *Wind Engineering*, vol. 44, no. 2, pp. 115–124, 2019. DOI: 10.1177/0309524X19836711. eprint: <https://doi.org/10.1177/0309524X19836711>. [Online]. Available: <https://doi.org/10.1177/0309524X19836711>.
- [14] B. LeBlanc and C. Ferreira, "Estimation of blade loads for a variable pitch vertical axis wind turbine from particle image velocimetry," *Wind Energy*, vol. 25, no. 2, pp. 313–332, 2022. DOI: <https://doi.org/10.1002/we.2674>. eprint: <https://onlinelibrary.wiley.com/doi/pdf/10.1002/we.2674>. [Online]. Available: <https://onlinelibrary.wiley.com/doi/abs/10.1002/we.2674>.
- [15] B. LeBlanc and C. Ferreira, "Estimation of blade loads for a variable pitch vertical axis wind turbine with strain gage measurements," *Wind Energy*, vol. 25, no. 6, pp. 1030–1045, 2022. DOI: 10.1002/we.2713. eprint: <https://onlinelibrary.wiley.com/doi/pdf/10.1002/we.2713>. [Online]. Available: <https://onlinelibrary.wiley.com/doi/abs/10.1002/we.2713>.
- [16] L. Lazauskas, "Three pitch control systems for vertical axis wind turbines compared," *Wind Engineering*, vol. 16, pp. 269–282, Jan. 1992.
- [17] T. Kiwata, T. Yamada, T. Kita, S. Takata, N. Komatsu, and S. Kimura, "Performance of a vertical axis wind turbine with variable-pitch straight blades utilizing a linkage mechanism," *Journal of Environment and Engineering*, vol. 5, pp. 213–225, Apr. 2010. DOI: 10.1299/jee.5.213. [Online]. Available: [https://www.jstage.jst.go.jp/article/jee/5/1/5\\_1\\_213/\\_article](https://www.jstage.jst.go.jp/article/jee/5/1/5_1_213/_article).
- [18] Y. Staelens, F. Saeed, and I. Paraschivoiu, "A straight-bladed variable-pitch vawt concept for improved power generation," in *ASME 2003 Wind Energy Symposium*, Jan. 2003. DOI: 10.1115/WIND2003-524.
- [19] Y. Guo, X. Li, L. Sun, Y. Gao, Z. Gao, and L. Chen, "Aerodynamic analysis of a step adjustment method for blade pitch of a vawt," *Journal of Wind Engineering and Industrial Aerodynamics*, vol. 188, pp. 90–101, 2019, ISSN: 0167-6105. DOI: <https://doi.org/10.1016/j.jweia.2019.02.023>. [Online]. Available: <https://www.sciencedirect.com/science/article/pii/S0167610518308808>.
- [20] I. S. Hwang, Y. H. Lee, and S. J. Kim, "Optimization of cycloidal water turbine and the performance improvement by individual blade control," *Applied Energy*, vol. 86, no. 9, pp. 1532–1540, 2009, ISSN: 0306-2619. DOI: <https://doi.org/10.1016/j.apenergy.2008.11.009>. [Online]. Available: <https://www.sciencedirect.com/science/article/pii/S0306261908002778>.
- [21] L. Zhang, Y. Liang, E. Li, S. Zhang, and J. Guo, "Vertical axis wind turbine with individual active blade pitch control," in *2012 Asia-Pacific Power and Energy Engineering Conference*, 2012, pp. 1–4. DOI: 10.1109/APPEEC.2012.6307108.
- [22] S. Abbaszadeh, S. Hoerner, T. Maître, and R. Leidhold, "Experimental investigation of an optimised pitch control for a vertical-axis turbine," *IET Renewable Power Generation*, vol. 13, no. 16, pp. 3106–3112, 2019. DOI: <https://doi.org/10.1049/iet-rpg.2019.0309>. eprint: <https://ietresearch.onlinelibrary.wiley.com/doi/pdf/10.1049/iet-rpg.2019.0309>. [Online]. Available: <https://ietresearch.onlinelibrary.wiley.com/doi/abs/10.1049/iet-rpg.2019.0309>.
- [23] C. Rainone, D. De Siero, L. Iuspa, A. Viviani, and G. Pezzella, "A numerical procedure for variable-pitch law formulation of vertical-axis wind turbines," *Energies*, vol. 16, no. 1, 2023, ISSN: 1996-1073. DOI: 10.3390/en16010536. [Online]. Available: <https://www.mdpi.com/1996-1073/16/1/536>.
- [24] D. Houf, "Active pitch control of a vertical axis wind turbine," Master of Science Thesis, Delft University of Technology and Technical University of Denmark, Sep. 2016. [Online]. Available: <https://repository.tudelft.nl/record/uuid:fde12a64-40b4-488b-8b7e-557191e2f669>.
- [25] C. Li, Y. Xiao, Y.-I. Xu, Y.-x. Peng, G. Hu, and S. Zhu, "Optimization of blade pitch in h-rotor vertical axis wind turbines through computational fluid dynamics simulations," *Applied Energy*, vol. 212, pp. 1107–1125, 2018, ISSN: 0306-2619. DOI: <https://doi.org/10.1016/j.apenergy.2017.12.035>. [Online]. Available: <https://www.sciencedirect.com/science/article/pii/S0306261917317531>.

- [26] P. Jain and A. Abhishek, "Performance prediction and fundamental understanding of small scale vertical axis wind turbine with variable amplitude blade pitching," *Renewable Energy*, vol. 97, pp. 97–113, 2016, ISSN: 0960-1481. DOI: <https://doi.org/10.1016/j.renene.2016.05.056>. [Online]. Available: <https://www.sciencedirect.com/science/article/pii/S0960148116304669>.
- [27] S. Horb, R. Fuchs, A. Immas, F. Silvert, and P. Deglaire, "Variable pitch control for vertical-axis wind turbines," *Wind Engineering*, vol. 42, no. 2, pp. 128–135, 2018. DOI: 10.1177/0309524X18756972. eprint: <https://doi.org/10.1177/0309524X18756972>. [Online]. Available: <https://doi.org/10.1177/0309524X18756972>.
- [28] D. De Tavernier, C. Ferreira, and A. Goude, "Vertical-axis wind turbine aerodynamics," in *Handbook of Wind Energy Aerodynamics*, B. Stoevesandt, G. Schepers, P. Fuglsang, and Y. Sun, Eds. Cham: Springer International Publishing, 2022, pp. 1317–1361, ISBN: 978-3-030-31307-4. DOI: 10.1007/978-3-030-31307-4\_64. [Online]. Available: [https://doi.org/10.1007/978-3-030-31307-4\\_64](https://doi.org/10.1007/978-3-030-31307-4_64).
- [29] H. A. Madsen, "The actuator cylinder - a flow model for vertical axis wind turbines," PhD Thesis, Aalborg University Centre, Jan. 1982. DOI: 10.13140/RG.2.1.2512.3040. [Online]. Available: [https://www.researchgate.net/publication/281449635\\_The\\_Actuator\\_Cylinder\\_-\\_A\\_Flow\\_Model\\_for\\_Vertical\\_Axis\\_Wind\\_Turbines](https://www.researchgate.net/publication/281449635_The_Actuator_Cylinder_-_A_Flow_Model_for_Vertical_Axis_Wind_Turbines).
- [30] D. De Tavernier and C. Ferreira, "An extended actuator cylinder model: Actuator-in-actuator cylinder (ac-squared) model," *Wind Energy*, vol. 22, no. 8, pp. 1058–1070, 2019. DOI: 10.1002/we.2340. eprint: <https://onlinelibrary.wiley.com/doi/pdf/10.1002/we.2340>. [Online]. Available: <https://onlinelibrary.wiley.com/doi/abs/10.1002/we.2340>.
- [31] D. Marten, "Qblade: A modern tool for the aeroelastic simulation of wind turbines," Doctoral Thesis, Technical University Berlin, 2020. DOI: 10.14279/depositonce-10646. [Online]. Available: <https://depositonce.tu-berlin.de/items/97024e53-c455-485a-9134-94ff77ac6391>.
- [32] T. D. Ashwill, "Measured data for the sandia 34-meter vertical axis wind turbine," Sandia National Labs., Albuquerque, NM (United States), Tech. Rep., Jul. 1992. [Online]. Available: <https://www.osti.gov/biblio/10170111>.
- [33] H. Seada and K. Deb, "U-nsga-iii: A unified evolutionary algorithm for single, multiple, and many-objective optimization," in *Evolutionary Multi-Criterion Optimization*, 2014. [Online]. Available: <https://api.semanticscholar.org/CorpusID:9620515>.
- [34] 3S Industry. "Wind energy." (2025), [Online]. Available: <https://www.3sindustry.com/wind-energy/> (visited on 06/27/2025).
- [35] E. Möllerström, "Noise, eigenfrequencies and turbulence behavior of a 200 kw h-rotor vertical axis wind turbine," PhD Thesis, Uppsala University, Jan. 2017. DOI: 10.13140/RG.2.2.15294.23361.
- [36] H. Holttinen and B. H. Jørgensen, *Iea wind tcp annual report 2023*, D. Wettergren, E. Slijepcevic, and M. G. Jørgensen, Eds., <https://iea-wind.org/iea-publications/annual-reports/>, Oct. 2024.
- [37] T. J. Larsen and H. A. Madsen, "On the way to reliable aeroelastic load simulation on vawt's," in *Proceedings of EWEA 2013*, European Wind Energy Association (EWEA), 2013. [Online]. Available: <http://www.ewea.org/annual2013/>.
- [38] C. S. Ferreira, H. A. Madsen, M. Barone, B. Roscher, P. Deglaire, and I. Arduin, "Comparison of aerodynamic models for vertical axis wind turbines," *Journal of Physics: Conference Series*, vol. 524, no. 1, p. 012 125, Jun. 2014. DOI: 10.1088/1742-6596/524/1/012125. [Online]. Available: <https://dx.doi.org/10.1088/1742-6596/524/1/012125>.
- [39] A. Li, "Double actuator cylinder (ac) model of a tandem vertical-axis wind turbine (vawt) counter-rotating rotor concept operating in different wind conditions," Master of Science Thesis, Technical University of Denmark, Jul. 2017. [Online]. Available: [www.vindenergi.dtu.dk%20https://resolver.tudelft.nl/uuid:b3b11052-184c-4435-883a-70197ce177a6](http://www.vindenergi.dtu.dk%20https://resolver.tudelft.nl/uuid:b3b11052-184c-4435-883a-70197ce177a6).
- [40] F. Noca, D. Shiels, and D. Jeon, "Measuring instantaneous fluid dynamic forces on bodies, using only velocity fields and their derivatives," *Journal of Fluids and Structures*, vol. 11, no. 3, pp. 345–350, 1997,

- ISSN: 0889-9746. DOI: <https://doi.org/10.1006/jfls.1997.0081>. [Online]. Available: <https://www.sciencedirect.com/science/article/pii/S0889974697900815>.
- [41] H. A. Madsen, U. S. Paulsen, and L. Vitae, "Analysis of vawt aerodynamics and design using the actuator cylinder flow model," *Journal of Physics: Conference Series*, vol. 555, no. 1, p. 012 065, Dec. 2014. DOI: 10.1088/1742-6596/555/1/012065. [Online]. Available: <https://dx.doi.org/10.1088/1742-6596/555/1/012065>.
- [42] K. Deb, "Multi-objective optimization," in *Search Methodologies: Introductory Tutorials in Optimization and Decision Support Techniques*, E. K. Burke and G. Kendall, Eds. Boston, MA: Springer US, 2014, pp. 403–449, ISBN: 978-1-4614-6940-7. DOI: 10.1007/978-1-4614-6940-7\_15. [Online]. Available: [https://doi.org/10.1007/978-1-4614-6940-7\\_15](https://doi.org/10.1007/978-1-4614-6940-7_15).
- [43] J. Blank and K. Deb, "Pymoo: Multi-objective optimization in python," *IEEE Access*, vol. 8, pp. 89 497–89 509, 2020.
- [44] J. Blank. "Reference directions." (2020), [Online]. Available: [https://pymoo.org/misc/reference\\_directions.html](https://pymoo.org/misc/reference_directions.html) (visited on 02/28/2025).
- [45] I. Das and J. E. Dennis, "Normal-boundary intersection: A new method for generating the pareto surface in nonlinear multicriteria optimization problems," *SIAM Journal on Optimization*, vol. 8, no. 3, pp. 631–657, 1998. DOI: 10.1137/S1052623496307510. eprint: <https://doi.org/10.1137/S1052623496307510>. [Online]. Available: <https://doi.org/10.1137/S1052623496307510>.
- [46] P. F. Melani, F. Balduzzi, G. Ferrara, and A. Bianchini, "An annotated database of low reynolds aerodynamic coefficients for the naca0021 airfoil," *AIP Conference Proceedings*, vol. 2191, no. 1, p. 020 111, Dec. 2019, ISSN: 0094-243X. DOI: 10.1063/1.5138844. eprint: [https://pubs.aip.org/aip/acp/article-pdf/doi/10.1063/1.5138844/13149194/020111\\_1\\_online.pdf](https://pubs.aip.org/aip/acp/article-pdf/doi/10.1063/1.5138844/13149194/020111_1_online.pdf). [Online]. Available: <https://doi.org/10.1063/1.5138844>.
- [47] C. S. Ferreira and F. Scheurich, "Demonstrating that power and instantaneous loads are decoupled in a vertical-axis wind turbine," *Wind Energy*, vol. 17, no. 3, pp. 385–396, 2013. DOI: 10.1002/WE.1581. eprint: <https://onlinelibrary.wiley.com/doi/pdf/10.1002/we.1581>. [Online]. Available: <https://onlinelibrary.wiley.com/doi/abs/10.1002/we.1581>.
- [48] E. Möllerström, F. Ottermo, J. Hylander, and H. Bernhoff, "Noise emission of a 200 kw vertical axis wind turbine," *Energies*, vol. 9, no. 1, 2016, ISSN: 1996-1073. DOI: 10.3390/en9010019. [Online]. Available: <https://www.mdpi.com/1996-1073/9/1/19>.
- [49] D. E. Berg, "Customized airfoils and their impact on vawt (vertical-axis wind turbine) cost of energy," in *Windpower '90 Conference*, Sandia National Labs., Albuquerque, NM (United States), Jan. 1990. [Online]. Available: <https://www.osti.gov/biblio/6821919>.
- [50] B. Montgomerie, "Methods for root effects, tip effects and extending the angle of attack range to  $\pm 180^\circ$ , with application to aerodynamics for blades on wind turbines and propellers," Swedish Defence Research Agency, Tech. Rep. FOI-R-1305-SE, Jun. 2004. [Online]. Available: <https://foi.se/rapporter/rapportsammanfattning.html?reportNo=FOI-R--1305--SE>.
- [51] D. De Tavernier, C. Ferreira, and G. van Bussel, "Airfoil optimisation for vertical-axis wind turbines with variable pitch," *Wind Energy*, vol. 22, Jan. 2019. DOI: 10.1002/we.2306.
- [52] *Fit*, version 2023a, 2023. [Online]. Available: <https://nl.mathworks.com/help/curvefit/fit.html> (visited on 02/27/2025).
- [53] D. M. Hawkins, "The problem of overfitting," *Journal of Chemical Information and Computer Sciences*, vol. 44, no. 1, pp. 1–12, Jan. 2004, ISSN: 0095-2338. DOI: 10.1021/ci0342472. [Online]. Available: <https://doi.org/10.1021/ci0342472>.
- [54] B. Strom, S. L. Brunton, and B. Polagye, "Intracycle angular velocity control of cross-flow turbines," *Nature Energy*, vol. 2, 8 Jun. 2017, ISSN: 2058-7546. DOI: 10.1038/nenergy.2017.103. [Online]. Available: <https://doi.org/10.1038/nenergy.2017.103>.
- [55] W. Munters and J. Meyers, "Towards practical dynamic induction control of wind farms: Analysis of optimally controlled wind-farm boundary layers and sinusoidal induction control of first-row turbines," *Wind Energy*

- Science*, vol. 3, no. 1, pp. 409–425, 2018. DOI: 10.5194/wes-3-409-2018. [Online]. Available: <https://wes.copernicus.org/articles/3/409/2018/>.
- [56] J. A. Frederik, B. M. Doekemeijer, S. P. Mulders, and J.-W. van Wingerden, “The helix approach: Using dynamic individual pitch control to enhance wake mixing in wind farms,” *Wind Energy*, vol. 23, no. 8, pp. 1739–1751, 2020. DOI: <https://doi.org/10.1002/we.2513>. eprint: <https://onlinelibrary.wiley.com/doi/pdf/10.1002/we.2513>. [Online]. Available: <https://onlinelibrary.wiley.com/doi/abs/10.1002/we.2513>.
- [57] V. Patil and D. Pawar, “The optimal crossover or mutation rates in genetic algorithm: A review,” *International Journal of Applied Engineering and Technology*, vol. 5, no. 3, pp. 38–41, 2015, ISSN: 2277-212X.
- [58] A. Hassanat, K. Almohammadi, E. Alkafaween, E. Abunawas, A. Hammouri, and V. B. S. Prasath, “Choosing mutation and crossover ratios for genetic algorithms—a review with a new dynamic approach,” *Information*, vol. 10, no. 12, 2019, ISSN: 2078-2489. DOI: 10.3390/info10120390. [Online]. Available: <https://www.mdpi.com/2078-2489/10/12/390>.
- [59] K. Deb, K. Sindhya, and T. Okabe, “Self-adaptive simulated binary crossover for real-parameter optimization,” in *Proceedings of GECCO 2007: Genetic and Evolutionary Computation Conference*, Jul. 2007, pp. 1187–1194. DOI: 10.1145/1276958.1277190.
- [60] K. Deb and R. Agrawal, “Simulated binary crossover for continuous search space,” *Complex Systems*, vol. 9, pp. 115–148, 1995.
- [61] J. Blank. “Crossover.” (2020), [Online]. Available: <https://pymoo.org/operators/crossover.html> (visited on 03/14/2025).
- [62] Jansen and Wegener, “The analysis of evolutionary algorithms—a proof that crossover really can help,” *Algorithmica*, vol. 34, no. 1, pp. 47–66, Sep. 2002. DOI: 10.1007/s00453-002-0940-2. [Online]. Available: <https://doi.org/10.1007/s00453-002-0940-2>.
- [63] T. Kötzing, D. Sudholt, and M. Theile, “How crossover helps in pseudo-boolean optimization,” in *Proceedings of the 13th Annual Conference on Genetic and Evolutionary Computation*, ser. GECCO ’11, Dublin, Ireland: Association for Computing Machinery, 2011, pp. 989–996, ISBN: 9781450305570. DOI: 10.1145/2001576.2001711. [Online]. Available: <https://doi.org/10.1145/2001576.2001711>.
- [64] K. Deb and S. Agrawal, “A niched-penalty approach for constraint handling in genetic algorithms,” in *Artificial Neural Nets and Genetic Algorithms*, Vienna: Springer Vienna, 1999, pp. 235–243, ISBN: 978-3-7091-6384-9. DOI: 10.1007/978-3-7091-6384-9\_40.
- [65] K. Deb and D. Deb, “Analysing mutation schemes for real-parameter genetic algorithms,” *International Journal of Artificial Intelligence and Soft Computing*, vol. 4, pp. 1–28, Feb. 2014. DOI: 10.1504/IJAISC.2014.059280.
- [66] D. Schlierkamp-Voosen, “Optimal interaction of mutation and crossover in the breeder genetic algorithm,” in *International Conference on Genetic Algorithms*, San Francisco, CA, USA: Morgan Kaufmann Publishers Inc., 1993.
- [67] P. Delafin, T. Nishino, L. Wang, and A. Kolios, “Effect of the number of blades and solidity on the performance of a vertical axis wind turbine,” *Journal of Physics: Conference Series*, vol. 753, no. 2, p. 022 033, Sep. 2016. DOI: 10.1088/1742-6596/753/2/022033. [Online]. Available: <https://dx.doi.org/10.1088/1742-6596/753/2/022033>.
- [68] M. S. Sakib and D. T. Griffith, “Parked and operating load analysis in the aerodynamic design of multi-megawatt-scale floating vertical-axis wind turbines,” *Wind Energy Science*, vol. 7, no. 2, pp. 677–696, 2022. DOI: 10.5194/wes-7-677-2022. [Online]. Available: <https://wes.copernicus.org/articles/7/677/2022/>.
- [69] A. Rezaeiha, H. Montazeri, and B. Blocken, “Towards optimal aerodynamic design of vertical axis wind turbines: Impact of solidity and number of blades,” *Energy*, vol. 165, pp. 1129–1148, 2018, ISSN: 0360-5442. DOI: <https://doi.org/10.1016/j.energy.2018.09.192>. [Online]. Available: <https://www.sciencedirect.com/science/article/pii/S0360544218319704>.



# Non-dominated Sorting Genetic Algorithm II

The non-dominated sorting genetic algorithm II (NSGA-II) is an elitist multi-objective genetic algorithm that is commonly used among researchers and in a wide range of applications [42]. NSGA-II is computationally efficient and finds multiple Pareto-optimal solutions while also maintaining good diversity among the solutions [42].

The steps in the NSGA-II algorithm are [42]:

1. Make a random initial population of size  $N_{pop}$ .
2. Call the parent population  $P_t$ . Perform non-dominated sorting on  $P_t$ .
3. Make an empty set,  $P_{t+1}$ , which is the next generation.
4. Make the offspring  $O_t$  by recombination and mutation of the parent population  $P_t$ .
  - The parents are chosen via a binary crowded tournament selection operator.
    - (a) Every individual has a non-domination rank and a crowding distance. The calculation of the crowding distance is explained in Step 8.
    - (b) Two individuals are compared to choose which one will be a parent. The individual with the better rank is selected. If both individuals have the same rank, then the one with the higher crowding distance is selected.
  - The crowding distance operator preserves the diversity of the population because it prefers individuals in less-crowded areas.
5. Make the new set  $R_t$  which is the combination of  $P_t$  and  $O_t$ .  $R_t$  is of size  $2N_{pop}$ .
6. Perform non-dominated sorting on  $R_t$  to get the non-dominated fronts.
7. Add the non-dominated fronts one at a time, in order, to the next generation  $P_{t+1}$  until a complete front cannot be added without the size of  $P_{t+1}$  exceeding  $N_{pop}$ .
  - Call the last front that could not be fully accommodated in  $P_{t+1}$  as  $F_l$ .
  - Delete all other fronts below  $F_l$ .
8. Choose  $K$  solutions from  $F_l$ , where  $K$  is the difference between  $N_{pop}$  and the size of  $P_{t+1}$ , based on crowding distance. This makes the new generation as diverse as possible.
  - (a) Calculate the crowding distance,  $d_i$ , of each solution in  $F_l$ . The crowding distance is a measure of how far away a solution is from other solutions in the objective space, i.e. if the space around a solution is densely or sparsely populated by other solutions.
  - (b) Crowding distance can be calculated in different ways. In NSGA-II, make a cuboid with the nearest neighboring solutions on either side of the solution along each objective as the vertices of the cuboid. The crowding distance is the average side length of the cuboid.
  - (c) The  $K$  solutions with the largest crowding distance are selected and added to  $P_{t+1}$ .
9. The output is  $P_{t+1}$ , the next generation.
10. Iterate, finding the next generation and so on, until the termination criterion is met.

Figure A.1 shows the NSGA-II algorithm schematically. The two steps of selection to create the next generation  $P_{t+1}$  are evident: first by non-domination rank, then by crowding distance.

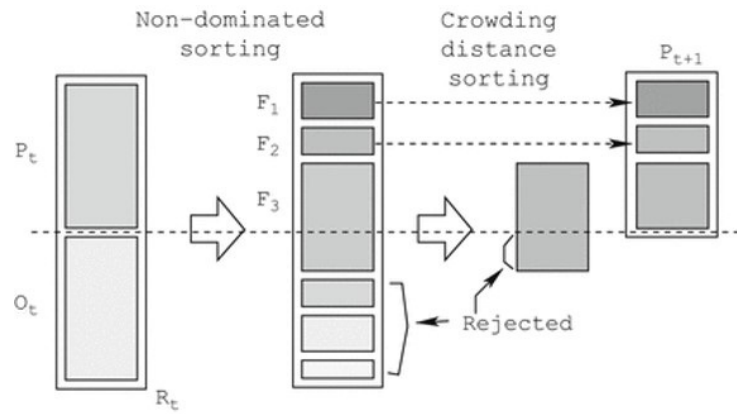


**Figure A.1:** NSGA-II procedure. The next generation  $P_{t+1}$  is created from the parent population  $P_t$  and offspring population  $O_t$  via non-dominated sorting and crowding distance sorting. Figure modified from Deb [42].

# B

## Additional 2D AC Model Validation

Figure B.1 compares the output of the 2D AC model to experiments conducted by LeBlanc and Ferreira [15] for fixed pitch offsets of  $5^\circ$ ,  $0^\circ$ , and  $-5^\circ$ . The experimental VAWT has two NACA 0021 blades, a diameter of 1.48 m, height of 1.508 m, and chord length 0.075 m. The turbine is operated at a tip speed ratio of 4 with incoming wind speed of 4 m/s. The authors use strain gages to measure the strain which is in turn translated into the normal force on the blade. In the 2D AC model implementation, the tangential force terms are included in the calculation of the induced velocities, the modified linear solution from Cheng *et al.* [8] is used, and dynamic stall is not modeled. The airfoil polars used are calculated using XFOIL for a NACA 0021 airfoil and Reynolds number 80,000. We use  $\Delta\theta = 5^\circ$  and  $f = 0.999$ . Only the normal force coefficients are compared because those are the results presented in [15]. As can be seen in Figure B.1, the curves do not line up completely. This is expected since we are comparing our AC model to experimental data. There is, however, some overlap and the overall range in magnitude of normal force coefficient is similar. There are also some trends in loading across the different fixed pitch offsets which the AC model does capture. Between  $0^\circ$  and  $90^\circ$  azimuth, the normal loading increases. When the pitch offset is positive ( $\theta_p = 5^\circ$ ), the loading is shifted earlier in the rotation compared to zero-pitch. When the pitch offset is negative ( $\theta_p = -5^\circ$ ), the loading is shifted later in the rotation compared to zero-pitch. We indeed do see this trend in the AC model results.

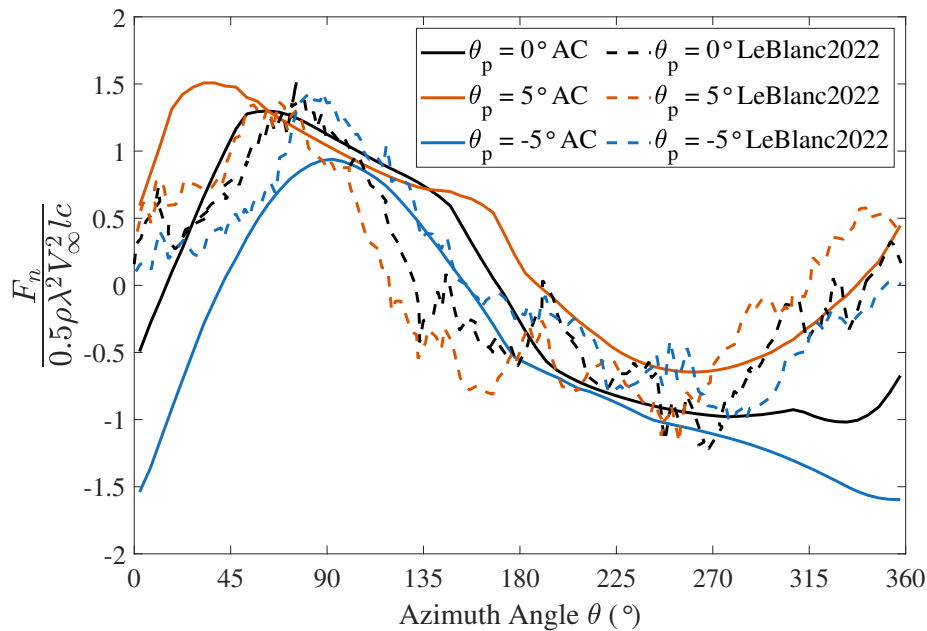


**Figure B.1:** AC model compared to experimental results using strain gages in LeBlanc and Ferreira [15]. Normal force coefficient for different fixed pitch offset:  $0^\circ$ ,  $5^\circ$ , and  $-5^\circ$ .  $B = 2$ ,  $D = 1.48$  m,  $c = 0.075$  m,  $\lambda = 4$ , and  $V_\infty = 4$  m/s. The Reynolds number is 80,000 and the airfoil is NACA 0021.

There are several reasons that could explain the differences between the experimental and model results. Firstly, dynamic stall is not modeled in the AC model. LeBlanc and Ferreira [15] propose that the blades experience dynamic

stall between  $\theta = 90^\circ$  and  $180^\circ$ , especially when  $\theta_p = 5^\circ$ , and also when  $\theta_p = 0^\circ$ . This leads to a steep decline in the normal force in this region, which is not seen in the AC model results (e.g. compare the red curves in Figure B.1). The case that does not experience dynamic stall ( $\theta_p = -5^\circ$ ) matches well with the experimental results in this region (blue curves in Figure B.1). However, in the downwind half, when  $\theta_p = -5^\circ$ , according to the authors, the blade does likely experience stall, which leads to low loading. We see that the AC model overestimates the load in this region, because it does not account for the stalling.

Secondly, the blade-vortex interaction and tower shadow that occur in the experiment create more turbulent wind conditions which affect the loading in the downwind half of the rotor in a way that is not captured in the AC model. Between  $\theta = 180^\circ$  and  $360^\circ$ , LeBlanc and Ferreira [15] cite blade-vortex interaction and tower shadow as causing jumps in the loading, neither of which are modeled in the AC. Therefore, the AC normal forces downwind are smoother than those from the experiments, and blade-vortex interaction and tower shadow could explain the differences between model and experimental results in the downwind half.

There are a few other differences between the experiment and AC model. LeBlanc and Ferreira [15] do not measure the blade tangential force, which could have a small effect on the results. Additionally, the experiment is conducted at a low Reynolds number. According to Melani *et al.* [46], when the Reynolds number is low ( $Re \leq 80,000$ ), the airfoil polars obtained from experimental and numerical studies do not agree and it is difficult to procure accurate airfoil polars for these low Reynolds numbers. In particular, the polars from XFOIL overestimate the lift coefficient in the linear region—the slope of the lift curve is too steep. The authors hypothesize that this is because XFOIL does not properly model the laminar separation bubbles. There is also no agreement among the lift curves from the several compared experimental and numerical studies in the nonlinear region. The authors conclude that XFOIL does not give a suitable prediction of the lift coefficient in both the linear and nonlinear regions. Therefore, the airfoil polars we used from XFOIL are not accurate, which makes a big impact on the AC model force results, but there is not a means to obtain more accurate polars.

Furthermore, there are uncertainties in the experimental measurements. Figure B.2 shows the results presented by LeBlanc and Ferreira [15]. The mean normal force coefficient is shown as a line along with a shaded region around it representing one standard deviation on either side. As can be seen, there is quite a bit of uncertainty. Some possible sources for these small errors are strain gage placement and the material properties [15]. The authors do note that the standard deviation is relatively consistent across azimuth angle, meaning there is a general noise level in the measurement. The darker shaded vertical bars in Figure B.2 show azimuthal sections where there is increased noise from the slip ring in the experimental set-up. This leads to higher uncertainty in the measurements which could potentially explain the difference in peak force magnitude between the experiment and AC model in the upwind section. Overall, the load curves from the experiment are not smooth and the level of uncertainty hinders our comparison to these experimental results.

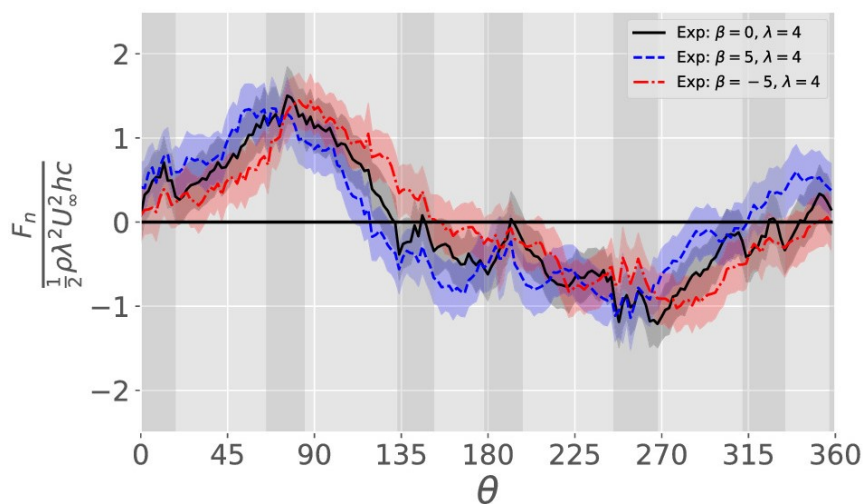


**Figure B.2:** Experimental normal force coefficient for different fixed pitch offset, showing the mean and standard deviation.  $\beta$  is the pitch angle. Figure from LeBlanc and Ferreira [15].